DRA

ADN, C4

NATIONAL AERONAUTICS AND SPACE ADMINISTRATION

The Deep Space Network
Progress Report 42-29

July and August 1975

(NASA-CR-145923) THE DEEP SPACE NETWORK Progress Report, Jul. - Aug. 1975 (Jet Propulsion Lab.) 218 p HC $7.75

N76-14296
THRU
N76-14310
Unclas
G3/31 39375

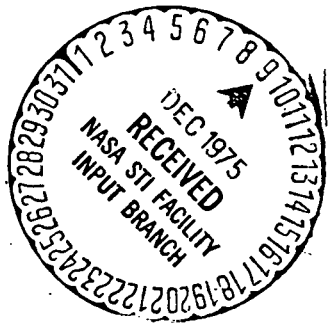

JET PROPULSION LABORATORY
CALIFORNIA INSTITUTE OF TECHNOLOGY
PASADENA, CALIFORNIA

October 15, 1975

NATIONAL AERONAUTICS AND SPACE ADMINISTRATION

The Deep Space Network
Progress Report 42-29

July and August 1975

JET PROPULSION LABORATORY
CALIFORNIA INSTITUTE OF TECHNOLOGY
PASADENA, CALIFORNIA

October 15, 1975

Preface

Beginning with Volume XX, the Deep Space Network Progress Report changed from the Technical Report 32- series to the Progress Report 42- series. The volume number continues the sequence of the preceding issues. Thus, Progress Report 42-20 is the twentieth volume of the Deep Space Network series, and is an uninterrupted follow-on to Technical Report 32-1526, Volume XIX.

This report presents DSN progress in flight project support, tracking and data acquisition (TDA) research and technology, network engineering, hardware and software implementation, and operations. Each issue presents material in some, but not all, of the following categories in the order indicated:

Description of the DSN

Mission Support
- Ongoing Planetary/Interplanetary Flight Projects
- Advanced Flight Projects

Radio Science
- Radio Science Support
- Special Projects

Supporting Research and Technology
- Tracking and Ground-Based Navigation
- Communications—Spacecraft/Ground
- Station Control and Operations Technology
- Network Control and Data Processing

Network Engineering and Implementation
- Network Control System
- Ground Communications
- Deep Space Stations

Operations
- Network Operations
- Network Control System Operations
- Ground Communications
- Deep Space Stations

Planning and Facilities
- TDA Planning
- Facility Engineering

In each issue, the part entitled "Description of the DSN" describes the functions and facilities of the DSN and may report the current configuration of one of the five DSN systems (Tracking, Telemetry, Command, Monitor and Control, and Test and Training).

The work described in this report series is either performed or managed by the Tracking and Data Acquisition organization of JPL for NASA.

Contents

Station Control and Operations Technology

Network Control and Data Processing

NETWORK AND FACILITY ENGINEERING AND IMPLEMENTATION

Network

Deep Space Stations

OPERATIONS

Network Operations

PROGRAM PLANNING

Quality Assurance

DSN Functions and Facilities

N. A. Renzetti
Office of Tracking and Data Acquisition

The objectives, functions, and organization of the Deep Space Network are summarized. Deep space station, ground communication, and network operations control capabilities are described.

The Deep Space Network (DSN), established by the National Aeronautics and Space Administration (NASA) Office of Tracking and Data Acquisition (OTDA) under the system management and technical direction of the Jet Propulsion Laboratory (JPL), is designed for two-way communications with unmanned spacecraft traveling approximately 16,000 km (10,000 mi) from Earth to the farthest planets of our solar system. It has provided tracking and data acquisition support for the following NASA deep space exploration projects, for which JPL has been responsible for the project management, development of the spacecraft, and conduct of mission operations:

(1) Ranger.

(2) Surveyor.

(3) Mariner Venus 1962.

(4) Mariner Mars 1964.

(5) Mariner Venus 1967.

(6) Mariner Mars 1969.

(7) Mariner Mars 1971.

(8) Mariner Venus/Mercury 1973.

The DSN has also provided tracking and data acquisition support for the following projects:

(1) Lunar Orbiter, for which the Langley Research Center carried out the project management, spacecraft development, and mission operations functions.

(2) Pioneer, for which the Ames Research Center carried out the project management, spacecraft development, and mission operations functions.

(3) Apollo, for which the Lyndon B. Johnson Space Center was the project center and the Deep Space Network supplemented the Spaceflight Tracking and Data Network (STDN), which is managed by the Goddard Space Flight Center (GSFC).

(4) Helios, a joint United States/West Germany project.

(5) Viking, for which the Langley Research Center provides the project management and Lander spacecraft, and conducts mission operations, and for which JPL provides the Orbiter spacecraft.

The Deep Space Network is one of two NASA networks. The other, the Spaceflight Tracking and Data Network, is under the system management and technical direction of the Goddard Space Flight Center. Its function is to support manned and unmanned Earth-orbiting and lunar scientific and advanced technology satellites. Although the DSN was concerned with unmanned lunar spacecraft in its early years, its primary objective now and into the future is to continue its support of planetary and interplanetary flight projects.

A development objective has been to keep the network capability at the state of the art of telecommunications and data handling and to support as many flight projects as possible with a minimum of mission-dependent hardware and software. The DSN provides direct support to each flight project through that project's tracking and data systems. This management element is responsible for the design and operation of the hardware and software in the DSN which are required for the conduct of flight operations.

As of July 1972, NASA undertook a change in the interface between the network and the flight projects. Since January 1, 1964, the network, in addition to consisting of the Deep Space Stations and the Ground Communications Facility, had also included the Mission Control and Computing Facility and had provided the equipment in the mission support areas for the conduct of mission operations. The latter facilities were housed in a building at JPL known as the Space Flight Operations Facility (SFOF). The interface change was to accommodate a hardware interface between the network operations control functions and the mission control and computing functions. This resulted in the flight project's picking up the cognizance of the large general-purpose digital computers, which were used for network processing as well as mission data processing. It also assumed cognizance of all of the equipment in the flight operations facility for display and communications necessary for the conduct of mission operations. The network has already undertaken the development of hardware and computer software necessary to do its network operations control and monitor functions in separate computers. This activity became known as the Network Control System implementation. A characteristic of the new interface is that the network provides direct data flow to and from the stations via appropriate ground communications equipment to Mission Operations Centers, wherever they may be; namely, metric data, science and engineering telemetry, and such network monitor data as are useful to the flight project. It accepts command data from the flight project directly into the ground communications equipment for transmission to the station and thence to the spacecraft in a standardized format.

In carrying out its functions, the network activities can be divided into two general areas. The first includes those functions which are associated with the in-flight support and in tracking the spacecraft; its configuration can be characterized as follows:

(1) *DSN Tracking System.* Generates radio metric data; i.e., angles, one- and two-way doppler and range, and transmits raw data to mission control.

(2) *DSN Telemetry System.* Receives, decodes, records, and retransmits engineering and scientific data generated in the spacecraft to Mission Control.

(3) *DSN Command System.* Accepts coded signals from Mission Control via the Ground Communications Facility (GCF) and transmits them to the spacecraft in order to initiate spacecraft functions in flight.

The second category of activity supports testing, training, and network operations control functions and is configured as follows:

(1) *DSN Monitor and Control System.* Instruments, transmits, records, and displays those parameters of the DSN necessary to verify configuration and validate the network. Provides operational direction and configuration control of the network and primary interface with flight project mission control personnel.

(2) *DSN Test and Training System.* Generates and controls simulated data to support development, test, training, and fault isolation within the DSN. Participates in mission simulation with flight projects.

The capabilities needed to carry out the above functions have evolved in three technical areas:

(1) The Deep Space Stations that are distributed around Earth and which, prior to 1964, formed part of the Deep Space Instrumentation Facility. The technology involved in equipping these stations is strongly related to the state of the art of telecommunications and flight/ground design considerations and is almost completely multimission in character. Table 1 gives a description of the Deep Space Stations and the Deep Space Communications Complexes (DSCCs) they comprise.

(2) Ground communications. This technology supports the Earth-based point-to-point voice and data communications from the stations to the Network Operations Control Area at JPL, Pasadena, and to the Mission Operations Centers, wherever they may be. It is based largely on the capabilities of the common carriers throughout the world which are engineered into an integrated system by the Goddard Space Flight Center for support of all NASA programs. The term "Ground Communications Facility" is used for the sets of hardware and software needed to carry out the functions.

The Network Operations Control Center is the functional entity for centralized operational control of the network and interfaces with the users. It has two separable functional elements; namely, Network Operations Control and Network Data Processing.

The functions of the Network Operations Control Center are:

(1) Control and coordination of network support to meet commitments to network users.

(2) Utilization of the network data processing computing capability to generate all standards and limits required for network operations.

(3) Utilization of network data processing computing capability to analyze and validate the performance of all network systems.

The personnel who carry out the above functions are on the first floor of Building 230, wherein mission operations functions are carried out by certain flight projects. Network personnel are directed by an Operations Control Chief. The functions of the Network Data Processing are:

(1) Processing of data used by Network Operations Control for the control and analysis of the network.

(2) Display in Network Operations Control Area of data processed in Network Data Processing Area.

(3) Interface with communications circuits for input to and output from Network Data Processing Area.

(4) Data logging and production of the intermediate data records.

The personnel who carry out these functions are located in Building 202, which is approximately 200 m from Building 230. The equipment consists of minicomputers for real-time data system monitoring, two XDS Sigma 5's, display, magnetic tape recorders, and appropriate interface equipment with the ground data communications.

Table 1. Tracking and data acquisition stations of the DSN

DSCC	Location	DSS	DSS serial designation	Antenna		Year of initial operation
				Diameter, m (ft)	Type of mounting	
Goldstone	California	Pioneer	11	26(85)	Polar	1958
		Echo	12	26(85)	Polar	1962
		(Venus)[a]	13	26(85)	Az-El	1962
		Mars	14	64(210)	Az-El	1966
Tidbinbilla	Australia	Weemala	42	26(85)	Polar	1965
		Ballima	43	64(210)	Az-El	1973
—	Australia	Honeysuckle Creek	44	26(85)	X-Y	1973
Madrid	Spain	Robledo	61	26(85)	Polar	1965
		Cebreros	62	26(85)	Polar	1967
		Robledo	63	64(210)	Az-El	1973

[a]A maintenance facility. Besides the 26-m (85-ft) diam Az-El mounted antenna, DSS 13 has a 9-m (30-ft) diam Az-El mounted antenna that is used for interstation time correlation using lunar reflection techniques, for testing the design of new equipment, and for support of ground-based radio science.

DSN Command System Mark III-75

W. G. Stinnett
DSN Systems Engineering Office

A description of the DSN Command System Mark III-75 configuration is presented. The functional operation of the system is discussed, as well as a brief description of the new implementation included in the Mark III-75 configuration.

I. Introduction

The DSN Command System, one of the six network systems, has almost completed the implementation of new capabilities and configurations to provide the required support to missions set for the 1975 to 1977 era. These changes will lead to completion of the Mark III-75 configuration. These configurations and capabilities will support the ongoing Pioneers 6 through 10, Pioneer Saturn, and Helios A missions. These configurations and capabilities will further support the Viking and Helios B missions. (At the time of submittal of this article, the first Viking Orbiter-Lander spacecraft had been launched and successfully supported by the DSN Command System. The second Viking launch is imminent.)

The DSN Command System Mark III-75 configurations are shown in Fig.1. The significant changes that have occurred, or are occurring, to complete the Mark III-75 configurations are denoted in Fig. 1. These changes are occurring in two areas: (1) The Network Operations Control Center (NOCC), and (2) The 64-meter deep space stations (DSSs). The purpose of the NOCC is to provide capabilities to control and monitor the operation of the DSN Command System in an environment where widely separated deep space stations are simultaneously supporting different spacecraft. The Mark III-75 NOCC will provide the control and monitoring functions. The significant changes that are occurring at the 64-meter deep space stations are: (1) the implementation of an additional receiver-exciter (Block IV), and (2) the implementation of a high-power (100-kW) transmitter at the 64-meter deep space stations in Australia and Spain.

II. Data Flow and Functional Operation

The data flow and functional operation of the DSN Command System can best be described by defining three periods of operation: (1) pre-track, (2) during track, and (3) post-track. The following paragraphs describe the operation of the system during these periods. (Refer to Fig. 1 for data flow description.)

A. Pre-Track Operation

Prior to a spacecraft track, the DSS operations personnel perform the station countdown. This involves the selection of the equipment to be used, and the validation that a complete and correct data path has been established and that all support equipment is operating

within specifications. After the station countdown is complete (approximately 30 minutes prior to spacecraft acquisition), the control of the station's command functions is accomplished remotely via high-speed data messages from the NOCC.

The appropriate standards and limits, corresponding to the configuration, are established via high-speed data messages. Spacecraft-dependent parameters, such as symbol period, command subcarrier frequency, exciter frequency, and appropriate abort limits, are established via these messages. After the proper configuration and standards and limits have been established, test commands are transmitted through the system to ensure that the system can accept spacecraft commands via high-speed data messages, temporarily store the commands, and properly confirm transmission. After NOCC operations personnel have established that the system is operating properly, the system is ready to be turned over to the flight project for acceptance of actual spacecraft commands during the spacecraft track period.

B. During Track Operation

Commands generated at the Mission Operations Center are placed in high-speed data blocks and transmitted to the DSS command stack. The command stack provides storage of high-speed data blocks (stack modules) of command data. Each stack module consists of up to six command elements. Each command element contains up to 71 bits of command data and, at project option, can be either timed or nontimed.

Commands can also be entered and controlled locally at the DSS via a manual input/output device at the Command Processor. A manual buffer in the Command Processor, capable of holding up to six command elements of up to 71 bits each, can be loaded via the local input/output device or by high-speed data messages from the Mission Operations Center. The entire contents of the manual buffer or any one command element in the buffer can be transferred to the command stack.

The top command element in the first stack module is eligible for transmission to the spacecraft. Nontimed commands are transmitted immediately after eligibility. Timed commands are transmitted after becoming eligible at the time specified in the high-speed data block. At the time of transmission of the command element, the Command Processor establishes the proper mode (see Fig. 2 for description of the various modes) and configuration of the Command Modulator Assembly; then the command is transferred to the Command Modulator Assembly for immediate transmission via the Receiver-Exciter, Transmitter, Microwave, and Antenna Subsystems. Related verification, confirmation, and abort criteria (if required) are established by the Command Processor.

During these command operations, events may occur in which high-speed data message transmission to the Mission Operations Center becomes necessary. The following events initiate message transmission to the Mission Operations Center:

(1) Confirmed command element.

(2) Aborted command element.

(3) DSS alarm or alarm clear.

(4) Response to a recall.

(5) High-speed data block rejection by the Command Processor.

(6) Acknowledged receipt of a high-speed data block.

A digital Original Data Record of DSN Command System activity is generated at the DSS. An analog record of the Command Modulator Assembly output is also generated at the DSS by the Pre-Post Detection Recording Subsystem.

During the spacecraft track, the NOCC receives all high-speed data messages being received by and generated by the DSS. DSN Command System verification, alarm diagnosis, and displays are accomplished by the NOCC.

C. Post-Track Operations

At the Mission Operations Center, during the commanding of the spacecraft, a data record is generated to provide a log of all commands transmitted to the spacecraft. The post-track operation period has been set aside to recover missing data, if, during the track, data failed to get logged on the data record. Data are extracted from the DSS Original Data Record and played back via high-speed data messages to the Mission Operations Center. The playback data are used to complete the data record at the Mission Operations Center.

III. NOCC Capabilities

The final configuration of the NOCC to support the Mark III-75 Command System is planned for completion in the last quarter of calendar year 1975. The NOCC has been implemented in three phases. The first two phases included minimum mandatory functions to accomplish Command System control and monitoring. These functions in many cases were awkward and inefficient to use. The third phase of implementation improves and adds to the

functions provided in the first two phases. The description below includes the functions to be provided in the third phase of implementation and completes the NOCC implementation for the Mark III-75 configuration.

A. High-Speed Data Message Generation

The NOCC will have the capability to generate the high-speed data messages required to be transmitted to the deep space stations. These messages include the following data:

(1) Configuration.

(2) Standards and limits.

(3) Test commands.

(4) Mode control.

(5) Recall request.

The first three types of data listed above contain spacecraft-unique parameters. Thus, numerous high-speed data messages are required. These messages are generally constructed and stored in advance of their use. However, the capability is provided to modify parameters within these messages for immediate transmission to a DSS.

B. High-Speed Data Message Transmission

Included in the capabilities at the NOCC are the functions of transmitting the high-speed messages to a DSS, verifying proper receipt at the DSS, and verifying proper processing by the DSS.

C. System Validation

During a spacecraft track, the NOCC monitors the operation of the system to ensure its proper functioning. Status messages from the DSS are received and processed, and displays are provided to DSN operations personnel. In the event of failure, these displays provide the necessary tools for failure isolation and system recovery.

IV. DSS Capabilities

As stated before, the major changes occurring to complete the Mark III-75 Command System at the deep space stations are: (1) the implementation of an additional receiver–exciter at the 64-meter stations, and (2) the implementation of 100-kW transmitters at the deep space stations in Spain and Australia. Completion of these implementations is planned within the next few months. The additional exciter will provide redundancy to a major element in the Command System. This will increase the ability of the DSN to provide faster command recovery times in support of the flight projects. The implementation of the high-power transmitters provides a significant increase in DSN uplink capabilities, as well as providing physical redundancy to another major element in the Command System.

V. Future Plans

After completion of the Mark III-75 configuration, the next major upgrade to the system is planned for support of the Mariner Jupiter/Saturn 1977 mission. Replacement of the obsolete Command Processors at the deep space stations is planned. This Mark III-77 configuration will include dedicated Command Processors at the deep space stations (current processors are shared between the command and telemetry functions at the DSS). These new processors will greatly increase processing speed and core available for the command functions at the DSS. This will allow the DSN to provide support to missions utilizing higher command bit rate transmissions. The relatively slow processing speed and core limitations existing in the current processor do not allow bit rate transmissions required by future spacecraft.

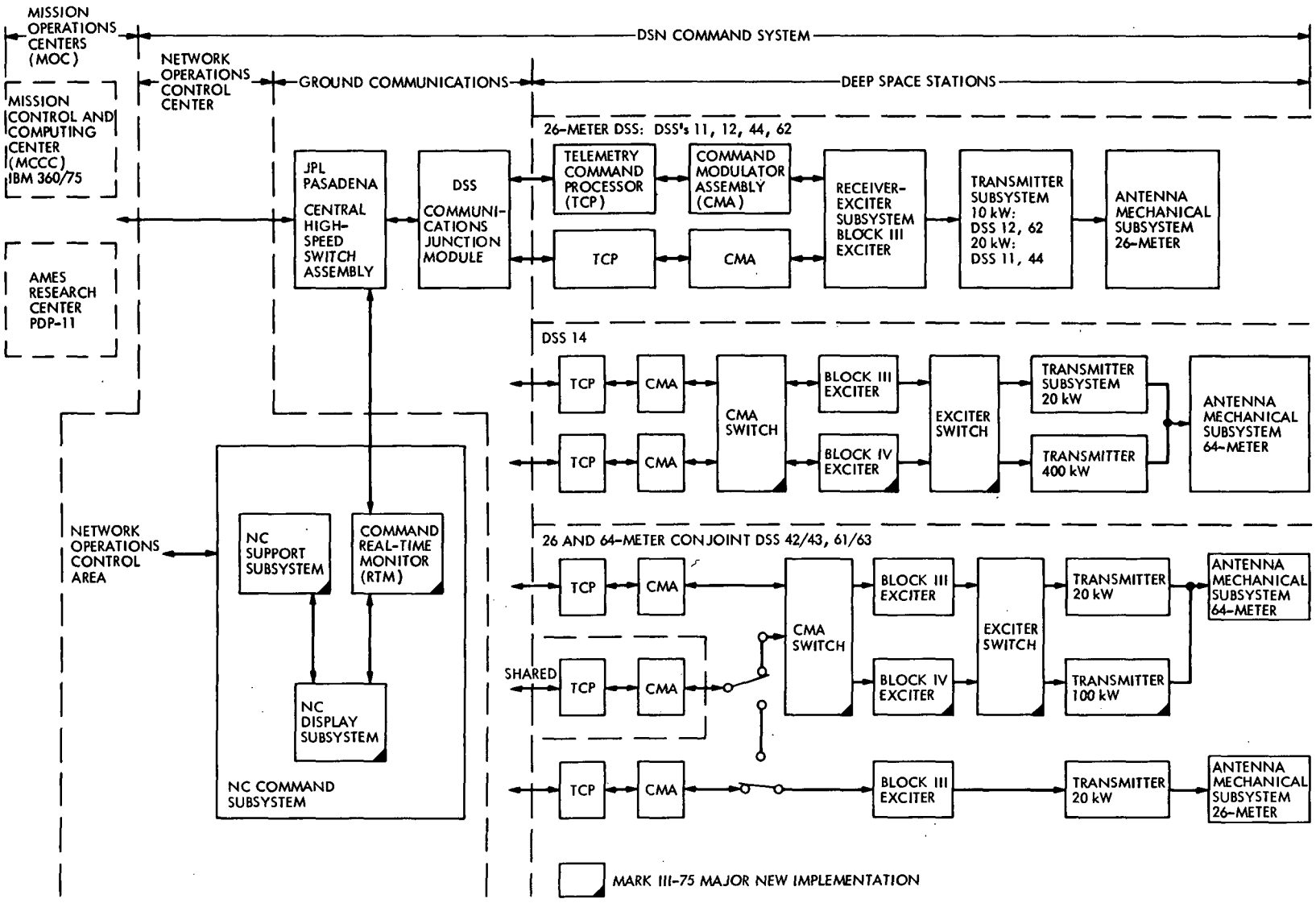

Fig. 1. DSN Command System Mark III-75 configuration

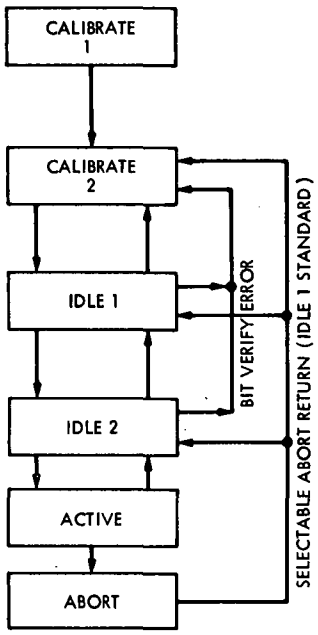

TCP MODE	PRIME PURPOSE	DATA ACCEPTED VIA HIGH SPEED	COMMENTS
CALIBRATE 1	ALLOWS DSS OPS PERSONNEL TO PERFORM INITIALIZATION TASKS	CONFIGURATION STANDARDS AND LIMITS, "MODE CONTROL," RECALL	UPON RECEIPT OF A STANDARDS AND LIMITS AND CONFIGURATION HSD BLOCK, THE CALIBRATE 2 MODE WILL BE ENTERED
CALIBRATE 2	STANDARD MODE FOR UPDATING STANDARDS AND LIMITS AND CONFIGURATION DATA VIA HIGH SPEED PRIOR TO SPACECRAFT ACQUISITION	CONFIGURATION STANDARDS AND LIMITS "MODE CONTROL," RECALL	MULTIMISSION STANDARD PROCEDURES SHOULD STATE THAT THIS MODE IS TO BE ENTERED FOR CHANGING SUBCARRIER FREQUENCY, BIT RATE
IDLE 1	SAFE MODE - CANNOT COMMAND. PROVISION FOR IDLE/ACQUISITION SEQUENCE. ALLOWS CONFIGURATION AND STANDARDS AND LIMITS TO BE CHANGED	CONFIGURATION STANDARDS AND LIMITS "MODE CONTROL," RECALL	ALL STANDARDS AND LIMITS AND CONFIGURATION DATA PARAMETERS WILL TAKE IMMEDIATE EFFECT IN THIS MODE
IDLE 2	ALLOWS ENTRY INTO ACTIVE MODE. PROVIDES IDLE/ACQUISITION SEQUENCE DURING COMMAND PERIODS	RECALL AND MODE CONTROL DATA ONLY	MODE CONTROL DATA CONTAINED IN THE COMMAND ELEMENT BLOCK FOR THE MARK III-75 COMMAND SYSTEM
ACTIVE	COMMAND TRANSMISSION	RECALL AND MODE CONTROL DATA ONLY	
ABORT	PROVIDES ABORT INSTRUCTION TO CMA	RECALL AND MODE CONTROL DATA ONLY	

NOTES: 1. COMMAND DATA MESSAGES WILL BE ACCEPTED IN ALL MODES
2. ALARM MESSAGES/ALARM DATA WILL BE TRANSMITTED TO THE MOC IN ALL MODES EXCEPT ABORT

Fig. 2. System mode description

Viking Mission Support

D. J. Mudgway and A. I. Bryan
DSN Systems Engineering Office
D. W. Johnston
DSN Operations Office

The work described in this article concludes all DSN preparations for the Viking A launch. The final spacecraft compatibility tests were completed by July 7, and the personnel test and training effort was concluded on August 7. The first spacecraft was launched on August 20, 1975, and a brief summary of the coverage provided in the near-Earth phase of the mission is included.

I. Background

The previous article in this series (Ref. 1) described the Viking compatibility testing with Viking Orbiter No. 1 in May 1975. This article describes the follow-on testing for Viking Spacecraft No. 2 (Orbiter and Lander combined). These tests mark the completion of formal radio frequency (RF) telecommunications compatibility testing between the DSN and the Viking Project for the 1975 mission. Also, in previous articles (Refs. 1, 2, and 3), the progress of the personnel test and training exercises at the deep space stations was described. Here, this activity is continued to its conclusion, and the strategy for initial acquisition has been included.

II. Viking Spacecraft Radio Frequency Compatibility Test

This assessment and status is derived from test results obtained between STDN(MIL 71) and Viking Spacecraft No. 2 at Cape Canaveral, Florida, on July 7, 1975. Procedures for conducting this test were prepared by the DSN with test parameters and design criteria provided by the Martin Marietta Corporation and the JPL Orbiter Telecommunications Section.

The total test time was 11 hours. The successful completion of the tests within the scheduled time period was due in large measure to the excellent cooperation and coordination between the Spacecraft Test Teams and the JPL/Goddard STDN(MIL 71) Team.

A. Test Objectives

The objectives of the compatibility tests were to verify, in the spacecraft configuration, the capability of:

(1) Viking Orbiter No. 2 to receive Viking Orbiter commands and reject Viking Lander Capsule commands.

(2) Viking Lander Capsule No. 2 to receive Viking Lander Capsule commands and reject Viking Orbiter commands.

These tests were accomplished in accordance with Ref. 4.

B. Test Conditions

Viking Spacecraft No. 2 was configured for mission operations and STDN(MIL 71) was configured to simulate a 64-m-antenna station. Viking Spacecraft No. 2 was located in the clean room of Spacecraft Assembly and Encapsulation Facility No. 1, Cape Canaveral, Florida, and STDN(MIL 71) was located at Merritt Island, Florida. An S-band RF link (approximately 5 km (3 mi)) was utilized between the flight article and the ground station.

The ground station software utilized in performing these tests was supplied by the DSN and was a subset of software officially released to the station for Viking Project support. The software consisted of the Telemetry and Command Program, which provides independent control of the commanding and telemetry functions. Commands may be controlled manually from the station or automatically from the Mission Control and Computing Center. Telemetry may be decoded, formatted, and transmitted to the Mission Control and Computing Center for decommutation and display.

C. Test Results

The following command tests were performed:

(1) Orbiter/Lander Command Discrimination Test 3A (Side 1).

(2) Orbiter/Lander Command Discrimination Test 3B (Side 2).

During the initial attempt to transmit commands to the spacecraft, commands were rejected because of an incorrect spacecraft identifier in the command bit structure. A new set of commands was then transmitted which contained the proper spacecraft identifier. All commands were successfully accepted and executed by the spacecraft. However, two commands (DC-2A, ranging channel ON, and DC-2AR, ranging channel OFF) gave indications of each command containing one bit error. This problem was traced to an error in the octal structure for these two commands.

In order for the DSN command modulator assembly to function correctly, the command modulator assembly command word must contain 63 bits, although only 62 bits are transmitted. Additionally, the 63rd bit of the command structure must always be high. This bit serves as a marker bit to flag the command software that the 62nd bit of the spacecraft command is the final bit to be transmitted. To verify that this was a true condition, the proper octals for DC-2A and DC-2AR were successfully transmitted to the spacecraft, accepted, executed, and gave no indication of bit errors or corrections.

III. DSN Test and Training

The test and training effort was concluded on August 10, 1975, with the successful completion of the DSN configuration verification test program. The following paragraphs summarize events leading to this readiness milestone.

A. Mission Configuration Tests

The system-level mission configuration test program for Viking launch and cruise was concluded successfully and included the following:

(1) Telemetry system strong and weak signal performance tests and telemetry simulation tests. In addition, planetary phase telemetry testing was accomplished at DSS 14 (Goldstone, California).

(2) Command system tests.

(3) Monitor and control system tests.

(4) Tracking system tests (radio metric data).

(5) Simulation system tests.

B. Operational Verification Tests

The launch/cruise series of operational verification tests was completed with all of the deep space stations (DSSs 11, 12, and 14 at Goldstone, California; DSSs 42, 43, and 44 in Australia; and DSSs 61, 62, and 63 in Spain). The personnel manning the stations, the Ground Communications Facility, and the Network Operations Control Center are considered fully trained to support the launch and cruise phases of the Viking mission.

Recent effort was directed toward the training of personnel at the prime and backup stations in Australia (DSSs 42 and 44) for the initial acquisition of the Viking spacecraft downlink signal and subsequent establishment of uplink capability (command, ranging, etc.) with the spacecraft. The initial acquisition sequence occurs shortly after spacecraft injection into the trans-Mars trajectory and separation from the launch vehicle.

Although "prime crews" are designated for the actual launches, initial acquisition operational verification tests were conducted with all crews at DSSs 42 and 44, as well

as the Network Operations Teams at the Jet Propulsion Laboratory. Dual-station initial acquisition operational verification tests with simulated anomalies have been conducted.

C. Configuration Verification Tests, Control, and Freeze

To ensure that all DSN facilities maintained their "ready" state for the Viking launch and cruise support, the facilities were placed under configuration control on July 4, 1975. This ensures that the facilities can return to the Viking configuration in less than 12 hours from notification.

On July 22, 1975, all deep space stations were placed under modified configuration control, which meant that no Engineering Change Orders could be initiated (for Viking planetary implementation, as well as other projects) without prior concurrence by the Viking Network Operations Project Engineer or DSN Manager.

Configuration freeze was applied to the initial acquisition stations in Australia (DSSs 42 and 44) on August 10, upon completion of a configuration verification test which concluded with the stations configured for the initial acquisition pass. This automatically prohibited the stations from supporting any other spacecraft tracks. This configuration control and freeze activity for Viking is shown in "bar chart timeline" form in Fig. 1.

D. Operational Readiness Test

An operational readiness test was conducted by the Project on August 6, 1975, and provided a final check on the ability of the deep space stations, the Ground Communications Facility, and the Network Operations Control Center to support the launch and cruise phases of the Viking mission.

E. Flight Operations Personnel Test and Training

The DSN has successfully participated in the flight operations personnel test and training exercises required to prepare the Viking flight team personnel for their role in supporting the Viking dual-spacecraft flight operations.

F. Initial Acquisition Strategy

The initial acquisition strategy was jointly worked out by the DSN and other Viking flight team members.

Several safeguards must be part of the initial acquisition configuration plan: (1) to ensure that the spacecraft locks to the ground transmitter signal, the S-band Acquisition Antenna must be used; and (2) to avoid receiver saturation, when receiving downlink on the S-band Cassegrain Monopulse (SCM) Antenna, the maser bypass mode must be used. The Project made a decision to run a Canopus Star map prior to Canopus Star lock. This dictates that uplink transmitter power from the "SCM Antenna" and "SCM Maser in" is required to ensure continuous up and down link lock during the 720-degree roll. The attitude of the spacecraft is such that nulls greater than 40 dB are anticipated.

All concerned agreed that the station reconfiguration should be done at L + 1 hour 36 minutes, but since telemetry was critical at this time, the reconfiguration had to be accomplished without loss of telemetry, which means that DSS 42 could not simply turn off its transmitter and reconfigure, as this would result in loss of two-way lock and 1 minute of telemetry data.

The plan worked out to accomplish the station uplink and downlink reconfiguration was to transfer the uplink to DSS 44 while DSS 42 reconfigured its transmitter and maser; then transfer the uplink back to DSS 42. This unusual transfer permitted the reconfiguration and ensured that valuable bioshield telemetry data would be continuously received.

The initial acquisition, initial conditions at DSSs 42 and 44, and the strategy are illustrated as a function of time in Figs. 2 and 3.

G. Additional Testing

Due to launch date slippage caused by problems with the Titan booster portion of the launch vehicle (defective vector control valve) and the Viking Orbiter spacecraft (battery power drain), it was necessary to formulate a plan to reverify certain stations of the DSN prior to any rescheduled launch time. This plan is illustrated in Fig. 4. The testing required for reverification included:

(1) Cruise phase operational verification tests for DSSs 11, 43, and 61.

(2) Mission configuration tests, configuration verification tests, and dual-station initial acquisition operational verification tests for DSSs 42 and 44.

(3) Extended precalibration checkouts of DSSs 42, 44, and 61.

This degree of retesting was needed in order to re-establish the high level of confidence prevailing at the originally scheduled launch time.

H. Summary

Because the Viking Project is the most complex deep space mission ever supported by the DSN, a heavy test schedule has been utilized to verify the various steps toward readiness and has resulted in a high degree of confidence in the ability of the Deep Space Network to support the launch and cruise phases of the Viking mission. Additionally, the Launch - 48-Hour Contingency Pre-launch Testing Plan ensures continued readiness regardless of slip in launch date.

Mission configuration and operational verification testing in preparation for Viking planetary operations is scheduled to begin in September 1975.

IV. Conclusions

With the completion of RF compatibility testing on both Viking Orbiters and Landers and personnel test and training exercises at all stations of the network, the DSN declared its readiness to support launch and cruise mission operations on July 23, 1975, at the formal Launch Readiness Review and again at an update review on August 9, 1975.

The lengthy planning, implementation, testing, and training activity required to achieve this state of readiness has occupied the DSN at various levels of activity for nearly seven years. During this time, demands have been made on all elements of the DSN and the Telecommunications Engineering Division to meet scheduled milestones and to find solutions to cope with unexpected problems. All who contributed to this effort are to be commended.

References

1. Mudgway, D. J., Bryan, A. I., and Johnston, D. W., "Viking Mission Support," in *The Deep Space Network Progress Report 42-28*, pp. 11–14, Jet Propulsion Laboratory, Pasadena, Calif., Aug. 15, 1975.
2. Mudgway, D. J., et al. "Viking Mission Support," in *The Deep Space Network Progress Report 42-27*, pp. 10–27, Jet Propulsion Laboratory, Pasadena, Calif., June 15, 1975.
3. Mudgway, D. J., and Johnston, D. W., "Viking Mission Support," in *The Deep Space Network Progress Report 42-26*, pp. 8–16, Jet Propulsion Laboratory, Pasadena, Calif., Apr. 15, 1975.
4. *Master Integrated Test Plan, Viking 75 Spacecraft/Orbiter/Lander to Launch and Flight Operations System and Tracking and Data System Compatibility Test Plan*, Rev. L, NASA Document PL-3710005, Mar. 29, 1975.

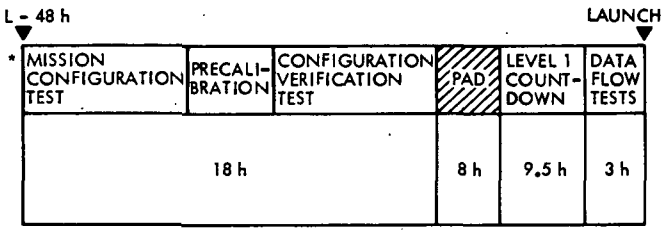

*APPROXIMATE 8-HOUR LEAD TIME REQUIRED PRIOR TO THIS TEST AND CALIBRATION BLOCK TO ENABLE THE EXERCISE TO BE SCHEDULED AND THE DSS SHIFT PERSONNEL ALERTED

Fig. 1. Contingency prelaunch testing plan

DSS 42/44 SCM D/L GAIN	= 53.3 dB (0.33 deg)
DSS 42/44 SCM U/L GAIN	= 51.8 dB (0.36 deg)
DSS 42 SAA D/L GAIN	= 21.7 dB (16 deg)
DSS 42 SSA U/L GAIN	= 18.9 dB (17 deg)
DSS 44 SAA D/L GAIN	= 20.8 dB (5 deg)

DSS 42	DSS 42
RECEIVER 5 - SCM (MASER BY-PASS)	RECEIVER 1 - SCM (MASER BY-PASS)
RECEIVER 6 - SAA (MASER 2)	RECEIVER 2 - SAA (MASER 2)
TXR (10 kW) SAA	TXR (1 kW) - SCM
T/MODE APS TAPE	T/MODE APS TAPE

Fig. 2. Initial acquisition strategy: initial conditions

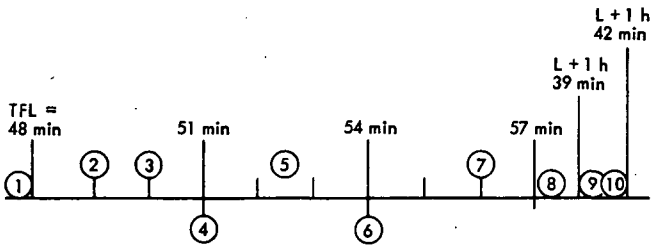

1 DSS 42 RECEIVER 6 1-WAY TELEMETRY TO LINE MD 1 PER SECOND
DSS 44 RECEIVER 2 1-WAY TELEMETRY TO LINE MD 1 PER 10 SECONDS

2 START SIDE BAND SEARCH DSS 42 RECEIVER 5/DSS 44 RECEIVER 1

3 CONFIRM MAIN CARRIER/MAIN BEAM

4 DSS 42 TXR ON - START TUNING SWEEP

5 DSS 42 COMPLETE TXR SWEEP - CONFIRM 2-WAY LOCK MAIN CARRIER
DSS 44 CONFIRM REACQUISITION 3-WAY

6 DSS 42 CONFIRM TRACKING RATES AND GO AUTO TRACK TELEMETRY FROM 5 OR 6 AT PROJECT DISCRETION

7 DSS 42 COMMAND MOD ON - CALIBRATION 2 MODE - GREEN FOR COMMAND

8 DSS 42 REMAIN TXR - SAA RECEIVER 5 SCM AUTO TRACK

9 DSS 42 XFER UPLINK TO DSS 44 - DSS 44 TX ON AT 1 kW SCM
(DSS 42 RECONFIGURE TX TO SCM/SCM TO MASER IN TCP-3 TLM TO HSDL)

10 DSS 44 XFER UPLINK BACK TO DSS 42 - DSS 42 TX ON AT 10 kW SCM
(DSS 44 RECONFIGURE SCM TO MASER IN/TCP-1 TLM TO HSDL)

Fig. 3. Initial acquisition strategy: time line

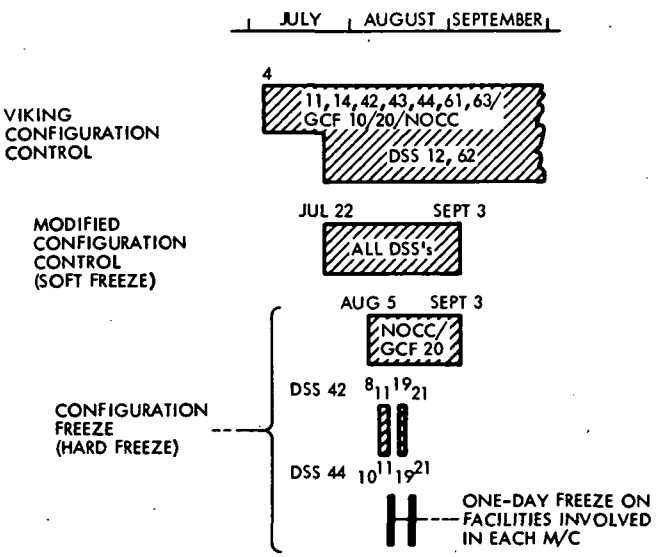

REF: NETWORK CONFIGURATION CONTROL/FREEZE SOP 842-129-20-225

Fig. 4. Viking DSN configuration control

Helios Mission Support

P. S. Goodwin
DSN Systems Engineering Office
W. G. Meeks, S. E. Reed, and R. E. Morris
Network Operations Office

Having successfully passed its first aphelion, the Helios-1 spacecraft is in excellent health and is preparing to enter its second solar occultation on its way to the second perihelion. DSN activities in support of Helios-B testing are increasing, with the results covered in this article.

I. Introduction

This is the fifth article in a series that discusses the Helios-1 flight support provided by the Deep Space Network (DSN). The previous article (Ref. 1) reported on the results of Helios-1 superior conjunction passage and initial Helios-B planning activities. This article covers that period between the first and second superior conjunctions in Helios-1 mission operations. Also included are Helios-1 tracking coverage and system performance as well as results of initial Helios-B testing.

II. Mission Status and Operations

A. Helios-1 Intraconjunction Operations

The Helios-1 mission has now progressed well into Phase III, which started with the entrance into the first superior conjunction in April 1975. Helios 1 is rapidly approaching its second superior conjunction on August 31, 1975. The intraconjunction activities have been, as expected (Ref. 1), relatively quiescent.

As Helios 1 approached an intraconjunction Sun-Earth-probe (SEP) angle of 7.4 degrees on July 26, 1975, the solar corona effects upon the telemetry and tracking data diminished. With near-normal data for the first time in several months, it appears that the Helios-1 spacecraft is in excellent condition for its second perihelion.

The second perihelion period will start September 9, 1975, and extend through October 3, 1975, with closest approach occurring on September 21. This perihelion represents an additional opportunity for the Helios science team to gather data which will enhance primary mission objectives.

The first day of the 25-day perihelion period (September 9) is also the last day of the second superior conjunction. Primary support for superior conjunction will be provided by the 64-meter antenna station at Goldstone, Calif. (DSS 14). Near-continuous coverage during the second perihelion operations will be provided by two complete subnets—one 64-meter and one 26-meter.

Inasmuch as Helios 1 is returning to its first closest approach to Earth, a large negative doppler shift which exceeds the capability of the standard doppler extractor will occur during the second perihelion. To compensate for this condition, 1 megahertz has been added to the standard doppler bias for a total of 2 megahertz. Testing is currently in progress.

On September 3, the deep space stations supporting Helios 1 will begin to operate on voltage-controlled oscillator (VCO) transmit S-band channel 20-b and receive S-band channel 22-a as opposed to channels 21-a and 21-b, which are normally used.

This change in frequency is required to compensate for the resultant perihelion doppler shift in both the transmit and receive frequencies. This doppler shift will be observed throughout most of September and October.

Helios-1 operational support is expected to decrease somewhat as Helios-B and other network facility commitments increase in the immediate future.

B. Helios-B Test and Training

The test and training for Helios B will follow essentially the same basic outline as that of Helios 1, except on an abbreviated scale. Only the Helios-B 26-meter subnet will be tested prior to launch. The 64-meter stations will perform a demonstration pass prior to assuming their active participation after launch.

1. Simulation System Tests. Helios-B testing will utilize the modified Helios-A mathematical model representation of the Helios-B spacecraft. No changes are anticipated to the Helios-A model subsystem subroutines. Minor changes have been made, however, to the executive subroutines to allow interface with the Mission Control and Computing Center (MCCC) multimission simulation software.

Several "in-core" data routing tests were conducted with the Helios mathematical model. The objectives were to test the hardware and software integration, the interface, and to retrain the Helios simulation engineers. After these tests, the first long-loop demonstration was a test with the JPL Compatibility Test Area (CTA 21), conducted on July 22, 1975. Although a portion of the test sequence was skipped due to lack of time, all test objectives were met. This test provided acceptance of the Simulation Data System/Mathematical Model for Ground Data System/Mission Operations System test and training support.

Other Simulation System tests are planned for the Helios 26-meter stations in September. These tests will verify long-loop operations of each deep space station (DSS) Simulation System with the mathematical model.

2. Ground Data System Tests. Five U.S. Ground Data System tests are planned for Helios B in August and September. They are designed to exercise those functions required of the Ground Data System that are not normally exercised in the daily tracking of Helios 1, but are necessary for the early operational phases of Helios B.

Two tests have been conducted to date: one with CTA 21 and another with DSS 61 (Madrid, Spain). The test with CTA 21 was generally successful.

The second test with DSS 61 (Madrid) was also successful. This exercise was performed simultaneously with a Helios-1 spacecraft track, providing the Mission Control and Computing Center with computer loading data.

3. DSN Test and Training. The DSN test and training effort started with the transmission of the Helios-B on-site Operator Training Plan and Sequence of Events to all Helios supporting stations. These on-site training exercises are designed to prepare the DSS operators in the use of hardware, software, and procedures required for Helios-B configuration and support.

With the daily tracking of the Helios-1 spacecraft, most Helios operations procedures are practiced on each track. The DSN Operations Verification Tests (OVTs) are designed to utilize the Helios-1 spacecraft telemetry and command systems to practice those operational requirements infrequently used in day-to-day operations, such as manual mode commanding and analog tape playback. Three tests were conducted with two stations at Goldstone, Calif. (DSSs 11 and 12) and one station in Australia (DSS 44). Manual mode commanding and analog tape playback were practiced as well as normal Helios-1 spacecraft support activities. All test objectives were met during each test.

The Helios-B Performance Demonstration Tests and spacecraft end-to-end testing with the spacecraft, the Spacecraft Tracking and Data System, the Mission Control and Computing Center, and the German Control Center are presently scheduled for October 1975.

4. Mission Operations System Testing and Training. Mission Operations System training and tests are scheduled to begin in October, with DSN support required in November. Training at JPL will be minimal because,

unlike Helios 1, Helios-B launch and Phase I operations are to be controlled from the German Space and Operations Center (GSOC). A backup Spacecraft Operations Team will be located at JPL during this time in the event of an emergency. The prime team for spacecraft attitude control operations will be located at JPL. The Project–DSN interface remains the same as for Helios-1 operations.

C. Actual Tracking Coverage Versus Scheduled Coverage

This portion of the report covers Helios-1 tracking coverage provided by the DSN from June 13 through August 14, 1975. During this time, the Helios-1 spacecraft was traversing from its first superior conjunction and approaching its second.

The Helios-1 tracking schedule called for only 36 tracks within this section of its trajectory. The total tracks available during this 63-day period were 189. Of these, the DSN supported Helios with 71% of the total available—135 tracks. The long-range scheduling forecast had requested four 64-meter tracks per week. The actual 64-meter coverage was slightly less than the forecast, but when the additional 26-meter tracks were provided, the weekly average was 15 passes per week.

The total Helios-1 tracking coverage support provided by the DSN was 1071 hours. The coverage provided by the 64-meter subnet accounted for 24.3% of this total. The average Helios-1 track was 7 hours and 56 minutes from acquisition-of-signal to loss-of-signal. The increase in coverage for Helios 1 is attributed to the redefinition of priorities by NASA Headquarters, which gives Helios-1 the same priority as Pioneers 10 and 11.

III. DSN System Performance for Helios

A. Command System

The DSN command activity in support of Helios 1 during June and July 1975 totaled 1803 transmitted commands. The cumulative total since launch is 15,283 commands. Command activity in June, due to the distance from Earth, was low; but as Helios 1 closed this distance, spacecraft scientific experiment interest again increased, resulting in an increase in the number of commands transmitted in July.

Lost command capability throughout the network decreased during this period (6.5 hours) from that experienced during the last reporting period (9 hours). Approximately 85% was attributable to DSS 14 (Goldstone); however, because of the great distance, this station accounted for a large percentage of the total tracking time during this interval. Two Command System aborts occurred during this period—one at DSS 11 (Goldstone) in June and one at DSS 43 (Australia) in July. One Project abort (a command disabled during transmission) was optioned in June at DSS 61 (Madrid).

Heavy Viking 1975 testing activity made its impact felt on the DSN during this period and probably contributed to three procedural errors affecting the Helios-1 command operations. Two procedural errors at DSS 14 (Goldstone) and one at DSS 42 (Australia) accounted for approximately two hours of Command System outage in the month of July.

B. Tracking System

The DSN Tracking System performance during this reporting period was very satisfactory. As Helios 1 completed its first superior conjunction in late June, the doppler noise, which had increased as the Sun–Earth–probe (SEP) angle decreased, began to slowly decrease again and ultimately leveled out well within the nominal range. The SEP angle increased to 7.4 degrees on July 26 before it started decreasing again as the spacecraft started toward its second superior conjunction on August 31.

It was this brief interlude in the Helios-1 trajectory which allowed the first normal doppler noise data measurements to be made since the SEP angle decreased to 5 degrees on April 7, 1975. The doppler noise, as expected, slowly started to increase as the SEP angle decreased. Figure 1 depicts the expected doppler noise from day of year (DOY) 212 (July 31, 1975) through DOY 256 (September 12, 1975); this covers the second superior conjunction period. There were no significant Discrepancy Reports during this reporting period.

C. Telemetry System

The Helios-1 Telemetry System performance, which has followed the predicted performance curves except during superior conjunction, has now returned to within the nominal predicted values. Following superior conjunction, the signal level residuals and the signal-to-noise ratio residuals were out of tolerance. The downlink telemetry performance improved markedly as the SEP angle increased and the solar effects diminished.

While there were no significant Helios-1 telemetry Discrepancy Reports, there were several isolated reports of signal level and signal-to-noise ratio residuals being out of tolerance. Prior to superior conjunction, there were two categories of failures being reported via the Discrepancy

Reporting System, which were contributing to approximately 50% of all telemetry failures. These were the Data Decoder Assembly, and the Automatic Total Recall System II failures. During June and July, no failures of Automatic Total Recall System II were reported, but Data Decoder Assembly failures continued to account for 25% of all telemetry failures.

Procedural errors increased to 21% of the total Discrepancy Reports as the Viking 1975 test and training effort made its impact fully felt on the operational elements of the DSN. As Helios-B test and training activities increase over the ensuing months, adding to the highly active operational commitments of the DSN, procedural reliability will be an important operational element to monitor, along with the current hardware and software systems required for Helios operations.

IV. Conclusions

With Helios 1 traversing its farthest distance from Earth and the Sun, preparations for a second superior conjunction and a second perihelion are underway. Renewed interest in the region of space in close proximity to the Sun awaits Helios-1 scientific instrument data readout and analysis. The passive experiments (Faraday rotation and celestial mechanics) will be of major importance during the superior conjunction, with the active experiments spotlighted during the second perihelion. Helios-B testing activities will increase as the DSN makes preparation for support of another Helios spacecraft, to be launched in early December 1975.

Acknowledgment

The authors wish to thank the following members of the Network Operations Analyst Group for their contribution of periodic network performance data: R. Frampton, B. Hoffman, and W. Tucker—Command; J. Hendricks and C. Lunde—Telemetry; and R. Schlaifer—Tracking.

Reference

1. Goodwin, P. S., et al., "Helios Mission Support," in *The Deep Space Network Progress Report 42-28*, pp. 23-28, Jet Propulsion Laboratory, Pasadena, Calif., Aug. 15, 1975.

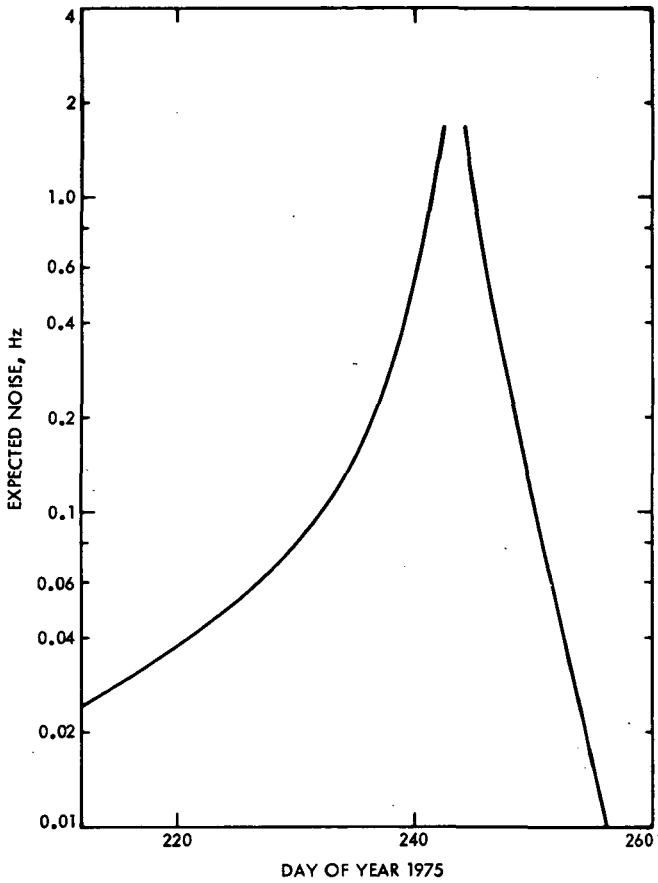

Fig. 1. Helios-1 doppler noise (expected) vs day of year

S-Band Zero-Delay Device Multipath Tests on the 64-Meter Antenna at DSS 43, DSS 63, and DSS 14

T. Y. Otoshi
Communications Elements Research Section

This article presents the results of a study to correlate the results of zero-delay subreflector tests with the multipath theory. Good agreement between theory and experiment was obtained on both S-band range and signal level data at DSS 43, DSS 63, and DSS 14. It is shown that a movable subreflector technique can be used to isolate the principal multipath errors and enable a more accurate determination of the actual ground station delay.

I. Introduction

With the exception of DSS 14, at Goldstone, California, all stations of the Deep Space Network use the conventional zero-delay ranging configuration, in which the zero-delay device (ZDD) is mounted on the paraboloidal reflector (dish) surface. A zenith range measurement via the airpath to a dish-mounted ZDD and a Z-correction (Ref. 1) provide needed ground station bias corrections for determining the true range to the spacecraft.

Results of airpath tests at DSS 14 showed that large changes in range occurred as a function of antenna elevation angle when a ZDD was mounted on the 64-m antenna dish surface (Ref. 2). Other airpath tests made on the 64-m antenna S/X system at DSS 14 showed that large range changes also occurred when small changes were made in axial focusing of the hyperboloidal subreflector. Similar type phenomena were also observed on the 64-m antenna systems at DSS 43, Canberra, Australia, and DSS 63, Madrid, Spain (Ref. 3). Since the range dependence on elevation angle could be due to a multipath phenomenon, one cannot assume that a zenith measured value is the correct value. Because of the described airpath problems, the ZDD configuration at DSS 14 has been operated in a cable configuration (Ref. 4) since January 12, 1974. However, DSS 43 and DSS 63 have continued to operate in the airpath configuration.

Because of the current range residuals of 10 to 15 meters between DSS 63 and DSS 43 for Mariner 10 results (Ref. 5), some attention has been devoted to the study of multipath as a possible cause of this discrepancy. A theory has recently been derived which results in good agreement between the multipath theory and experimental data. The purpose of this article is to present the results of some of this recent work. It will be shown that the multipath theory (with the aid of a com-

puter program) can be used to determine the true range delay of the station in the absence of multipath and thereby determine a correction to the observed station delay in the presence of multipath. Furthermore, the theory can be used to determine the physical location of the multipath source and its magnitude.

II. Theoretical Equations for Subreflector Tests

In the subreflector test, ranging measurements are performed via the airpath to a ZDD mounted on the dish surface. The test configuration may be seen in Fig. 1. The range-coded uplink signal, radiated out of the radio-frequency (RF) feed horn, is reflected off the hyperboloidal subreflector toward the dish surface. The dish-mounted ZDD horn receives a portion of this energy, and after mixing with a coherent local oscillator frequency, a coherent downlink signal is radiated back toward the hyperboloidal subreflector and reflected back toward the RF feed. The range-coded downlink signal received by the RF feed travels to the receiver system and subsequently arrives at the ranging machine.

In the ranging test, the total system round trip delay time is measured as a function of subreflector position. If the major part of the multipath signal is interacting in the region between the feed horn and the feed cone or its support structure, the subreflector movement will cause the multipath signal to go in and out of phase with the primary signal. Since the only required modification to previous theoretical work published by this author (Ref. 6) is to express the differential path length in terms of indicated subreflector position, only the equations will be presented. The derivations can be found in Ref. 6.

For the configuration of Fig. 1 the equation for two-way range can be expressed as

$$(t_g)_T = K_1 + \varepsilon_{ga} + \varepsilon_{gb} \tag{1}$$

where

K_1 = total system group delay (uplink and downlink) in the absence of multipath, s

ε_{ga} = error in the uplink delay due to multipath, s

ε_{gb} = error in the downlink delay due to multipath, s

For simplicity, assume that the primary and leakage paths are the same for the uplink and downlink signals (see Fig. 1). Then from the equations derived in Ref. 6, and assuming a free space media for both leakage and primary paths,

$$\varepsilon_{ga} = \left(\frac{(\ell_2 - \ell_1)}{c}\right) A \left(\frac{A + \cos\theta_a}{1 + 2A\cos\theta_a + A^2}\right) \tag{2}$$

$$\varepsilon_{gb} = \left(\frac{(\ell_2 - \ell_1)}{c}\right) A \left(\frac{A + \cos\theta_b}{1 + 2A\cos\theta_b + A^2}\right) \tag{3}$$

where

$$\theta_a = \frac{-2\pi f_a}{c}(\ell_2 - \ell_1) + \psi_a \tag{4}$$

$$\theta_b = \frac{-2\pi f_b}{c}(\ell_2 - \ell_1) + \psi_b \tag{5}$$

and

A = ratio of the magnitudes of the leakage and primary signals as measured at the output port of the ZDD horn (see Fig. 1)

ℓ_1, ℓ_2 = physical path lengths, respectively, of the primary and leakage paths going one-way, cm

c = speed of light ($\approx 3 \times 10^{10}$ cm/s)

f_a, f_b = uplink and downlink frequencies, respectively, Hz

ψ_a, ψ_b = phase angles of reflection coefficients (if any) in the leakage path for uplink and downlink signals, respectively, rad

The exact relationship of $(\ell_2 - \ell_1)$ to subreflector movement is difficult to derive due to defocusing effects and the changes in incidence angles that differ for the primary wave and the multipath wave. As a first-order approximation,

$$\ell_2 - \ell_1 \approx (\Delta\ell_0 + 2S_1)\,2.54 \tag{6}$$

where

$\Delta\ell_0$ = differential path length when the indicated subreflector position is zero, in.

S_i = indicated subreflector position, in.[1]

[1]The subreflector position on the equipment is indicated in inches rather than in centimeters. To be meaningful this indicated position should not be converted to the metric system.

The automatic gain control (AGC) downlink signal level change observed by the ground receiver will vary according to the relationship

$$|F_T|_{dB} = 10 \log_{10} [(1 + 2A \cos \theta_a + A^2)(1 + 2A \cos \theta_b + A^2)] \quad (7)$$

and the AGC signal level (in dBm) observed at the ground receiver is

$$AGC = K_2 + |F_T|_{dB} \quad (8)$$

where K_2 = the AGC signal level which would be observed in the absence of multipath (in dBm).

III. Theoretical and Experimental Data

A. Subreflector Tests

Figures 2 through 7 are computer printouts and plots showing a comparison of theoretical and experimental data obtained from subreflector tests at DSS 43, 63, and 14. The uplink and downlink test frequencies were approximately the Helios spacecraft frequencies of 2115 and 2297 MHz, respectively.

The printouts and plots were generated by a computer program to perform a least squares fit of theoretical values to experimental data. The theoretical data are based upon Eqs. (1) through (8), and a best fit is made first to the experimental ranging data to determine the best fit value of (1) true station delay K_1 in the absence of multipath, (2) the differential length $\Delta\ell_0$ as defined by Eq. (6), and (3) the relative strength of the leakage signal A expressed in decibels. The program then uses these best fit values of $\Delta\ell_0$ and A to calculate the theoretical AGC signal levels as a function of subreflector settings.

This sequence for best fit was chosen because the range data are a result of long term averaging, while the AGC data are either typically noisier or generally lag behind real-time changes. The AGC data are also dependent upon the accuracy of the calibration curves and operation only at the signal levels where the calibration curves apply.

Note from the computer printouts on Figs. 2, 4, and 6 that the best fit values of $\Delta\ell_0$ are typically about 3327.4 cm (1310 in.). This value compares favorably with values of approximately 3332.5 cm (1312 in.) obtained from measuring physical path lengths on scaled drawings (see table in Fig. 1). From Fig. 1, it can be seen that this value is associated with a multipath wave reflected off the cone platform. The values of approximately −15 to −20 dB for A_{dB} agree with those calculated independently by Ludwig (Ref. 7). These values are also consistent with beam efficiency values published in Ref. 8 for the portion of the beam illuminating the cone platform. An attempt to explain the higher value of about −10 dB for A_{dB} at DSS 63 will be made later after discussion of the plotted curves.

Examination of the plotted curves shows that reasonably good agreement was obtained between theory and experiment for DSS 43 and DSS 14. The typical deviations in range are about 3 ns, and typical deviations in AGC are about 0.3 dB. These deviations might be due to another smaller multipath effect caused by a wave bouncing off the cone roof and not accounted for by the theory.

The larger discrepancy for DSS 63 was previously attributed to a cone missing from the cone platform. However, it was recently learned that a cone was also missing from the cone platform on the DSS 43 antenna during 1974 and during the subreflector test. Therefore, the stronger multipath effect and larger discrepancy at DSS 63 might be due to the location of the missing cone with respect to the location of the ZDD. The ZDD locations and tricone configurations at DSS 43, DSS 63, and DSS 14 for the subreflector tests are shown in Fig. 8. Note that at DSS 63 the missing cone is at Bay 1, while at DSS 43, the missing cone is at Bay 3. Because of the different locations of the missing cone with respect to the ZDD, a stronger multipath signal could exist at DSS 63 than at DSS 43.

The large disagreement of calculated and experimental AGC values at DSS 63 can be explained as follows. The AGC calibrations at DSS 63 were performed in the region of −140 to −170 dBm while actual multipath tests were performed at −120 dBm. The measured signal levels for the tests were outside the calibrated region, and therefore the measured AGC variations were much smaller than the actual variations. G. Pasero at DSS 63 stated that when the test was repeated for AGC data only at a later date in the calibrated range of the receiver, the peak-to-peak AGC variation observed was about 10 dB. This peak-to-peak variation agrees favorably with the calculated values shown on the plots.

All of the subreflector test results presented apply only to the antenna pointed at zenith and at the S-band test frequencies involved. Results of subreflector tests at 45 and 20 deg elevation angles have been reported in Ref. 3, but as yet no curve fit has been made to these data.

B. Antenna Tipping Test

Another airpath test that is often performed is the antenna tipping test. In this test the total system range delay is continuously measured while the antenna is slowly tipped from the zenith position to the horizon. Figures 9 and 10 show the results of the tipping test for DSS 43 and DSS 63, respectively. No current tipping test data were obtained at DSS 14. The tipping tests were performed on a different day from the subreflector tests, and the measured zenith range delays differed by about 10 to 20 ns. To avoid confusion, the tipping test data were converted to show changes relative to the zenith position. A polynomial curve fit was made to the data to show trends only. The polynomial curve fit is not based on the multipath equations. However, it is interesting to note that when the antenna is tipped from the zenith position to the horizon, the subreflector moves from the normal operating point outward about 0.5 to 0.7 in. (Ref. 9). If one examines the subreflector data for DSS 43 and DSS 63, (see Figs. 3a and 5a) and moves from the operating point to a point about 0.5 in. in the positive direction, the magnitude and phase (sign) of the range change generally agree with the antenna tipping data. Therefore one can assume that the phenomena associated with the antenna tipping tests are correlated to the same multipath phenomenon observed on the subreflector test.

IV. Corrections to Measured Station Range Delay

In the preceding section it was shown that the true station delay could be determined with the aid of a computer program. The definition of true range is that which would have been measured in the absence of multipath. Since the subreflector position during pre- and post-track zero-delay calibration is known and since the true range is given by the computer program, one can calculate a correction for the measured station delay. In addition, one can predict what the observed range residuals would be between stations. For example, let

$BIAS'_{DSN}$ = measured DSS round trip delay in the *presence* of multipath

$BIAS_{DSN}$ = true DSS round trip delay in the *absence* of multipath

Using the equation in Ref. 1 the measured round-trip light time (RTLT) will be

$$RTLT' = R_{total} - BIAS_{S/C} - BIAS'_{DSN} + Z \qquad (9)$$

but the true RTLT is

$$RTLT = R_{total} - BIAS_{S/C} - BIAS_{DSN} + Z \qquad (10)$$

where R_{total} is the total measured range and Z is the Z-correction.

If $BIAS'_{DSN}$, $BIAS_{DSN}$ are given in nanoseconds the range residual in meters is computed from

$$\underset{\text{(meter)}}{\textit{Range Residual}} = [\underset{\text{(ns)}}{RTLT'} - \underset{\text{(ns)}}{RTLT}]\,[0.15] \qquad (11)$$

Substitutions of Eqs. (9) and (10) into Eq. (11) gives

$$\underset{\text{(meter)}}{\textit{Range Residual}} = [\underset{\text{(ns)}}{BIAS_{DSN}} - \underset{\text{(ns)}}{BIAS'_{DSN}}]\,[0.15] \qquad (12)$$

For DSS 43, the 1974 pre- and post-track ZDD calibrations were done with the subreflector at 0 in. Then from the data on Fig. 2

$$BIAS_{DSN} - BIAS'_{DSN} = 3198.4 - 3227.2$$
$$= -28.8\,\text{ns}$$
$$\textit{Range Residual} = -4.3\,\text{meters}$$

For DSS 63, the 1974 pre- and post-track ZDD calibrations were done with the subreflector at −0.5 in. From the data on Fig. 4,

$$BIAS_{DSN} - BIAS'_{DSN} = 4210.8 - 4155.9$$
$$= 54.9\,\text{ns}$$

and

$$\textit{Range Residual} = 8.2\,\text{meters}$$

Since DSS 14 does not operate in the airpath configuration, there is no need to compute residuals for DSS 14.

It is interesting to note that the above residuals are in excellent agreement with the residuals published by Christensen for Mariner 10 at Mercury Encounter I on March 29, 1974 (Ref. 5). Unfortunately, the results presented here cannot be used conclusively to explain the residuals. The main reason is that during Mariner 10 Mercury Encounter I on March 29, 1974, the ZDD horn at DSS 43 was located at the outer edge of the 64-m dish surface. The ZDD horn was moved to a new location closer to the center of the antenna on August 1, 1974 (see Fig. 8). The DSS 43 test results reported in this article were obtained at the new location.

Another reason why the results may not apply to the Mariner 10 residuals is the slight differences in test frequencies. If one were to assume that the same multipath conditions existed at DSS 63 as during the Mariner 10 Mercury Encounter I period, calculations show that for the Mariner 10 uplink/downlink frequencies of 2.11352 GHz/2.29523 GHz, the range residual would have been +5.0 meters. It can generally be expected that the multipath-caused residuals will change significantly with uplink/downlink frequency changes as small as 1 or 2 MHz.

Since the multipath error can change in magnitude and phase with (1) frequency, (2) ZDD horn location, or (3) the RF feed configuration, it is important to document these parameters for future reference. The test configurations for the tests done at DSS 43, DSS 63, and DSS 14 are shown in Fig. 8. Table 1 shows the critical parameters of interest which if altered would invalidate the range correction data obtained.

V. Summary and Recommendations for Future Work

It has been shown that even though multipath effects are present on the antenna, the effect can be separated out by the movable subreflector technique. This method assumes that the dominant interaction is occurring between the subreflector and the cone or its support structure. If there are multipath effects outside this region, one must use a movable ZDD horn on the dish surface such as that described in Ref. 6. Range measurements made over a band of frequencies might also reveal multipath effects and enable identification of multipath sources.

If the station periodically (every 3 months) obtains data from the subreflector test, then through the use of the computer program, one could determine the station delay more accurately. Since the computer program also assists in locating the multipath source, a simple antenna redesign might be done to eliminate the problem entirely. One solution may be to restore the hyperboloid vertex plate which is not present on 64-m antennas.

Although good agreement was obtained between theory and experiment for the tests described in this article, it is still desirable to confirm the location of multipath source. Plans are being made to perform an experiment placing absorbers on the cone platform of the DSS 14 64-m antenna and seeing if the dominant multipath effect disappears for both S- and X-band. The results of this test will be reported in a future issue of this publication.

References

1. *TRK-2-8 Module of DSN System Requirements Detailed Interface Design Document 820-13, Rev. A*, Jet Propulsion Laboratory, Pasadena, Calif., July 1, 1973 (an internal document).
2. Stelzried, C. T., Otoshi, T. Y., and Batelaan, P. D., "S/X Band Experiment: Zero Delay Device Antenna Location," in *The Deep Space Network Progress Report 42-20*, pp. 64–68, Jet Propulsion Laboratory, Pasadena, Calif., Apr. 15, 1974.
3. Otoshi, T. Y., and LuValle, J., "Zero Delay Device Airpath Tests at DSS 43 and 63," IOM 3333-75-048, Jet Propulsion Laboratory, Pasadena, Calif., Apr. 1, 1975 (an internal document).
4. Otoshi, T. Y., and Stelzried, C. T., "S/X Experiment: A New Configuration for Ground System Range Calibrations With the Zero Delay Device," in *The Deep Space Network Progress Report 42-20*, pp. 57–63, Jet Propulsion Laboratory, Pasadena, Calif., Apr. 15, 1974.

References (contd)

5. Christensen, C., "Corrected Mariner 10 Range Residuals," IOM 391.8-268, Jet Propulsion Laboratory, Pasadena, Calif., Apr. 24, 1975 (an internal document).

6. Otoshi, T. Y., "S/X Band Experiment: A Study of the Effects of Multipath on Two-Way Range," in *The Deep Space Network Progress Report 42-25,* pp. 69–83, Jet Propulsion Laboratory, Pasadena, Calif., Feb. 15, 1975.

7. Ludwig, A. C., "Multipath Calculations for Range Error Calibration Probe," IOM 3333-75-161, Jet Propulsion Laboratory, Pasadena, Calif., Aug. 22, 1975 (an internal document).

8. Bathker, D. B., *Predicted and Measured Power Density Description of a Large Ground Microwave System,* Technical Memorandum 33-433, Jet Propulsion Laboratory, Pasadena, Calif., Apr. 15, 1971. See Eta S Column in Table II, p. 31.

9. Katow, M. S., "64-m Subreflector–Gravity Deflections," IOM 3324-75-136, Jet Propulsion Laboratory, Pasadena, Calif., Sept. 2, 1975 (an internal document).

Acknowledgments

The author would like to acknowledge the assistance of J. LuValle of Network Operations in writing the test procedure for overseas station tests. Splendid cooperation was obtained from G. Pasero of DSS 63 and R. Denize of DSS 43, who took the data and furnished additional details about the test configurations. H. Marks of Informatics wrote the Engineering Calibration Program used in the tests and has made the program tapes and documentation available to all stations in the Network. T. Cullen of the Communications Elements Research Section wrote the sophisticated computer program that enabled the theoretical portion of this work to be successful. The subreflector technique was originally suggested by Dr. R. W. Beatty, Consulting Electronics Engineer, for purposes of checking ranging system measurement accuracy. His suggested subreflector tests subsequently led to the discovery of the multipath phenomenon.

Table 1. Multipath test configuration and tabulation of critical multipath-dependent parameters

DSS	Test frequencies, GHz		Normal subreflector operating position, in.	ZDD horn location	S-band cone	S/X dichroic plate installed	Approximate period for which test results are valid
	Uplink	Downlink					
43	2.115770	2.297670	0	Dish surface as indicated on Fig. 8	SPD	No	August 1, 1974 (new horn location) to February 13, 1975 (when XRO[a] cone and S/X feed installed)
63	2.115700	2.297593	−0.5 (0.5 in. IN)	Dish surface as indicated on Fig. 8	SPD	No	Throughout 1974 to February 1975 (when S/X feed installed)
14	2.115650	2.297540	−0.5 (0.5 in. IN)	Box on side of Mod III section on same level as cone platform (Fig. 8)	SPD	Yes	March 19, 1975 when SPD[b] cone/ XRO cone installed) to present

[a]X-band receive only.

[b]S-band polarization diversity.

APPROXIMATE PATH LENGTHS FOR PRIMARY AND MULTIPATH (LEAKAGE) WAVES			
ZDD HORN LOCATION	DISTANCE FROM RF FEED PHASE CENTER TO ZDD HORN PHASE CENTER		
	LEAKAGE WAVE PATH LENGTH, cm (in.)	PRIMARY WAVE PATH LENGTH, cm (in.)	DIFFERENTIAL PATH LENGTH, cm (in.)
"A"	6941.82 (2733)	3609.34 (1421)	3332.48 (1312)
"B"	7569.20 (2980)	4231.64 (1666)	3337.56 (1314)

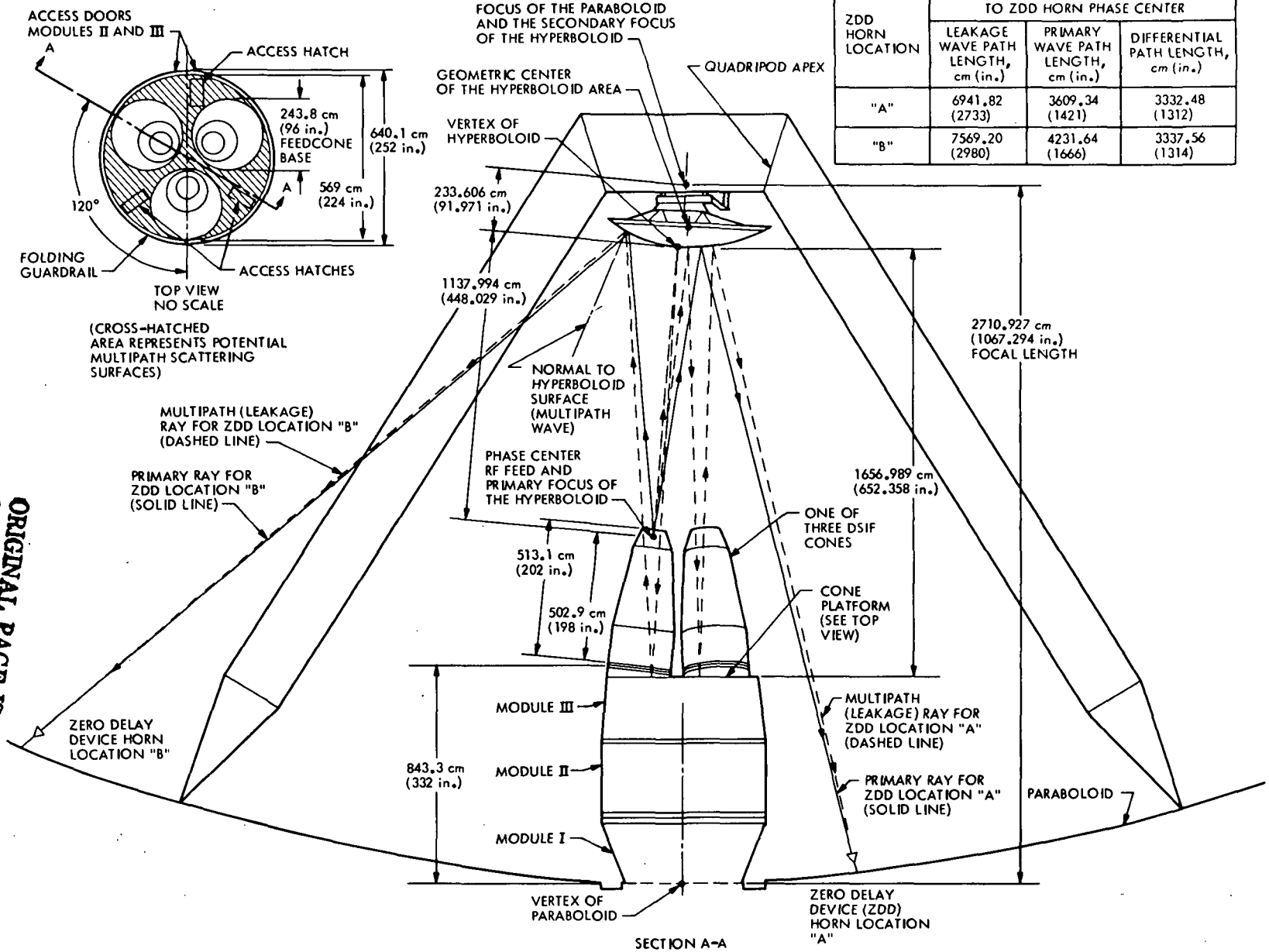

ORIGINAL PAGE IS OF POOR QUALITY

Fig. 1. 64-m antenna geometry for multipath tests

DSS 43 SUBREFL TESTS AT ZENITH, 1974 GMT DAY 362

FA= 2.115770 GHZ FB= 2.297670 GHZ

ADBL=-24.0000 DB ADBU=-15.0000 DB

DLZL= 1295.000 INCH DLZU= 1325.000 INCH

SUBREF POSITION (INCH)	EXPER. RANGE DELAY (NS)	CALC. RANGE DELAY (NS)	RANGE DIFF. (NS)	EXP AGC (DBM)	CALC AGC (DBM)	AGC DIFF. (DB)
-3.000	3226.80	3223.15	3.646	-121.14	-120.72	-.421
-2.500	3227.90	3227.77	.126	-120.00	-120.25	.252
-2.000	3202.20	3203.23	-1.028	-122.34	-122.47	.135
-1.500	3162.60	3164.89	-2.286	-125.59	-125.20	-.385
-1.000	3171.20	3174.40	-3.203	-125.22	-124.55	-.668
-.500	3210.80	3211.96	-1.164	-121.98	-121.70	-.272
.000	3227.20	3226.98	.220	-119.87	-120.35	.481
.500	3210.40	3212.25	-1.845	-121.07	-121.66	.586
1.000	3181.40	3178.36	3.040	-124.05	-124.21	.165
1.500	3178.60	3172.65	5.954	-124.55	-124.70	.155
2.000	3195.50	3196.94	-1.440	-122.81	-122.79	-.026

BEST FIT VALUES FOR OPTION 1

	K1 (NS)	ADB (DB)	DLZ (INCH)	K2 (DBM)
FIRST ESTIMATE	3198.51	-15.45	1311.500	
FINAL ESTIMATE	3198.41	-15.38	1311.286	-122.6793

Fig. 2. Sample printout of computer program for DSS 43 subreflector tests

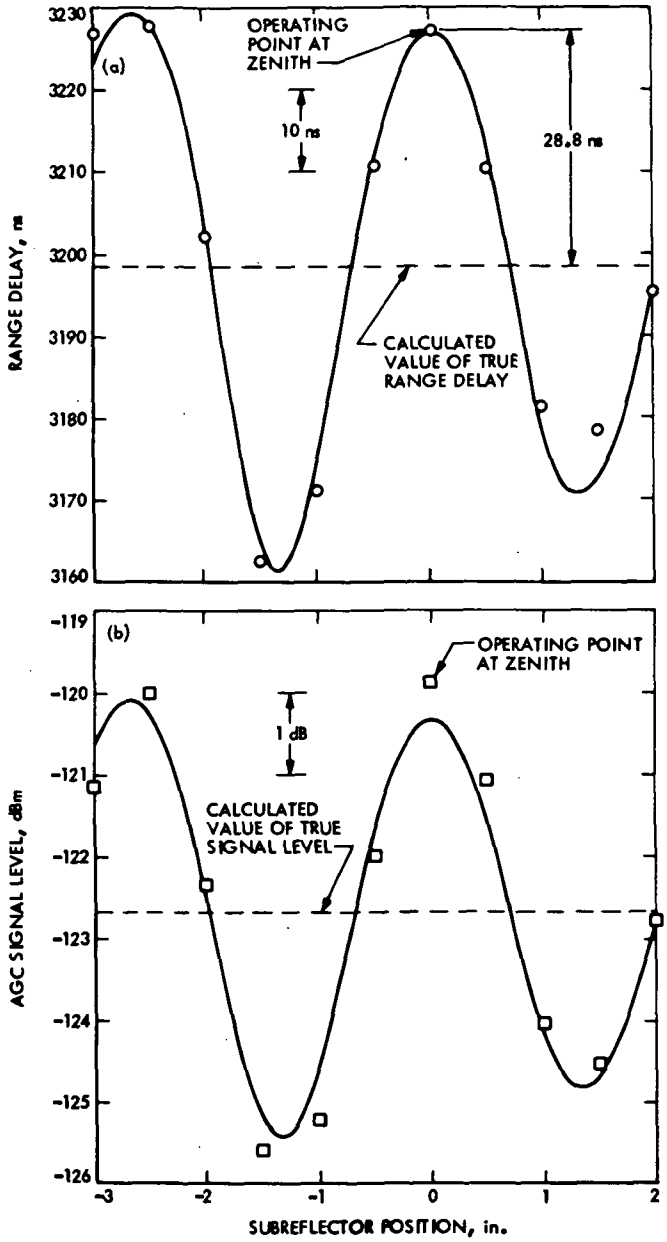

Fig. 3. Comparison of theoretical and experimental results for subreflector tests at DSS 43 on 1974 GMT Day 362 (zenith measurement): (a) Range delay, (b) Downlink received signal level

DSS 63 SUBREFL TESTS AT ZENITH, 1975 GMT DAY 29

FA= 2.115700 GHZ FB= 2.297593 GHZ

ADBL=-24.0000 DB ADBU=-12.0000 DB

DLZL= 1295.000 INCH DLZU= 1325.000 INCH

SUBREF POSITION (INCH)	EXPER. RANGE DELAY (NS)	CALC. RANGE DELAY (NS)	RANGE DIFF. (NS)	EXP AGC (DBM)	CALC AGC (DBM)	AGC DIFF. (DB)
-3.000	4217.20	4198.45	18.746	-127.47	-129.64	2.173
-2.500	4258.40	4255.99	2.415	-127.27	-124.21	-3.057
-2.000	4253.10	4263.42	-10.317	-127.27	-123.17	-4.105
-1.500	4213.30	4235.41	-22.106	-127.30	-126.62	-.677
-1.000	4122.60	4134.17	-11.572	-128.25	-133.43	5.186
-.500	4155.90	4159.18	-3.278	-128.16	-132.18	4.020
.000	4253.30	4245.23	8.070	-127.33	-125.58	-1.748
.500	4276.90	4264.77	12.128	-127.27	-122.99	-4.275
1.000	4256.10	4250.93	5.169	-127.27	-124.90	-2.373
1.500	4201.10	4178.04	23.064	-127.67	-131.02	3.352
2.000	4122.40	4121.87	.534	-128.69	-133.94	5.247
2.500	4201.70	4223.11	-21.406	-127.71	-127.68	-.026
3.000	4259.60	4261.05	-1.446	-127.28	-123.56	-3.718

BEST FIT VALUES FOR OPTION 1

	K1 (NS)	ADB (DB)	DLZ (INCH)	K2 (DBM)
FIRST ESTIMATE	4219.10	-12.00	1299.500	
FINAL ESTIMATE	4210.83	-9.74	1299.573	-127.8646

Fig. 4. Sample printout of computer program for DSS 63 subreflector tests

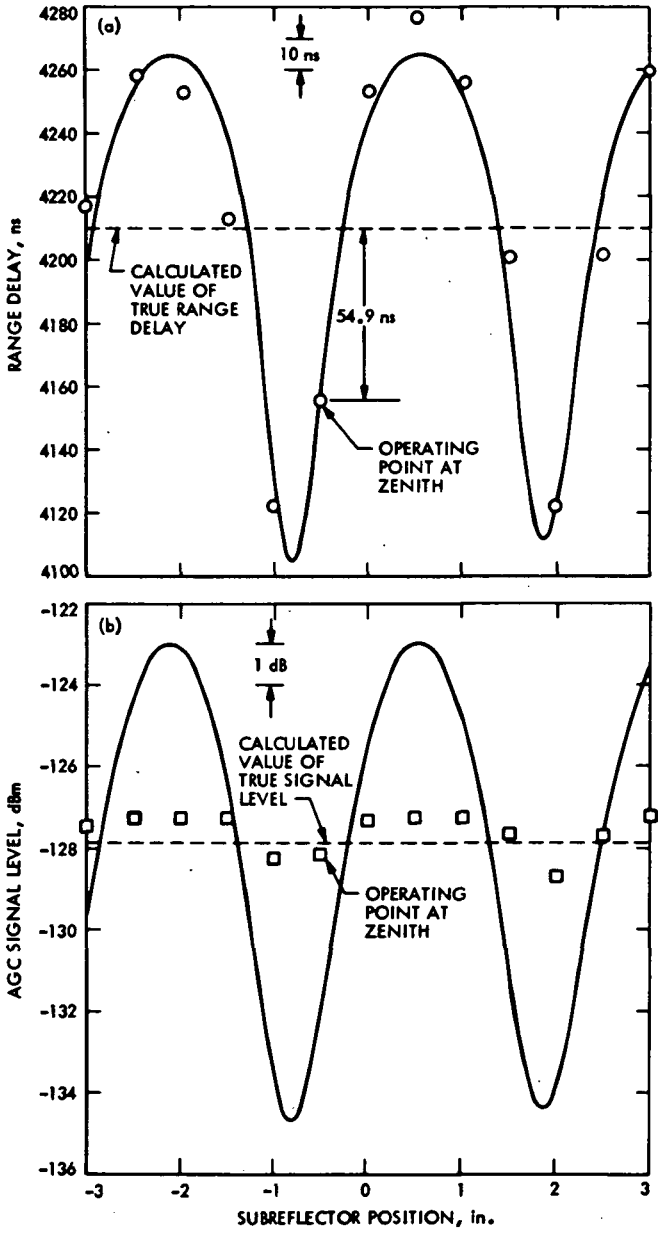

Fig. 5. Comparison of theoretical and experimental results for subreflector tests at DSS 63 on 1975 GMT Day 29 (zenith measurement): (a) Range delay, (b) Downlink received signal level

HELIOS PASS 215 POST CAL DSS 14, 1975 GMT DAY 193

FA= 2.115650 GHZ FB= 2.297540 GHZ

ADBL=-24.0000 DB ADBU=-15.0000 DB

DLZL= 1295.000 INCH DLZU= 1325.000 INCH

SUBREF POSITION (INCH)	EXPER. RANGE DELAY (NS)	CALC. RANGE DELAY (NS)	RANGE DIFF. (NS)	EXP AGC (DBM)	CALC AGC (DBM)	AGC DIFF. (DB)
-3.000	3276.20	3272.74	3.465	-135.64	-135.57	-.070
-2.500	3255.90	3261.34	-5.442	-136.50	-136.34	-.163
-2.000	3286.10	3285.53	.574	-134.68	-134.61	-.066
-1.500	3304.30	3305.28	-.983	-132.40	-132.93	.532
-1.000	3305.30	3304.02	1.275	-132.73	-133.05	.318
-.500	3279.60	3282.72	-3.118	-134.88	-134.81	-.071
.000	3266.50	3263.51	2.995	-136.14	-136.19	.051
.500	3276.60	3275.99	.605	-135.32	-135.29	-.026
1.000	3295.00	3298.83	-3.834	-133.22	-133.50	.277
1.500	3306.70	3305.02	1.685	-132.75	-132.97	.217
2.000	3289.00	3290.37	-1.370	-134.72	-134.17	-.548
2.500	3266.60	3270.71	-4.107	-136.36	-135.67	-.687
3.000	3278.70	3271.84	6.856	-135.35	-135.59	.236

BEST FIT VALUES FOR OPTION 1

	K1 (NS)	ADB (DB)	DLZ (INCH)	K2 (DBM)
FIRST ESTIMATE	3286.38	-19.05	1308.500	
FINAL ESTIMATE	3286.46	-19.15	1308.580	-134.4510

Fig. 6. Sample printout of computer program for DSS 14 subreflector tests

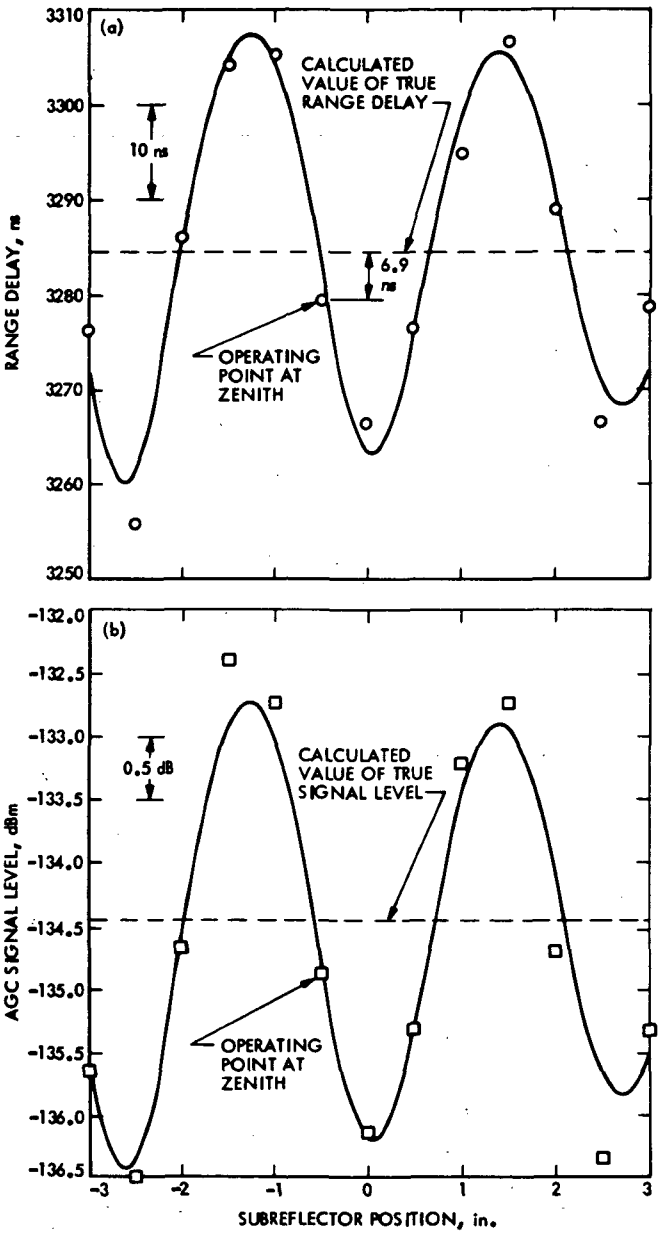

Fig. 7. Comparison of theoretical and experimental results for subreflector tests at DSS 14 on 1975 GMT Day 193 (zenith measurement): (a) Range delay, (b) Downlink received signal level

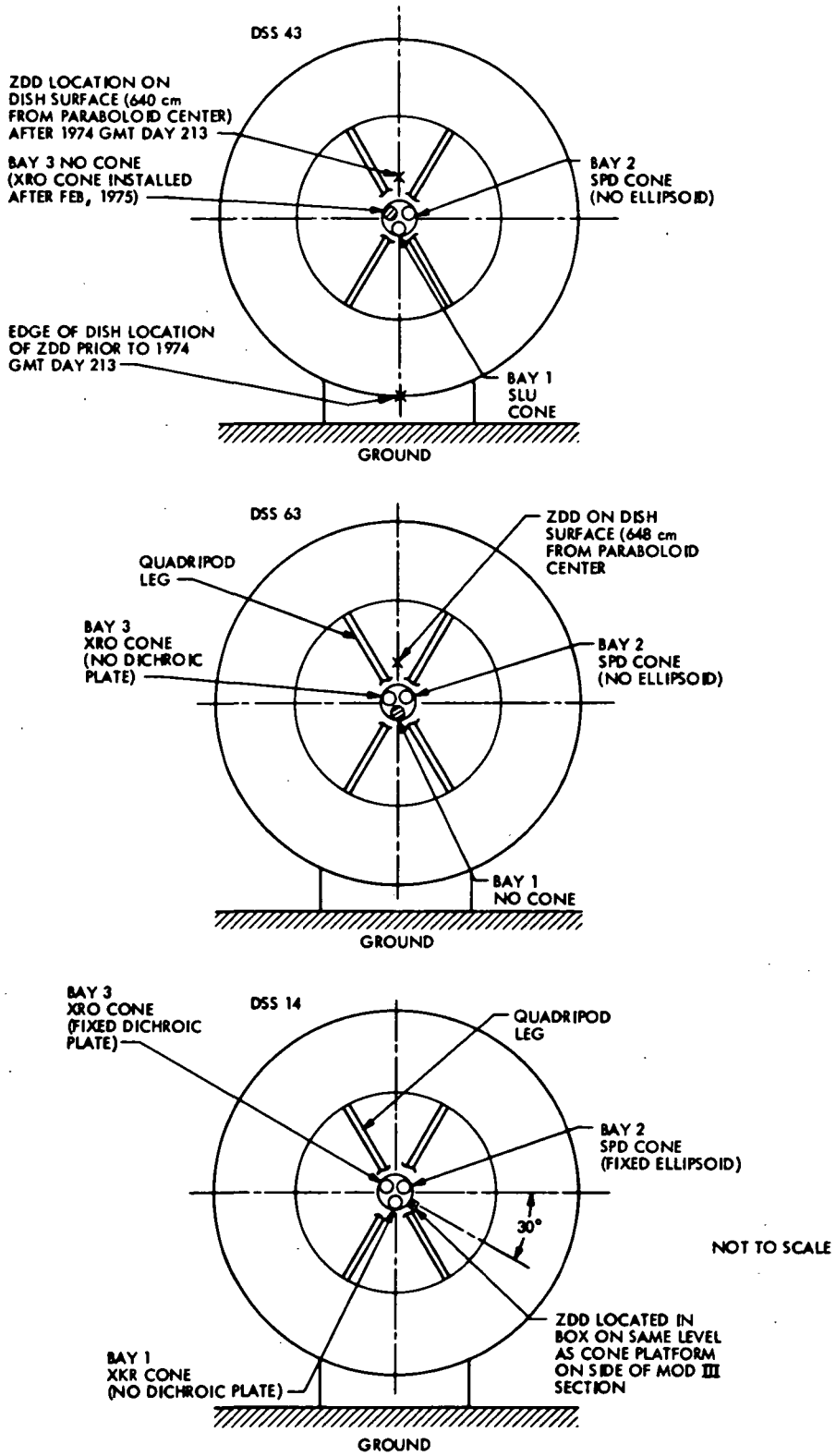

Fig. 8. DSS 43, DSS 63, and DSS 14 zero-delay device locations and tricone configuration for subreflector tests

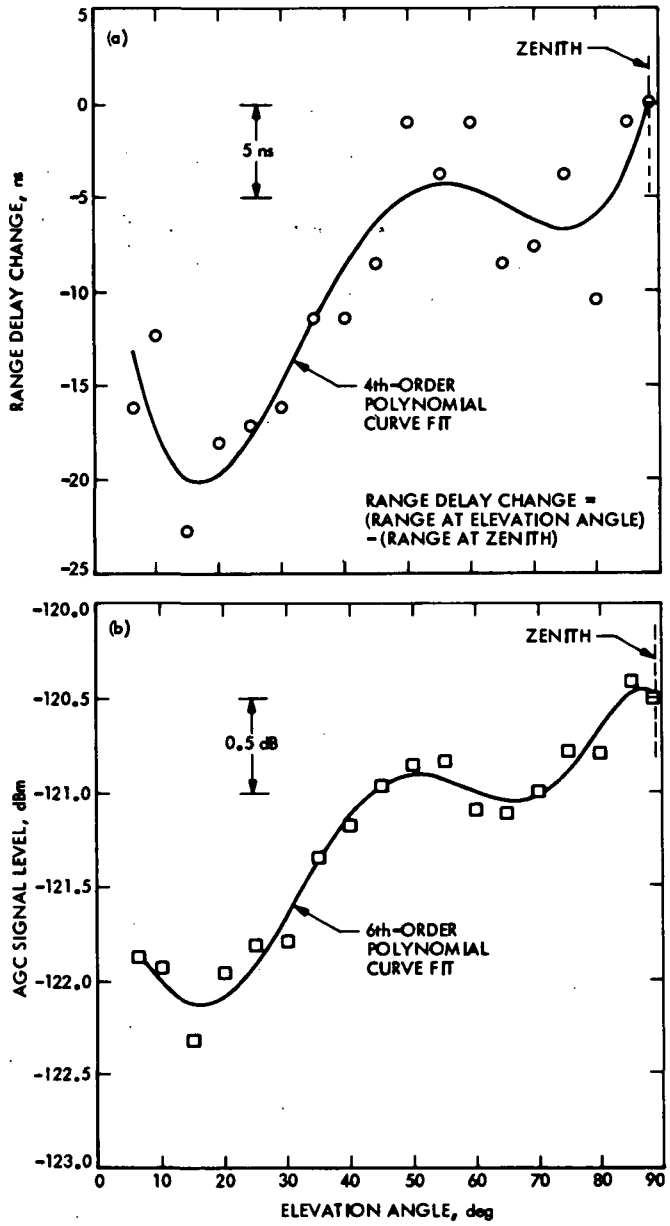

Fig. 9. DSS 43 antenna tipping tests at S-band, 1974 GMT Day 359: (a) Range delay change, (b) Downlink received signal level

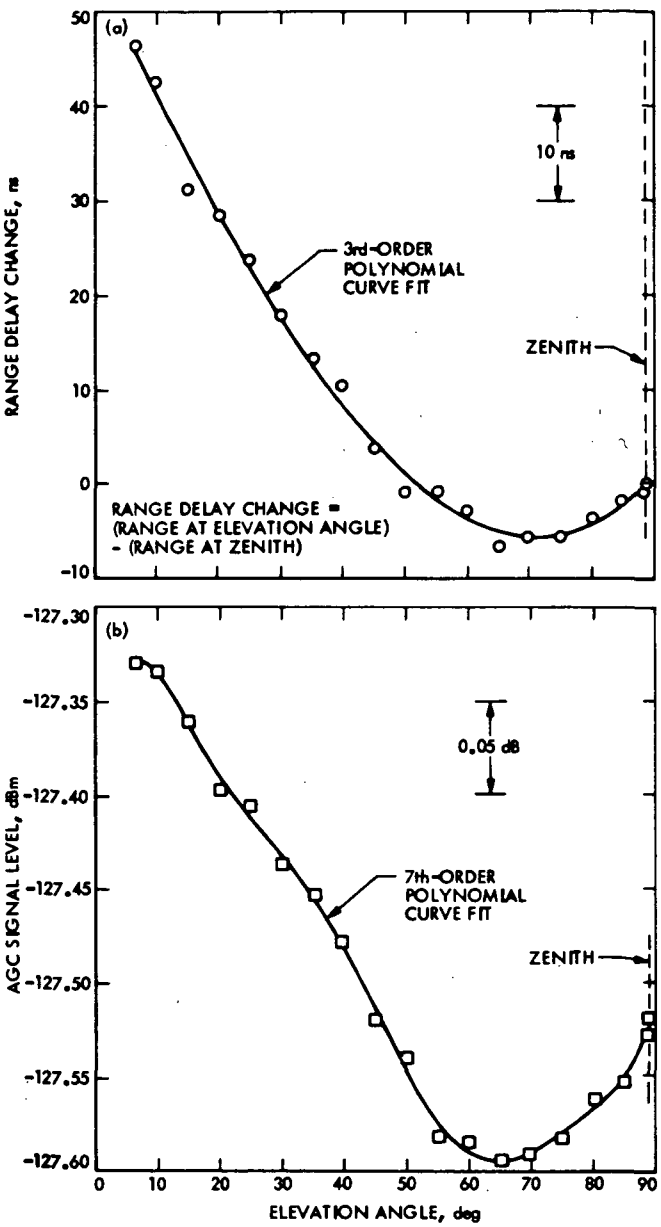

Fig. 10. DSS 63 antenna tipping tests at S-band, 1975 GMT Day 27: (a) Range delay change, (b) Downlink received signal level

Calculating Acquisition Behavior for Completely Digital Phase-Locked Loops

J. R. Lesh
Communications Systems Research Section

The acquisition behavior of completely digital first and second-order phase-locked loops is considered. It is shown that modeling the loop by its difference equations allows the acquisition behavior to be computed using a procedure wherein the number of computations as well as the required storage grow only linearly with the size of the state space. It is also shown that the procedure can be easily modified to include the effects of doppler, finite length accumulators, and initial phase estimate jamming.

I. Introduction

At present very little is known analytically about the acquisition behavior of phase-locked loops. The primary reason for this is that the linearizing or simplifying assumptions used in calculating steady-state performance parameters are not applicable when the loop is in the acquisition mode. However, if one considers completely digital phase-locked loops (Refs. 1, 2), then any implementation of such a loop is necessarily a finite state machine. In such cases if one is given an initial state distribution vector, then one can, at least in principle, compute any subsequent time–state distribution vector by considering the loop as a finite state Markov chain and multiplying the initial state distribution vector by the appropriate power of the Markov transition matrix. Unfortunately the number of computations as well as the storage required for this procedure both increase as the square of the size of the state space, making such a procedure quite unattractive for all but the smaller state spaces. For example, Chadwick (Ref. 3) used this technique to compute the acquisition behavior of a digital tracking loop which, even after restricting himself to a most likely subset of the state space, resulted in a one-step Markov transition matrix having 6.25×10^5 entries.

The important point, which seems to have been overlooked in the past, is that for tracking loops of the kind described in Refs. 1 and 2 most of the entries in the Markov transition matrix are zeros. Consequently, if one characterizes the loop by its difference equations then only the essential computations need be performed. This results in a tremendous savings both in computations and storage. In this article we will use the difference equation approach for computing acquisition performance of first- and second-order digital loops. We will see that this

approach can be easily modified to include the effects of finite accumulators (for the second-order loop) and doppler. Finally, we will show how this approach can be used to evaluate the merits of initial phase estimate jamming.

II. First-Order Loop

Consider the completely digital first-order phase-locked loop shown in Fig. 1. In this loop the input signal (a squarewave signal immersed in additive white gaussian noise) is filtered, sampled at the Nyquist rate and is applied to the transition sample selector. The transition sample selector, which is controlled by the phase shifter, extracts the sample of the input signal which is believed to have occurred at the transition of the received signal and corrects for the expected sign of this sample. The result is then accumulated until a sufficiently high signal-to-noise ratio is obtained to estimate (with high probability) whether the loop reference supplied by the phase shifter is leading or lagging the received signal. If the reference is leading the received signal, the accumulator will accumulate positively whereas it will accumulate negatively if the reference is lagging. After the accumulation has been completed, the sign of the accumulator output is used to shift or bump the phase of the loop reference signal one step in the direction to reduce the expected phase error, and the accumulator is reset.

The steady-state behavior of such a loop has been amply studied by Holmes (Ref. 1). For the acquisition behavior let us consider that the phase bump size is $2\pi/K$ radians. Then the loop can be considered as a Markov chain having K states. Let us consider (without loss of generality) that the phase of the received signal is zero. Furthermore, we will take the pessimistic approach by assuming that the phase error when the loop is in the kth state ϕ_k is

$$\phi_k = \frac{(2k-1)\pi}{K} \text{ radians} \tag{1}$$

for $k = 1, 2, \cdots, \frac{K}{2}$, and

$$\phi_k = \frac{(2K-2k-1)\pi}{K} \text{ radians} \tag{2}$$

for

$$k = \frac{K}{2}+1, \frac{K}{2}+2, \cdots, K$$

A state diagram for this loop is shown in Fig. 2.

We now define the state probability vector

$$\mathbf{s}_t = \begin{bmatrix} s_t(1) \\ s_t(2) \\ \cdot \\ \cdot \\ \cdot \\ s_t(K) \end{bmatrix} \tag{3}$$

where $s_t(k)$ is the probability of being in state k at time t. Since the loop is discrete, we assume that t belongs to the index set (i.e., $t \in \{0, 1, 2, \cdots\}$). Then, from Fig. 2 and the theory of Markov chains we know that

$$\mathbf{s}_t = [\mathbf{P}]\,\mathbf{s}_0 \tag{4}$$

where $\mathbf{s}_0$ is the initial state distribution vector and $\mathbf{P}$ is the K by K one-step Markov transition matrix given by

$$\mathbf{P} = \begin{bmatrix} 0 & p & & & & & & & & p \\ q & 0 & p & & & & & & & \\ & q & 0 & p & & & & & & \\ & \cdot & \cdot & \cdot & & & & & & \\ & & \cdot & \cdot & \cdot & & & & & \\ & & \cdot & \cdot & \cdot & & & & & \\ & & & q & 0 & p & & & & \\ & & & & q & 0 & q & & & \\ & & & & & q & 0 & q & & \\ & & & & & & p & 0 & q & \\ & & & & & & \cdot & \cdot & \cdot & \\ & & & & & & \cdot & \cdot & \cdot & \\ & & & & & & & p & 0 & q \\ p & & & & & & & & p & 0 \end{bmatrix} \tag{5}$$

($\frac{K}{2}$ marks the vertical extent of the middle column.)

In this equation p is the probability that the accumulation will cause a phase bump in the direction to decrease the phase error, $q = 1 - p$, and the blanks are assumed to be filled with zeros.

In order to compute the state probability distribution after one accumulation using this procedure we must store (aside from the distribution vectors themselves) a matrix having K^2 entries and perform K^2 computations. However, if one characterizes the loop by its stochastic difference equations, a tremendous savings in both stor-

age and computations is achieved. In particular we note that the loop can be characterized by

$$s_{t+1}(k) = \begin{cases} ps_t(k+1) + ps_t(k-1+K); & k=1 \\ ps_t(k+1) + qs_t(k-1); & k \in [2, K/2-1] \\ qs_t(k+1) + qs_t(k-1); & k = K/2, K/2+1 \\ qs_t(k+1) + ps_t(k-1); & k \in [K/2+2, K-1] \\ ps_t(k+1-K) + ps_t(k-1); & k=K \end{cases} \tag{6}$$

By using this characterization the one-step probability distribution vector can be computed with only $2K$ computations and with a storage only slightly greater than that required to store the probability vectors themselves.

III. Second-Order Loop

The first-order loop of Fig. 1 can be converted to a second-order loop by inserting a filter of the form shown in Fig. 3 between the accumulator sign detector and the phase shifter. The effect of this filter is to cause the phase shifter to be bumped by

$$u \cdot n + x_2$$

units where $u = \pm 1$ is the output of the accumulator sign detector, n is an integer gain factor and x_2 is the value (after u is added) of the loop filter accumulator. For such loops one must specify the values of two state variables in order to characterize the state of the loop. We shall use the instantaneous phase error, as we did in the first-order case, for one of these variables and the output x_2 of the loop filter summer as the other.

It is convenient to view the state space of the second-order loop as a series of rings similar to the one shown in Fig. 2, where each ring corresponds to all possible values of instantaneous phase when the second state variable is fixed at some value. Note, however, that for the second-order loop no transitions within a given ring are allowed (except possibly at the extremes which will be considered later) and that only certain transitions between rings are allowed. One can further visualize this series of rings as forming a tube with each ring on the tube being rotated about the tube axis by an amount dependent on the location of the ring (value of x_2) as well as the value of n.

With this picture in mind, let us define $s_t(k, \ell)$ as the probability of being in the kth error state at time t with a loop filter value of ℓ. We can further consider a ring probability vector

$$\mathbf{s}_t(\ell) = \begin{cases} s_t(1, \ell) \\ s_t(2, \ell) \\ \vdots \\ s_t(k, \ell) \end{cases} \tag{7}$$

The loop stochastic difference equations are (assuming no restriction on ℓ):

(a) $|\ell| \leq n$

$$s_{t+1}(k, \ell) = \begin{cases} ps_t(k+\ell+n, \ell-1) + ps_t(k+\ell+K-n, \ell+1); & k \in [1, n-\ell] \\ ps_t(k+\ell+n, \ell-1) + qs_t(k+\ell-n, \ell+1); & k \in \left[n-\ell+1, \frac{K}{2}-n-\ell\right] \\ qs_t(k+\ell+n, \ell-1) + qs_t(k+\ell-n, \ell+1); & k \in \left[\frac{K}{2}-n-\ell+1, \frac{K}{2}+n-\ell\right] \\ qs_t(k+\ell+n, \ell-1) + ps_t(k+\ell-n, \ell+1); & k \in \left[\frac{K}{2}+n-\ell+1, K-n-\ell\right] \\ ps_t(k+\ell+n-K, \ell-1) + ps_t(k+\ell-n, \ell+1); & k \in [K-n-\ell+1, K] \end{cases} \tag{8a}$$

(b) $\ell < -n$

$$s_{t+1}(k,\ell) = \begin{cases} qs_t(k+n+\ell+K, \ell-1) + ps_t(k+K+\ell-n, \ell+1); & k\varepsilon\,[1, -n-\ell] \\ ps_t(k+n+\ell, \ell-1) + ps_t(k+\ell-n, \ell+1); & k\varepsilon\,[1-n-\ell, n-\ell] \\ ps_t(k+n+\ell, \ell-1) + qs_t(k+\ell-n, \ell+1); & k\varepsilon\left[n-\ell+1, \frac{K}{2}-n-\ell\right] \\ qs_t(k+n+\ell, \ell-1) + qs_t(k+\ell-n, \ell+1); & k\varepsilon\left[\frac{K}{2}-n-\ell+1, \frac{K}{2}+n-\ell\right] \\ qs_t(k+n+\ell, \ell-1) + ps_t(k+\ell-n, \ell+1); & k\varepsilon\left[\frac{K}{2}+n-\ell+1, K\right] \end{cases} \tag{8b}$$

and

(c) $\ell > n$

$$s_{t+1}(k,\ell) = \begin{cases} ps_t(k+\ell+n, \ell-1) + qs_t(k+\ell-n, \ell+1); & k\varepsilon\left[1, \frac{K}{2}-n-\ell\right] \\ qs_t(k+\ell+n, \ell-1) + qs_t(k+\ell-n, \ell+1); & k\varepsilon\left[\frac{K}{2}-n-\ell+1, \frac{K}{2}+n-\ell\right] \\ qs_t(k+\ell+n, \ell-1) + ps_t(k+\ell-n, \ell+1); & k\varepsilon\left[\frac{K}{2}+n-\ell+1, K-n-\ell\right] \\ ps_t(k+\ell+n, \ell-1) + ps_t(k+\ell-n, \ell+1); & k\varepsilon\,[K-n-\ell+1, K+n-\ell] \\ ps_t(k+\ell+n-K, \ell-1) + qs_t(k+\ell-n-K, \ell+1); & k\varepsilon\,[K+n-\ell+1, K] \end{cases} \tag{8c}$$

where it is assumed that the interval (set) $[a,b]$ is empty if $b < a$.

As in the first-order case, we see that the amount of storage necessary to accommodate these equations is essentially the same as the amount of storage necessary to store the state probabilities. Therefore, the storage grows linearly with the range of ℓ $(=x_2)$. Note also that the number of computations grows linearly with the size of the state space.

IV. Practical Considerations

(a) Accumulator Truncation

In any implementation of a discrete second-order phase-locked loop, the accumulator in the loop filter will have a finite range. For example, we will let $x_2\varepsilon\,[L_{\min}, L_{\max}]$. This is equivalent to placing saturating boundaries at the $L_{\max}$ and $L_{\min}$ rings of the tubular state space. Any attempt to penetrate beyond the $L_{\max}$ $(L_{\min})$ ring results in a transition back onto a state in the $L_{\max}$ $(L_{\min})$ ring.

The difference equations of the second-order loop can be easily modified to accommodate this saturation of the state space. First, we note that each of the expressions in Eq. (8) is of the form

$$s_{t+1}(k,\ell) = \alpha s_t(k',\ell-1) + \beta s_t(k'',\ell+1)$$

over the appropriate range of k. If ℓ is one of the saturating boundaries, then one of the two rings $(\ell+1)$ or $(\ell-1)$ does not exist. In fact, the only way to get to the ℓth ring is to either be on the interior ring next to ℓ or to be on the ℓth ring already. As a consequence, we see that if $\ell = L_{\max}$ then we can add the set of equations

$$s_{t+1}(k,L_{\max}) = \alpha s_t(k',L_{\max}-1) + \alpha s_t(k',L_{\max}) \tag{9}$$

over the appropriate range of k and where the quantities α and k' are determined by the range of ℓ in equation 8

corresponding to $\ell = L_{max}$. Similarly, if $\ell = L_{min}$ then we add the equations

$$s_{t+1}(k,L_{min}) = \beta s_t(k'',L_{min}) + \beta s_t(k'',L_{min}+1) \tag{10}$$

again over the appropriate ranges of k. Thus, the Eqs. (8) apply to all interior rings and one need only add the set of modified equations for each boundary ring.

(b) Doppler

The effects of doppler can be quite easily handled provided one is willing to use a finite-state approximation approach. For example, if a loop has K phase error states and phase bumps every t_{up} seconds then one can approximate a doppler offset of D/Kt_{up} Hz (D an integer) by cyclically shifting each ring probability vector by D positions after each phase bump interval. If D is not an integer then one can either bound the desired result by using the appropriate neighboring integer or can further approximate by periodically selecting the amount of cyclic shift from a set of neighboring integers.

V. Initial Phase Estimate Jamming

Let us now assume that the received signal

$$s(t,\xi) = A \operatorname{sgn}\{\sin[\omega t + \xi]\} \tag{11}$$

where

$$\xi \varepsilon \left[-\frac{\pi}{16}, \frac{\pi}{16}\right]$$

and is uniformly distributed in this interval. Assume also that $s(t,\xi)$ is to be correlated over the interval

$$t\varepsilon\left[-\frac{M^*T}{2}, \frac{M^*T}{2}\right]$$

with each of the reference signals

$$s_i(t) = \operatorname{sgn}\{\sin[\omega t + \xi_i]\}; \qquad i = -7,-6,\cdots,7,8 \tag{12}$$

where

$$\xi_i = \frac{\pi i}{8} \text{ and } T = \frac{2\pi}{W}$$

If we denote

$$R_{\xi(i)} = \int_{\frac{-M^*T}{2}}^{\frac{M^*T}{2}} s(t,\xi)s_i(t)dt \tag{13}$$

and perform the integration, we obtain

$$R_\xi(i) = \begin{cases} A_i M^*T\left(1 - \frac{2}{\pi}\left|\xi_i - \xi\right|\right); & i = -7,-6,\cdots,6,7 \text{ or } i = 8 \text{ and } \xi > 0 \\ -A_i M^*T\left(1 - \frac{2}{\pi}\left|\xi\right|\right); & i = 8 \text{ and } \xi < 0 \end{cases} \tag{14}$$

We note that if $A_i = A$ Eq. (14) does not include the effects of doppler. To include doppler, one need only replace A_i by $\alpha_d(i)A$ where

$$\alpha_d(i) = \frac{B(i,\lambda)}{B(i,\lambda = 0)} \tag{15}$$

is the effective signal loss factor due to doppler. Expressions necessary for computing $\alpha_d(i)$ are given in the Appendix.

We next allow $s(t,\xi)$ to be received in additive white gaussian noise $n(t)$ of one sided spectral density N_0 W/Hz. We also define the noisy correlator output by

$$g_i(\xi) = \int_{\frac{-M^*T}{2}}^{\frac{M^*T}{2}} [s(t,\xi) + n(t)]s_i(t)dt; \qquad i = -7,-6,\cdots,7,8 \tag{16}$$

We note that the $g_i(\xi)$ can be expressed as

$$g_0(\xi) = R_\xi(0) + \sum_{i=1}^{8} n_i - \sum_{i=1}^{8} n_{-i} \tag{17}$$

$$g_1(\xi) = R_\xi(1) + \sum_{i=1}^{8} n_i - \sum_{i=1}^{8} n_{-i} + 2n_{-1} - 2n_8 \tag{18}$$

etc., where the n_i's, i = $\pm1, \pm2, \cdots, \pm8$ are independent zero-mean gaussian random variables with variance

$$\frac{N_0 M^*T}{32}$$

The purpose of all this is to select the ξ_i corresponding to the most likely phase of $s(t,\xi)$ so that the loop can be initially set (i.e., jammed) to that phase. Of primary in-

terest is the mean square phase error immediately after the phase jamming. We shall be satisfied with computing a close bound to this mean square error. Toward this end, we note that

$$\Pr\{g_0 = \max_j g_j\} \leq \Pr\{g_0 > g_1\} \Pr\{g_0 > g_{-1}\}$$

$$= \left[\tfrac{1}{2} + \tfrac{1}{2}\operatorname{erf}\left(\frac{R_\xi(0) - R_\xi(1)}{\sqrt{\frac{N_0 M^* T}{2}}}\right)\right]$$

$$\times \left[\tfrac{1}{2} + \tfrac{1}{2}\operatorname{erf}\left(\frac{R_\xi(0) - R_\xi(-1)}{\sqrt{\frac{N_0 M^* T}{2}}}\right)\right] \quad (19)$$

as well as

$$\Pr\{g_i = \max_j g_j\} \leq \Pr\{g_i > g_0\}$$

$$= \left[\tfrac{1}{2} + \tfrac{1}{2}\operatorname{erf}\left(\frac{R_\xi(i) - R_\xi(0)}{\sqrt{\frac{N_0 M^* T|i|}{2}}}\right)\right]; \quad i \neq 0 \quad (20)$$

Finally, we note that

$$E\{(\xi - \hat{\xi})^2 | \xi\} \leq E\left\{(\xi - \hat{\xi})^2 | \xi = \frac{\pi}{16}\right\}$$

$$= \frac{\pi^2}{(16)^2}\left\{\sum_{i=-7}^{7} (1 - 2i)^2 \Pr\{g_i = \max_j g_j\} + 225 \Pr\{g_8 = \max_j g_j\}\right\} \quad (21)$$

where $\hat{\xi}$ is the estimated phase. Substituting (19) and (20) into (21) yields the final bound.

VI. Examples

(a) First-Order Loop

The acquisition performance of a first-order loop having 256 states is shown in Figs. 4 and 5. It is assumed that the loop is updated (bumped) every M cycles of the received signal and that the initial phase estimation is based on an observation of the signal for $M^* = NM$ cycles. For $N = 0$ (i.e., no initial estimation), the initial state distribution vector is uniform. For $N > 0$, the mean square phase error due to phase estimation is first computed using the results of Section V. The initial state distribution is then taken as a quantized gaussian distribution with zero mean and this mean square error as a variance. The time axes have been normalized by the time required for M cycles (t_{up}).

Figure 4 represents the acquisition behavior when the loop update SNR

$$\rho = \frac{MTA^2}{N_0 4} = 2.5$$

and when no doppler is present. Figure 5 illustrates the behavior under the same conditions, except that a doppler offset was simulated by cycling the state probability vector one position every two updates.

(b) Second-Order Loop

Figures 6 to 8 demonstrate the acquisition behavior of a second-order loop similiar to the one described in Ref. 4. Here the phase variable has 256 discrete values and the proportional control gain factor $n = 4$. The range of the second state variable x_2 was restricted to the interval $[-3, 4]$. Figure 6 shows the acquisition with no doppler. Figures 7 and 8 illustrate the acquisition behavior when the numbers of doppler-generated shifts per loop update are 2 and 4, respectively.

(c) Discussion

By examination of Figs. 4 to 8, we see that if one is interested in fast acquisition then a large portion of the acquisition time should be allocated to phase estimate jamming. This is particularly true for the first-order loop, since the closed-loop time constant is generally quite large. For the second-order loop much less is to be gained by jamming unless the doppler offset is quite large. Note, however, that the doppler cannot be allowed to increase indefinitely since, as is shown in the appendix, if the estimator integration time equals the time needed to accumulate one complete doppler shifted cycle, the received signal will be orthogonal to all estimator reference signals.

VII. Summary

Described herein is a procedure for computing acquisition performance of first- and second-order digital loops which requires only a linear increase in storage and computations with the size of the state space. The procedure was found to be easily modified to account for finite accumulators and doppler. Expressions for the initial state mean square error after phase jam estimation were developed and several examples were presented to show the relative merits of phase jamming as an initial part of acquisition.

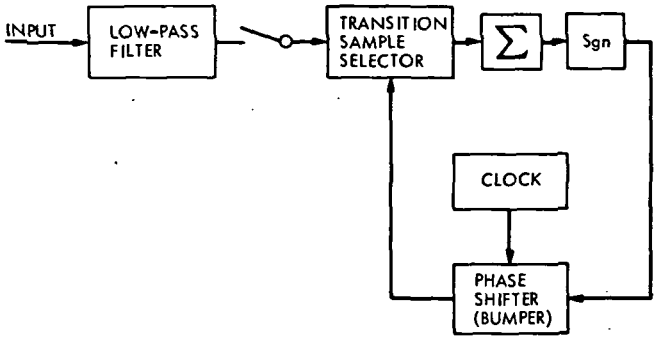

Fig. 1. First-order phase-locked loop block diagram

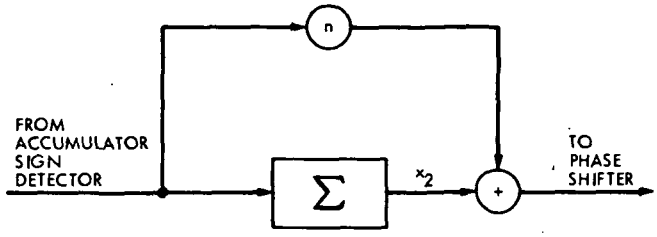

Fig. 3. Second-order digital PLL loop filter

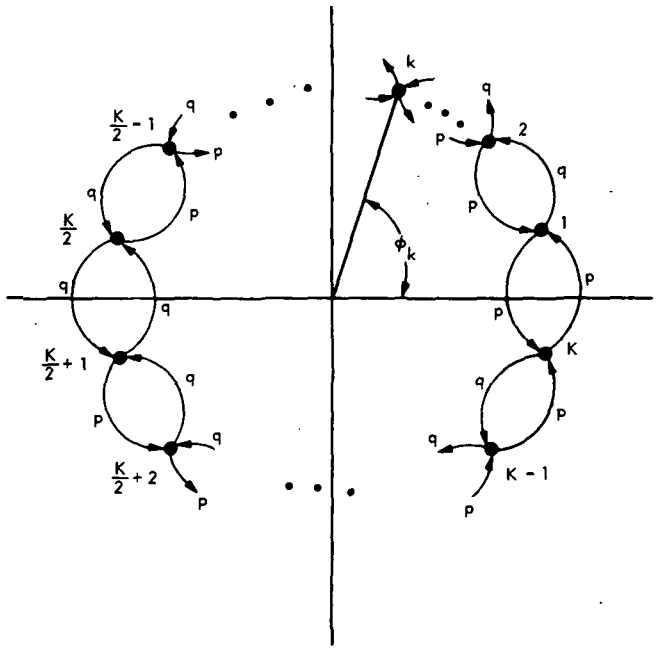

Fig. 2. Representation of state space for first-order PLL

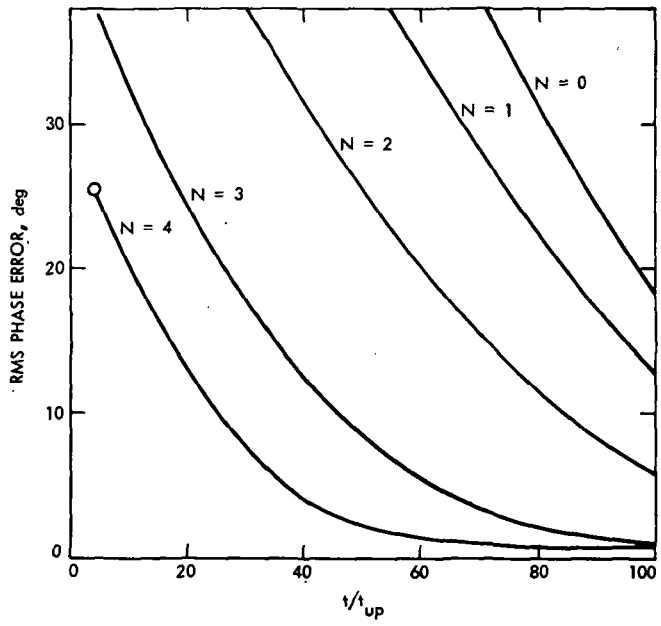

Fig. 4. Acquisition performance of first-order digital loop (no doppler)

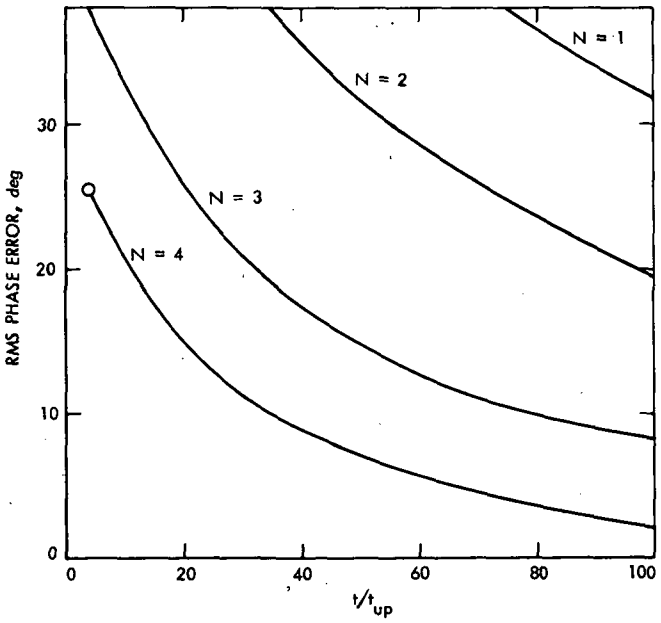

Fig. 5. Acquisition performance of first-order digital loop (one doppler state shift every two updates)

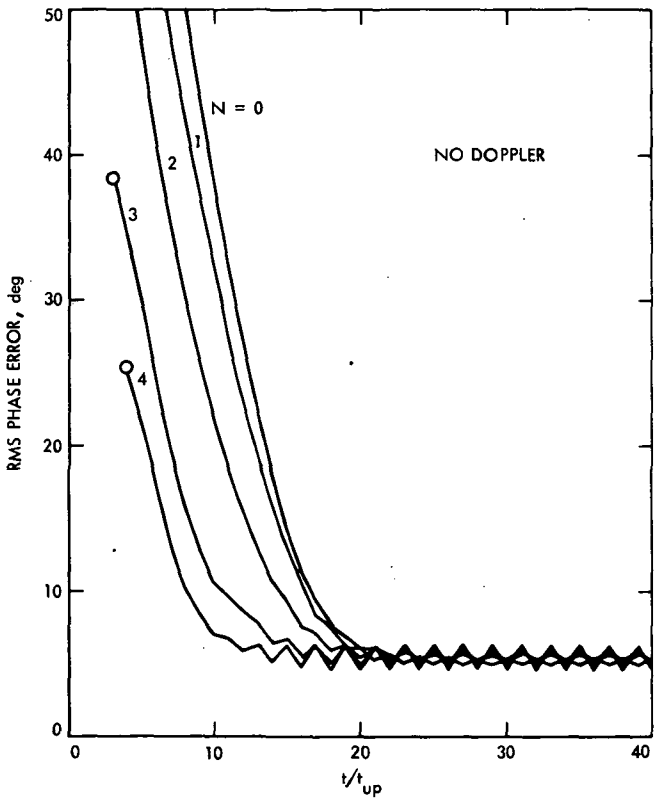

Fig. 6. Acquisition performance of second-order loop (no doppler)

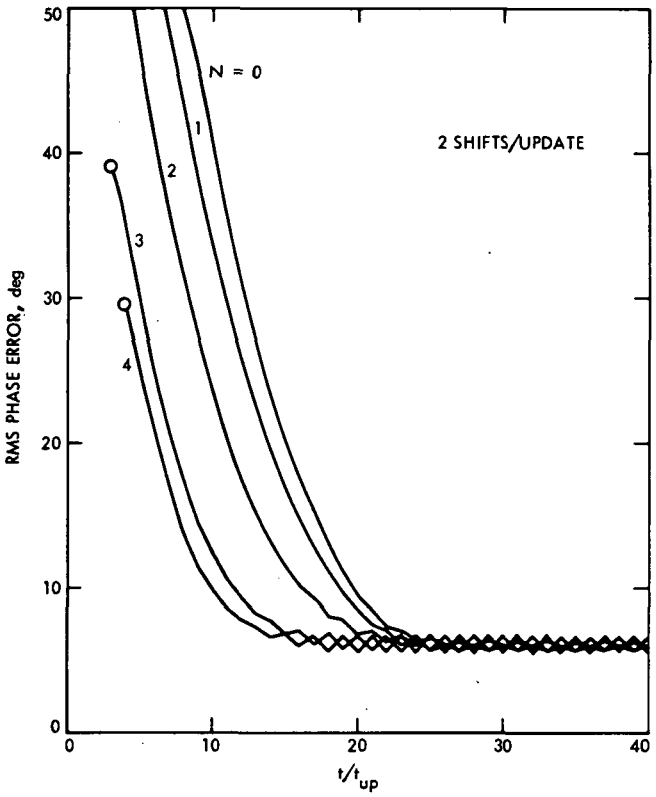

Fig. 7. Acquisition performance of second-order loop (2 doppler shifts per update)

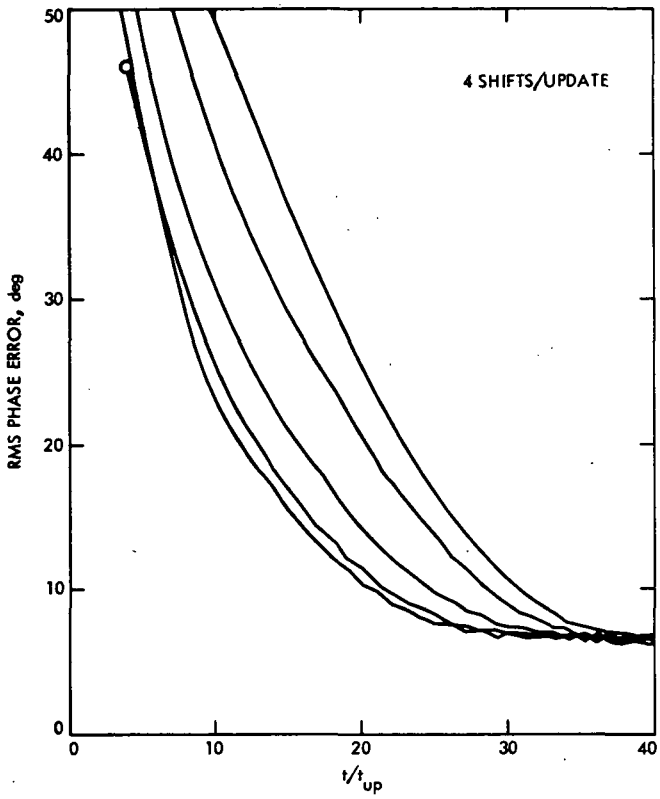

Fig. 8. Acquisition performance of second-order loop (4 doppler shifts per update)

Appendix

Signal Correlation in the Presence of Doppler

Consider a reference signal $s(t)$ of the form

$$s(t) = \text{sgn}\{\sin[W_0(t-\theta)]\}$$

and a received signal of the form

$$s'(t) = A\,\text{sgn}\{\sin[W_1(t-\theta')]\}$$

Let the two signals be correlated for a time interval of M^*T seconds where $T = 2\pi/W_0$ and M^* is an even integer. The correlator output at the end of this interval will be

$$\int_{-\frac{M^*T}{2}}^{\frac{M^*T}{2}} s(t)s'(t)dt = 2\sum_{k=-\infty}^{\infty}\sum_{l=-\infty}^{\infty}\frac{C_kC_l'\sin\left[(kW_0+lW_1)\frac{M^*T}{2}\right]}{kW_0+lW_1} \tag{A-1}$$

where

$$C_k = \begin{cases} \dfrac{2\exp(-jkW_0\theta)}{jk\pi} & ; \quad k \text{ odd} \\ 0 & ; \quad k \text{ even} \end{cases}$$

and

$$C_k' = \begin{cases} \dfrac{2A\exp(-jkW_1\theta')}{jk\pi} & ; \quad k \text{ odd} \\ 0 & ; \quad k \text{ even} \end{cases}$$

Substituting the C's into (A-1) and defining

$$\delta = \frac{W_1 - W_0}{W_0}$$

gives

$$\int_{-\frac{M^*T}{2}}^{\frac{M^*T}{2}} s(t)s'(t)dt = -32A\sum_{\substack{k=1\\k\text{ odd}}}^{\infty}\sum_{\substack{l=1\\l\text{ odd}}}^{\infty}\frac{\sin[l\delta M^*\pi]}{kl\pi^2[k^2W_0^2 - l^2W_1^2]}[kW_0\cos(kW_0\theta)\cos(lW_1\theta') + lW_1\sin(kW_0\theta)\sin(lW_1\theta')] \tag{A-2}$$

Now let us assume that θ' is uniformly distributed and define for $T' = 2\pi/W_1$ the intervals

$$\Delta_i' = \left\{\theta' : \frac{(2i-1)T'}{32} \le \theta < \frac{(2i+1)T'}{32}\right\} \quad i = 0,1,2,\cdots,15$$

Furthermore, assume that if $\theta' \epsilon \Delta_i'$

then

$$\theta = \frac{(i - J)T}{16} \tag{A-3}$$

for $J \epsilon \{0,1, \cdots ,15\}$. Note that for δ small, then $T' \approx T$ and θ corresponds to the midpoint of one of the 16 intervals Δ'_i. Next, define $B_i(J,\delta,M^*)$ as the average over $\theta' \epsilon \Delta'_i$ when θ is given by (A-3). Performing this average yields

$$B_i(J,\delta,M^*) = -\frac{(16)^2}{\pi^3} A \sum_{\substack{k=1 \\ k \text{ odd}}}^{\infty} \sum_{\substack{l=1 \\ l \text{ odd}}}^{\infty} \frac{\sin[l\delta M^*\pi] \sin\left(\frac{l\pi}{16}\right)}{kl^2[k^2W_0^2 - l^2W_1^2]}$$

$$\times \left[(kW_0 - lW_1) \cos\left(\frac{(k+l)\pi_i}{8} - \frac{kJ\pi}{8}\right) + (kW_0 + lW_1) \cos\left(\frac{(k-l)\pi_i}{8} - \frac{kJ\pi}{8}\right)\right] \tag{A-4}$$

It is our intent to average (A-4) over the 16 values of i. However, in most practical systems some band limiting exists, and hence the use of equations which display unlimited harmonic content is quite unnecessary. Therefore, we will restrict equation (A-4) to summations up to the seventh harmonic. Then, averaging over i we get

$$B(J,\delta,M^*) = (16)^2 AM^*T \left\{ \sum_{\substack{k=1 \\ k \text{ odd}}}^{7} \frac{\sin((8-k)\delta M^*\pi) \cos\left(\frac{k\pi}{16}\right) \cos\left(\frac{kJ\pi}{8}\right)}{2\pi^4 k(8-k)^2[8+\delta(8-k)]M^*} + \sum_{\substack{k=1 \\ k \text{ odd}}}^{7} \frac{\sin(k\pi\delta M^*) \sin\left(\frac{k\pi}{16}\right) \cos\left(\frac{kJ\pi}{8}\right)}{2k^4\pi^4\delta M^*} \right\}$$

However, if δ is small, the second term dominates the equation so that

$$B(J,\delta,M^*) = AMT \sum_{\substack{k=1 \\ k \text{ odd}}}^{7} \frac{(16)^2 \sin(k\pi\lambda) \sin\left(\frac{k\pi}{16}\right) \cos\left(\frac{kJ\pi}{8}\right)}{2(k\pi)^4\lambda}$$

$$= B(J,\lambda) \tag{A-5}$$

where

$$\lambda = \delta M^*$$

Equation (A-5) represents the average signal correlation of a reference signal and a signal which is uniformly distributed in an interval J sixteenths of a period away from the reference.

Finally, we note that if the doppler goes to zero then

$$B(J,\lambda = 0) = AMT \sum_{\substack{k=1 \\ k \text{ odd}}}^{7} \frac{(16)^2 \sin\left(\frac{k\pi}{16}\right) \cos\left(\frac{kJ\pi}{8}\right)}{2(k\pi)^3}$$

The ratio

$$\frac{B(J,\lambda)}{B(J,\lambda = 0)}$$

can be considered as the effective signal reduction factor due to doppler.

Figure A.1 illustrates the behavior of $|B(J,\lambda)|$ (after normalization) as a function of λ, the number of doppler-shifted cycles contained in the signal correlation integration time. It is instructive to note that as λ increases the peaks of the triangular squarewave correlation curve are suppressed more than the interior points. This causes the correlation function or S-curve to become more rounded. This rounding continues until the integration time encompasses one complete doppler-shifted cycle at which time the received signal is orthogonal to all of the reference signals.

References

1. Holmes, J. K., "Performance of a First-Order Transition Sampling Digital Phase-Locked Loop Using Random-Walk Models," *IEEE Trans. Comm.* Vol. COM-20, No. 2, pp. 119–131, April 1972.
2. Holmes, J. K., and Tegnelia, C. R., "A Second Order All Digital Phase Locked Loop," *IEEE Trans. Comm.* Vol. COM-22, No. 1, pp. 62–68, January 1974.
3. Chadwick, H. D., "A Markov Chain Technique for Determining the Acquisition Behavior of a Digital Tracking Loop," *JPL Quarterly Technical Review,* Vol. 1, No. 4, pp. 49–57, January 1972.
4. Lesh, J. R., "A Multiple-Rate Digital Command Detection System With Range Cleanup Capability," in *The Deep Space Network Progress Report 42-26,* pp. 91–101, April 15, 1975.

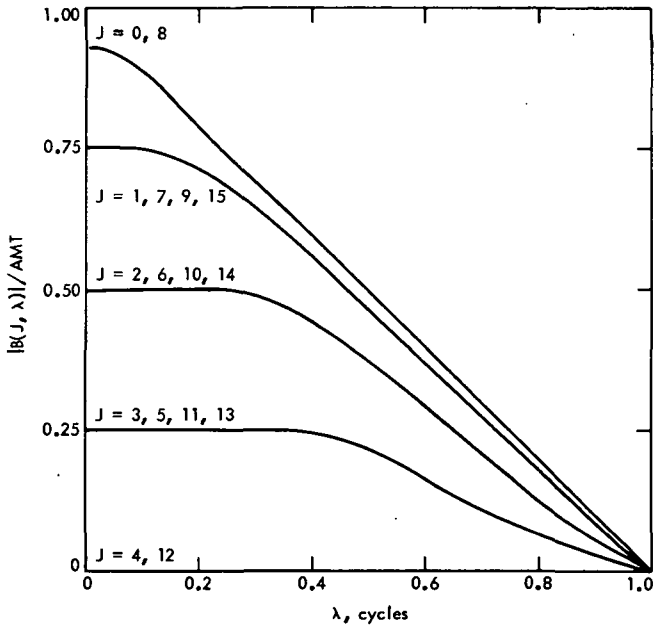

Fig. A1. Signal correlation loss due to doppler

The Effect of Noise and Diversity on Synthetic Array Radar Imagery

S. Butman and R. G. Lipes
Communications Systems Research Section

This article investigates synthetic aperture radar (SAR) image quality as a function of received signal-to-noise ratio, multiple looks or diversity averaging of "speckle," contrast, and resolution. Theoretical and simulation results are presented. The data are useful for tradeoff analyses in the design of the SAR, the image processing system, and the telemetry system. Photographs have been made to show the effect of the above-mentioned parameters. The general conclusion is that diversity averaging produces an image far superior to that obtained via equivalent receiver signal-to-noise improvement.

I. Introduction

One aspect of the DSN Advanced Systems Program is investigation of the flight–ground–mission control interfaces. This has the salutary feature of resource savings to NASA through optimum (in the sense of multimission support cost) flight and ground system design. A good example is the standard command detector breadboard development. Other tradeoff areas are also being examined including, in the near term, operational problems, and in the longer term, a look at likely flight projects which will require higher link performance and instrumentation.

A Venus-Orbiting Imaging Radar (VOIR) mapper has been proposed for the 1980's. The likelihood for such a mission is high, particularly since a similar Earth-orbiting mission, Sea Satellite (SEASAT), has been approved. When a VOIR-type mission is approved it will require a link capability up to 20 dB better than the current Mariner Jupiter-Saturn spacecraft/64-m antenna combination can provide at X-band. Furthermore, once such a high rate link (5–25 megabits/s) comes into being, it will be necessary to equip the Network with appropriate instrumentation to receive, detect, decode, and handle these data. These science data can be anticipated to be essentially raw radar echoes received on the spacecraft and telemetered to Earth, either in real-time or after temporary storage on board. These raw data will require processing into an image either at a DSN station or at the mission communication and control center, depending on processing cost vs ground communication cost. In either case, the DSN will need a capability to meet certain performance criteria pertaining to data quality (in this case, synthetic array radar image quality).

The purpose of this paper is to report some progress on the relationship between image quality, signal-to-noise ratio, and processing techniques. This type of information is expected, ultimately, to influence the design of the spacecraft and the ground system. Here we will be discussing picture formation via synthetic array radar signal processing. Pictures obtained in this manner exhibit "speckle" or self-noise, which can be removed through the introduction of diversity. We first give a brief theoretical discussion of the underlying causes of speckle and its removal, followed by a discussion of simulation results and conclusions on this phase of the study.

II. Speckle

When monochromatic coherent radiation is scattered off a surface, the return is a coherent superposition of contributions from the elementary scattering centers of the surface. When the roughness or height variation of the surface is approximately equal to or greater than the wavelength of the radiation,[1] the phases of the contributions from the elementary scattering centers can be closely approximated as independent random variables uniformly distributed between 0 and 2π. When the number of scattering centers is sufficiently large so that the central limit theorem can be applied to the superposition of elementary contributions, the amplitude of the return signal can be closely approximated as a Rayleigh distributed random variable.[2] The power s of the return will be exponentially distributed, having the probability density function

$$P(s) = e^{-s/S}\frac{1}{S} \qquad (1)$$

where S is the mean power of the return. This phenomenon has recently been called "speckle" by the workers in optics (Refs. 2–4), although it has been noted by the workers in radar (Ref. 5) and certainly dates back to Lord Rayleigh (Ref. 6).

In many cases we want to obtain information about the features of the illuminated surface from the return signal. However, the features of a certain area are related to the mean power S of the return from this area, while the actual power s of the return is probabilistic. For this reason we need to employ some form of diversity reception to obtain the average power. Typically, this diversity takes the form of space diversity, which means that the surface is observed from independent vantage points and the results of the independent "multiple looks" are averaged. Another common form is frequency diversity, in which results from independent looks with radiation of different frequencies are averaged. Whatever the form, the results from multiple looks must be added incoherently to approximate the average power return from the surface.

III. Speckle Reduction via Multiple Looks

In this study we wanted to simulate the effects of the "speckle" phenomenon as it would apply to a picture processed from satellite radar data. We chose an Earth Resources Technology Satellite (ERTS) optical picture that was put on magnetic tape with picture elements (pixels) representing 57- × 79-m resolution cells. The picture shown in Fig. 1 (low contrast original) represents the ERTS data from an area approximately 15.4 km left-right by 21.3 km up-down (270 × 270 pixels). Each pixel is quantized to 6 bits on the tape, representing 1 of 64 shades between black and white. To simulate the radar "speckle" we replaced each pixel value with a random variable exponentially distributed according to Eq. (1), with the mean value S taken as the original pixel value. This resulted in the picture (low contrast, 1 look) shown in the lower center of Fig. 1. As one can see, the image content is almost entirely lost. This photograph represents an extreme effect that the radar speckle would have on a single "look."

We then repeated this procedure 4, 16, and 64 times, and averaged the independent results to generate the pictures (low contrast series) shown in the center region of Fig. 1. Mathematically, we generated N identically distributed random variables, $s_1, \cdots, s_M$ and computed and plotted

$$s_M = \frac{1}{M}\sum_{i=1}^{M} s_i \qquad M = 1,4,16,64$$

for each pixel. Here, M represents the number of "looks."

[1]This admittedly crude definition of a "rough" surface is qualitatively the Rayleigh criterion, which states that a surface is rough or smooth depending on whether the height variation at grazing angle is respectively greater than or less than $\lambda/8 \sin \gamma$, λ being the wavelength of the radiation. For a discussion of the validity of the Rayleigh criterion, see Ref. 1.

[2]The theoretical hypotheses under which the amplitude will be Rayleigh-distributed are enumerated in Ref. 1, Chapter 7. Published data that verify the validity of these hypotheses are surprisingly rare; in fact, we have been unable to find any data of terrestrial radar returns that directly exhibit a Rayleigh amplitude distribution. Reference 1, page 463, presents evidence for the lunar radar return with a Rayleigh-distributed amplitude. Reference 5, pages 515–518, gives experimental evidence of Rayleigh-distributed amplitudes in radar returns from the sea.

The mean of s_M is still S, but the variance

$$\sigma_M^2 = \overline{(s_M - S)^2} = \frac{S^2}{M} \tag{2}$$

is reduced by the factor $1/M$ compared to a single look. Therefore, the signal-to-noise ratio (SNR) per pixel as defined by ratio of power in signal to standard deviation of that power

$$SNR_{pixel} = \frac{S}{\sigma_M} = \sqrt{M} \tag{3}$$

increases 3 dB per 4-fold increase in M. From these photographs we see that a reasonable facsimile of the original picture is obtained for some number of looks between 16 and 64.

The original Earth Resources Technology Satellite (ERTS) picture and the pictures simulating the multiple looks are all of a scene with rather low contrast. Figure 2 shows a histogram of the original pixels in the scene. The ordinate is the number of pixels n_s having a given value S (between 0 and 63), and the abscissa is the value S. Even though 64 contrast levels are available, these pictures are effectively using only about 10 levels. To increase contrast in the developed original image we uniformly "stretched" the pixel values to cover the full dynamic range of 64 levels by rescaling the data on the tape. This was accomplished for each pixel by the mapping.

$$S \rightarrow S' = 13(S - 10)/3 \tag{4}$$

where S' is the new pixel value given the cell that originally had pixel value S. (Of course, new pixel values less than 0 or greater than 63 were set to 0 and 63, respectively.) The high-contrast ERTS picture now has the histogram shown in Fig. 3. This higher-contrast original was once again studied for the effects of speckle. The resulting ERTS picture and those simulating 1, 4, 16, and 64 looks (high contrast series) are shown in the left-hand column of Fig. 1. Higher original contrast considerably improves the speckled image. In fact, the 16-look simulation reveals most of the features of the original high-contrast ERTS picture.

IV. Resolution vs Multiple-Look Tradeoff

Next, we studied the procedure of sacrificing resolution to increase the effective number of looks. This was accomplished by averaging returns from adjacent resolution cells. We took the multiple-look pictures of the center column of Fig. 1 (low contrast series) and replaced the pixel values of 4 adjacent pixels (2 up-down and 2 left-right) by the average of the 4. This procedure is illustrated in Fig. 4. Notice that the effective resolution cell area has increased by a factor of 4 as the result of this averaging, so we have sacrificed resolution to obtain more looks. Since we have increased the effective number of looks by a factor of 4, the information content of the low-resolution M look system should be close to that of the original $4M$-look system. The problem in making a visual comparison is that the resolution limit of the original system is determined by the area of a single pixel, while for the low-resolution system, it is determined by the area of 4 adjacent pixels. To facilitate this comparison we have decreased the area of the low-resolution series by a factor of 4. In Fig. 1 we see the resolution vs multiple-look tradeoff by comparing the center and right-hand columns. The information content of low-resolution M-look system is greater than that of the original M-look system and approaches but does not reach that of the original $4M$-look system for $M = 1$, 4, and 16.

V. Effect of Additive Noise

To investigate the effects of receiver and downlink noise on picture quality, we introduced varying amounts of additive white Gaussian noise (AWGN) to the multi-look pictures. Since each pixel is formed by envelope-detecting an in-phase and a quadrature signal, which are themselves contaminated by receiver noise, the situation is described by

$$\begin{aligned} v_I &= a_I + n_I \\ v_Q &= a_Q + n_Q \end{aligned} \tag{5}$$

where a_I, a_Q are the in-phase and quadrature voltages in the pixel from the scene in the absence of noise, and n_I, n_Q are the corresponding contaminating voltages in the pixel due to noise. The signal power s, noise power n, and total power v in the pixel are given by

$$\begin{aligned} s &= a_I^2 + a_Q^2 \\ n &= n_I^2 + n_Q^2 \end{aligned} \tag{6}$$

and

$$v = (a_I + n_I)^2 + (a_Q + n_Q)^2$$

These random variables are exponentially distributed since they are sums of squares of pairs of independent, identically distributed, zero mean gaussian random

variables. Moreover, since a_I, a_Q, n_I and n_Q are all statistically independent,

$$\bar{s} = \overline{a_I^2 + a_Q^2} = S$$
$$\bar{n} = \overline{n_I^2 + n_Q^2} = N \tag{7}$$

and

$$\bar{v} = S + N = V$$

Consequently,

$$p(v) = \frac{1}{V} e^{-v/V} \tag{8}$$

and we can produce the effect of noise by generating exponentially distributed pixels with parameter $S+N$, where S depends on the value of the original pixel and N is determined by the amount of noise we wish to introduce. This receiver signal-to-noise ratio is then

$$SNR = \frac{S}{N} \tag{9}$$

The pixel SNR will now be given by

$$SNR_{pixel} = \frac{S}{\sqrt{\overline{(v_M - V)^2}}} \tag{10}$$

where v_M is the M look average of the noisy observables $v_1, v_2, \cdots, v_M$, i.e., $v_M = \frac{1}{M} \sum_{i=1}^{M} v_i$. Using Eq. (2) we see this can be expressed as

$$SNR_{pixel} = \sqrt{M} \frac{S}{S+N} \tag{11}$$

which reduces to the "noiseless" case (3) as it should when $N = 0$. We chose values of N, the average noise power, to be 25, 12.5, 6.25, 2.5, and 0.79, corresponding roughly to receiver SNRs of 0, 3,6, 10, and 15 dB, respectively, since, as can be seen from Fig. 2, the average pixel intensity over the picture is close to 25. We replaced each pixel value S with the random variable v distributed according to Eq. (8) with $V = S+N$ from which N was subtracted. This subtraction was performed so that the nonlinearity imposed by the 6-bit quantization would not introduce unnecessary distortion by exceeding the dynamic range. The results for 0-, 3-, 6-, 10-, and 15-dB receiver SNR are shown respectively in Fig. 5 for M look systems where M = 1,4, 16, and 64. As one can see, increasing receiver SNR improves picture quality but not nearly as dramatically as increasing the number of looks. We can gain a rough understanding of the relationship between picture quality, number of looks, and receiver SNR by considering a typical pixel SNR. Admittedly, a single number such as pixel SNR cannot represent an entire picture, but it is commonly used to provide a rough index of picture quality. The mean power from the ith cell is $S_i + N$, but the "signal" portion of this return is S_i. The standard deviation of the power in an M-look system is $M^{-1/2}(S_i + N)$, so the pixel SNR is

$$SNR_{pixel} = \frac{\sqrt{M}\, S_i}{(S_i + N)} = \frac{\sqrt{M}}{(1 + 1/SNR_i)} \tag{12}$$

To obtain some feeling for the relation, consider an M-look system with infinite receiver SNR. A typical pixel SNR is $\sqrt{M}$. Now consider a system with $4M$ looks. This system will be better in terms of pixel SNR than the original zero receiver noise M-look system so long as its receiver SNR is greater than 1. We see that this result is borne out by comparing the M-look pictures of 10 and 15 dB with the $4M$-look pictures of 0 dB. We see that the $4M$-look pictures of 0 dB are better in each case shown (M = 1, 4, and 16). Also, from Eq. (12) and the pictures of Fig. 5 we see that receiver SNRs greater than 10 dB do little to enhance picture quality.

VI. Conclusions and Discussion of Results

In this study we have presented our results by demonstrating photographs of varying numbers of looks, contrast, resolution, and receiver SNR to be compared visually with original photographs of high and low contrast, fixed resolution, and infinite receiver SNR. We have seen qualitatively that with large receiver SNR, 64 looks in the low-contrast case, and perhaps as few as 16 looks in the high-contrast case provide a picture that certainly contains the salient features of the original. Of course, the fidelity required of the multilook image and the comcomitant criteria to measure this fidelity determine the actual number of looks and receiver SNR which the system must have. This in turn determines the coverage, resolution, and telemetry data rate of the overall system.

References

1. Beckman and Spizzichino, *The Scattering of Electromagnetic Waves from Rough Surfaces*, MacMillan Co., New York, 1963.
2. Schiffner, G., *Proc. IEEE*, 53, 1245, 1965.
3. Gabor, D., *IBM J. Theo. Develop.*, 14, 509, 1970.
4. Enloe, L., *Bell Sys. Tech. J.*, 46, 1479, 1967.
5. MIT Radiation Laboratory Series, Vol. 13, edited by D. E. Kerr.
6. Lord Rayleigh, *The Theory of Sound*, MacMillan Co., 3rd Edition, London, 1896.

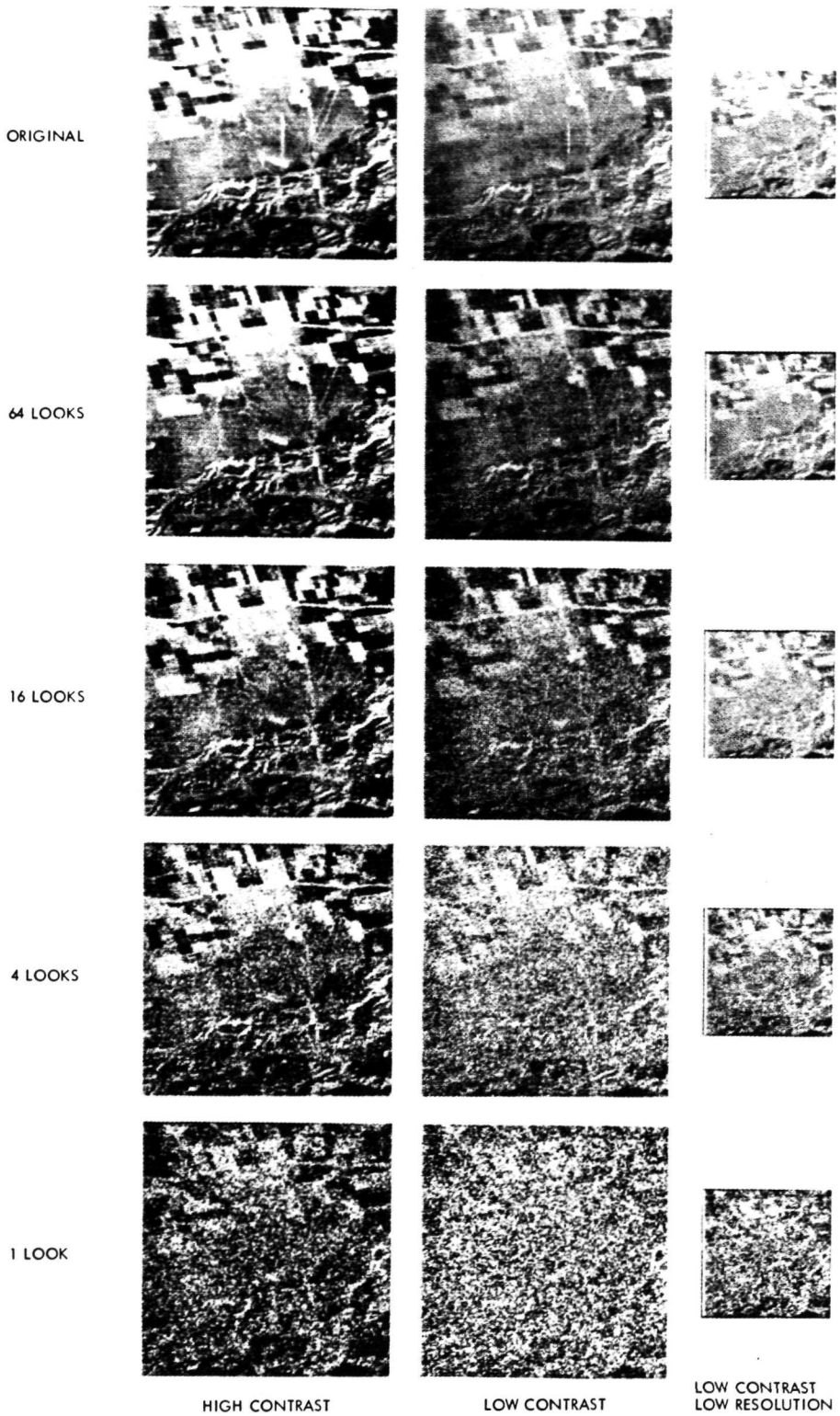

Fig. 1. Original ERTS photograph and photographs showing effects of 1, 4, 16, and 64 looks for high-contrast, low-contrast and for low-contrast, low-resolution series

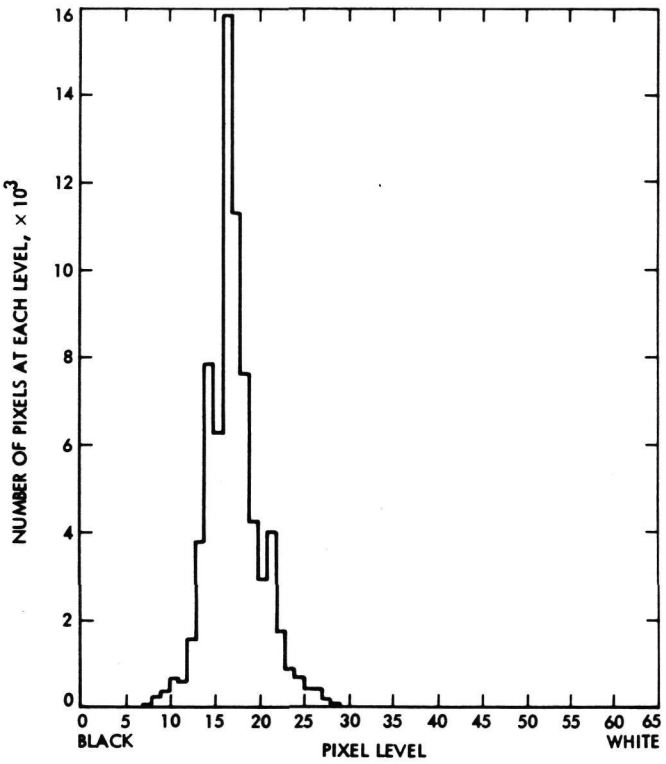

Fig. 2. Histogram for low-contrast ERTS original showing number of pixels having a value S vs the value S_n (S = 0, • • • , 63)

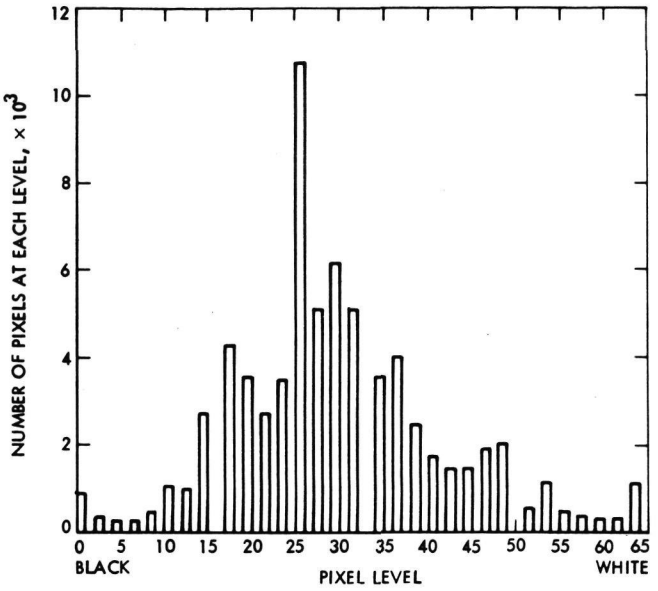

Fig. 3. Histogram for high-contrast original showing number of pixels having a value S vs the value S (S = 0, • • • , 63)

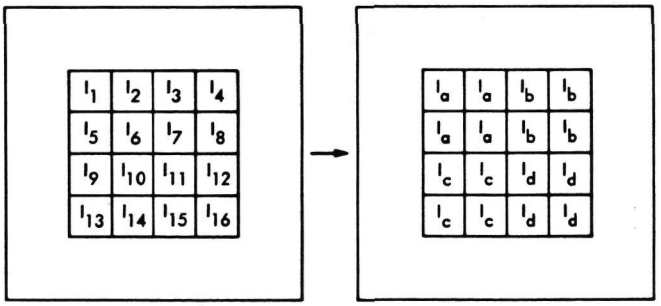

$I_a = 1/4\ (I_1 + I_2 + I_5 + I_6)$

$I_b = 1/4\ (I_3 + I_4 + I_7 + I_8)$

$I_c = 1/4\ (I_9 + I_{10} + I_{13} + I_{14})$

$I_d = 1/4\ (I_{11} + I_{12} + I_{15} + I_{16})$

Fig. 4. Diagram illustrating how resolution cell averaging was performed for low-contrast, low-resolution series

Fig. 5. High-contrast photographs illustrating effects of varying number of looks (M = 1,4,16, and 64) and varying receiver signal-to-noise ratio (SNR = 0,3,6,10, and 15 dB) on simulated SAR image quality

An X-Band Radiometer for the Microwave Weather Project

M. S. Reid, O. B. Parham, and R. A. Gardner
Communications Elements Research Section

A stabilized high-resolution X-band radiometer has been designed, constructed, and is presently operating at the Venus Deep Space Station in the Goldstone Deep Space Communications Complex in California. The radiometer is an automatically switched and automatically calibrated noise-adding radiometer and is used for atmospheric propagation research for the Microwave Weather Project. This report describes the radiometer, its sensitivity, and gives examples of its performance.

I. Introduction

The Microwave Weather Project forms part of an overall Radio Systems Development Project which seeks to optimize the spacecraft-to-ground communications link. The objective is to provide a mathematical model of atmospheric transmission at X- and K_u-bands. This model will allow practical predictions of link performance to be made and will also form the basis of a specification of the receiving sensitivity of a Deep Space Network ground station. The model, which contains both probabilistic and deterministic elements, is based on the statistical correlations of weather and communications capability at X- and K_u-bands. Previous reports (Refs. 1, 2) have discussed the Microwave Weather Project and described the method and equipment used to build a suitable data base from which the mathematical model can be designed. They also described the difficulty of acquiring sufficient data of good quality using the existing X- and K_u-band radiometers on the 64-m antenna at DSS 14 at Goldstone DSCC.

In order to improve both the quantity and quality of the X-band data, a radiometer has been designed, built, and installed at DSS 13. This radiometer is a high-precision instrument that is dedicated to the Weather Project and which operates 24 hours-per-day automatically collecting data. This report describes this radiometer and its method of operation.

II. The Equipment

Figure 1 shows a block diagram of the X-band radiometer. The antenna is a corrugated horn which is directly coupled to a waveguide switch. The switch can connect the receiver to the horn, an ambient termination or a liquid nitrogen-cooled termination. The horn is built to the same design as the X-band horns used in the X-band radar, transmit-receive; K-band receive (XKR) cone on the 64-m antenna at DSS 14 and the Multiple Frequency X- and K-Band (MXK) cone which preceded it on the antenna. The gain of the horn is 22.3 dB; the dissipation

loss in the horn contributes 1K, +0.5, −0.25 (K) in noise temperature; the 3-dB beamwidth is 7 deg (half angle) and the gain is down 10 to 12 dB at a half angle of 15 deg. The receiver is a mixer and IF amplifier, the output of which feeds a detector which has been described in several previous reports, (Refs. 3–6). The computing counter and programmer form a noise adding radiometer (NAR), (Ref. 7), whose noise diode feeds into the receiver through a coupler, as shown in the diagram. The output from the NAR feeds a data acquisition system, which is described elsewhere. The block diagram shows that two local oscillators (LO) are available, only one of which is used at a time. These two solid state LO's are set a few hundred megahertz apart, which allows ample frequency agility to avoid interference by microwave communication links or X-band transmitters. The LO presently in use is set at 8498 MHz.

The noise diode and its input coupler, the receiver, the local oscillators and all the interconnecting lines between these items are all temperature controlled to ±2°C in an environmental enclosure. This is shown schematically in the diagram.

In normal operation the radiometer is automatically switched between the horn and the ambient load. This is an additional calibration capability and is described in the next section. The liquid nitrogen-cooled load is not used in routine operation; it is a precision calibration tool which is used manually, approximately once per month.

The waveguide system and horn are pressurized with dry nitrogen gas. The radiometer is enclosed in a suitable box, which is mounted on an elevation-over-azimuth electric antenna drive. Figures 2 and 3 are photographs of the system.

III. Calibration by the Cryogenic Load

A precision calibration using the cryogenic load is carried out manually at periodic intervals. This serves primarily to calibrate the noise temperature of the noise diode (T_N). Regular measurements of T_N will keep a check on the noise diode aging, and thus remove the possibility of these effects (or other slow drifts) from contaminating the data quality. The calibration is carried out by adjusting the value of T_N so that the NAR output corresponds with the calibrated thermal noise temperature of the cryogenic load when the receiver is connected to this load.

IV. Routine Operation

In routine operation the waveguide switch is automatically controlled by the NAR programmer to switch the receiver to the horn for one minute and then to the ambient load for one minute. This cycle is repeated continuously during normal operation.

With the receiver connected to the ambient load the NAR measures a system operating noise temperature in kelvins (T_{op}), such that

$$T_{op}|_{load} = T_E + T_P \tag{1}$$

where

T_E = receiver front-end excess noise temperature (K)

T_P = physical temperature of the ambient load (K).

The reference plane for T_E is the input to the waveguide switch. T_P is measured by a quartz thermometer in the ambient load and therefore the programmer can solve for T_E. The value for T_E is calculated every second minute when the receiver is connected to the ambient load.

When the receiver is connected to the horn the NAR measures a system operating noise temperature ($T_{op}|_{horn}$) such that

$$T_{op}|_{horn} = T_{atmos} + T_E + T_C + T_H \tag{2}$$

where

T_{atmos} = noise temperature due to the atmosphere (K)

T_C = cosmic background temperature (K)

T_H = noise temperature due to horn losses and a waveguide component, consisting of a stepped transition from circular to rectangular guide and about 3 cm in length, and any possible mismatches (K)

The values for T_C and T_H are assumed constant,

$$T_C + T_H = 2.7 + 1.7 = 4.4\ \text{K} \tag{3}$$

T_E has been automatically measured and calculated by the NAR from Eq. (1) and therefore the NAR computes the noise temperature due to the atmosphere by

$$T_{atmos} = T_{op}|_{horn} - (T_E + T_C + T_H) \tag{4}$$

On a clear day with the horn at zenith the atmospheric noise temperature is usually about 2.6 K.

V. Radiometer Sensitivity

The sensitivity of the NAR has been shown (Ref. 7) to be:

$$\Delta T_{min} = \frac{2\,T_{op}\left(1 + \frac{T_{op}}{T_N}\right)}{(\tau B)^{1/2}} \text{ kelvins} \qquad (5)$$

where

B = detector bandwidth, Hz

τ = equivalent integration time of the output integrator, sec

The bandwidth of the system is presently set at 20 MHz (10-MHz double sideband centered at 8448 and 8548 MHz). T_{op}, with the receiver connected to the horn, is approximately 600 K, and with the receiver connected to the ambient load, T_{op} is approximately 900 K. In either position the NAR switches the noise diode on and off 130 times in 52 sec. Thus 130 T_{op} measurements are calculated and averaged every minute. The equivalent integration time is therefore 52 sec. The NAR measures T_P both before and after each set of 130 Y-factor measurements on the ambient load. These two T_P measurements are averaged and used in the calculation for T_E. T_N is presently set to 1300 K. With these parameters the system sensitivity becomes (from Eq. (5)):

$$\Delta T_{min}|_{load} = 0.09 \text{ K}$$

$$\Delta T_{min}|_{horn} = 0.05 \text{ K}$$

so that the combined sensitivity (or resolution for relative atmospheric measurements, $\Delta T_{min}|_{atmos}$) is 0.1 K.

Figure 4 shows two elevation profiles made at DSS 13 on Aug. 4, 1975 with the horn tipping to the South (azimuth 180 deg). Atmospheric noise temperature in kelvins is plotted against elevation angle in degrees. The solid data points were made at 10:00 a.m. PST in clear sky; the open data points were made at 3:00 p.m. PST with some thin clouds to the south.

VI. Conclusions

A stable radiometer with high resolution has been constructed at X-band for the Weather Project. It is presently operating 24 hours per day at DSS 13. The addition of a similar K_u-band radiometer is under investigation.

References

1. Reid, M. S., "A Description of the Weather Project," Technical Report 32-1526, Vol. X, pp. 116-122, Jet Propulsion Laboratory, Pasadena, Calif., August 15, 1972.

2. Reid, M. S., Booth, R. W. D., "Preliminary Analysis of the Microwave Weather Project Data for CY 1971," Technical Report 32-1526, Vol. XI, pp. 111-120, Jet Propulsion Laboratory, Pasadena, Calif., October 15, 1972.

3. Reid, M. S., Gardner, R. A., Stelzried, C. T., "A New Broadband Square Law Detector," Technical Report 32-1526, Vol. XVI, pp. 78-86, Jet Propulsion Laboratory, Pasadena, Calif., August 15, 1973.

4. Reid, M. S., Gardner, R. A., Stelzried, C. T., "Improvement in the Accuracy of the New Broadband Square Law Detector," Technical Report 32-1526, Vol. XVIII, pp. 94-98, Jet Propulsion Laboratory, Pasadena, Calif., December 15, 1973.

5. Gardner, R. A., Stelzried, C. T., Reid, M. S., "Radiometric Applications of the New Broadband Square Law Detector," Technical Report 32-1526, Vol. XIX, pp. 89-92, Jet Propulsion Laboratory, Pasadena, Calif., February 15, 1974.

6. Reid, M. S., Gardner, R. A., Stelzried, C. T., "A New Broadband Square Law Detector," Technical Report 32-1599 (to be published).

7. Batelaan, P. D., Goldstein, R. M., Stelzried, C. T., "A Noise Adding Radiometer for use in the DSN," Space Programs Summary 37-65, Vol. 2, pp. 66-69, Jet Propulsion Laboratory, Pasadena, Calif.

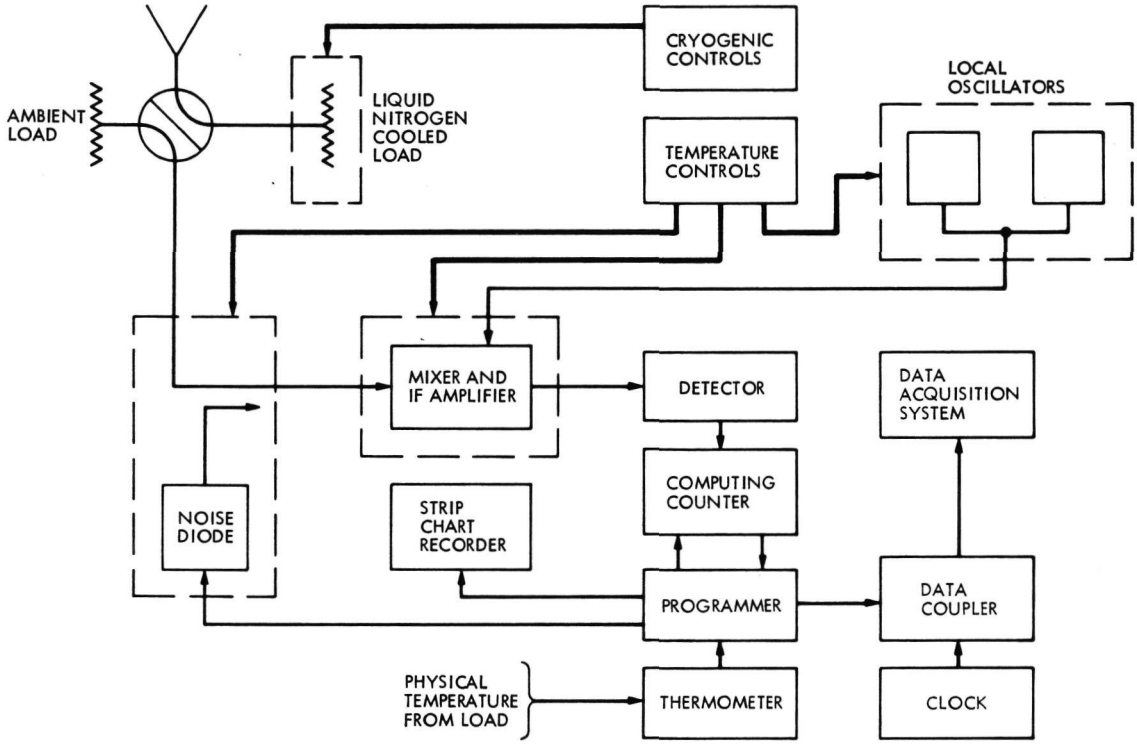

Fig. 1. Block diagram of the X-band radiometer

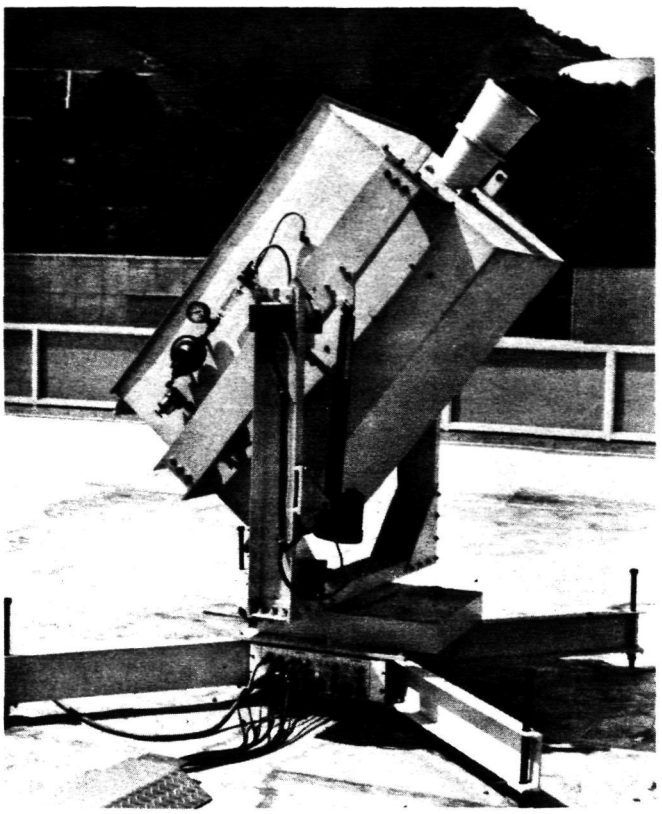

Fig. 2. Photograph of the X-band radiometer

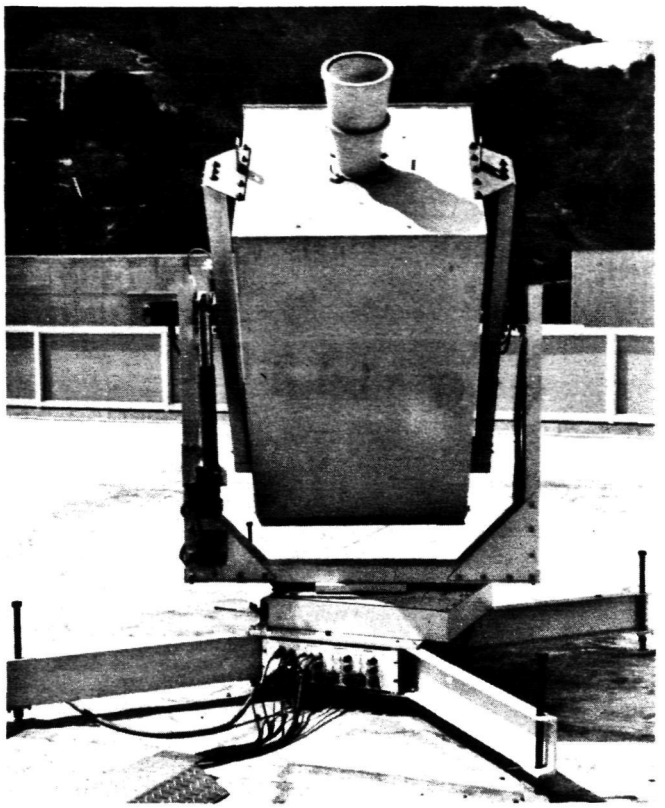

Fig. 3. Photograph of the X-band radiometer

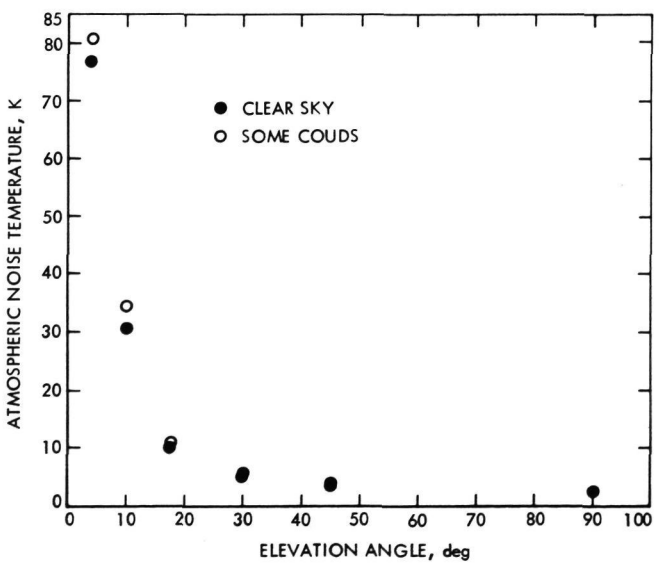

Fig. 4. Elevation profile of atmospheric noise temperature

Aerodynamic Static Differential Pressure Values for the 50 Percent Porous Reflector Dish

M. S. Katow
DSN Engineering Section

Although the solid and the 25 percent porous thin paraboloidal dishes were instrumented with static pressure tubes and tested in the wind tunnel, the porosity used for the 64-m antenna was 50 percent for economic reasons. The extrapolation to 50 percent porosity, to date, has resulted in conservative values. This report describes a method of extrapolating from the available data the 50 percent porous pressure coefficient differences. The method is verified by checking the available wind tunnel static pressure data against the force data.

I. Introduction

A series of antenna models were tested in a wind tunnel (Refs. 1 and 2) to provide wind loading data for the design of the 64-meter antenna. The parameters of the models were selected on the basis of preliminary design results. For example, the complete antenna model used a 25 percent porous reflector surface for the outer 25 percent radius. However, reflectors with solid, 25 percent porous, and 50 percent porous dishes were tested for their aerodynamic force and moment values. Only the solid and the 25 percent porous dishes were tested for the static pressure values used primarily to determine the wind loading on the reflector's surface panels. The wind loading was then applied to the reflector structural models to determine the rms distortions from a paraboloidal shape, which is useful for radio frequency (RF) gain calculations.

As part of the cost reduction effort, the porosity of the dish was increased to 50 percent in the final design so that lower wind designing loads could be used. This caused the generation, by interpolation and extrapolation, of applicable force and moment curves for the whole antenna under wind loading. New curves for the static pressure values were also generated. The results, available to date (Ref. 1), show that the force and moment curves were accurate. However, the static pressure curves used for the design proved to be too conservative.

This report describes a method for extrapolating the 50 percent porous static pressure data from the solid and the 25 percent porous static pressure values. The accuracy of the result (estimated within 10 percent) should be well within the requirements for structural analysis.

The verification of the calculating method was proved by first applying it to available solid dish and 25 percent porous dish static wind tunnel pressure data. The answers resulted in a good match between the wind tunnel force and moment test values and the integrated values of the static pressures. Since force and moment values for the 50 percent porous dish from the wind tunnel tests are available, correctly extrapolated static pressure for the 50 percent porous dish, when integrated, should match the wind tunnel values.

II. Description

The static pressure values were described in Ref. 2 as pressure coefficient differences across a thin paraboloidal surface with a focal length-to-diameter (F/D) value of 0.33. An example is Fig. 1 with the average pressure coefficient difference values shown for the 25 percent porous dish by a solid curve, where the pitch angle is equal to 180 degrees and the yaw angle equal to zero. In other words, the wind is blowing along the symmetric axis of the dish into the convex side. The solid curve represents the average of the static pressure readings of the pressure tap locations shown in Fig. 2.

Working toward the solution of the static pressure values for the 50 percent porous dishes, static pressure orifices located on a sample porous plate were tested by the Thermophysics and Fluid Dynamics Section in a small wind tunnel available at JPL. The results showed that the static pressure accurately measures the pressure differences across the 50 percent porous plate placed in a wind stream.

Figure 1 shows that the pressure difference coefficient values are higher for the 25 percent porous dish than for the solid. It follows that these values could be higher by the same increment for the 50 percent porous dish as shown by the extrapolated dotted line.

To test the accuracy of the static coefficient differences, as applied to the surface panels of a reflector dish, the static pressure data were interpolated for the pitch angle of 120 degrees by use of curves shown in Fig. 3. The sample values for the 15-degree angle row of static orifices are shown in Fig. 4, where only the windward-half values from one column of static orifices are shown. The other half of the dish was very lightly loaded for porous dishes at a pitch angle of 120 degrees.

The pitch angle of 120 degrees was selected since the pitching moment is the maximum. Also, since the pressure differences have the largest asymmetry at this pitch angle, the reflector distortion should also be the maximum.

A computer program was coded to calculate the solid surface areas applicable to each pressure coefficient difference, followed by integration of the forces with final calculations of the aerodynamic-type coefficients.

In Table 1, the wind tunnel test values (Ref. 1) for the forces and moments are compared with the values computed from the static pressure data from the wind tunnel test values (Ref. 2) for the solid and the 25 percent porous dishes, as well as for the extrapolated curves for the 50 percent porous dish.

III. Conclusions

The drag coefficients for the wind directly into the front and back of the solid and 25 percent porous dishes between the wind tunnel force tests and the integration of the static data compare very closely as presently computed. Of course, this check was also made during the wind tunnel tests for data verification purposes. This match now also serves to check our computer program and the calculations for the 50 percent porous data.

The extrapolated 50 percent porous curve need only be increased slightly in Fig. 1 for a good match of data.

For the 120-degree pitch angle case, the values for axial (body axis) force and the pitching moment coefficients match closely. The normal force coefficient from the static pressure data is substantially smaller. The major part of the difference may be explained as follows: As the direction of this component is normal to the symmetric axis of the reflector, there is a wind force existing in the wind tunnel models not present in the static pressure integrating computations. This wind force arises from the wind hitting the sides of the 9.5-mm (3/8-in.) holes in the 3-mm (1/8-in.)-thick dish plate, and is referred to as shear force or skin friction force.

The axial force coefficients for the solid dishes from the two methods show some difference, which is still not understood at this time.

It is concluded that the extrapolated curves for the 50 percent porous dish will produce accurate aerodynamic coefficient values for paraboloidal dishes of this porosity in the wind.

Acknowledgment

The author wishes to acknowledge the contributions of Robert W. Weaver, JPL Thermophysics and Fluid Dynamics Section, for his work in conducting the tests and providing the results on the sample porous plate, for his general review of this report, and for his many helpful comments.

References

1. Fox, N. L., and Dayman, B., Jr., *Preliminary Report on Paraboloidal Reflector Antenna Wind Tunnel Tests*, IM CP-3, Feb. 28, 1962 (JPL internal document).
2. Fox, N. L., *Load Distributions on the Surface of Paraboloidal Reflector Antennas*, IM CP-4, Feb. 28, 1962 (JPL internal document).
3. Katow, M. S., and McGinness, H. D., "Wind Load Predictions for the 64-meter-diameter Antenna," in *The Deep Space Network Progress Report*, Technical Report 32-1526, Vol. XV, pp. 96–101, Jet Propulsion Laboratory, Pasadena, Calif., June 15, 1973.

Table 1. Aerodynamic coefficients of thin paraboloidal dishes

Configuration	Pitch = 0° Yaw = 0°	Pitch = 0° Yaw = 180°	Pitch = 60°; Yaw = 180°		
	C_{AXIAL}	C_{AXIAL}	C_{AXIAL}	C_{NORMAL}	C_{MOMENT}
Solid					
A	1.50	−1.02	−0.187	0.195	0.127
B	1.52	−1.05	−0.280	0.166	0.129
25% porous					
A	1.17	−0.94	−0.321	0.203	0.109
B	1.30	−0.96	−0.349	0.149	0.116
50% porous					
A	0.83	−0.83	−0.294	0.217	0.093
B		−0.77	−0.293	0.125	0.097

F/D = 0.33; moment center at paraboloid's vertex

A = values from wind tunnel's force data

B = values from pressure coefficient difference integration

C_{AXIAL}, C_{NORMAL}, C_{MOMENT} = body axis force and moment coefficients

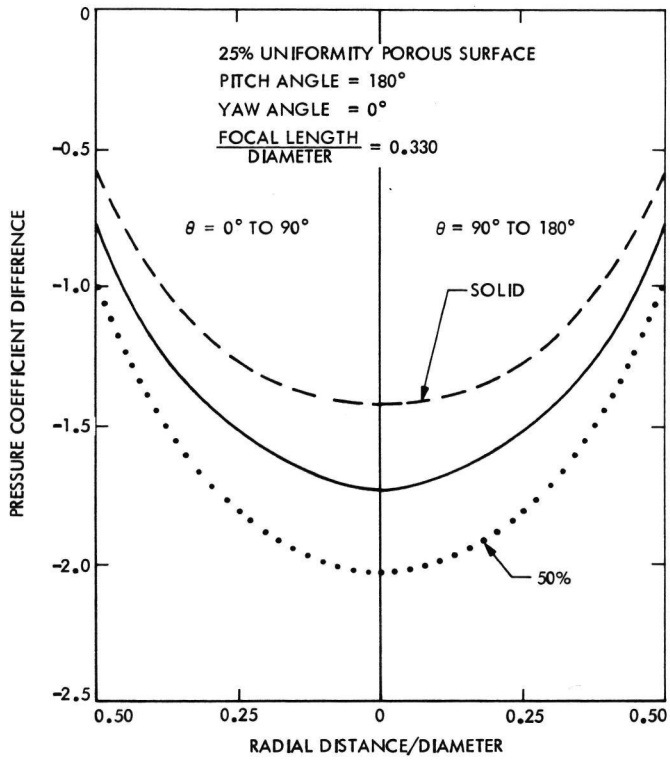

Fig. 1. Pressure coefficient differences across a thin paraboloidal 25 percent uniformly porous surface at pitch angle of 180 deg

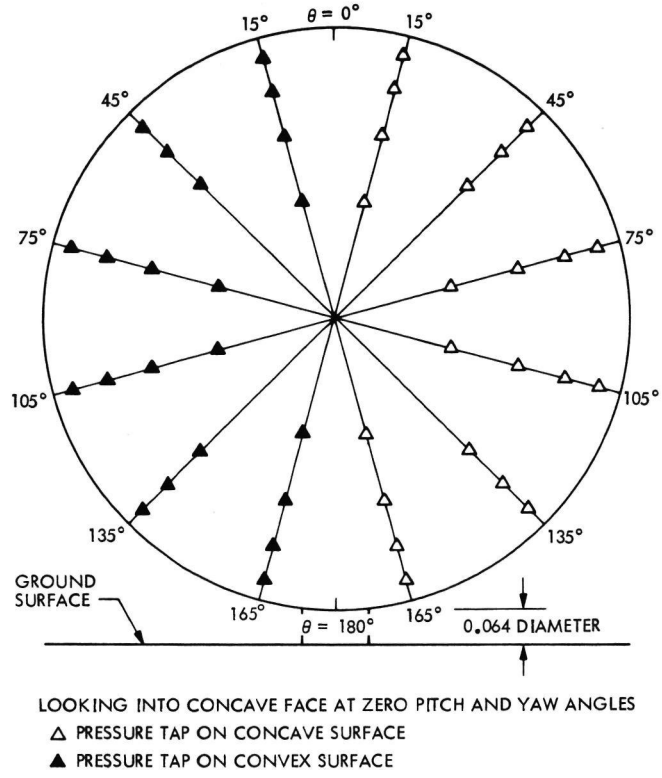

Fig. 2. Pressure tap locations on model

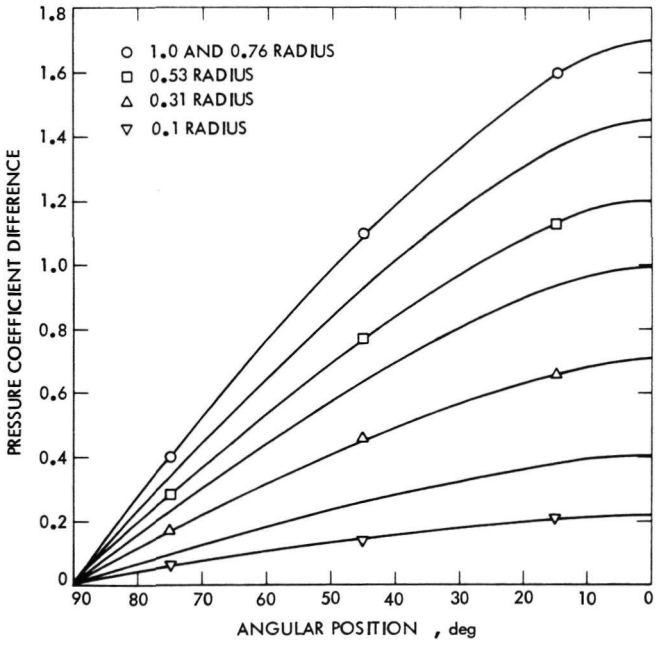

Fig. 3. Pressure coefficient difference: interpolated values

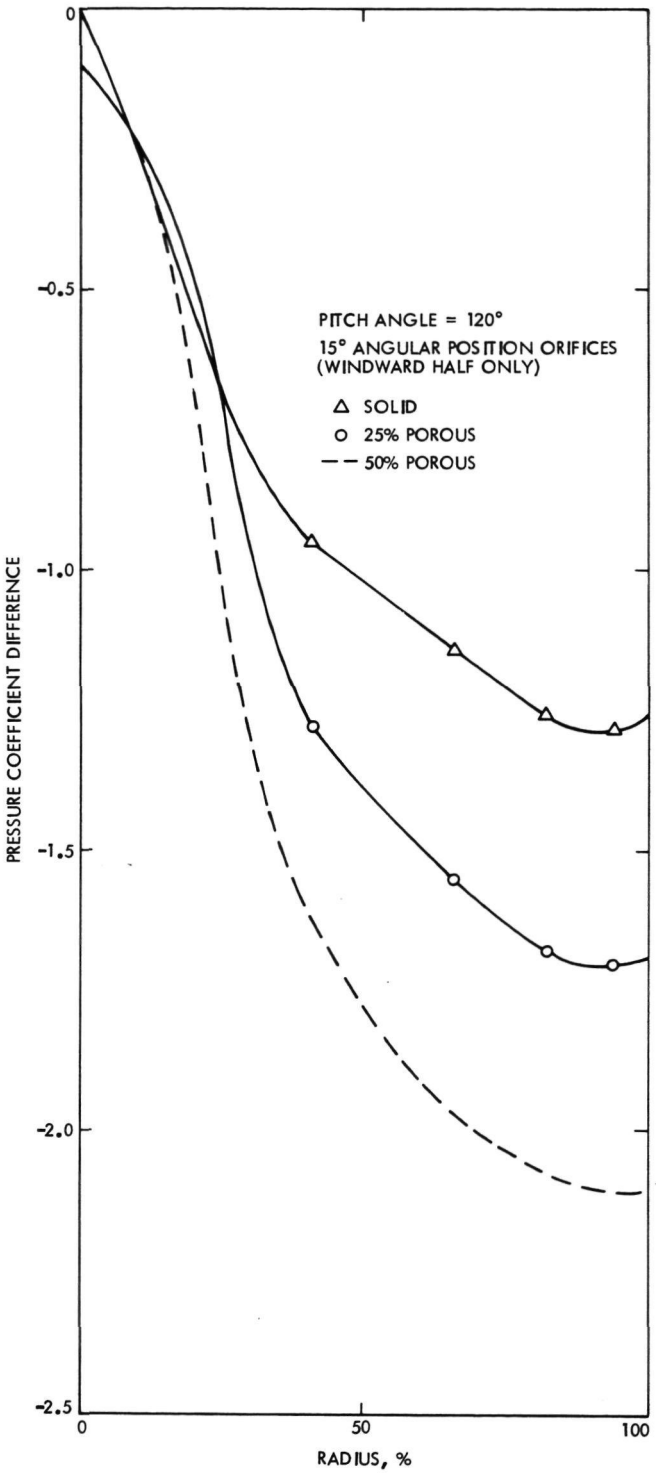

Fig. 4. Pressure coefficient difference at pitch angle of 120 deg

RF Automation Demonstration

R. B. Crow
R. F. Systems Development Section

The radio frequency (RF) automation demonstration was conceived to gather data for a life cycle study to evaluate the cost and operational effectiveness of automation. The RF automation demonstration, as originally envisioned, performs a very important function of "qualifying" the system in that it checks both the necessary conditions (i.e., that the receive/transmit system can be configured and calibrated) and the sufficient conditions (by automatically acquiring the carrier and subcarrier). Continuous monitoring also allows real-time repair of those "necessary conditions" (relay operation, references, etc.) so that the system can be maintained at a higher level of readiness than is now possible.

I. Introduction

The RF (radio frequency subsystem) automation demonstration was conceived to gather data on an operational system so that criteria for managing DSN automation could be developed. The RF "subsystem," consisting of the microwave subsystem, two Block IV receivers and one exciter, two Block IV Subcarrier Demodulator Assemblies (SDAs), the noise-adding radiometer (NAR), and the 400-kW S-band operational transmitter located at DSS 14, was chosen since the hardware evolution made automation possible, and the administrative control for the development of this equipment was contained primarily within one section. Each subassembly was capable of either manual or computer control (selected by a front panel configuration switch). A computer was used to control each type of subassembly while system control and coordination were performed by the RF demonstration computer. The RF automation demonstration, as originally envisioned, performs a very important function of "qualifying" the system, in that it checks both the necessary conditions (i.e., that the receive/transmit system can be configured and calibrated) and the sufficient conditions (by automatically acquiring the carrier and subcarrier). Continuous monitoring also allows real-time repair of those "necessary conditions" (i.e., relay operation, references, etc.) so that the system can be maintained at a higher level of readiness than is now possible.

II. Demonstration Plan

The RF automation demonstration was managed by developing a functional requirements document describing the scenario for the RF automation demonstration,

software standards, a development schedule, and manpower assignment.

Each subassembly controller software design was reviewed to assure compliance with the functional requirements before further development was undertaken. Maximum checkout at JPL was attempted to minimize the DSS 14 installation and checkout time.

Figure 1 is a functional block diagram of the RF system automation demonstration configuration. Each of the major subassemblies shown was controlled by its own computer; system control and coordination were performed by the RF demonstration computer, which also served as the operation interface.

The remainder of this report defines the original demonstration ground rules and reviews the actual demonstration performed at DSS 14. Observations and data on the experiment are listed. The report concludes with a summary of the important data of this demonstration, a proposed plan for future work, and criteria for future automation implementation.

III. Demonstration Ground Rules

A functional requirements document for the RF automation demonstration was written, setting forth the following ground rules:

(1) All software would be top-down design, implemented in a high-level language using structured programming.

(2) Available research and development (R&D) computers would be utilized (three PDP-11/20 minicomputers and one Intel 8080 microcomputer; see Fig. 1).

(3) The hardware interfaces between existing hardware and subsystem controllers would not be changed from those existing prior to this demonstration.

(4) The hardware interfaces between subsystem controllers and RF demonstration controller would be new installations utilizing the DSN standard 14-line interface and standard teletype.

(5) The interface between the operator and the RF demonstration controller would be simple English words.

(6) The RF demonstration computer would accept all configuration messages from the operator and distribute them to the correct subsystem controller. The RF demonstration controller would receive the necessary feedback from the subsystem controller and perform all necessary coordination between subsystem controllers to effect automatic configuration, calibration, acquisition, and failure backup.

(7) The RF demonstration controller would appear transparent to each subsystem controller in that diagnostic messages from each subsystem controller would be printed at the operator terminal exactly as sent by the subsystem. In this way, the design of diagnostics in the subsystem controller would not impact the design of the RF demonstration controller.

(8) Polling of the interfaces would be used to communicate between computers.

IV. Description of the RF Automation Demonstration

The RF demonstration controller was programmed to execute five phases of operational sequences which are described in the following paragraphs. Figure 2 is a flow diagram describing the demonstration software.

BEGIN. To begin a mission, the RF demonstration controller polled the subassembly controller to determine which of the subassembly devices were under computer control. The RF demonstration controller then sent a message to the operator indicating which devices were under computer control. The transmitter controller was then directed to turn on the filaments and coolant system, and to check all monitor facilities and the crowbar safety device. During this time, the Block IV SDAs were directed to calibrate so as to determine their operational status. When the transmitter became ready for precalibration (PRECAL) and both SDAs had been internally calibrated, the operator was notified to load the mission configuration into the RF demonstration controller's paper tape reader and type 'CAL' to begin PRECAL.

PRECAL. The mission configuration data were read in from a paper tape. The RF demonstration controller then sent all configuration messages to the appropriate subassembly controllers. After the messages had been received and acknowledged by the subassembly controller, the RF demonstration controller then sent calibration commands.

The noise-adding radiometer (NAR) was used to automatically measure system noise temperature. These data were sent to the receiver controllers where they were available to determine the signal power in the automatic-gain control (AGC) calibration process.

The RF demonstration controller coordinated the calibration phase by monitoring the status and issuing calibration commands at the appropriate time (i.e., after RCV 3 had completed calibration, SDAs 5 and 6 were commanded to calibrate with reference to RCV 3).

The operator was kept apprised of the progress of the calibration sequence by messages from the subassembly controller (through the RF demonstration controller) which were displayed on the operator's CRT control unit.

When all subassemblies were calibrated, the RF demonstration controller issued a standby command. The operator was then prompted to start the mission (by typing 'START').

OPERATE. When the operator typed a 'START' command, the transmitter was turned on and an automatic carrier acquisition sequence was initiated. The operator (and the RF demonstration controller) was notified by message generated by the receiver controller when each receiver had acquired. The RF demonstration controller automatically commanded the appropriate SDA to acquire once its input receiver was in lock. The operator was informed when each SDA acquired lock.

During this phase of the mission, the noise-adding radiometer automatically measured the open-loop gain of the maser preamplifier and front end of the S-band receiver. Changes in gain (greater than 0.02 dB) were sent to the receiver in order that the signal power versus AGC calibration could be corrected so that a more accurate carrier power estimate was available.

Each subassembly controller maintained a constant monitor on the "necessary" conditions for operation. If a failure was observed, the subassembly controller automatically reconfigured the appropriate subassembly to the predetermined (part of the original configuration input) backup configuration. The operator (and the RF demonstration controller) was notified of the configuration change and automatic acquisition was initiated. The operator then received the appropriate diagnostics/instruction to repair the failed unit.

The RF demonstration controller coordinated reacquisition (i.e., when a receiver failed, not only must it be functionally replaced with its predetermined backup, but the necessary configuration changes must be made to the SDAs to accept a new receiver input) and subsequent reacquisition of the carrier and subcarrier.

The operator terminated the mission by typing 'HALT' which automatically started the post-calibration (POSTCAL) sequence.

POSTCAL. The operator's 'HALT' command caused the transmitter to turn off. When the transmitter controller confirmed that the transmitter was in standby, the RF demonstration controller initiated a post-calibration sequence by first configuring the microwave equipment and then issuing post-calibration commands to the transmitter, receiver-exciter, and SDA subassembly controllers.

A similar sequence was followed as in pre-calibration (i.e., the RF demonstration controller coordinates the receiver and SDA calibration sequence). Noise temperature was automatically obtained from the NAR as in pre-calibration.

When all subsystems had completed post-calibration, the operator was prompted to type 'RESTART' to run another mission or type 'END' to secure the RF subsystem.

END MISSION. The transmitter controller was commanded to secure the transmitter (i.e., an orderly turnoff sequence in which the coolant system cools the power amplifier before turning itself off). All other subsystems were placed in a "standby" configuration.

V. Demonstration Results and Observations

The receive channel (i.e., the antenna microwave subsystem, Block IV receiver-exciter, Block IV SDA, see Fig. 1) successfully demonstrated automatic configuration, calibration, and acquisition (both carrier and subcarrier) of a simulated signal during the first tests. The transmit channel was not tested during this time (due to a hardware failure of the 400-kW S-band operational transmitter). However, a later demonstration was run with the 400-kW R&D transmitter, where automatic configuration, calibration, and output power control were successfully demonstrated.

Several observations made during the RF automation demonstration effort are listed below to document some of the more interesting characteristics.

(1) *Actual Time to Automatically Control the Receive Channel.* The BEGIN phase took 6 to 7 minutes to poll all controllers and internally calibrate the Block IV SDAs.

The PRECAL phase took 6 to 8 minutes to input and distribute the mission configuration data and an additional 10 minutes to calibrate receivers 3 and 4 (the receivers were calibrated in series) and 0.5 minute to calibrate SDAs 5 and 6.

This performance was far slower than the original estimate of 5 minutes for a complete PRECAL sequence. Future effort will be directed at reducing the PRECAL and configuration time.

(2) *Intra-computer Communications.* Software implementation of data transfer over a 14-line interface was used. This routine was written in both RT-11 (DEC) BASIC and PL/M (high-level language used in the Intel 8080). The BASIC software data transfer was very slow (6 bytes/second). The PL/M software, when transferring data to the Block IV SDA, operated at 600 bytes/second and should operate at 300 bytes/second if transferring data to another 8080 microcomputer.

Polling was used in lieu of interrupts in an attempt to simplify the software development and determine if polling performance was adequate for real-time hardware control of this type. It was found, however, that polling is probably the largest contributor to the poor communication speed, since as much as one minute was spent waiting for some of the controllers to process a message before accepting new data. This characteristic became a serious problem when it was necessary to continue handling low priority (diagnostic) messages while operational "action" messages were left waiting for several minutes.

Both 14-line and serial interfaces were used during the demonstration. No known noise or communication failures were noted. One hardware failure occurred, and a possible "start up" problem in the serial interface hardware was noted.

(3) *Program Size/Development Time.* Table 1 indicates the size of each program and the approximate software development effort. Several factors should be considered when reviewing these data:

(a) The RT-11 operating system had software bugs in its "overlay" option that forced the RF demonstration program to be rewritten to achieve a reasonable software reliability.

(b) The PDP-11's with the large number of unibus loads (i.e., Dectape, several digital input/output (I/O) interfaces, analog-to-digital converter (ADC), teletype (TTY), etc.) were unreliable. Random system failures occurred with no known hardware failure to explain them. During the course of the demonstration, several hardware failures did occur (i.e., memory failure, TTY failure, paper tape reader failure). The PDP-11's poor reliability record stood out in stark contrast to the 8080 microcomputer which has operated *without* failure since its purchase in December 1974.

(c) The RT-11 operating system required 10.5 kilowords of core. The core requirement of the programs (listed in Table 1) required "chaining" in all PDP-11 computers except the receiver–exciter controller where 24 kilowords of core existed.

(d) Proper structuring of the software from both the instructional and data viewpoints was hindered by the use of RT-11 BASIC and the lack of memory. For example, in the receiver–exciter controller, sets of bits had to be packed into floating point variables conserving core, but creating awkward, time-consuming BASIC constructs to manipulate them.

(4) *Operational Effectiveness.* The demonstration pointed out the need for more flexible operator controls so that nonstandard operations could be handled (i.e., it should be possible: (a) to change the receiver's acquisition characteristics by merely typing "RCV 3, Δf = -100 kHz" and lower the original S-band acquisition window by 100 kHz, (b) to change the receiver doppler rate, and (c) to change SDA symbol rate and modulation index by similar high-level operator inputs, etc.).

(5) *High-Level Language.* RT-11 BASIC was used for all controllers except the SDA controller (which used PL/M). The BASIC language was slow, had no capability for bit manipulation (required in configuration control), and was not well suited for structured programming.

PL/M is a high-level language currently available as a cross compiler installed in the Univac 1108 to generate code for Intel 8080 as compiled object code. PL/M provides a more favorable speed and memory characteristic than does the RT-11 BASIC. The present PL/M operating system contains a two-pass compiler and an 8080 simulator. This facility is flexible and was used with good results for correcting a software problem while at DSS 14.

(6) *Top-Down, Structured Design.* This design method produced efficient readable code. Changes were

easily made (due to modular code that resulted from using a structured design).

VI. Summary of the RF Automation Demonstration

Lack of operational reliability was the single most troublesome factor in demonstrating automation feasibility. The importance of reliable hardware and software with built-in fault isolation and diagnostic capability was recognized and will be incorporated into future designs.

A much better understanding now exists of the needed operator controls and the environment in which they are used.

The RF automation demonstration served as an excellent "breadboard" in that it offered a stage where several concepts turned out quite well (i.e., top-down, structured software design, use of 8080 microcomputer utilizing the PL/M language, etc.), while others turned out quite poorly (i.e., BASIC was a poor language for this demonstration, polling did not work satisfactory, the PDP-11's were unreliable, etc.).

VII. Recommendations

Automation should be implemented when:

(1) The automation controllers to be implemented are reliable enough so that the added burden imposed on the station is more than offset by improved performance and station availability.

(2) The system is flexible enough to permit the operators to handle all nonstandard events that are presently accomplished.

Other general recommendations are:

(3) Polling should not be used; instead the system should be interrupt driven.

(4) Future interface hardware design should contain built-in fault isolation aids to facilitate system repair.

(5) Failure analysis and automatic functional backup should save valuable mission data while the subassembly diagnostic should minimize down-time and so should be actively pursued.

(6) RT-11 BASIC is too slow for a real-time control system. This observation coupled with the poor reliability of the PDP-11 hardware and software indicate the PDP-11 should not be used again as the controller.

(7) The PL/M language used by the 8080 appears efficient in time and memory and should be used in another demonstration.

(8) Adequate memory should be planned for.

(9) In the foreseeable near future it seems wise to concentrate on providing the operators with improved tools (i.e., useful macro commands, RCV 3:Δf = -100 kHz, DOP = 200 Hz) without trying to solve costly operational problems that occur infrequently (i.e., it would be possible to conduct an automatic organized search of carrier, subcarrier, symbol rate in the event of major trauma to the spacecraft; however, our current state of development does not as yet offer this capability as a cost-effective option).

(10) Software standards should be created using top-down, structured design with a high-level language so that eventually one software sustaining engineer could maintain the RF subsystem software.

VIII. Future Plans

A second RF automation demonstration is presently planned for April 1976. This demonstration will follow the basic plan established for the first demonstration but will emphasize system reliability, operator flexibility, and improvement of the automation data base. A preliminary study will be undertaken to determine the current stage of hardware automation in each major subassembly and will present management options for future automation.

Table 1. RF demonstration program size/development time

Controller name	Total number of BASIC or PL/M statements	Core requirement in 1000 16-bit words	Software development time, man days			Computer type/language
			Design	Code	Debug	
Demonstration configuration	1250	14	40	15	25	PDP-11 BASIC
RF demonstration	1050	10	35	20	60	PDP-11 BASIC
Receiver–exciter	1000	10	20	10	25	PDP-11 BASIC
Transmitter	700	10	50	15	50	PDP-11 BASIC
SDA	650	9 (8-bit words)	30	15	10	8080 PL/M
Microwave	200	4	10	2	5	PDP-11 BASIC

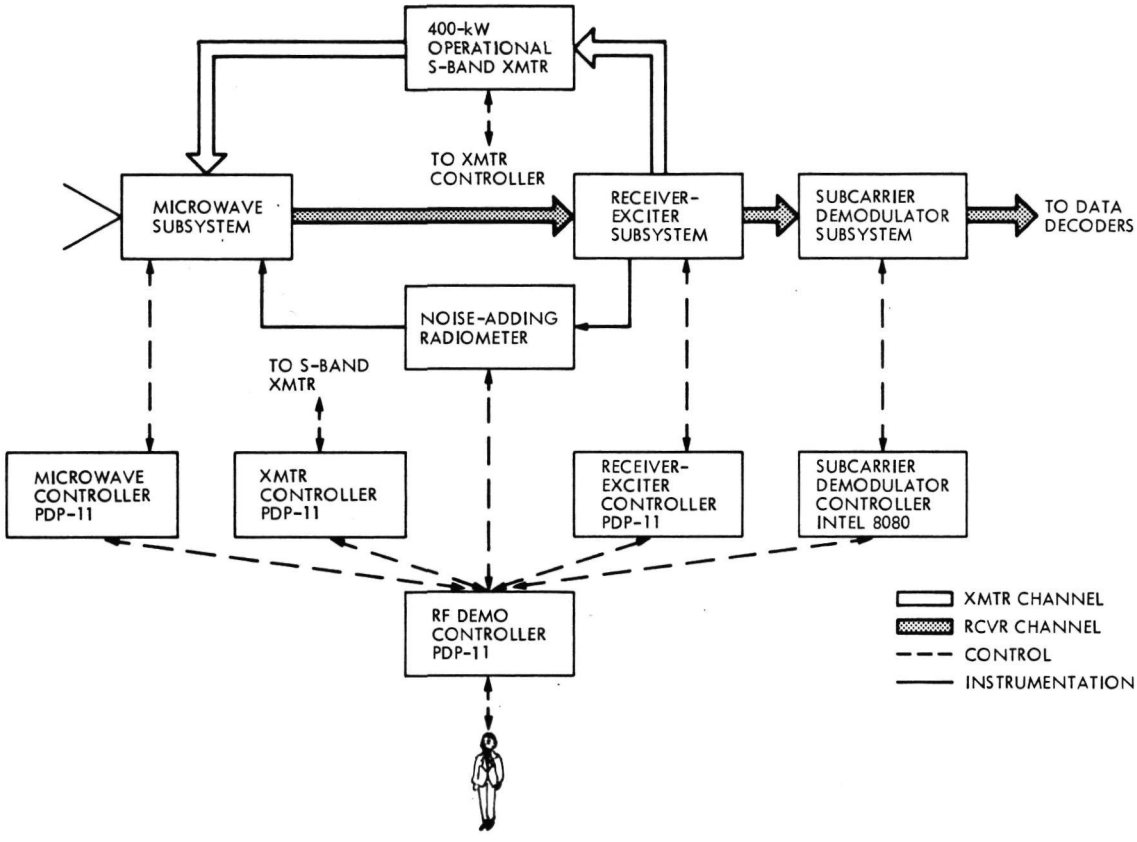

Fig. 1. RF automation demonstration functional block diagram

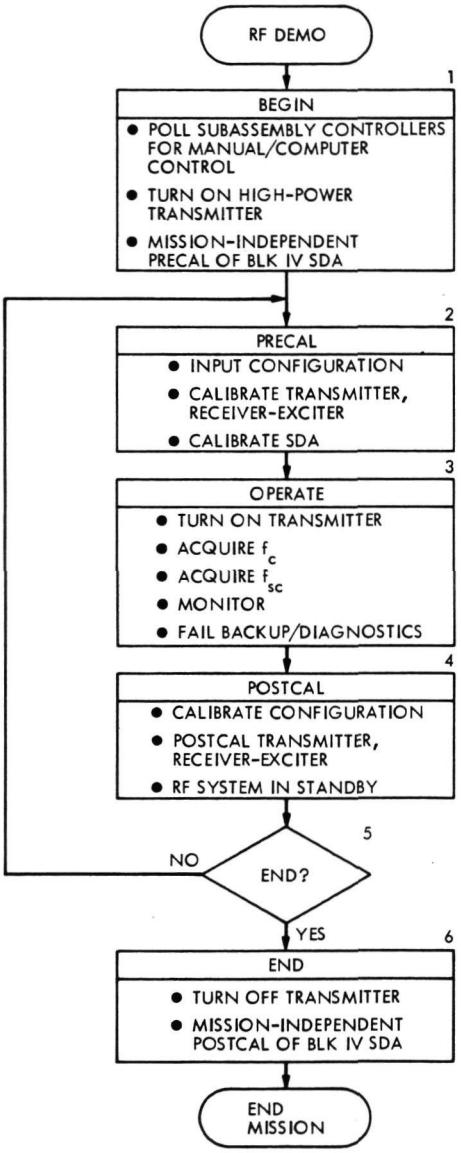

Fig. 2. Flow diagram of RF demonstration control program

Transmitter Automation

R. M. Gosline
R. F. Systems Development Section

As part of the radio frequency automation demonstration, the transmitter subsystem at DSS 14 was automated to perform a simulated spacecraft mission with pre-mission and post-mission calibrations. Schedule and budgetary restrictions required the use of existing hardware wherever possible. A PDP-11 minicomputer was available and used for the subsystem controller.

I. Introduction

As part of the radio frequency (RF) automation demonstration, the transmitter subsystem at DSS 14 was automated to perform a simulated spacecraft mission with pre-mission and post-mission calibrations. Schedule and budgetary restrictions required the use of existing hardware wherever possible. A PDP-11 minicomputer was available and used for the subsystem controller.

II. Hardware Description

Three junction boxes were installed in the pedestal research and development (R&D) control room near the R&D remote control console (RCC). All monitor and control lines were switched with three rotary switches, enabling the station to return easily to the normal configuration. Logic level converters were used to interface the 28-volt transmitter control logic to the standard 5-volt transistor–transistor logic (TTL) used by the PDP-11. The PDP-11 monitored 64 input lines, 10 analog channels, and provided 19 command lines. The 14-line interface was converted to a serial bit pattern requiring only two twisted pairs for the 370-meter (1200-foot) communication cable to the demonstration controllers located in the DSS 14 control room. A converter at the other end converted back to standard 14 lines. The PDP-11 was equipped with an analog-to-digital converter and a 16-channel multiplexer. The memory size was 16,384 although only 6,000 was available for the control program. A Dectape dual magnetic tape drive was also available.

III. Software Description

The major part of the project involved software development. Top-down structured programming principles were followed, and most of the programming was done in DEC RT-11 BASIC. Even the standard 14-line interface algorithm was implemented in BASIC as a last resort when assembly language routines failed to link string variables properly. Although reliable, only 5 ASCII characters were transferred per second between comput-

ers. The program was designed to decode and act on six commands from the demonstration controller as follows (Fig. 1).

INT: The initialize command caused the subsystem to indicate status (manual mode or computer control) to the demonstration controller. If in computer mode, the control power supply, the coolant system, and the filaments were turned on, starting the five-minute filament time delay.

CFG: A configuration command indicated that power and frequency data were following. The received values were checked for proper range and converted for internal use.

CAL: A calibration command would be rejected if INT and CFG were not complete. If accepted and in the waterload position, the crowbar logic was tested, perveance data obtained, and klystron saturated by manipulation of the beam voltage and drive power. Verification of the power meter calibration at the mission power level was checked. Finally, the beam was turned off and the standby state entered.

STB: The standby state could be commanded at any time provided CAL had been completed.

PWR: The power command caused the beam voltage to be turned on to the value specified in CFG provided CAL had been completed. The value of output power was reported to the demonstration controller.

OFF: An off command was only accepted if not in PWR state. An orderly shutdown was performed, allowing time to cool the klystron before shutting off the coolant system. Finally, the computer executes a stop command requiring manual intervention to restart.

All command messages were echoed to the demonstration controller, if possible, otherwise placed on the message output queue to try later. When not performing commands or handling messages, the program entered a monitor loop in which the subsystem parameters were compared to those expected. Anomalies were acted upon, if possible, and reported to the demonstration controller in any case. All analog channels could be corrected for slight drifts without mission interruption. Transmitter interlocks would be reset three times before issuing a diagnostic message requesting manual assistance.

IV. Performance

Many difficulties were encountered with the PDP-11, even though the computer had been reconditioned at the vendor facility. Many RT-11 operating system problems were also discovered for which the vendor could not find solutions.

The second major problem was communication speed due to the software 14-line interface and a polling system instead of interrupts. Long messages could tie up the demonstration controller for minutes while others were polling to see if the controller was ready to listen.

In spite of these difficulties, an automated system was demonstrated, although the klystron saturation algorithm was not completely verified in the demonstration.

V. Conclusions

It should be pointed out that although the automation demonstration provided much data and experience at the system level, few improvements were made within the transmitter subsystem. Instead, the operator was automated at the control panel. There are undoubtedly greater benefits to be obtained by designing certain devices and techniques into the equipment first; then integration into a system demonstration becomes a relatively easy task.

The top-down structured programming technique is a useful method but the rules must be followed rigorously even under schedule pressure to obtain the maximum benefits.

An interrupt system, rather than the polling technique, would greatly improve program execution.

The BASIC language, because of its resident compiler, does not seem to make efficient use of core or machine time. Also, bit manipulations and special device input/output operations are difficult. An assembly language program would seem to offer more advantages as well as preserve the on-line near-real-time correction capability.

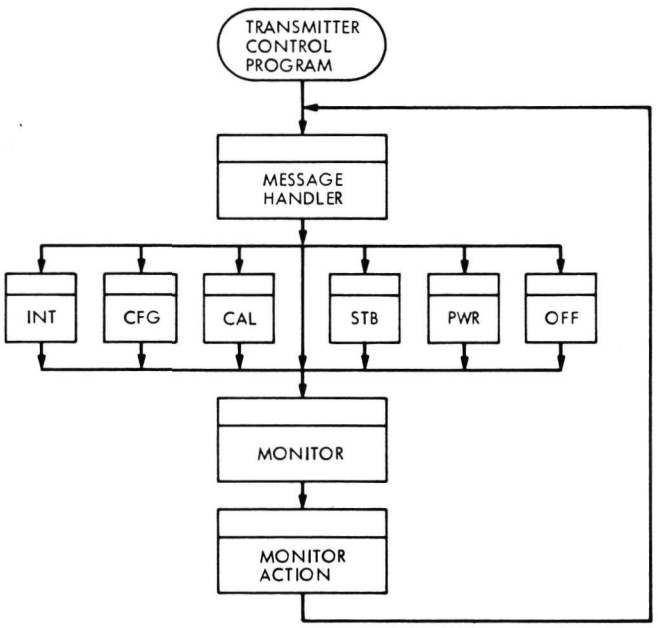

Fig. 1. Transmitter control program top-level flow chart

Automatic Microwave Configuration Control

J. G. Leflang
R. F. Systems Development Section

Several radio frequency subsystems were recently operated at DSS 14 using minicomputers for data input, calibration, control, monitoring, and failure backup and diagnosis. As part of that test, the microwave configuration control portion of the antenna microwave subsystem was interfaced with a PDP-11/20 computer.

I. Introduction

Recently, practical computer control and monitoring of several radio frequency (RF) subsystems was demonstrated at DSS 14. A portion of the antenna microwave subsystem, the configuration control group, was included in the demonstration. The equipment in the configuration control group provides a means of controlling and reading 120 switch positions. Approximately 80 switch positions are presently used.

II. Hardware Design

Switch control is manually accomplished by actuating a push-button that completes a dc return path for one coil of a set of relays which control the 110-volt ac power applied to the microwave switch motors. The computer interface utilizes an open collector peripheral driver connected to the dc return path for each relay in a wire-OR configuration (Ref. 1). Thus, either manual push-buttons or the peripheral drivers may be used to actuate relays (and thereby switches) in the configuration control hardware.

Switch position indication is accomplished by using a 24-volt dc signal to illuminate the manual push-buttons which correspond to the switch position. The original technique for controlling and monitoring switch positions used opto-isolators for noise rejection and for shifting to transistor–transistor logic (TTL) levels (Ref. 1). Field tests using the original design equipment proved that the opto-isolators were unnecessary, and the equipment used for the RF demonstration used lower cost resistive voltage dividers for shifting from 24 volts dc to TTL levels, and did not use opto-isolators in the peripheral driver circuits.

The computer interface assembly is composed of a DSN standard interface, a function decoder, and five 24-bit shift registers. The shift registers provide 120 parallel outputs which drive all five switch groups (bays) within the

configuration control hardware. The function decoder reads three bits of each input byte to determine the required function.

Of the eight possible function codes, five are used. The functions are:

(1) Output six data bytes which contain information on power supply status and the state of a computer input enable/disable flip-flop.

(2) Output 24 data bytes which contain information on the output state of all shift registers.

(3) Enable relay driver outputs.

(4) Disable relay driver outputs.

(5) Output 24 data bytes which contain information on all switch position indicators.

The use of a three-bit function code of value zero causes the shift registers to accept configuration data.

III. Software Design

The configuration control software was designed as two modules that are part of a nonreal-time sequence of processes which combine the receiver and microwave software in one computer. Coding was done in Digital Equipment Corporation's RT-11 BASIC.

Configuration commands are received as strings of two-digit numbers. Each number represents a macro configuration which is a useful functional portion of some configuration required for operations. One of the two software modules, the input message processor, segments the command string and validates each command. Valid commands are stored in a prime command stack if not specifically identified as a failure backup command by the prefix "FB." After the command string is stored, the stack is scanned one command at a time, and the corresponding macro is overlayed into an array which is then shifted in 24 bytes into the hardware registers. The registers are tested by reading back into the computer and comparing them to the macros specified in the prime command string. If the registers are properly loaded, an enable command is given to drive the switch control relays. This process is repeated for all storage cells in the command stack. Any register error is reported as a macro failure.

The second module provides a periodic monitor of switch positions specified by the command string. Switches not specified are not monitored. This module reports any discrepancies, loads the failure backup command, if any, into the prime command stack, reloads and tests the shift registers, enables the relay drivers, tests the switch position indicators for correct position, and reports the backup action to the monitor console.

IV. Results

The configuration control hardware operated reliably and precisely as intended. All circuits appeared to have noise margins which are adequate for operation in the station environment. In spite of the 305-meter (1000-foot) cable runs, opto-isolators were not required, but it should be pointed out that noise, not ground loops, is the only concern because the relay coils and contacts used for indicators are not grounded to the antenna.

Similarly, the software functioned well. However, core size restrictions prevented the use of extensive diagnostic routines. Also, the macro configuration tables were originally stored in magnetic tape virtual memory because of the shortage of memory. However, the long access time associated with reading a file from the tape prompted a software modification which stored the macro tables in memory. Prior to the modification, it was possible to consume many minutes performing diagnostics and failure backups.

At first, manual override of a computer-generated configuration required that the switch in question be moved twice because the computer would attempt to restore the original configuration once after any manual change. This proved to be very annoying, and the software was changed to permit human operators to move switches at any time. However, any manual operation which alters a computer-specified configuration still is detected by the computer and is identified on the display console.

V. Conclusions

Automatic configuration control of the microwave subsystem is feasible. We have developed a simple, compact, and reliable hardware design that interfaces the configuration control group with any computer which has a DSN interface and can support the necessary software. The use of software instead of hardware is very desirable for the purposes of establishing and testing functional combinations of switch positions (modes). The resulting hardware is low cost, and the software provides the flexibility necessary to adjust to changing mission requirements without large monetary expenditures.

The software functioned fairly well, but it did prove to be unreasonably slow and to require a large amount of

memory to store the system executive and the basic interpreter (21.2 kbytes).

Because of low speed and large memory requirements, BASIC is not attractive as a programming language for use in the microwave subsystem. There are other languages which offer speed and compactness, and the use of one of these will permit a hardware/software package which will prove to be of substantial value to operations and will not carry a prohibitive price tag.

Reference

1. Leflang, J. G., "Automation of Microwave Configuration Control," in *The Deep Space Network Progress Report 42-21*, pp. 59–64, Jet Propulsion Laboratory, Pasadena, Calif., June 15, 1974.

Three-Dimensional Plotting on a Two-Dimensional Surface

S. K. Skedzeleski
Communications Systems Research Section

Data collected over a two-dimensional surface are often test-displayed as a surface whose height above the plane represents the function's value at the corresponding coordinates. One algorithm for producing such a plane is described, using horizontal lines to define the surface. It has been implemented as a FORTRAN subroutine on the SDS 930 computer.

I. Introduction

It is often desirable to display data which are a function of two variables as a surface whose height above the coordinate plane represents the function's value at the corresponding coordinates. A very simple algorithm has been used for several years to display the results of radar mapping, but it has been done ad hoc and built directly into each program as it was needed. A FORTRAN subroutine which is very brief, both in time and space, has been written to do this plotting on the SDS 930 computer.

The subroutine, DDD, takes data one line at a time (in the constant Y direction) and outputs line segments to the plotting routines that are available on this system. One initialization call is needed to set the boundaries of the plot, and such information is passed in blank COMMON. It would be better to logically separate it in a labeled COMMON block, but RTFTRAN on the 930 computer does not have that capability.

II. The Algorithm

For reading clarity, the following notation is used:

$f_{x,y}$	the function value at (x,y)
$z_{x,y}$	$y + f_{x,y}$
NX	number of points in the x direction
Δx	spacing between sample points in the X direction
Δy	spacing between sample points in the Y direction

The algorithm used in DDD is very simple. For each point (x,y) a line segment is drawn from $(x - \Delta x, z_{x-\Delta x,y})$ to $(x,z_{x,y})$. The first point of each line is handled differently from the rest of the points since the pen is merely positioned there. This algorithm does not conceal hidden

lines. A first-order improvement is easy to implement by keeping track of the maximum value of $z_{x',y'}$ for each $x' = x_{min}, x_{min} + \Delta x, \cdots, x_{max}$, over $y' = y_{min}, y_{min} + \Delta y, \cdots, y_{current}$ (initially zero). This is done in the array ZMAX (length NX). If the current point is hidden (i.e., $z_{x,y} < ZMAX_x$), then do not draw the line segment, but move the pen to $(x,z_{x,y})$ with the pen up. This produces acceptable plots when the grid size is not "too large."

An improvement that is used in DDD is to try to determine at what point a line disappears and to draw the visible portion of the line segment $(x - \Delta x, z_{x-\Delta x,y})$, $(x,z_{x,y})$. This is implemented by keeping an extra array of length NX, called ZMAXPREDECESSOR. ZMAXPREDECESSOR gives the position of the other end of the line segment drawn to ZMAX, for each x position. (This is not totally true. If the line segment just drawn is a partial line segment—because the previous point was a hidden point—the value is still $z_{x-\Delta x,y}$, not the point at which this line segment became visible). One more value, $ZLAST$ $(= z_{x-\Delta x,y})$, is needed to calculate the point at which lines became visible and hidden. There are two cases which must be considered: a line disappearing and a line reappearing.

In Case I, the current point is hidden, but the last point was visible (line disappearing). In the drawing below, the line segment (z_2,z_3) was drawn previously; z_1 was the last point, and z_4 is the current point. We wish

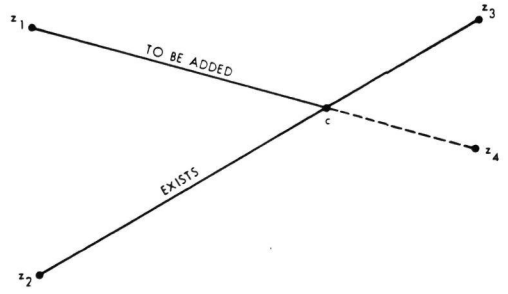

to add the line segment (z_1,c) and then move the pen to z_4 with the pen up. Setting $z_1 = ZMAX(x - \Delta x)$, $z_2 = ZMAXPREDECESSOR_x$, $z_3 = ZMAX_x$ and $z_4 = z_{x,y}$, we see that we must have $z_1 + \alpha(z_4 - z_1) = z_2 + \alpha(z_3 - z_2)$, where α is the fraction of Δx from $x - \Delta x$ to Δx where the line segments cross. Solving for α we get $\alpha = z_1 - z_2 / z_1 - z_2 + z_3 - z_4$, which gives the crossing point $c = (x - \Delta x + \alpha \cdot x, z_2 + \alpha(z_3 - z_2))$.

In Case II, the current point is visible, but the last point was hidden (line reappearing). In the drawing below, the line segment (z_1, z_4) was drawn previously; z_2 was the last point, and z_4 is the current point. We wish

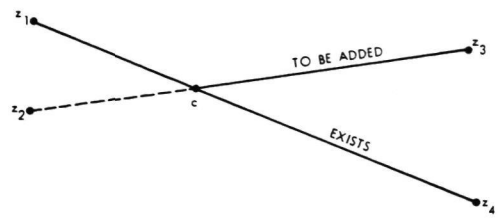

to move the pen (still up) to point c, then move to the point z_3 with the pen down. Setting $z_1 = ZMAX_{x-\Delta x}$, $z_2 = ZLAST$, $z_3 = z_{x,y}$ and $z_4 = ZMAX_x$, we can substitute into the formula in Case I and determine point c.

A. Caveat

It should be noted that this method of removing hidden lines is not foolproof. There are situations in which it will cause a line segment to extend past another already drawn. Specifically, if between $x - \Delta x$ and x the line segment which ends at $(x, ZMAX_x)$ is not above all other line segments in that interval, an error can occur (see following sketch). The line segment drawn should be hidden,

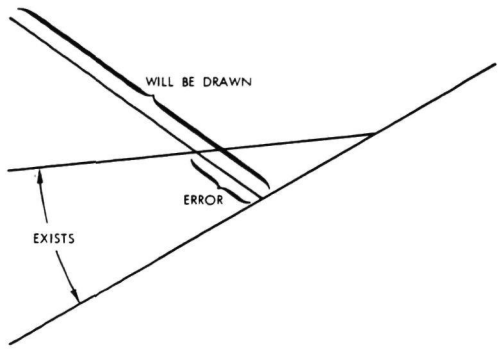

yet DDD will draw it. In practice, this situation does not seem to occur often enough or with enough visual impact to justify doing a better job than is now done. However, it was found that by simplifying this procedure further by not keeping track of ZMAXPREDECESSOR and using ZLAST instead, obnoxiously visible crossings were occurring on almost all transitions from visible to hidden points. Hence the current degree of detail.

B. Sideviewing

The algorithm described so far is for a view of the surface which is directly in front of and slightly above the surface. The angle of view depends on rate of change of Y with vertical height and hence is essentially programmable. With certain kinds of data it is necessary to view the surface from a slight angle instead of head-on. One method of doing this is to offset each line in constant Y by one or more Δx positions. It is then possible to "peek around" tall parts of the surface. It is easy to modify the algorithm described so far to allow this. It suffices to keep ZMAX indexed on the position of the plotter, rather than having it coincident with a given x position. The points are then plotted at $x + x_{offset}$, and x_{offset} is incremented as each line is finished.

C. Edge Lines

If only horizontal lines are drawn, as in DDD, the line segments will be dangling on each end. It is particularly annoying on the near edge when side viewing is used, since this is where the eye expects to see the effects of "slicing" this portion of the surface from the entire surface. By adding a line segment from the last point of the current line to the last point of the previous line, the edges are effectively tied down. The edge on the far side is more difficult to connect since there are noticeable (bad) effects from connecting hidden points.

III. User's Guide

To draw a surface containing *NX* by *NY* points, *NY* + 1 calls are made to DDD. The first call initializes variables used by DDD, and the remaining calls actually draw the surface. Before the first call is made, the following variables in COMMON must be given values.

COMMON XLIM,YLIM,NX,XSCALE, IYDELT,IROUTE,IERR

XLIM,YLIM the boundaries of the plotting area (in inches for the plotter)

NX the number of points across a line

XSCALE scaling factor applied to $f_{x,y}$. It is used to adjust the height of each value above the baseline

IYDELT the number of Δx positions to shift each line, for side viewing

IROUTE must be set to 1

Calling Sequence:

Call DDD (*ARRAY,NY*) *ARRAY* is the array of *NY* data points to be plotted.

The first call to DDD returns the following values:

IROUTE

is set to 2

IERR

returns to 0 if the arrays in DDD are large enough to handle this plot, 1 otherwise. Currently there can be 512 Δx positions across the entire page (not across just one line of the plot).

Each succeeding call to DDD draws one line across the plot.

To restart DDD, set *IROUTE* to 1, and reset any variables that need to be changed. DDD does not automatically advance to a new sheet of paper or do any "nonstandard" centering of the plot on the page.

Rapid Access Disks Utility Programs for the SDS 930 Computer

S. K. Skedzeleski
Communications Systems Research Section

This article describes three utility programs for the SDS 930 computer with rapid access disks (RADs). Two of these programs transfer data between magnetic tape and an RAD, and the third is a diagnostic program. All programs operate in a multitasking environment using MULTI, a small 930 operating system.

I. Introduction

A pair of programs has been written for the SDS 930 computer to supplement the data transfer program MEDIA. It allows rapid access disks (RADs) to magnetic tape to RAD transfers of data. Using these programs, one can selectively save the contents of an RAD in a sector-by-sector tape dump. All or part of the RAD or tape file can be transferred.

A simple RAD diagnostic was also written. It uses the 930 multiprogramming task master MULTI (Ref. 1) to perform a read-write-verify test on selected portions of the RAD. It was written to provide our section with an easy to understand diagnostic that can be easily changed as conditions necessitate, and also as a checkout for the 930 version of MULTI. The program is designed to run for long periods of time, and will provide an error summary as output.

II. User's Guide for RAD Diagnostic

There are two parameters necessary to run this program: the range of RAD addresses to test, and the test pattern to use. The addresses are selected by using the RAD's file protection switches. Only those sectors which are not protected will be tested. The pattern to be used is entered on the display and entry panel (DEP) thumbwheel switches (Ref. 2). It is copied into a 64-word buffer, which is written onto the RAD sectors. Another buffer is filled with the ones complement of the buffer just written, and the sector is read back in. The two buffers are then compared word by word, and errors are tabulated by the band number, sector within a band, and word within a sector. To obtain a listing of all errors without stopping the program, the console interrupt button is pressed. A listing of the errors is written on the line printer while the diagnostic continues.

III. User's Guide to RADTAPE

RADTAPE transfers contiguous sectors from a 930 RAD to magnetic tape. The RAD sectors are dumped in separate records containing sixty-five 24-bit words (the extra word contains the RAD address). The program uses the third version of the multiprogramming task master MULTI to overlap input and output functions.

Multiple buffering allows tasking to overlap tape and input/output (I/O) operations. When no other tasks are active, a task is run which allows core locations to be displayed on the DEP device attached to the 930. Sense lights on this panel are also used, with one of ten lights being lit whenever a given task or interrupt routine is being executed. This turned out to be very valuable while debugging the program.

The program begins by typing the prompt

> ENTER TAPE UNIT AND NUMBER OF FILES TO SKIP

The user types the logical tape unit selected, and a decimal number of files to skip (zero is acceptable; negative numbers are not acceptable). If the tape is write-protected, new numbers must be entered and the prompt will be repeated. After these values are read, the prompt

> ENTER RANGE OF ADDRESSES TO DUMP (IN OCTAL)

appears. The user gives a range of octal RAD sector addresses to dump. Two addresses must be entered, and the first address must be less than or equal to the second address. If not, the prompt is repeated and another pair of addresses must be entered.

When typing in the addresses, the backspace character will delete the previous digit of the current number being typed. To delete the entire line, the delete character (←) is typed. This causes a carriage return and a line feed to be echoed. The following characters serve as separaters of numbers:

> blank
> comma
> dash
> carriage return

More than one number can be entered on a line. For example, the following lines are equivalent:

> 0,5
>
> 0-5
>
> 0 5

RADTAPE writes a double end of file after each block of contiguous sectors is written, but back spaces over the second end of file (EOF) after it is written. After this is done, the prompt

> ENTER RANGE OF ADDRESSES TO DUMP (IN OCTAL)

is repeated, and another set of RAD sectors can be dumped. By repositioning the tape in front of the second EOF, single EOF marks will separate blocks of sectors, while the last block is followed by a double EOF. The program is stopped by changing the RUN-IDLE-STEP switch to IDLE, and booting in the system from the RAD.

In case of an error detected by the tape controller while writing, the program attempts to rewrite the record three times before erasing that section of the tape and trying again farther down the tape. Instead of backspacing over the record in error, the program skips backward to the previous EOF mark (or bottom of text (BOT) mark) and skips forward over the records previously written. This avoids a problem that can occur when the tape drives are not perfectly tuned. They might then erronously move back into the previous record while backspacing or erasing reverse, destroying part of the previous record.

Errors detected by the RAD controller or Y channel cause the message

> **RAD ERROR**

to be typed, and the program halts.

IV. User's Guide to TAPERAD

TAPERAD transfers sectors previously stored on magnetic tape by the program RADTAPE to the RAD, using the multiprogramming taskmaster MULTI (Ref. 1). The files stored on tape are blocks with contiguous RAD sector addresses, each record containing 65 words. Multiple buffers allow the use of tasks to overlap the input and output operations. As in RADTAPE, a background task is run which continuously displays a location in memory, and the sense lights are used to indicate active tasks.

The program begins by typing the prompt

> ENTER TAPE UNIT

The user types the logical tape unit selected, and the program continues by typing

ENTER NUMBER OF FILES TO SKIP, NUMBER TO PROCESS

A decimal number is entered for each item, and the number to process must be nonzero. If not, the prompt is repeated, and both numbers must be reentered. The second number is used when the user wants to dump several blocks which are on adjacent files:

ENTER RANGE OF ADDRESSES TO DUMP (IN OCTAL)

The user gives the acceptable upper and lower bounds for sector addresses to be transferred. Entering 0–17777 will dump all records in the number of files specified. If the first address is greater than the second address, the prompt is repeated and the numbers must be reentered.

The program now begins skipping any files requested and then transferring any records in the range given above. Three errors can occur:

RAD IS FILE PROTECTED. TOGGLE BPT 4 TO RETRY

The program then loops until the position of BPT 4 is changed, and will try to write the sector again:

RAD ERROR

This is typed when a Y channel error occurs, or the coupler signals an error. The program halts.

ENTER 0 TO RETRY, 1 TO USE IT, 2 TO SKIP IT

This is typed when a tape error is signalled. TAPERAD tries to read each record at most five times; then it prints the above message and waits for the operator to type a response. 0 causes five more tries, 1 accepts the record as last read, and 2 causes the record to be ignored.

The programs RADTAPE and TAPERAD can be used in lieu of SYSGEN, by saving the system, its libraries, and the disk directory. This would be done by writing two files: one from 0 to the last address used by the libraries, and another block to get the directory at the other end of the RAD. To restore the system, the user would process two files, giving the range 0–17777 of addresses to dump.

When finished processing the given number of files, the program is ready to continue, and again asks for the number of files to skip to and process. The program is terminated by moving the RUN-IDLE-STEP to IDLE, and booting in the system from the RAD.

References

1. Erickson, D. E., and Layland, J. W., "An Experiment in Remote Monitoring of Mu-Ranging Operation at Mariner Mars 1971 Superior Conjunction," in *The Deep Space Network Progress Report*, Technical Report 32-1526, Vol. XV, pp. 156–166, Jet Propulsion Laboratory, Pasadena, Calif., June 15, 1973.
2. Brokl, S. S., "Computer Display and Entry Panel," in *The Deep Space Network Progress Report*, Technical Report 32-1526, Vol. IX, pp. 44–48, Jet Propulsion Laboratory, Pasadena, Calif., June 15, 1972.

Doppler Spectrum Extraction of Planetary Radar Data Using Computer FFT and Integration

D. E. Wallis
Communications Systems Research Section

A computer program to extract integrated doppler spectra of planetary radar returns is described. The program input data are discrete, complex-valued time series obtained for each of 64 range gates. The data record is subdivided into successive subseries of 256 time-points, and each 256-point time series is discrete-Fourier-transformed using the fast Fourier transform (FFT). Power spectra are obtained by magnitude-squaring. The power spectra, containing positive- and negative-frequency doppler components, are assumed statistically stationary during receive-runs of 10 to 15 minutes duration, and so may be (SNR)-enhanced by integration (summation) of successive 256-point power spectra. Program output is a highly compressed power spectrum tape containing 64 integrated spectra, together with identification and parameter values, for all receive runs made during each day of a total of six days of radar observations of the planet Mercury in calendar year 1974. Brief discussions of the on-site data-taking process and the doppler interpretation of the discrete Fourier transform are included.

I. Introduction

This report describes a computer program to extract integrated doppler power spectra of planetary radar returns. The description of the on-site data-taking process and data-reduction requirements in Sect. II is used to introduce the detailed descriptions of data-tape formats in Sect. III and the computational flowchart in Sect. IV. To anticipate and answer some questions of users of the program, a brief discussion of the doppler interpretation of the Discrete Fourier Transform (DFT) is included in Sect. V.

II. Background: The On-Site Data-Taking Process

In the radar observations of the planet Mercury in summer 1974, digital complex-valued (quadrature-pair) amplitude samples of approximately 15-bit maximum resolution are obtained from the radar receiver-detector

system. The detector system has 64 range gates, 32 of which are assigned to Coder 1, with the remainder assigned to Coder 2. The operations of Coder 1 and Coder 2 are interleaved, so that Coder 1 produces data for even ranges 0,2,4,$\cdots$,62 and Coder 2 produces data for odd ranges 1,3,5,$\cdots$,63, where 0,1,2,3,$\cdots$,62,63 is the ordering of range itself. At each range assignment, the coders output their complex-valued amplitude samples to the on-site XDS 930 computer, which merges the 128 numbers from the coders with serial-number, time-of-day, and various experimental parameters to form a 192-word record to be written on standard 7-track tape at 800 bits/inch. Each 192-word record, then, contains 64 complex-valued amplitude samples, the set of which may be regarded, for purposes of power-spectrum computation, as representing a vector-valued sample at a single point in time. Two tape drives are operational for the on-site data recording process, so that one drive unit is available on line to the computer while the other unit is being rewound and reloaded. In a given day's observations, 18 to 19 reels of tape are written, and the succession of 192-word records is continuous from each tape reel to the next, except that a 4K-word core dump is always the first record written at the beginning of each reel used. The condition for continuing the data recording onto the available alternate tape drive is, effectively: If not end-of-tape, write to present unit; if end-of-tape, switch units, write a core-dump record, and resume data recording without loss of continuity. Because of variable distances to the planet under observation, the number of records written during each receive-run (duration of approximately one round-trip-light-time) varies. To maximize utilization of recording tape, the recording process is suspended in mid-tape at the end of a receive run, so that recording may resume without loss of footage as data from the next receive run become ready to record. Each 192-word, time-point record contains a serial number which serves, along with a notation of time-of-day for each record, to ensure that data for truly successive points in time can be identified in the subsequent data reduction. The boxes of tapes for a given day's observations are accompanied by a computer typeout of the serial numbers marking the ends of the successive receive-runs, together with other station log information not used in the present program.

A. Requirements for the Data Reduction Program

The computer program to be described in the following must, of course, contain program logic to read data tapes organized as described above. Additionally, the program must anticipate and guard against possible errors in the on-site data-taking process which, due to heavy real-time computational demands, cannot be corrected on-line without incurring other unacceptable losses. A further requirement on the present program is to produce intercomputer compatible output, so that the power spectrum tapes to be produced are suitable for dissemination to users demanding high confidence in data validity and processing integrity.

Embedded within the above requirements, are the more purely mathematical operations of the discrete Fourier transform, spectrum computation, and spectrum integration. The Fourier transform is accomplished by the now traditional FFT technique, and program requirements reduce to ensuring that computations are correctly scaled, free from overflows, that spectral extraction is correct, and that output formats are as specified.

III. Input and Output Tape and Record Formats

Input to the computer program comprises time tapes generated at the station, plus certain entries obtained from the radar log, which are typed into the computer at processing time by the computer operator. Output from the computer program is an intercomputer compatible spectrum tape, incidentally accompanied by a computer typeout of important processing milestones, plus a record of occurrences of computational overflow. The input and output tapes are 7-track, 800 bits/in. and their formats are given in Tables 1–4. Explanatory remarks are included with the figures. Section II (q.v.) may be consulted in connection with the time tape formats. The content of the spectrum tape header records is for the most part copied from certain portions of the time tape data records, but the content of the spectrum tape power spectrum records is derived by Discrete Fourier Transform (DFT) and magnitude-squaring from the time-tape time series.

IV. Description of Program Flowchart

At the start of the program (Fig. 1), the table of values of the complex exponentials required by the DFT/FFT is computed. (See Sect. V for a discussion of the exponential table). Also computed at the start of program is a table of indirect address keys designed to manipulate any 256-point time series of normal sequential ordering into the so-called "shuffled" or "sorted" order required by the particular canonical form of FFT used.

The program asks for input of date parameters required to be included in the spectrum tape output from the program. Also, in advance of each receive run to be processed, the program asks for the record serial number delimiting the last record of the run. The program tests for end-of-tape prior to reading each data record and calls for the next tape in sequence to be mounted. The core dump record, which is the first record written on each new reel of tape, is always skipped. Since the integration of power spectra is always over all spectra computed in the course of a given receive run, the integration accumulator is cleared to zero prior to processing data for the run.

The program's logic effectively makes the reading of successive records continuous in spite of the reel-to-reel transition, and does not "lose" any records either reel-to-reel or run-to-run. Processing of a given receive run terminates when a record of greater serial number than that for end-of-run is encountered. This record is retained and used as the first record of the next receive run. The requirement that only continuous, successive time-records be FFT'ed is enforced by checking the incrementation of record serial numbers and also checking the incrementation of the recorded time-of-day words on the successive records.

Data from the time tapes are read in 256-record blocks in order to gather the time series to be transformed. Somewhat unfortunately, however, 256-point complex-valued time series are obtained for all 64 range gates at once. Since a total of 32,768 data words are obtained, it was found necessary to use drum storage (RAD) to hold the full data set. The program, therefore, organizes the reading of a 256-record block as eight (8) 32-record blocks, and exploits the fact that each 32-record block (4096 words) conveniently fills one band of the drum, thereby tending to minimize drum loading time. The 4096-word record written to the drum band is derived by reading 32 records from tape to core memory in such a way that the 32 successive complex numbers for each range gate versus time are grouped contiguously.

The data for each range gate are made available to the FFT computations by reading selectively from the 8 drum bands containing the total 256-record block and loading these data to a scratch pad area of core memory. The time-sequential order of the data is altered to the "shuffled" order used by the transform. A conventional complex FFT is done for each range-gate's data, with monitoring of any computational overflows which may occur anywhere in the processing of the 32,768-word block. Since the first receive run of a given day's records is actually a delay calibration of the transmitter-receiver system, rather than a planetary return, the somewhat larger measurement values of the delay calibration are handled by right shifting all data 2 bits, with subsequent left shift correction in the computed results. The 256-point (512-word) complex-valued transform computed by the FFT for each range gate is magnitude-squared to produce a 256-word single-precision power spectrum for the gate. The power spectrum is accumulated in a double-precision accumulator assigned to each gate number.

When all full 256-record blocks of the receive run have been processed (with any remaining number of records less than 256 being ignored), the integrated spectrum for each gate is normalized by left-shifting until the largest spectral element is scaled to maximum positive magnitude. The number of shifts required for the maximum element is then applied to all elements of the spectrum, thereby yielding a normalized spectrum for the gate. The number of shifts required to normalize each spectrum is incorporated into a computed scale factor, whereby the normalized spectrum can later be un-normalized, if desired, by the user.

When processing of data for each receive run is finished, the 65 records for the computed run are written on the output spectrum tape. The successive 65-record blocks comprise the output for each day's records. In the Mercury data processed, data for six days records appear on the spectrum tape.

V. Doppler Interpretation of the Discrete Fourier Transform

The following necessarily brief discussion is intended to address various user questions which have arisen in connection with the content and mathematical interpretation of doppler spectra generated by the present computer program.

Suppose that a discrete time series of N complex-valued detector-output amplitude samples $\{Z_i\}$, $0 \leq i \leq N-1$, has been obtained at a uniform sampling rate. Suppose further that the discrete samples are actually samples of a continuous waveform representable as a sum of harmonics in the usual sense of Fourier analysis, in which the frequencies of the assumed harmonics are expressible as integer multiples of a lowest- or fundamental-frequency sinusoid. With N discrete samples available, it is known that N harmonics are sufficient to fit the time series exactly. The N assumed harmonics comprise a dc (constant)

waveform, plus $N-1$ sinusoids whose frequencies are integer multiples of a sinusoid having one period of oscillation in the time required to gather the N samples. In planetary radar, the amplitudes of all the harmonics are of interest, and these are computed by the Discrete Fourier Transform (DFT). The DFT is a computation which may be indicated by (but is not usually computed by) the following symmetric $N \times N$ matrix times N-vector multiplication:

$$\begin{bmatrix} s_0 \\ s_1 \\ \vdots \\ s_{N-1} \end{bmatrix} = \frac{1}{N} \begin{bmatrix} \exp\left(-j\frac{2\pi}{N}nm\right) \end{bmatrix} \begin{bmatrix} Z_0 \\ Z_1 \\ \vdots \\ Z_{N-1} \end{bmatrix}$$

N = dimension of transform

$0 \leq n < N-1$ column index

$0 \leq m < N-1$ row index

j = imaginary unit

Recalling that the determination of the harmonic amplitudes in a conventional Fourier analysis involved multiplication of the given time function by one of the assumed harmonic functions and integrating, it will be evident that the DFT involves an analogous procedure. The analogue may be seen by examination of any of the row-times-column products in the multiplication: Each row of the DFT matrix is simply a tabulation of the complex exponential (sinusoid) for integer frequency m (row index) versus time n (column index). Thus, the complex exponential for frequency m is being multiplied by the time series $\{Z_i\}$, with summation (integration) of this product with respect to time to produce the harmonic amplitude s_m for frequency m. This process, for a given row (frequency), will extract the value (Fourier amplitude coefficient) of *one* of the unknown amplitudes. If the time series $\{Z_i\}$ is assumed to be represented as a sum of harmonics

$$Z_m = \sum_{n=0}^{N-1} c_n \exp\left(+j\frac{2\pi}{N}nm\right) \qquad \begin{matrix} 0 \leq m \leq N-1 \text{ (time)} \\ 0 \leq n \leq N-1 \text{ (frequency)} \end{matrix}$$

where n may be regarded as the harmonic number and m as the time argument, then the product of the kth row of the DFT matrix times the time-series,

$$s_k = \frac{1}{N}\sum_{m=0}^{N-1} \exp\left(-j\frac{2\pi}{N}km\right)\left\{\sum_{n=0}^{N-1} c_n \exp\left(+j\frac{2\pi}{N}nm\right)\right\}$$

is well known to reduce to the result $s_k = c_k$.

Thus, the kth row of the DFT matrix, which is a negative-exponent, complex exponential of the form

$$\exp\left[-j\frac{2\pi}{N}km\right]$$

extracts from the time series the Fourier amplitude coefficient of any component, or *harmonic content*, having the positive-exponent, complex exponential form

$$\exp\left[+j\frac{2\pi}{N}km\right]$$

The DFT, then, is an operation which computes all of the Fourier amplitude coefficients at once. This set, represented as the column vector $\{s_i\}$, $0 \leq i \leq N-1$, is called the discrete Fourier transform, or discrete Fourier amplitude spectrum, of the given time series. The set of N rows of the DFT matrix is sufficient, i.e., *complete*, so that not only does every time series have a computable transform, but also that from the transform the time series may be reconstructed exactly. Thus, the transform is invertible.

Before proceeding to a doppler interpretation of the DFT, it is well to mention that the scalar factor $1/N$ which multiplies all elements of the matrix-vector product is usually dropped in discussions of the computational implementation of the DFT, e.g., by the so-called Fast Fourier Transform (FFT). Indeed, the factor $1/N$ is not included in the calculations accomplished by the present computer program. The factor $1/N$ is required, however, for certain mathematical purposes other than relative spectrum computation, such as expressing *Parseval's equation* (conservation of power), and for making the DFT matrix *unitary*, if such matters are of interest.

Returning now to the interpretation of the DFT, examination of the rows of the matrix reveals that the (positive-exponent) 0th,1st,2nd, $\cdots$, $(N-1)$st frequency component amplitudes in the time series will be extracted by the corresponding rows of the transform matrix. This observation is correct, but the following additional remarks bear on the interpretation: Suppose $N = 256$, for example. Then the highest-frequency harmonic in the time-series is understood to be the 255th. The 255th harmonic is visualized as a sinusoidal waveform having 255 periods of oscillation in the period of the fundamental. If this 255th harmonic were tabulated at the Nth time-points (and no others) the tabulation happens not to show the fine structure expected to reflect 255 periods of oscillation but, rather, would seem to show only *one* period of oscillation. Thus, the *apparent* frequency of the 255th harmonic in the tabulation is actually that of the fundamental. More precisely, since complex exponentials are involved, the tabulation for harmonic number 255 coincides with the tabulation for harmonic number -1, if harmonic number 1 is taken as the fundamental. These remarks will introduce the applicability of the identity

$$\exp\left(-j\frac{2\pi}{N}nm\right) \equiv \exp\left[-j\frac{2\pi}{N}(nm \bmod N)\right]$$

and, more specifically,

$$\exp\left(-j\frac{2\pi}{N}nm\right) \equiv \exp\left(-j\frac{2\pi}{N}[-N-n)]m\right)$$

From the latter identity, for $0 \leq n,m < N$, it may be seen that postulating high positive harmonic numbers, such as 255, is mathematically indistinguishable from postulating low *negative* harmonic numbers, such as -1.

The *completeness* of the transform with respect to postulated frequency components at the harmonic numbers $0,1,\cdots,(N-1)$ is retained if arbitrary (and possibly noncontiguous) harmonic numbers outside this range are postulated, provided that the set of the chosen harmonic numbers is congruent to $0,1,\cdots,(N-1)$ *modulo* N. Thus instead of postulating harmonic numbers $0,1,2,\cdots,255$, it would be entirely equivalent, for example, to postulate that the frequencies $+128$, -127, $-126,\cdots,-1,0,1,2,\cdots$, 126,127 are contained in a 256-point time series. For doppler amplitude samples obtained from planetary radar, for example, such a choice seems natural: on physical grounds, it is known *a priori* that (a) the doppler return does in fact contain frequency components above, below, and at the carrier frequency, and (b) all frequency components lie in the immediate neighborhood of the carrier frequency. Now, heterodyning of the doppler return to dc (zero frequency) would be expected to produce positive- and negative-frequency components with respect to dc. Therefore, if the function of the DFT is to extract a spectrum of this form, the *user* is postulating a set of harmonic numbers such as $+128$, -127, $-126,\cdots$, $-1,0,1,2,\cdots,126,127$ rather than any of the other choices he could have made congruent modulo 256. The burden of justifying an assignment of the spectrum values computed by the DFT to any postulated set of frequencies, then, necessarily rests with the user.

The present computer program accommodates the $+128$, -127, $-126,\cdots,-1,0,1,2,\cdots,125,126,127$ assignment by computing the DFT *without* regard to this assignment, and then permuting the order of the elements so as to reflect the user's view. The permutation may be indicated schematically as:

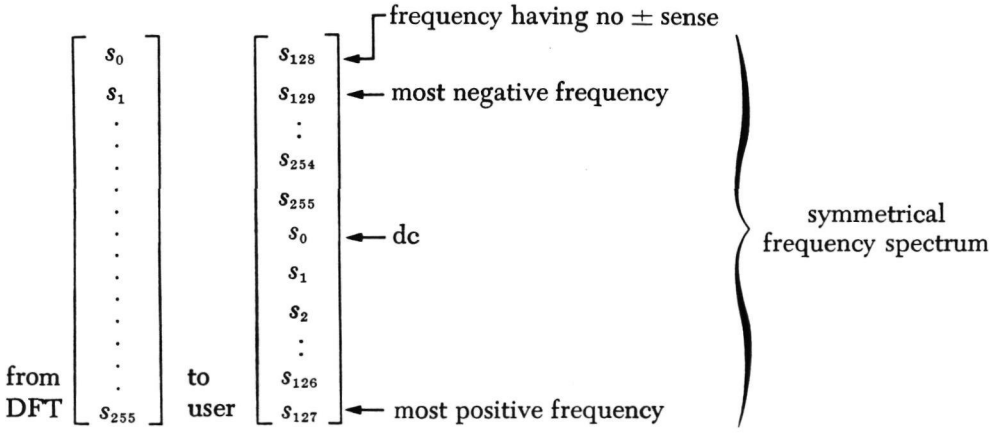

With an even number of points assumed in the time series (256 in the present discussion) the +128th harmonic number gives a waveform identical to that for the −128th (+128 ≡ −128 mod 256). Since only one of these could be computed (either, with the same computational result), there seems to be no meaningful interpretation of s_{128} as a doppler frequency amplitude component. Interpretation is not, however, a part of the computational requirements. Thus, s_{128} is computed for the sake of completeness of the transform, and is furnished to the user along with the other spectral elements.

Intentionally omitted from the foregoing discussion was elaboration of the fact that a *power* spectrum is the computational result furnished to the user. A power spectrum is obtained from the amplitude spectrum (computed by DFT) by magnitude-squaring the elements, and summing all spectra computed in successive 256-point blocks making up a given receive run. Thus, the user gets:

$$\sum_{\substack{\text{all trans-}\\ \text{forms in a}\\ \text{receive-run}}} \begin{bmatrix} |s_{128}|^2 \\ |s_{129}|^2 \\ \vdots \\ |s_0|^2 \\ \vdots \\ |s_{126}|^2 \\ |s_{127}|^2 \end{bmatrix}$$

By the statistical stationarity assumed for the spectra of successive 256-point time series, the computed spectra are simply SNR-enhanced by the summation, i.e., an SNR-improved estimate of the doppler spectrum is obtained. The magnitude-squaring operation wipes out the phase information for each frequency component, and preserves only a power measure of each component.

Table 1. Time tape record format and contents

Time tape record format	
BOT marker	
Core dump record: 4096 words, dumped from memory locations $0\text{-}4095_{10}$.	
Data record: 192 words Data record: 192 words ⋮ Data record: 192 words	all data records formatted identically
EOT marker	

Time tape 192-word data record contents				
Word No. (1-192)				
1	Record serial number (binary integer)			
2	Time of day in seconds (binary integer)			
3 4 ⋮ 63 64	Parameters			
65	Real sample	Gate 0	Coder 1	0
66	Imag sample			
67	Real sample	Gate 1		2
68	Imag sample			
⋮	⋮	⋮		⋮
127	Real sample	Gate 31		62
128	Imag sample			
129	Real sample	Gate 0	Coder 2	1
130	Imag sample			
131	Real sample	Gate 1		3
132	Imag sample			
⋮	⋮	⋮		⋮
191	Real sample	Gate 31		63
192	Imag sample			

Table 2. Spectrum tape record format

BOT		
Long erasure		
EOF		
Header record Spectrum record, range 0 Spectrum record, range 1 ⋮ Spectrum record, range 63	Receive run 0	1st Days records
Header record Spectrum record, range 0 Spectrum record, range 1 ⋮ Spectrum record, range 63	Receive run 1	
⋮		
Header record Spectrum	Last receive run of day	
EOF		
⋮		
EOF		
Header record Spectrum record, range 0 Spectrum record, range 1 ⋮ Spectrum record, range 63	Receive run 0	6th Days records
⋮	Receive run 1	
⋮	Last receive run of day	
EOF		
EOF (extra EOF)		

Table 3. Spectrum tape 197-word header record contents

Word No. (1-197)	
1	ID initially 00000000, increments 1000_8 after each receive run of day
2	No. of words in record -2, $= 195_{10}$, binary integer
3	Record type = 5 if Run 0, otherwise = 4, binary integer
4	Date record written (processed), 6-digit BCD packed in single 24-bit word, YYMMDD
5	Date data taken (from radar log), 6-digit BCD, single 24-bit word, YYMMDD
6 7 . . . 68 69	64-word record, exact copy of time tape data record header, for the *first* time point of the *first* continuous 256-record time-tape data block successfully transformed in the receive run
70 71 . . . 132 133	64-word record, exact copy of time tape data record header, for the *last* time point of the *last* full continuous 256-record time-tape data block successfully transformed in the receive run
134 135 . . . 196 197	63-word record, listing the record serial numbers of the first records of all of the full, continuous 256-record blocks whose power spectra contribute to the accumulation of spectra for the receive run.

Table 4. Spectrum tape 262-word power spectrum record contents

Word No. (1-262)		
1	ID 1-word field has the 8-digit octal form rrrrrggg. Field rrrrr is initially zero; and increments by 1 after each receive run of day. Field ggg is the gate number for which the spectrum was computed. Field ggg is of the form abb: a = 1 or 2 (for Coder number 1 or 2, respectively), and bb is the gate number $0\text{-}31_8$.	
2	No. of words in record-2, $= 260_{10}$, binary integer	
3	Record type = 3, binary integer	
4	Date record written (processed), 6-digit BCD packed in single 24-bit word, YYMMDD	
5	Date data taken (from radar log), 6-digit BCD packed in single 24-bit word, YYMMDD	
6	SF (scale factor). A positive binary integer giving the number of right shifts required, for all words in the power spectrum, to restore the absolute scaling of the spectrum. The absolute scaling is that which obtains when integer time series are Fourier-transformed using the conventional FFT (with factor 1/256 omitted), with squaring and accumulation of spectra for all 256-record blocks in a given receive run.	
7	Power spectrum point, frequency ± 128	256-point power spectrum for a given range gate
8	Power spectrum point, frequency -127	
9	Power spectrum point, frequency -126	
.		
.		
.		
135	Power spectrum point, frequency 0	
.		
.		
.		
261	Power spectrum point, frequency $+126$	
262	Power spectrum point, frequency $+127$	

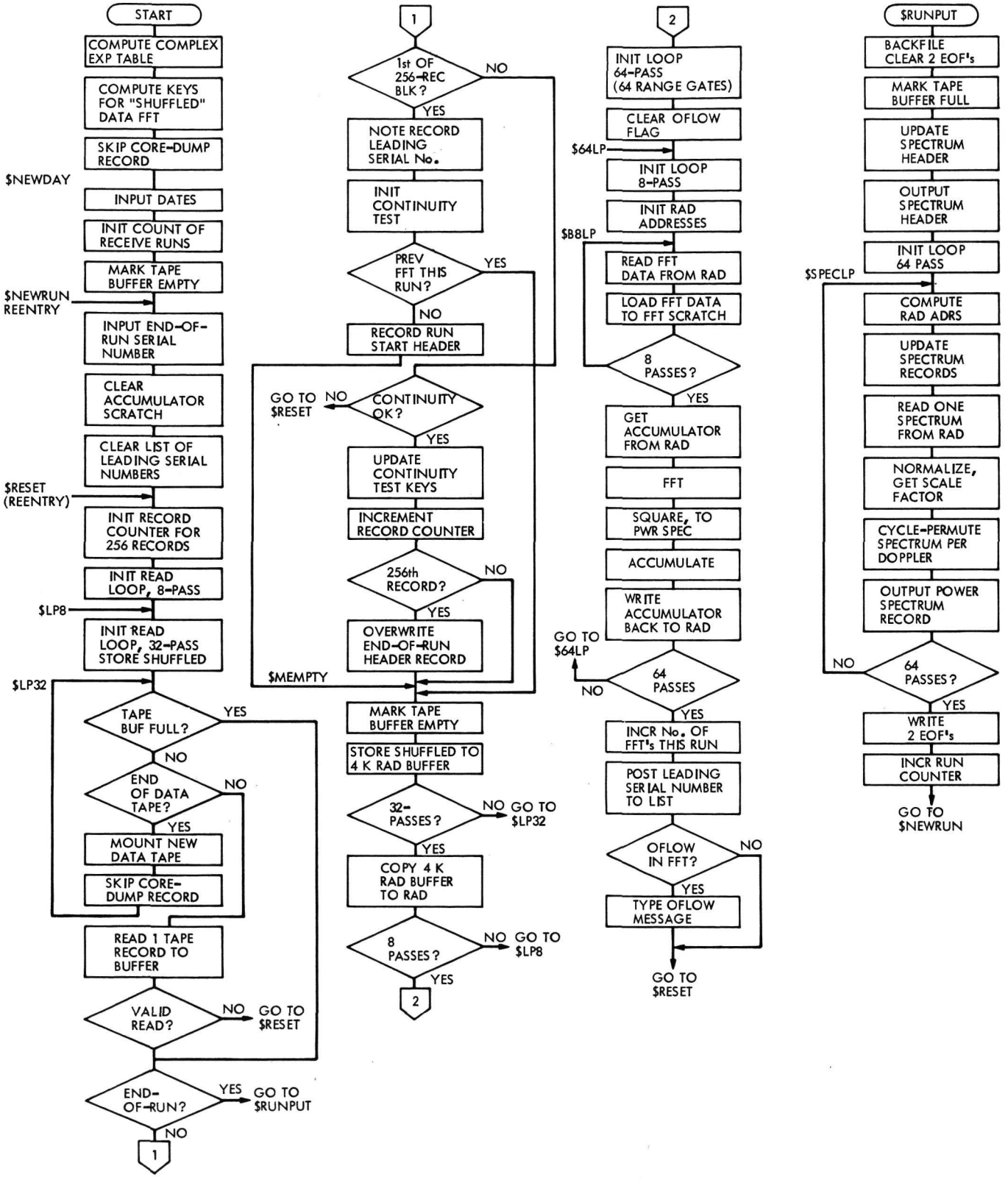

Fig. 1. Computer program flow chart

Radar Ranging of the Planet Mars at 8495 MHz

G. S. Downs and P. E. Reichley
Communications Systems Research Section

A simulation was performed for the radar system in order to ensure detection of the planet Mars at the start of the 1975 series of radar probes of the surface. Appropriate parameters were found. Appropriate parameters were also found for use at opposition (December 1975). Systematic errors in the measured delay with changes in surface roughness were observed. This effect is shown to be many times larger than the expected rms fluctuations in the measured delays.

I. Introduction

The surface of the planet Mars will be probed with S- and X-band radar signals during 1975 and 1976, all in preparation for the landing of two spacecraft in 1976. The measurements to be performed at JPL will use the R & D radar system at DSS 14, Goldstone, California, at a frequency of 8495 MHz. In preparation, several series of radar data sets were simulated and processed. That is, the expected power in the reflected signal was calculated as a function of time delay and frequency for several sets of radar system parameters. The random fluctuations caused by receiver noise were superimposed using a random number generator. The appropriate signal-to-noise ratio was calculated for certain distances to the planet, assuming appropriate X-band antenna parameters. The round-trip time delay of the signal reflected from the surface of the planet was determined. Up to 120 delay measurements were made to allow determination of the detection probability and the measurement accuracy. An appropriate set of radar parameters was chosen in light of the results of this study.

II. How Delay Is Measured

The basic radar data set consists of a matrix of received power as a function of time delay and excess doppler shift. Separate regions on the surface will exhibit separate time delays because of the spherical shape of the planet.

Let θ represent the angle between the line of sight from the radar to the center of the planet and the radius to the

point on the surface. The time delay τ of the signal reflected from that surface point back to the radar is given by

$$\tau = \frac{2R}{c}(1 - \cos\theta) + \frac{2D}{c} \tag{1}$$

where R is the radius of the planet and c is the speed of light; D is the distance along the line of sight to the closest point on the surface. Note that θ is also the angle of incidence of the signal on the surface. θ and D are each functions of time. The large delay due to D is removed at the time of data collection. The small changes in θ due to the relative motion of Mars and Earth in the time interval $2D/c$ are neglected. The locus of a curve of a constant τ is a circle in the plane perpendicular to the line of sight and whose center lies on the line of sight. Regions of a particular delay are isolated by modulating the phase of the transmitted signal with a pseudo-random binary code. If the bit length of the code is T seconds, the normalized cross correlation function of the transmitted signal with the received signal is given by

$$R_r(\tau) \approx \begin{cases} 1 - \dfrac{1}{T}|\tau - \tau_0|; & |\tau - \tau_0| \leq T \\ 0 \qquad\qquad\quad ; & |\tau - \tau_0| > T \end{cases} \tag{2}$$

where τ_0 is the round trip delay. A band of surface elements located within T seconds of τ_0 can be isolated. In practice, the received signal is passed through a bank of correlators, the ith corresponding to a round trip delay τ_{0i}. The power in the output of the ith correlator is then the sum of the power in the reflected signals corresponding to the delays $\tau_{0i} - T \leq \tau \leq \tau_{0i} + T$, each delay component being weighted by the range window $R(\tau) = R_r^2(\tau)$. There is an ambiguity in the delay τ_0 of the reflected signal which is equal to the length of the binary code. That is, $R(\tau)$ is periodic in time mT, where m is the number of bits in the code. Usually the planetary ephemeris is good enough to resolve this ambiguity in time delay. There remains, however, a small perturbation to the total reflected power from the region defined by $R(\tau_{0i})$ since contributions are obtained from all regions centered at $\tau = \tau_{0i} \pm nmT$, where n is any integer.

Further resolution of the planet's surface is usually obtained by taking advantage of the doppler spreading of the reflected signal caused by the rotation of Mars. Loci of constant doppler shift are circles on the surface, parallel to the plane defined by the apparent spin axis of the planet and the line of sight. The intersections of the circles of constant range and the circles of constant doppler shift then isolate particular small regions on the surface (see Fig. 1). Therefore, the discrete power spectrum of the output of each correlator is estimated using discrete time samples. The power at each discrete frequency f_0 in the spectrum is in fact the sum of power from regions of varying doppler shift f. Each region is weighted by the familiar function

$$D(f) = \frac{\sin^2[\pi N(f - f_0)/\Delta f]}{N^2 \sin^2[\pi(f - f_0)/\Delta f]} \tag{3}$$

where $\overline{N}$ is the number of discrete frequencies, separated by Δf, in the power spectrum.

The delay-doppler geometry imposed on the planet's surface is pictured in Fig. 1, where the planet is viewed from the direction of the apparent spin axis. The angle of incidence θ is the angle between the direction to Earth and N, the local normal to the mean sphere. The shape of the range window $R(\tau)$ is shown at the left for the case of $T = 6$ μs. The shape of the doppler window $D(f)$ is shown at the right for the case of $\Delta f = 10.2$ Hz, when $\lambda = 12.55$ cm. As is often the case in these measurements, the correlators are separated such that $\tau_{0(i+1)} - \tau_{0i} = T/2$. Note that as the planet rotates, any given region near the doppler equator (a great circle perpendicular to the circles of constant doppler shift and bisecting the rings of constant range) is probed at a variety of angles of incidence. Each set of received power as a function of delay and doppler (a data frame) represents a snapshot of the surface near the doppler equator. An example of such a data frame appears in Fig. 2.

Consider for the moment the power vs time delay at a fixed doppler shift. The reflected power corresponds to a narrow region at a particular longitude and a minimum angle of incidence. The location of the planet at that particular doppler shift is taken to be the delay at which the power is a maximum. As the planet rotates, a series of delay functions corresponding to particular values of θ become available for a particular longitude. With the extra delay due to curvature of the surface removed, the collection of delay functions is usually added to produce a composite delay function in which the signal-to-noise ratio is larger. The delay corresponding to the peak power then defines the distance to the planet.

In practice, the presence of noise will cause errors in locating the planet. Also, the weak signal case gives rise to a finite possibility of a false detection of the planet.

The following discussion is devoted to a determination of the probability of a correct detection and the measurement error, once detection has been established. These probabilities and errors are dependent on the signal-to-noise ratio, which in turn is dependent on the parameters of the radar system and the surface characteristics. The radar system parameters and surface characteristics are varied over an appropriate range in the discussion below.

III. The Data

An example of simulated data is presented in Fig. 2. The spectrum of the output of 32 correlators is presented in Fig. 2(a) for the noise-free case. The magnitudes of the spectral components are proportional to the received power expected for the case of $T = 6$ μs and $\Delta f = 36.2$ Hz at $\lambda = 3.53$ cm. Note that correlators are offset progressively in delay by $T/2 = 3$ μs. These magnitudes were calculated by evaluating the radar equation:

$$P(f_0,\tau_0) = \frac{P_x G_x G_r \lambda^2}{64\pi^3 D^4} \cdot \frac{\rho_0 C}{2} \iint_{S(f,\tau)} ds \frac{R(\tau-\tau_0)\, D(f-f_0)}{[\cos^4\theta + C\sin^2\theta]^{3/2}} \tag{4}$$

where P_x and G_x are the transmitting power and antenna gain, respectively. G_r is the receiving antenna gain. The transmitter operates at wavelength λ. The planet, located at distance D, is characterized by a reflectivity ρ_0 and roughness parameter C. The denominator of the integrand in Eq. (4) (sometimes called the Hagfors backscatter function, Refs. 1 and 2) describes how the power scattered back toward the receiver varies with the angle of incidence, where θ is now a function τ and f. The surface S over which the integration takes place is determined by the position of the range and doppler windows relative to the planet. The details of the evaluation of the integral, and in particular the effects of aliasing in frequency and ambiguity in range will be discussed in a forthcoming article.

The received power $P(f,\tau)$ was calculated for 32 delays and 64 frequencies for values of $\Delta f = 36.2$, 72.5 and 145 Hz with $T = 6$ μs and for $\Delta f = 145$ Hz with $T = 12$ μs. In each case, $\tau_{0(i+1)} - \tau_{0i} = \Delta\tau = T/2$. In the case of Mars, these values of Δf correspond to $N - S$ slices on the surface of widths of 0.16, 0.32 and 0.64 deg in longitude, respectively. The transmitter power P_x was taken to be 400 kW, operating at 8495 MHz, so $\lambda = 3.53$ cm. The gains G_x and G_r were taken to be equal, and these values were deduced from data provided by Freiley (Ref. 3). A nominal value of system efficiency of 0.40 was assumed from the data of Ref. 3. This value corresponds to a value 1 σ lower than the mean transmit system efficiency at an elevation of 70 deg. The corresponding antenna gains are 71.1 dB. The 4 sets of values of $(\Delta f,\tau)$ were subdivided into sets of different values of D, where D varied between 0.56 AU (closest approach during the 1975 opposition) and 1.5 AU. These subsets were, in turn, subdivided even further to correspond to roughness $C = 50$, 150, 300, 1000, 2000 and 5000. A total of 78 distinct sets of data frames were then generated from Eq. (4). A value of $\rho_0 = 0.08$ was assumed for all evaluations of Eq. (4). This value is an average obtained from previous radar probes of Mars. Although ρ_0 varies between 0.01 and 0.15, most regions have a reflectivity close to 0.08.

In practice, data frames similar to those of Fig. 2(b) are measured at regular time intervals. To improve the signal-to-noise ratio, several sequential data frames are usually added together. The magnitude of each spectral component then represents an energy. That is, a signal of intensity $P = P(f,\tau)$ watts is integrated for t_I seconds to produce Pt_I joules. Now, t_I should be long enough to allow a particular region on the planet's surface to rotate from one discrete doppler frequency to the next. In this analysis, t_I was chosen such that the planet rotated about 0.75 of that distance. For example, when $\Delta f = 36.2$ Hz (0.16 deg in longitude), t_I was chosen to be 30 seconds, an interval in which the planet rotates 0.12 deg.

The superimposing of a noisy signal of the proper magnitude was performed in the following manner. A series of random numbers with a variance of 1.0 was generated. The scale of the variance was chosen by noting that the receiver noise power is $kT_s\Delta f$ watts for each spectral component, where k is Botzmann's constant and T_s is the system noise temperature. In time t_I the mean energy obtained by integrating this component of the noise is $kT_s\Delta ft_I$ and the variance associated with the measurement of this component is $(kT_s)^2\Delta ft_I$. The measurement of the planetary component Pt_I also is subject to random fluctuations. The total variance is calculated assuming that the wideband receiver component and the planetary component are each nearly Gaussian random processes. (They are in fact Rayleigh processes in which the mean is much larger than the root-mean-square fluctuation.) The total variance is then $(kT_s)^2\Delta ft_I + (Pt_I)^2/\Delta ft_I$.

In the generation of the series of random numbers it was assumed that $Pt_I << kT\Delta ft_I$, so that the planetary component of the variance could be ignored. The series

of random numbers, so scaled, and the mean value of the receiver noise were added to the function $P(f,\tau)$ to obtain a simulated data frame. T_s was taken to be 23 K. A data frame similar to Fig. 2(b) was generated from the noise-free frame of Fig. 2(a) in the above manner. The data in Fig. 2(b) correspond to $D = 0.56$ AU and $C = 300$. The constant wide-band component of the receiver noise has been subtracted. A total of 70 data frames containing independent additive noise, representing integrations over t_I seconds, were generated to provide a good measure of the statistics of interest.

IV. The Delay Measurements

In practice, one cannot probe the planet's surface with a monostatic radar system (one antenna) on a continuous basis, since the transmitter must be turned off during reception. Hence, the simulated data frames were arranged in time to duplicate the case in which the radar signal is transmitted for a time interval equal to the round-trip time between Earth and Mars, and then received for one round-trip time. Reception immediately follows transmission for an equal time interval. Clearly, in one round-trip time one will usually collect several data frames, each representing an integration of t_I seconds. Since the transmitter is not on continuously, only ½ of the available angles of incidence will be probed. A view window, of width equal to the amount of rotation accomplished in one round-trip time, slides over the surface allowing some angles of incidence and omitting others.

The results of the delay measurements are presented in Tables 1-4. At first, the radar system parameters T and Δf were chosen to be equal to those used in earlier work on Mars at 2388 MHz. The doppler shifts were scaled from 2388 to 8495 MHz such that Δf corresponded to a longitude interval ΔL of 0.16 deg. At each of the four values of D in Table 1, six values of roughness C were chosen to cover the range expected at 8495 MHz. A number N_T (between 90 and 120) composite delay functions, each representing a different mixture of angles of incidence, were available for each combination of D and C. If the peak amplitude of a composite delay function was 2.5 to 3 times larger than the rms noise level, the planet was considered detected and the corresponding delay τ was recorded. However, in N_D detections, a certain number N_F are false detections which usually occur in the weak signal case. Values of τ which placed the planet more than T μs away from the known position of the planet were considered false detections. The fraction P_d of successful detections and the fraction P_e of these detections that were false are listed in Table 1 and calculated from

$$P_d = \frac{N_D - N_F}{N_T}$$
$$P_e = \frac{N_F}{N_D} \tag{5}$$

The values of N_D, the mean τ_{b0} in the range estimates, and the associated rms fluctuation $\sigma_{\tau 0}$ presented in Table 1 represent averages over all the available data. However, some of the composite delay functions contain contributions from angles of incidence primarily near 0 deg (the maximum is about 2 deg in this simulation). These delay functions were isolated and, finding N_c of them, the mean τ_{bc} of this set and the associated rms fluctuations $\sigma_{\tau c}$ were calculated and listed in Table 1.

The true mean and variance are represented by τ_{bc} and $\sigma_{\tau c}$. The reason for this can be understood by examining Fig. 3. The delay τ of each composite delay function has been presented vs the centroid $\bar{n}_d$ of the angle-of-incidence view window. The centroid is expressed in units of ΔL (or Δf). In Fig. 3, where $C = 5000$, the shape of the backscatter function changes rapidly with θ, so the shape of the delay function flattens markedly as $\bar{n}_d$ increases. A positive drift in the delay of the peak amplitude and a decrease in the magnitude of the peak accompany this flattening. The positive drift is readily observable in Fig. 3(a). Noise fluctuations are low since the corresponding distance is only 0.56 AU. The distance is 1.14 AU in Fig. 3(b), and the larger scatter in τ for $\bar{n}_d > 6$ is evidence of the decreasing peak amplitude. By including only the values of τ for which $\bar{n}_d < 6$ in the statistics, a true representation of the measurement accuracy is obtained. Including all available values of τ produces a larger variance because of the systematic drift in τ with window position.

The mean τ_{bc} is a function of the roughness parameter C. In Fig. 4(a) the measurements of τ are presented vs $\bar{n}_d$ for $C = 150$ at a distance of 0.56 AU. The drift in τ with $\bar{n}_d$ is not as extreme as in Fig. 3(a) since the backscatter function varies more slowly with θ. Note however that τ_{bc} for $\bar{n}_d < 6$ is not identical to the similar value in Fig. 3(a). This bias is again caused by the retarded, flatter delay functions characteristic of low values of C or

larger values of θ. The data of Fig. 4(b), corresponding to $D = 0.8$ AU, show how small signal-to-noise ratios mask the effects discussed above.

At opposition $D = 0.56$ AU. The results of Table 1 indicate that maximum ranging accuracies of 40 to 300 ns can be obtained. The systematic changes of τ with $\overline{n}_d$ and C are large compared to these hypothetical accuracies. It will then be desirable to apply corrections to the estimates of τ to obtain the minimum possible rms fluctuations.

The data of Tables 3–4 were obtained in a search of the data-frame parameters which ensure detection of the planet Mars at the start of the 1975 series of measurements (during August, when Mars is at 1.2 AU). The parameters underlying Table 4 ($T = 12$ μs, $\Delta L = 0.64$ deg) provide a reasonable probability of detection of rough as well as smooth surfaces at 1.2 AU. These are the parameters to be used at the start of the series of measurements. Tables 2 and 3 are useful as an aid in determining what T and ΔL should be as Mars progresses towards opposition.

References

1. Hagfors, T., "Backscattering from an Undulating Surface with Applications to Radar Returns from the Moon," *JGR*, 69, pp. 3779–3784, 1964.
2. Hagfors, T., *Radar Astronomy*, Evans, J. V., and Hagfors, T., eds., Chapter 4, pp. 187–218, McGraw-Hill, New York, 1968.
3. Freiley, A. J., "DSS-14 XKR Cone Performance," JPL Interoffice Memo No. 3331-75-001, Mar. 10, 1975 (an internal document).

Table 1. Detection probability and σ_τ for $T = 6$ μs, $\Delta L = 0.16$ deg, $\rho_0 = 0.08$

D, AU	C	P_d, %	P_e, %	N_D	$\sigma_{\tau 0}$, μs	τ_{b0}, μs	N_c	$\sigma_{\tau c}$, μs	τ_{bc}, μs
0.56	50	98	1	118	0.44	2.6	64	0.30	2.4
	150	100	0	120	0.26	2.4	64	0.12	2.25
	300	100	0	120	0.31	2.3	64	0.08	2.1
	1000	100	0	120	0.31	2.0	64	0.09	1.75
	2000	100	0	120	0.38	1.7	56	0.04	1.4
	5000	100	0	120	0.45	1.4	56	0.04	1.1
0.80	50	56	10	65	1.33	–	40	1.38	–
	150	97	0	113	0.65	–	61	0.42	–
	300	100	0	117	0.62	–	61	0.15	–
	1000	100	0	117	0.39	–	61	0.11	–
	2000	100	0	117	0.40	–	55	0.04	–
	5000	100	0	117	0.54	–	55	0.04	–
1.00	50	3	57	4	1.80	–	–	–	–
	150	62	1	76	1.18	–	42	0.98	–
	300	83	1	102	0.72	–	54	0.57	
	1000	95	0	117	0.62	–	58	0.33	–
	2000	95	0	117	0.55	–	55	0.32	–
	5000	92	0	113	0.57	–	52	0.22	–
1.14	50	2	50	2	1.34	–	–	–	–
	150	38	10	38	1.52	–	29	1.44	–
	300	73	3	73	0.94	–	39	0.80	–
	1000	86	0	86	0.45	–	50	0.38	–
	2000	91	0	91	0.54	–	52	0.45	–
	5000	88	0	88	0.50	–	49	0.35	–

Table 2. Detection probability and σ_τ for $T = 6$ μs, $\Delta L = 0.32$ deg, $\rho_0 = 0.08$

D, AU	C	P_d, %	P_e, %	N_D	$\sigma_{\tau 0}$, μs	τ_{b0}, μs	N_c	$\sigma_{\tau c}$, μs	τ_{bc}, μs
1.00	50	12	–	13	1.47	–	8	1.18	–
	150	81	3	91	1.09	2.5	56	1.24	2.5
	300	82	3	83	0.81	2.5	46	0.68	2.5
	1000	93	0	94	0.61	2.0	52	0.58	2.0
	2000	94	0	95	0.49	1.6	47	0.56	1.6
	5000	93	0	94	0.74	1.5	46	0.54	1.2
1.14	50	4	–	4	1.15	–	–	–	–
	150	60	6	61	1.50	–	34	1.50	–
	300	82	3	83	0.81	–	46	0.68	–
	1000	93	0	94	0.61	–	52	0.58	–
	2000	94	0	95	0.49	–	47	0.56	–
	5000	93	0	94	0.74	–	46	0.54	–
1.50	50	–	–	–	–	–	–	–	–
	150	–	–	–	–	–	–	–	–
	300	30	10	26	1.37	–	20	1.28	–
	1000	76	0	67	0.53	–	41	0.59	–
	2000	83	0	73	0.63	–	37	0.65	–
	5000	84	0	74	0.45	–	37	0.51	–

Table 3. Detection probability and σ_τ for T = 6 μs, ΔL = 0.64 deg, ρ_0 = 0.08

D, AU	C	P_d, %	P_e, %	N_D	$\sigma_{\tau 0}$, μs	τ_{b0}, μs	N_c	$\sigma_{\tau c}$, μs	τ_{bc}, μs
1.00	50	46	12	49	1.92	3.3	31	1.72	3.1
	150	92	1	98	0.93	2.7	65	0.98	2.9
	300	100	0	106	1.00	2.7	70	0.65	2.6
	1000	100	0	106	0.91	2.2	70	0.51	2.0
	2000	100	0	106	0.61	1.7	53	0.29	1.5
	5000	100	0	106	0.67	1.4	53	0.20	1.1
1.14	50	11	31	10	1.60	–	6	2.0	–
	150	78	6	74	1.50	–	48	1.55	–
	300	95	0	90	1.00	–	57	0.84	–
	1000	100	0	95	0.75	–	62	0.53	–
	2000	100	0	94	0.64	–	49	0.56	–
	5000	98	1	93	0.71	–	50	0.82	–
1.50	50	–	–	–	–	–	–	–	–
	150	9	–	8	1.5	–	7	1.40	–
	300	49	5	44	1.62	–	27	1.20	–
	1000	78	0	69	0.72	–	44	0.65	–
	2000	80	0	71	0.47	–	37	0.46	–
	5000	84	0	75	0.64	–	37	0.25	–

Table 4. Detection probability and σ_τ for $T = 12$ μs, $\Delta L = 0.64$ deg, $\rho_0 = 0.08$

D, AU	C	P_d, %	P_e, %	N_D	$\sigma_{\tau 0}$, μs	τ_{b0}, μs	N_c	$\sigma_{\tau c}$, μs	τ_{bc}, μs
1.00	50	82	4	91	2.62	5.4	86	2.66	5.4
	150	100	0	111	1.48	5.0	103	1.50	5.0
	300	100	0	111	1.10	4.4	103	0.74	4.4
	1000	100	0	111	0.78	3.4	103	0.70	3.2
	2000	100	0	111	1.12	2.8	53	0.32	2.4
	5000	100	0	111	1.48	7.0	53	0.36	1.6
1.14	50	44	10	49	3.40	–	30	3.40	–
	150	91	2	101	2.00	–	63	2.20	–
	300	98	1	109	1.75	–	70	1.96	–
	1000	100	0	111	1.28	–	71	0.92	–
	2000	98	0	109	1.44	–	55	0.77	–
	5000	95	0	106	0.93	–	51	1.14	–
1.50	50	–	–	–	–	–	–	–	–
	150	30	10	30	3.10	–	19	3.60	–
	300	68	0	69	1.84	–	42	1.92	–
	1000	76	1	77	1.08	–	44	1.10	–
	2000	80	0	81	1.08	–	38	1.38	–
	5000	80	0	80	1.04	–	37	1.30	–

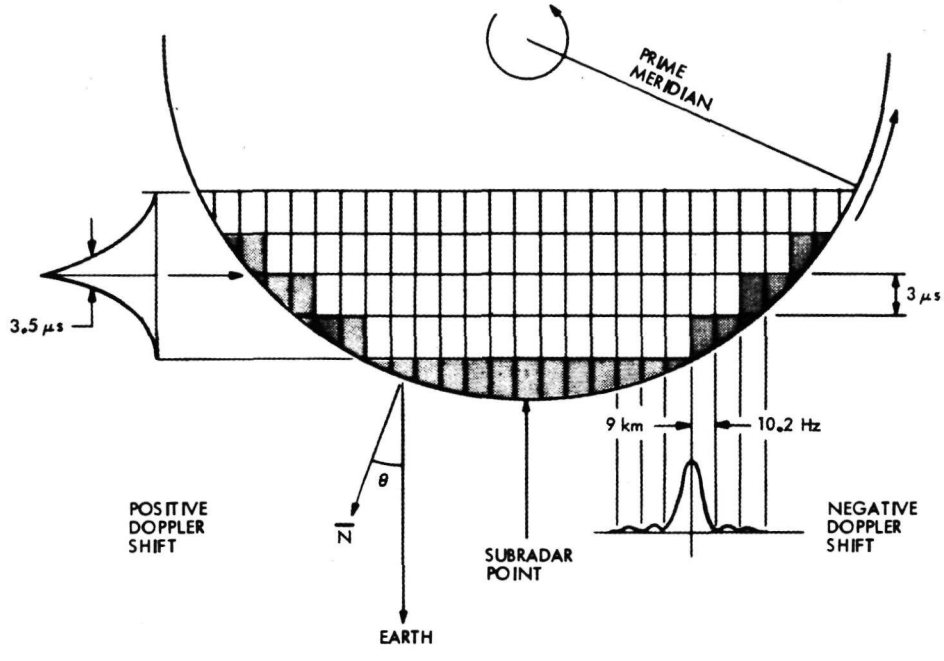

Fig. 1. Partitioning of Mars by the radar system

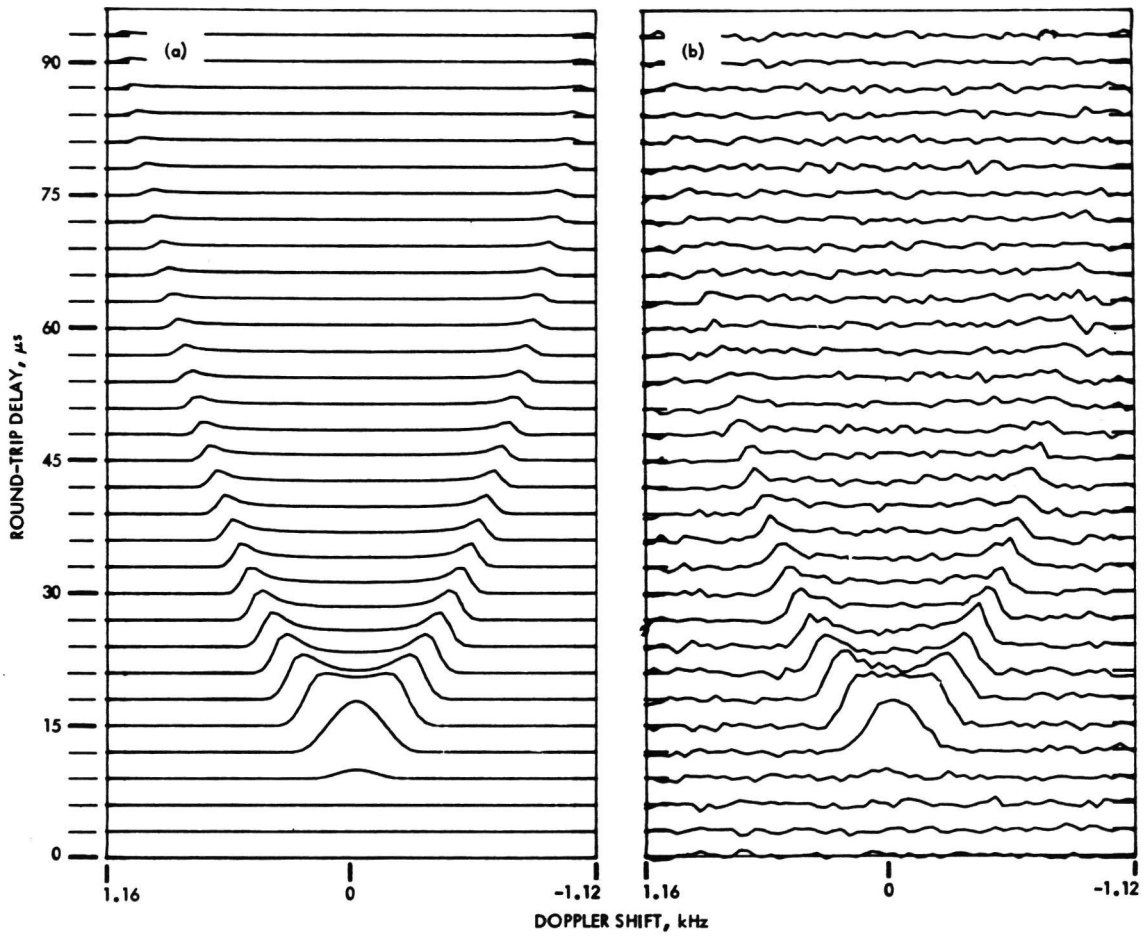

Fig. 2. Received power vs doppler shift and delay for Δf = 36.2 Hz, T = 6μs, ρ_0 = 0.08, and C = 300: (a) noise-free case, (b) noisy case (see text for noise parameters)

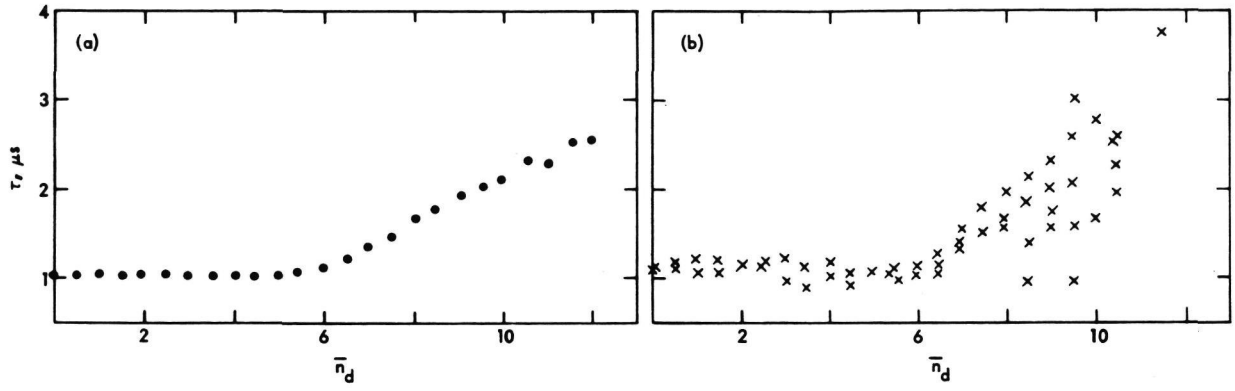

Fig. 3. Estimation of τ vs the centroid $\bar{n}_{/\!/}$ of the angle-of-incidence window for $C = 5000$:
(a) $D = 0.56$ AU, (b) $D = 1.14$ AU

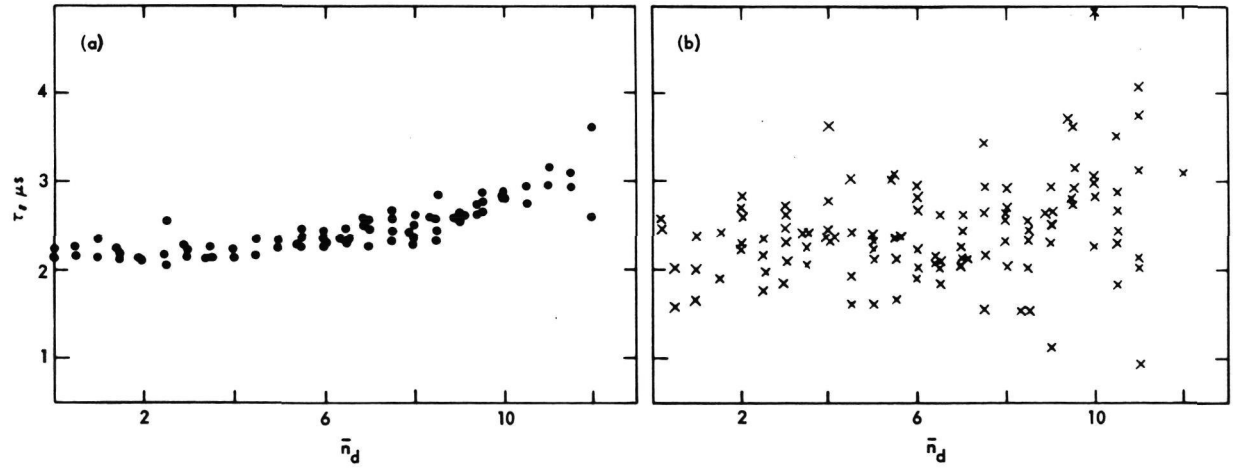

Fig. 4. Estimation of τ vs the centroid $\bar{n}_{/\!/}$ of the angle-of-incidence window for $C = 150$:
(a) $D = 0.56$ AU, (b) $D = 0.8$ AU

Automatic Control of DSS 13

K. I. Moyd
Communications Systems Research Section

The hardware, software, and control of the automatic pulsar data acquisition system at DSS 13 are described. Details of one observing run using the system are given. Modifications to be made in order to control the system remotely from JPL are described.

I. Introduction

The automatic pulsar data acquisition system at DSS 13 is now operational. The station is controlled completely by the station computers once it is put into a specified initial configuration. Operator intervention can only be accomplished through a computer typewriter. The establishment of automatic control of DSS 13 is one stage in the demonstration of remote automatic control of DSS 13.

In Section II the hardware is described, including the modifications which were made. In Section III the software is described, and in Section IV the operation of the system is summarized. The details of one observing run are given in Section V, and plans for future development are discussed in Section VI.

II. Hardware

Three SDS computers at DSS 13 are involved in the control. The 16-kiloword memory SDS 930 computer is the central computer. It is connected by twin coaxial cable communication links to two 8-kiloword memory SDS 910 computers (Ref. 1). The 910A controls a programmable local oscillator; the 910B controls the antenna. Each of the computers has two timing interrupts: a one-pulse per second (pps) interrupt synchronized with UT and a 50-pps interrupt synchronized with the 1 pps. Each communication link has two associated interrupts at each end. A data interrupt occurs when a word has been sent or received; a status interrupt occurs when the incoming carrier signal is turned off (the normal end-of-message indication) or if an error has occurred. A status register can be read to determine the cause of the status interrupt. The four antenna pointing system (APS) panel interrupts in the 910B corresponding to offset entry and offset clear for each axis are used; the rest are ignored. There is an interrupt generated in the 930 when the pulsar data collector has finished an observation. The interrupts are listed in Table 1.

A few modifications to the hardware at the station were required in order to accomplish the automatic control. The 930 computer memory was increased from 8 to 16 kilowords. The antenna system was modified so that the brakes and speed switches could be controlled by the

910B, and various monitors were added. The integrators in the antenna servo system were bypassed. The switch from antenna input to ambient load was made computer controllable. A special pulsar data collector (Ref. 2) and a control card for the pulsar receiver were built. With these exceptions the station configuration is the same as that for the standard pulsar observing.

III. Software

The 930 is programmed in real-time FORTRAN, which is a standard FORTRAN with modifications for real-time operation. It accepts assembly language code interspersed with FORTRAN code. This allows communication with nonstandard external devices and allows time-critical operations to be written in the more efficient assembly language with access to variables defined in FORTRAN.

The 930 program is an interrupt-driven real-time program. That is, most actions are done in response to interrupts rather than in a specific sequential manner. The background level (the portion of the program executed when no interrupts are active) takes care of operator communication, data processing, and overall program control. In response to the 1-pps interrupt, the instructed antenna position is calculated, and parameters are established for use in the 50-pps routine. Data collection is initiated if requested. A new frequency is sent to the 910A, and the returned frequency is checked when appropriate.

In the 50-pps routine, the information received from the 910B is used to generate antenna commands, and transmission of these commands to the 910B is initiated.

There are two routines for each of the link interrupts, depending on whether the 930 is sending to or receiving from the 910 involved. The 930 is kept in the receiving mode, except when it is actually transmitting a message. Because the data interrupt occurs at a high rate (12 words are sent in each direction between the 930 and the 910B during 20 ms) and the overhead in letting FORTRAN handle the interrupts is high (about 1/2 ms per interrupt), the routines for the data interrupts are written in assembly language.

Because operator communication and data recording both use the same input/output (I/O) channel, they are not allowed to interrupt each other. Both are therefore done on the background level. The only action in response to the data collector interrupt is the setting of a flag.

The 910 programs are written in META-SYMBOL, their assembly language. The communications links are controlled by the same routines (translated into assembly language) as on the 930. The 910A program is controlled by the 930. When a frequency is received from the 930, it is sent to the programmable local oscillator in the 1-pps interrupt routine. In response to the next 1-pps interrupt, the frequency is read in from the oscillator and sent to the 930. The 930 compares the instructed and read-in values and re-sends the instructed value in case of disagreement.

The 910B does most of its computation in the background and in the 50-pps routine. It receives commands and display information from the 930 and sends status information to the 930 fifty times a second. The command in each axis is compared with the previous command and is modified if the acceleration or deceleration is too great. In order to read the positions and send the commands to the antenna at approximately uniform intervals, these are done in the 50-pps routine. The displays and the noncritical status information are taken care of in the background.

IV. System Control

The system is controlled by means of Tutorial Input, a standardized human computer interface developed by A. I. Zygielbaum (Ref. 3) and modified by K. I. Moyd (Ref. 4). The list of Tutorial Input commands is given in the Appendix.

The commands fall into three groups: basic parameter entry, antenna, and data collector. The commands in the basic parameter entry group are used to change the values of antenna parameters and data collector parameters which have been set to default values. Under normal operating conditions the default values are used.

There are two basic antenna modes. In the observing mode the specified coordinates are right ascension (RA) and declination (DEC). The antenna is moved to the assigned source position (subject to wrap-up limitations) and then tracked at the sidereal rate. Observing is initiated when antenna position and velocity errors are less than the tolerances given by the corresponding basic parameters. Tracking continues until the antenna is stopped or until a new antenna command is given.

In the nontracking mode the specified coordinates are azimuth (AZ) and elevation (EL). The antenna is moved to these coordinates and held there (without setting the brakes). No observations are taken. The STOW command has the same effect as an AZEL command with AZ = 180

degrees and EL = 85 degrees in the center wrap-up region.

The antenna can be stopped in two ways. In case a panic stop is needed, a sense switch on the 930 computer is checked once each second. The antenna cannot be moved by the computer as long as the switch is set. A STOP command stops the antenna until a new antenna command is given. In both cases the antenna is safely decelerated in both axes, the brakes are set, and the speed switch is set to low speed.

The data collector takes data in phase with the pulsar period. This is done by setting a reference oscillator to a frequency related to the pulsar period. The data collector uses this reference frequency to generate internal clocks which determine when to sample the input signal and when to reset to the beginning of the period. There are three different ways to initiate a new observation. The observation can be started at the next 1 pps with the data collector memory being cleared first (start-next-second); the observation can be started in phase with the previous observation with the new data being added to the previous data (start-in-phase-add) or with the memory being cleared first (start-in-phase-clear). The first observation on a source is initiated automatically when the antenna is on target with a start-next-second instruction. If no commands are given, subsequent observations are initiated by start-in-phase-add instructions. When a new frequency is set by a PLO command, when an observation is aborted by an ENDO command, or when a TSYN command is given, the next observation is initiated by a start-next-second instruction.

The data collector can be configured to expand the resolution of the data by collecting all the data points during only a fraction of the pulsar period while staying in phase with the preceding observation. The fraction of the period to be observed and the expansion factor are set by an EXP command. The first observation is initiated by a start-in-phase-clear instruction; following observations are initiated by start-in-phase-add instructions. The expansion parameters are used until another data collector command (except WAIT and CONT) is given.

V. Observing Run

On March 20, 1975 the automatic control system at DSS 13 was used for observing pulsars. The station was put into a specified configuration before the observing run was started. Once the computers were given control, all operator interaction was by Tutorial Input through the 930 typewriter with the exception of some offset tests, for which the offsets were entered through the 910B APS panel. Seven different pulsars were observed over a period of eleven hours. Each observation was recorded on magnetic tape and plotted. The magnetic tape has been processed in the same manner as the regularly collected pulsar data. The observations are tabulated in Table 2.

At the end of the observing run, the antenna was moved by the computers to the position to be used for the sky survey and the brakes were set.

VI. Future Development

The object of this project is the demonstration of remote automatic control of DSS 13. The establishment of local automatic control is one stage in the demonstration of remote automatic control. No additional hardware modifications will be necessary in order to include the remote control. There is already a teletype line between the 930 at DSS 13 and an SDS 920 at JPL and a twin coaxial cable link between the 920 and a Sigma 5 at JPL. The software in the 910's at DSS 13 will not have to be changed. The 930 program will be changed so that the Tutorial Input will be done through the Sigma 5 terminal rather than through the 930 typewriter. The Tutorial Input exchanges will be typed out at DSS 13 so that the station personnel will be aware of what is being commanded. A condensed form of the data will be sent to JPL as will various status and error messages. The primary data record will still be the magnetic tape recorded at DSS 13.

References

1. Lushbaugh, W. A., "A Driver/Receiver Unit for an Intercomputer Communications Link," in *The Deep Space Network Progress Report*, Technical Report 32-1526, Vol. XV, pp. 109–115, Jet Propulsion Laboratory, Pasadena, Calif., June 15, 1973.

2. Brokl, S. S., "Automated Pulsar Data Collector," in *The Deep Space Network Progress Report 42-25*, pp. 129–136, Jet Propulsion Laboratory, Pasadena, Calif., Feb. 15, 1975.

3. Zygielbaum, A. I., "'Tutorial Input'—Standardizing the Computer/Human Interface," in *The Deep Space Network Progress Report 42-23*, pp. 78–86, Jet Propulsion Laboratory, Pasadena, Calif., Oct. 15, 1974.

4. Moyd, K., "FORTRAN Implementation of Tutorial Input," in *The Deep Space Network Progress Report 42-24*, pp. 88–99, Jet Propulsion Laboratory, Pasadena, Calif., Dec. 15, 1974.

Appendix
GTS Tutorial Input Commands for DSS 13 Automation

I. Basic Parameter Entry

Command	*Parameter*	*Description*
OFFD		Change default offsets. New values will be used immediately.
	AZDF	Default azimuth offset in degrees. Initially: .145.
	ELDF	Default elevation offset in degrees. Initially: 0.
DIST		Change pointing parameters. The new values will not be used until a new antenna command is given. Values are to be entered in millidegrees (i.e., 10 degrees is entered as 10000).
	HSPD	Minimum azimuth pointing error for which high speed is to be used. Elevation value is half of azimuth value. Initially: 12000.
	DECL	Azimuth pointing error at which high-speed deceleration is started. Elevation value is half of azimuth value. Initially: 10000. (It is required that DECL < HSPD.)
	TRKD	Maximum pointing error (in each axis separately) for on-target condition to be satisfied. Initially: 50.
	TRKV	Maximum velocity error (in each axis separately) for on-target condition to be satisfied. Initially: 25.
PDCL		Change default pulsar data collector parameters. The new values will be used the next time parameters are sent to the data collector (i.e., following an OBJ, GO, TSYN, ENDO or EXP command).
	XDEF	Number of synthesiser pulses between observations. Initially: 200.
	YDEF	Number of observations per period. Initially: 5000.
DATE		Enter date. (Date is based on UT, not on local time.)
	MON	Month — up to 4 numbers or letters.
	DAY	Day of the month.
	YEAR	Year — 4 digits.

II. Antenna Commands

A. New Position

These are acted upon immediately if the previous antenna command was STOP, AZEL, or STOW; if the antenna was stopped by the computer for another reason (breakpoint 4 set and then reset, elevation too low); or when the program is first started. Otherwise they will be acted on after the current observation is finished and the data processed.

Command	*Parameter*	*Description*
AZEL		Move the antenna to the specified azimuth and elevation and hold it there. Do not collect data.
	AZ	Azimuth between 0 and 360 degrees with up to three decimal places. The decimal point must be typed.
	EL	Elevation in degrees with up to three decimal places. The decimal point must be typed.
	REGN	Wrap-up region. 'R' for right, 'L' for left. Anything else will be interpreted as center.
STOW		Move the antenna to the stow position (AZ = 180 degrees, EL = 85 degrees, center region) and hold it there.
OBJ		Move the antenna to the specified right ascension (RA) and declination (DEC) and track. When the antenna is on-target, initiate data collection with a start-next-second.
	ID	Pulsar identification number — up to 4 digits.
	RA	Hours of RA.
	RAM	Minutes of RA.
	RAS	Tenths of seconds of RA (i.e., 34.5 seconds is put in as 345).
	DEC	Degrees of DEC. Include sign if negative.
	DECM	Minutes of DEC, no sign.
	DECS	Seconds of DEC (2 digits), no sign.
	TMCN	Time constant setting for the pulsar receiver.

B. Other Control Commands

STOP	Stop the antenna (decelerate safely, put on the brakes, change to low speed). Ignore any data being taken. Acted upon immediately. To resume operation, one of the other antenna commands must be given.
GO	Resume observation of the object entered by the previous OBJ command. Used after the antenna has been stopped. Acted upon immediately unless breakpoint 4 is set.

III. Data Collection Commands

All of the commands except ENDO are acted upon only after the data from the current observation has been processed.

Command	*Parameter*	*Description*
LINK		Enable the 930 — 910A link.
NLNK		Disable the 930 — 910A link. (This is the initial condition.)
PLO		Entry of oscillator frequency. If the 930 — 910A link is enabled, the frequency will be sent to the local oscillator and the setting will be confirmed. The next observation will be a start-next-second.
	FREQ	Oscillator frequency in hertz. Up to 10 characters including the decimal point.
WAIT		Do not start the next observation until another command has been received. This allows the operator to see the data before specifying a new observation.
CONT		Initiate a start-in-phase-add after a WAIT command has been given.
TSYN		Initiate a start-next-second. (This is done automatically for the first observation after an OBJ, GO, PLO or ENDO command.)
ENDO		Abort the current observation and ignore the data. It is acted upon immediately if an observation is in progress. Otherwise it has no effect. If no other command is received, the next observation will be a start-next-second.
EXP		Subsequent observations are to be expanded. The parameters are based on the data taken as the result of the previous start-next-second command. These expansion parameters will be used until an antenna command, PLO, TSYN, ENDO or another EXP command is given.
	DEL	The original data point (between 0 and YDEF-1) corresponding to the 0th observation (i.e., origin) for the expanded observations. If DEL = 0, the origin is in phase with the second at which the original observation was taken.
	IINT	The number of *original* data points to be included in the expanded observations.
	IEXP	The expansion factor (number of observation points for each original observation). IEXP must be a factor of XDEF. IEXP × IINT $\leq$ 5000.

Table 1. Interrupts

	Level[a]	Interrupt
910 A		
	201	1 pps
	220	Link to 930 – data interrupt
	221	Link to 930 – status interrupt
910 B		
	200	50 pps
	205	Enter azimuth offset
	206	Enter elevation offset
	214	Clear azimuth offset
	215	Clear elevation offset
930		
	200	Link to 910 B – data interrupt
	201	Link to 910 B – status interrupt
	202	Link to 910 A – data interrupt
	203	Link to 910 A – status interrupt
	204	50 pps
	205	1 pps
	207	Data collector

[a]The lower the level, the higher the priority.

Table 2. Pulsar observations on March 20, 1975

ID number	Start time, UT	Number of observations
1929	17 51 24	27
0329	20 40 28	14
0628	22 20 59	7
0355	23 46 11	14
0823	01 01 03	16
0736	02 28 34	6
0833	03 21 45	8
0329	04 01 47	4
0833	04 38 25	4

Easy Complex Number Manipulation With MBASIC

C. A. Greenhall
DSN Systems Engineering Office

This article shows how to use MBASIC to manipulate complex scalars and matrices.

I. Introduction

The interpretive MBASIC language processor does not have complex data types in its present implementation at JPL on the Univac 1108 systems. Nevertheless, complex arithmetic can easily be simulated by using the MBASIC matrix handling ability. The method is fast because it uses the machine-coded matrix arithmetic subroutines of the processor; it is convenient because subscript bookkeeping is avoided. After a small amount of machinery has been set up, complex expressions can be written almost as if actual complex data types were being used. A disadvantage of the method is that 4 words of storage are needed for each complex number, rather than 2.

II. Scalars

The complex number system can be simulated by a class of 2 by 2 matrices. The identification is:

$$a + bi \quad \leftrightarrow \begin{bmatrix} a & -b \\ b & a \end{bmatrix}, \; a \text{ and } b \text{ real.}$$

Thus

$$1 \leftrightarrow \text{REU} = \begin{bmatrix} 1 & 0 \\ 0 & 1 \end{bmatrix} \quad \text{(real unit)},$$

$$\text{i} \leftrightarrow \text{IMU} = \begin{bmatrix} 0 & -1 \\ 1 & 0 \end{bmatrix} \quad \text{(imaginary unit)},$$

$$0 \leftrightarrow \text{ZERO} = \begin{bmatrix} 0 & 0 \\ 0 & 0 \end{bmatrix} .$$

If $z \leftrightarrow \text{Z}$ and $w \leftrightarrow W$, then $\overline{z} \leftrightarrow \text{TRN(Z)}$ and $z+w \leftrightarrow \text{Z}+W$. Also, $zw \leftrightarrow \text{Z*}W$, for if $z=a+ib$, $w=c+id$, then

$$zw = ac - bd + i(ad + bc),$$

$$\text{Z*}W = \begin{bmatrix} a & -b \\ b & a \end{bmatrix} \begin{bmatrix} c & -d \\ d & c \end{bmatrix}$$

$$= \begin{bmatrix} ac-bd & -ad-bc \\ ad+bc & ac-bd \end{bmatrix} .$$

If $z \neq 0$, then $1/z \leftrightarrow$ INV(Z), $w/z \leftrightarrow W$*INV(Z).

The squared magnitude $|z|^2$ can be obtained as a scalar real by calling DET(Z), or as a complex real by using:

$$Z^*TRN(Z) = \begin{bmatrix} |z|^2 & 0 \\ 0 & |z|^2 \end{bmatrix} .$$

Example: A digital filter has the z-transform transfer function

$$h(z) = 1 + \left(\frac{1-z}{2z-1}\right)^3 .$$

The following MBASIC program prints $|h(e^{i2\pi f})|^2$ vs f for $f = 0, 0.05, 0.1, \cdots, 0.5$ Hz:

```
>LIST
10 REAL REU(2,2)/IDN(2)/, IMU(2,2)/0,-1,1,0/,
  Z(2,2) H(2,2)

20 PRINT 'HZ','RESPONSE' \ HZ, DET(H) WHERE
  HZ=K/20, OMEGA=2*PI*HZ, Z=COSR(OMEGA)
  *REU + SINR(OMEGA)*IMU, H=REU + ((REU
  -Z)*INV(2*Z-REU))**3 FOR K=0 TO 10

>RUN
HZ              RESPONSE
 0                1
 .5E-01           1.0460479
 .1               1.1580165
 .15              1.087936
 .2               .92637333
 .25              .776
 .3               .66241923
 .35              .58356814
 .4               .53269148
 .45              .50431055
 .5               .49519892
>
```

III. Matrices

A powerful extension of the technique allows arithmetic with complex matrices without resorting to subscript manipulation. With the complex m-by-n matrix $A+iB$, associate the real partitioned $2m$ by $2n$ matrix

$$E = \begin{bmatrix} A & -B \\ B & A \end{bmatrix} ,$$

which can be constructed by a declaration:

```
>REAL M=2, N=3, A(M,N)/1,2,3,4,5,6/, B(M,N)/7,
  & 8,9,10,11,12/
>REAL E1(2*N,M)/TRN(A),TRN(-B)/,&
  E2(2*N,M)/TRN(B),TRN(A)/,&
  E(2*M,2*N)/TRN(E1),TRN(E2)/
>PRINT USING '(6(4%)/)': E
   1   2   3  -7  -8  -9
   4   5   6 -10 -11 -12
   7   8   9   1   2   3
  10  11  12   4   5   6
>
```

Similarly, A and B can be reconstructed from E:

```
>REAL ZERO(N,N), REPT(2*N,N)/IDN(N)/,&
   IMPT(2*N,N)/ZERO,-IDN(N)/
>REAL E3(M,2*N)/E/, A(M,N)/E3*REPT/,&
   B(M,N)/E3*IMPT/
>PRINT A:\\B:
 1  2  3  4  5  6
 7  8  9  10  11  12
>
```

Complex matrices can be added and multiplied (if conformable) by doing the operations on their E-matrices. In particular, a nonsingular n-by-n complex matrix can be inverted by using the function INV on its E-matrix.

We can also associate a complex n-vector $X+iY$ with the column vector

$$\begin{bmatrix} X \\ Y \end{bmatrix} .$$

Then the multiplication $(A+iB)(X+iY)$ can be executed by performing

$$\begin{bmatrix} A & -B \\ B & A \end{bmatrix} \begin{bmatrix} X \\ Y \end{bmatrix} = \begin{bmatrix} AX-BY \\ BX+AY \end{bmatrix}$$

Example. The following MBASIC program solves complex n-by-n linear systems $AX=B$. It is run with the example

$$A = \begin{bmatrix} 1 & i \\ 2-i & 1 \end{bmatrix} , \quad B = \begin{bmatrix} 1+i \\ 0 \end{bmatrix} .$$

```
>LIST
10 INPUT USING 'DIMENSION: #':N
20 REAL AR(N,N), AI(N,N), BR(N), BI(N)
30 PRINT 'INPUT REAL PART OF A, THEN IMAG-
   INARY PART'
40 INPUT AR,AI
50 PRINT 'INPUT REAL PART OF B, THEN IMAG-
   INARY PART'
60 INPUT BR,BI
70 REAL A1(2*N,N)/TRN(AR),TRN(-AI)/,
   A2(2*N,N)/TRN(AI),TRN(AR)/,
   A(2*N,2*N)/TRN(A1),TRN(A2)/,
   B(2*N)/BR,BI/, X(2*N)/INV(A)*B/
80 PRINT 'REAL PART OF SOLUTION' \ X(K); FOR
   K=1 TO N \\ 'IMAGINARY PART OF SOLU-
   TION' \ X(K); FOR K=N+1 TO 2*N

>RUN
DIMENSION: 2
INPUT REAL PART OF A, THEN IMAGINARY PART
?1,0,2,1
?0,1,-1,0
INPUT REAL PART OF B, THEN IMAGINARY PART
?1,0
?1,0
REAL PART OF SOLUTION
-.49999998    .5
IMAGINARY PART OF SOLUTION
  .49999999   -1.5
>
```

It is also possible, though perhaps not as convenient, to associate the m-by-n complex matrix $(a_{jk} + ib_{jk})$ with the real $2m$-by-$2n$ matrix

$$F = \begin{vmatrix} Z_{11} & \cdots & Z_{1n} \\ \vdots & & \\ Z_{m1} & & .Z_{mn} \end{vmatrix}$$

where Z_{jk} is the 2-by-2 matrix we were associating with the complex number $a_{jk} + ib_{jk}$. These F-matrices can be manipulated just like the E-matrices. One can go from one to the other by row and column permutations. In this connection, we mention that

$$\mathrm{DET}(E) = \mathrm{DET}(F) = |det\,(A+iB)|^2 \quad .$$

Is there a way to compute $\det(A+iB)$ in the same spirit?

R. J. Hanson showed that if $A+iB$ is Hermitian, then its E matrix has the same eigenvalues, with the multiplicities doubled (Ref. 1). L. W. Ehrlich (Ref. 2) showed that inversion of $A+iB$ with complex arithmetic can be carried out faster and more accurately than inversion of E with real arithmetic. Of course, if the complex inversion has to be coded step by step in the source language of an interpretive processor, it cannot compete in speed with real inversion of E by a machine-language subroutine.

References

1. Hanson, R. J., *Remarks on the Calculation of Eigenvalues and Eigenvectors for Complex Hermitian Matrices*, Technical Memorandum 205, Jet Propulsion Laboratory, Pasadena, Calif., October, 1968.

2. Ehrlich, L. W., "Complex matrix inversion versus real," *Communications of the ACM*, Vol. 13, pp. 561–62, 1970.

DSN Standard Practices for Software Implementation

D. C. Preska
TDA Planning Office

DSN Standard Practices for implementing software are being applied to all new computer programs and modifications to be transferred to DSN Operations. This article presents an overview of the DSN methodology and prescribed practices. The methodology is based on established good engineering practices combined with newer software technologies involving structured programming, top-down principles, and concurrent construction and documentation. The practices provide the DSN with a means of producing maintainable software which is correct, on schedule, and within cost limitations. The ultimate goal is to permit DSN engineers and managers to concentrate their efforts not on details of machines and languages but rather on the tracking and data acquisition problem to be solved.

I. Introduction

To more effectively produce software, elements of the DSN Programming System have been defined to allow refinement and application of new methods in an orderly manner. The ultimate goal is to permit DSN engineers and managers to concentrate their efforts not on details of machines and languages but rather on the tracking and data acquisition problem to be solved. The DSN Programming System includes (1) implementation methodology, (2) Standard Practices for applying adopted methods, (3) language and data base standards, and (4) implementation aids. In conjunction with the Programming System, a DSN Software Management Seminar with wide participation was established and several pilot software implementation projects were undertaken. This report presents an overview of the Standard Practices (Ref. 1) developed from both the methodology research and continuous input from the Software Management Seminar.

The prescribed methodology combines proven, well-established engineering practices with emerging techniques that are mathematically sound and have been demonstrated by many independent workers involved in software development. The elements of the methodology and the management practices involved in their application are discussed, followed by a set of brief statements

that sum up the essence of the Standard Practices for software implementation.

II. Methodology

The methodology used for implementing DSN operational software makes use of the theorems of structured programming and its consequent enabling of top-down construction of programs. Application of structured programming and top-down practices further allows design and documentation to be performed concurrently with the coding and correctness testing in orderly, hierarchical builds. These terms will be defined below. The elements of the methodology are:

(1) Principles of Structured Programming

(2) Top-Down Construction

(3) Concurrent Design and Documentation, Coding, and Testing

A. Principles of Structured Programming

Structured programming is a program organizing and implementing technique that involves the concept of representing the control logic of arbitrary computer programs with iterations of a limited set of primary program (or flowchart) structures. The objectives of structured programming are increased clarity, increased commonality (interchangeability/module-to-module, program-to-program, project-to-project), reduced complexity, and simplified maintenance. Also, structured programming allows the top-level main program control to be designed and documented while leaving the lower levels of detailed computational design to be rigorously designed later.

The Structured Programming Theorem states that any program, arbitrarily large and complex, can be expressed by primary structures that need include only the operations for performing (a) functional sequencing, (b) conditional branching, and (c) conditional iteration (looping). Application of the concept of iterating only a small number of standard structures results in a highly organized and structured representation of the design and subsequent code that is easy to implement, read, test, and understand. Coding of the design by using prescribed primary code structures is referred to as "structured coding" which typically also encompasses code indentation and line spacing to display the program flow and modularity clearly to persons reading the code.

The ease with which the primary structures can be translated into code depends upon the characteristics of the programming language. To facilitate this translation, the DSN intends to adopt the language MBASIC as its standard for nonreal-time programs. The main advantage to a DSN standard language, however, is the full portability of DSN applications programs from one machine to another.

Limiting the complexity of a flowchart enhances its clarity and readability. This can be achieved by using the "striped module" technique (Ref. 2) to indicate that further detail is provided elsewhere. Unstriped modules contain sufficient detail to be translated directly into code.

B. Top-Down Construction

The top-down approach involves the concept of stating the total problem in its operational environment and progressing in a systematic manner to greater levels of detail. This provides the capability for engineers and managers to fully understand the problem and to define a solution (a proposed program) based on this understanding. The early stages of this program-defining process are characterized by iteration and nearly parallel thought processes, of which most, ideally, should have been completed in advance of the formal implementation. An orderly, more serial process of program production or construction follows, and includes: final detail design, translation of this design to code, auditing and testing the code, and documentation of the design, code, and test processes. The top-down procedure for this construction process is referred to as *top-down construction.*

Top-down construction is especially adapted to structured programming because the Structure Theorem allows the top levels to be constructed first and then the lower levels to be detailed (unstriped) and constructed in an orderly and rigorous fashion. Specifically, in terms of detailing and flowcharting in preparation for construction, one starts with a single striped module (level zero). That module is analyzed and expanded into a flowchart with two or more modules. The structure of the flowchart must be either a prescribed structure or a permitted combination of prescribed structures where any or all of the modules may be striped. Each striped module at this point (level 1) is expanded into a flowchart in the same way. The modules which are not striped need not be expanded and this means that they can be directly translated into code without further design. This process is repeated at the next level and continued until there are no striped modules which have not been expanded. The expansion can be completed in some paths before it is completed or even started in others.

External interfaces are defined, negotiated, and implemented early, and then used in the subsequent develop-

ment. This minimizes the occurrence of possible serious program integration problems after the internal development has been completed. Also, the need for developing program "drivers" is reduced or eliminated. This progression of the implementation from the interfaces into the detailed program computations is consistent with the theory of computable functions, which requires that at any point of computation all elements needed to compute the next value have already been computed.

The top-down approach is also a valuable management tool, in that the resulting end-to-end overall definition of the proposed program and its component parts and structure provide program design guides and data needed for estimating the scope of the total job, for determining the nature of the work and needed resources, for planning and scheduling work through the various phases, and for managing and conducting design reviews.

C. Concurrent Design and Documentation, Coding, and Testing

Concurrent activities of design and documentation, along with coding and testing in *hierarchical builds* (module-by-module program expansions, each increasing in lower level detail) are enhanced by the use of structured programming and top-down practices. Timely documentation, resulting from use of these practices, provides ready access to current program detail and status. Management of the effort and provision for Quality Assurance are both facilitated. Potential problem areas can be identified early for timely action. Also, a large-scale separate documentation effort at the end of the project, with its attendant problems, is avoided.

In terms of coding and testing, any unstriped module can be coded as soon as the flowchart on which it appears has been completed and signed off. Moreover, the program can be run provided any striped modules are properly represented by modules of temporary code called *dummy stubs* (code which produces data values which are needed to run the rest of the program along other paths). The dummy stubs are intended to work for one or more special test cases. There is a correctness theorem in Structured Programming which says that if the part already coded is proven to be correct, then it will still be correct after the rest of the program is coded, and thus need not be checked again. The test cases verify, build-by-build, the correctness of the module when imbedded in higher builds of code by testing every module-connecting path and by performing other tests as needed to uncover, for example, errors in logic, computation, formatting, timing, recovery, and documentation. Correcting errors as they are introduced minimizes rework and avoids later serious impacts due to compounding of errors. It can therefore be expected that the total amount of testing (correctness and acceptance) will be greatly reduced, since, at completion of coding, there is no need to repeat extensive internal program (correctness) testing; the program *is* correct. Needed are only those tests (acceptance) that demonstrate to the user the program's responsiveness to requirements in its full operational environment.

Figure 1 represents the process followed in doing concurrent design and documentation, coding, and testing from the top down. The figure shows that the module design as documented must be approved before the module coding and correctness test design are begun, both of which must, in turn, be completed and checked before the correctness testing is performed. However, after design approval, the test is designed at the same time as the coding is being done. Testing, and approval of the results of the test and code audit, formally completes the build at this level. Symbols for scheduling as shown are provided for planning and monitoring the implementation progress within each build.

III. Management

The methodology enables effective application and management of the practices and concepts, and also enables effective team operations for large efforts.

The DSN software implementation process extends from an initial program justification activity through program transfer to operations and involves (1) planning and specifying requirements, (2) design definition, (3) design and production, (4) acceptance, and (5) operations and maintenance. Major milestones are defined mainly at the end of each phase of activity, above. Figure 2 presents an overview of a typical DSN software implementation sequence, and Figure 3 summarizes the DSN software management and implementation plan, as derived from Fig. 2. The figures are self-explanatory; however, further description of the management and implementation activities can be found in Ref. 1. Supporting DSN Standard Practices shown in Fig. 3 are being produced.

The implementation process using the prescribed methods is flexible and can accommodate both large and small efforts. For large efforts, an implementation team can be established, which is directed by a Cognizant Development Engineer (CDE) who is responsible for the implementation. The CDE is provided with functional support as shown in Fig. 4, such as (but not limited to): a Programming Secretariat for administrative assistance,

project communications, and data handling; Quality Assurance services; and technical specialist support as required, spanning the disciplines of design, coding, and test design, conduct, and evaluation. The functional tasks are independent but are not necessarily related on a one-to-one basis to team personnel. The Programming Secretariat maintains the project's development records, controls the completed code, and serves as the center of communications for the entire team. Specialists, as required, are functionally separated but work as a team on a module-by-module basis and provide needed expertise to the implementation, as well as providing, to a degree, "checks and balances" to the total process. Quality Assurance provides independent code auditing services to the team on a module-by-module basis. Reference 1 provides additional detail on these and other functional tasks involved, their interaction, and a functional task statement of responsibilities for each.

Smaller efforts may require that the functional tasks be spread among fewer available personnel, which tends to lessen both the independence of each task and the inherent self-checking of the implementation process. This can be partially compensated for during the design reviews, where independent views can be factored in. Also, as for large efforts, independent code auditing on a module-by-module basis is required, and provides some of the checking needed.

IV. Summary

The following brief statements summarize the baseline software implementation guidelines that are applicable to DSN operational programs. Further comments, explanations, and examples of their application can be found in Ref. 1. Figure 5 displays the Table of Contents of Ref. 1 to show the overall organization of information upon which these guidelines are based.

(1) *Adherence to DSN Software Standard Practices.* DSN Standard Practices governing software implementation and documentation are to be followed for all computer programs to be transferred to operations.

(2) *Adherence to Referenced Practices.* Referenced practices, standards, and requirements are considered to be part of the DSN Standard Practices and are to be followed as an extension of Item (1), above.

(3) MBASIC/*Standard Language for Nonreal-Time DSN Computer Programs.* It is the intent of the DSN to use MBASIC as the standard language for nonreal-time DSN computer programs.

(4) *Top-Down Concurrent Implementation.* Software will be implemented in a top-down manner to allow the design and documentation as well as coding of the program to progress concurrently with the generation of correctness test procedures and the correctness testing itself.

(5) *Use of Structured Programming Principles.* Only prescribed programming structures will be used for flowcharting the design and translating the design into computer code.

(6) *Modular Implementation.* By applying Items (4) and (5), modules will be implemented in hierarchical subordinating levels of detail. Each module will be limited in length and complexity to a single page-size (8 1/2 × 11-in. (22 × 28-cm)) flowchart by using the Striped Module technique of hierarchical expansion.

(7) *Implementation Team.* For sufficiently large projects, the Cognizant Development Engineer will establish and direct an implementation team that is supported by the following main functions:

(a) Programming Secretariat

(b) Quality Assurance

(c) Design, coding, test design, and testing specialties, as needed

(8) *Standard Project Milestones.* Standard project milestones will be used for technical and management planning and control of the software implementation.

(9) *Project Scheduling.* Schedules for meeting the project milestones will be established and periodically assessed by the Cognizant Development Engineer and controlled by the cognizant manager.

(10) *Project Reviews.* During the planning phase, dates will be set for all formal design reviews; the Cognizant Development Engineer will coordinate and conduct the reviews.

(11) *Project Documentation.* Documentation will be compiled concurrently with the implementation progress and will be available on a continuous basis for use and review.

(12) *Quality Assurance.* Quality Assurance (QA) will provide an independent check on DSN software quality.

Acknowledgment

The author is indebted to the members of the DSN Software Management Seminar, whose support emanated from JPL Organizations 15, 33, 39, 65, and 91, as well as from the DSN itself.

References

1. *Software Implementation Guidelines and Practices*, DSN Standard Practice 810-13, Aug. 15, 1975 (JPL internal document).
2. Tausworthe, R. C., *Standardized Development of Computer Software*, Jet Propulsion Laboratory, Pasadena, Calif. (in preparation).

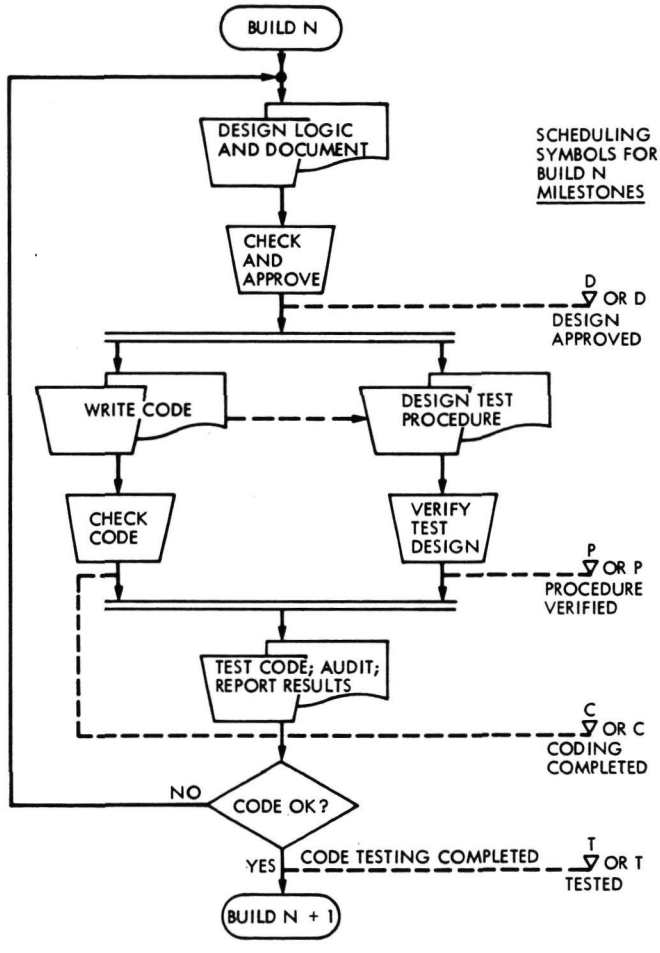

Fig. 1. Top-down, concurrent construction process for Build N

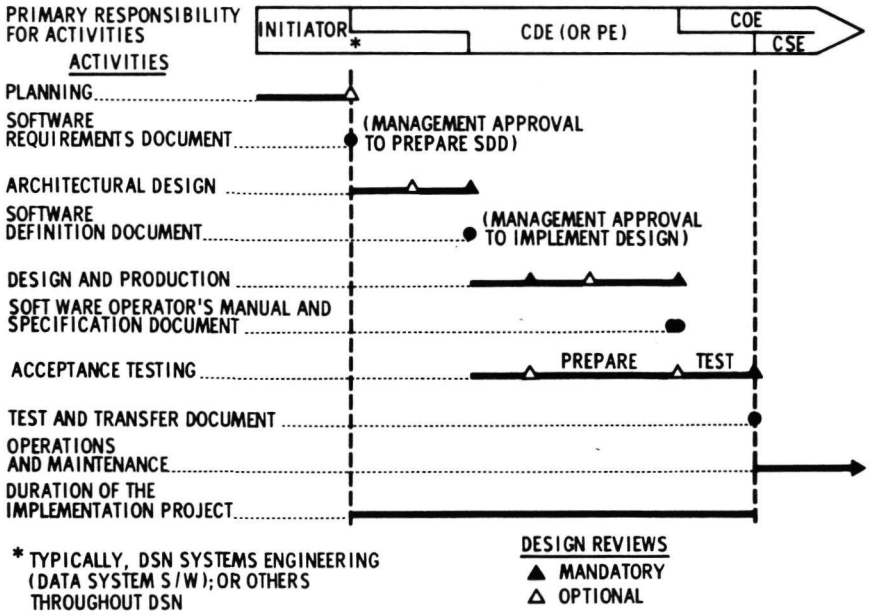

Fig. 2. Sequence of activities in a typical DSN software implementation project

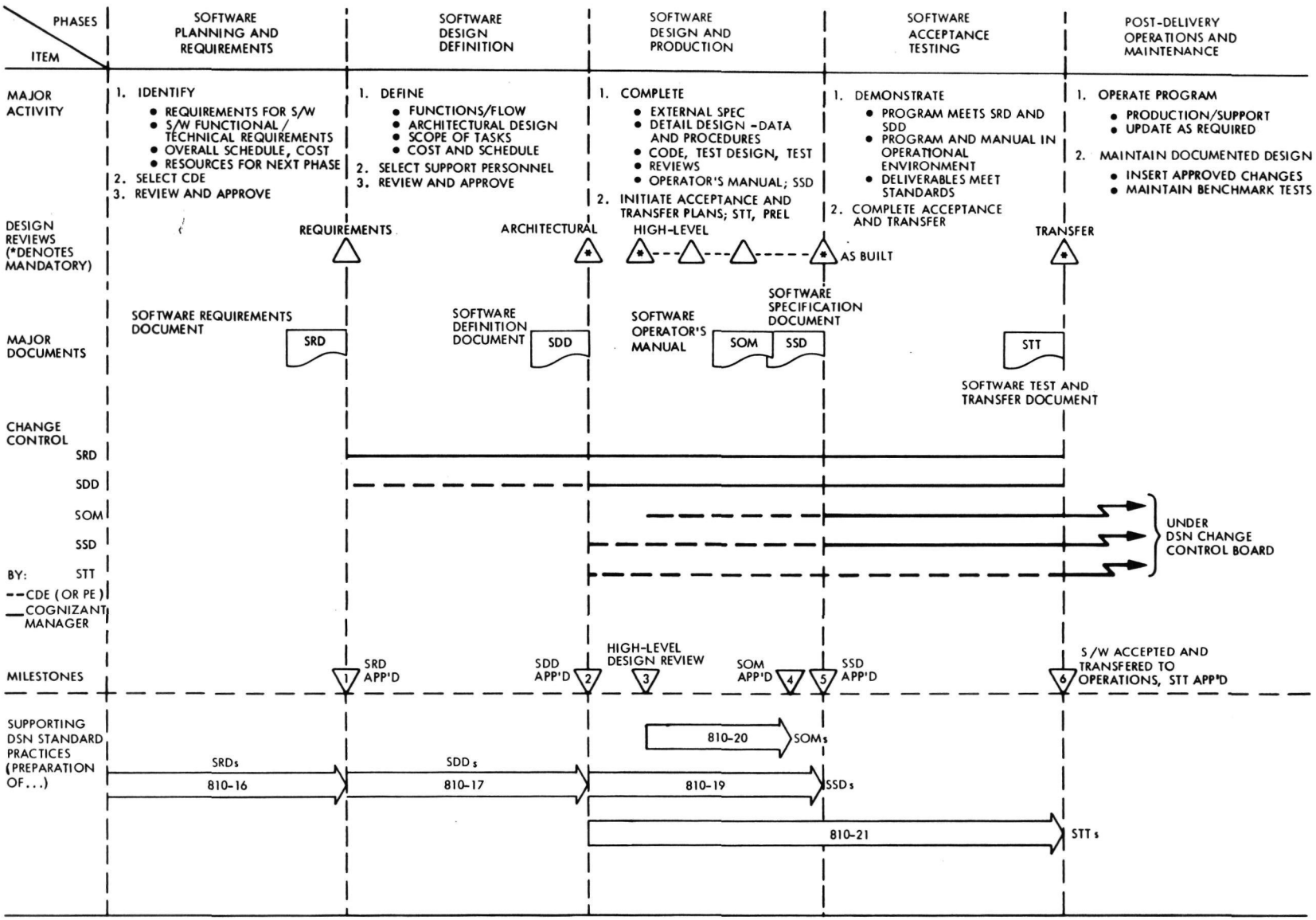

Fig. 3. DSN software management and implementation plan

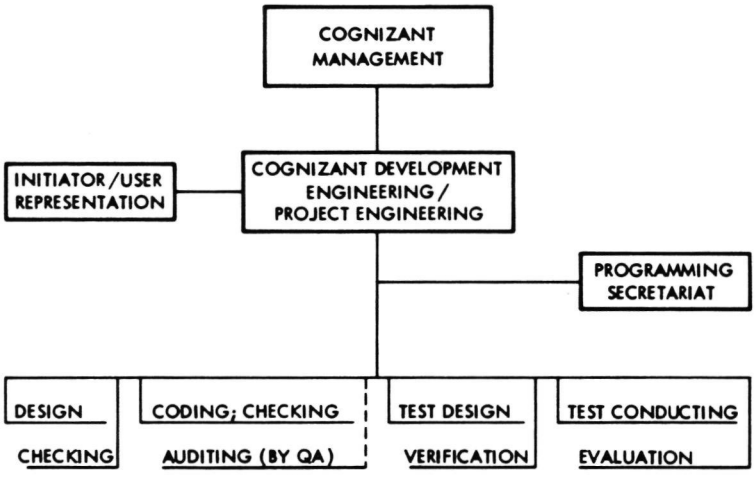

Fig. 4. Software implementation functional tasks

CONTENTS

Fig. 5. Contents of DSN Standard Practice 810-13, "Software Implementation Guidelines and Practices"

CONTENTS (cont'd)

Fig. 5 (contd)

CONTENTS (cont'd)

Fig. 5 (contd)

Receiver Stability

H. G. Nishimura and E. J. Serhal, Jr.
R. F. Systems Development Section

This article reports the results of phase stability investigation of the Dana Digiphase Synthesizer being used in the Block IV Receiver-Exciter Subsystem, with comparative data on the Hewlett-Packard Synthesizer used in the Block III Receiver-Exciter Subsystem. This is the first of a series of articles to verify that the stability of the Block IV Receiver-Exciter is adequate for very long baseline interferometry measurements.

I. Introduction

In the early stages of the Block IV Receiver-Exciter design (Ref. 1), primary consideration was given to developing a receiver with minimum variation in phase and group delays to obtain more accurate doppler and ranging data. To determine which portions of the receiver-exciter contributed the major portions of the phase and group delay variations, a series of tests was conducted on a Block III Receiver-Exciter. These tests indicated that the major contributors to phase and group delay variations are the oscillators, phase modulators, and frequency multipliers. In addition, these tests showed that these variations are primarily a function of changes in ambient temperature. In order to reduce the magnitude of the phase and group delay variations, the following designs are incorporated into the Block IV Receiver-Exciter:

(1) The doppler signal is extracted from the local oscillator at S- or X-band. In this configuration, the receiver phase loop compensates for any phase variation in the local oscillator chain, thus resulting in no phase error appearing in the doppler output due to these variations.

(2) Phase delay variations in the exciter frequency multipliers and transmitter are corrected by using a stable frequency multiplier chain to generate a reference signal and then using the reference signal to control the phase of the transmitter output.

(3) The range phase modulator is enclosed in an oven to minimize group delay variations of this temperature sensitive circuit.

(4) A Dana Digiphase Synthesizer is used in the exciter in order to reduce oscillator phase variations. Phase stability characteristics of this synthesizer are discussed in this article and also in Ref. 2.

With these designs, the Block IV Receiver-Exciter doppler and ranging stabilities have been significantly improved over the Block III design, easily complying with existing navigational requirements.

II. Receiver Stability Investigation

The Block IV Receiver-Exciter design emphasis was on phase and group delay stability for good doppler and ranging data in the closed-loop receiver configuration. With the proposed use of the Block IV Receivers in the open-loop configuration for interferometry measurements, the phase delay stability of the receiver's local oscillators now becomes as important as the phase and group delay stability of the rest of the receiver. The phase delay stability of these local oscillators as well as other portions of the receiver must be investigated to verify that the actual stability of the Block IV Receiver-Exciter is adequate for very long baseline interferometry (VLBI) measurements regardless of the fact that the present specification had been developed for doppler and ranging accuracy requirements. To determine this, an investigation of phase and group delay stability has been initiated. The first item under investigation is the Dana Digiphase Synthesizer being used as the oscillator in the receiver's first local oscillator. The results of this investigation are reported in this article together with similar data on the Hewlett-Packard (HP) Synthesizer used in the Block III Receiver-Exciter for comparison. These data were taken in three separate tests: the Dana Synthesizer, the HP Synthesizer, and a comparison of the two.

A. Test 1—Dana Digiphase Synthesizer (7010-S-241)

The Dana Synthesizer was tested by comparing its 50-MHz reference input against its output which was programmed at 50 MHz (see Fig. 1). The input reference and output were compared by using a Hewlett-Packard Vector Voltmeter 8405A in order to measure the phase variations in the Dana. The test was conducted for a period of 2 hours. The temperature during this 2-hour period varied approximately 1°C. The measured phase drift of the Dana was 0.13 degrees peak-to-peak per degree Celsius and varied directly with the temperature. The measured phase stability of the Dana unit was within the specified limit of ±0.1 degree per degree Celsius.

B. Test 2—Hewlett-Packard Synthesizer (HP5100A)

The Hewlett-Packard unit was also tested for a period of 2 hours in a similar manner (see Fig. 2). The HP unit again showed greater phase delay variations than the Dana Synthesizer as it did in earlier tests when the Dana was selected rather than the HP for the Block IV Receiver-Exciter. The measured phase delay variation was approximately 3.0 degrees of phase per degree Celsius; the phase delay also varied directly with temperature.

C. Test 3—Comparison of Dana and Hewlett-Packard

A third test was conducted by comparing a 45-MHz output of each unit for phase deviation (see Fig. 3). As expected, after a 2-hour test period, the total phase drift was approximately 3.0 degrees of phase per degree Celsius. The phase drift of the Dana Synthesizer is negligible when compared to that of the Hewlett-Packard unit. These data were consistent with previous data on the HP Synthesizer, as seen in Fig. 2.

The stability of the instrumentation, used during these tests, was checked to assure that the measured phase delay drifts were within the synthesizers themselves (see Fig. 4). The maximum peak-to-peak measured phase delay variation of the instrumentation was 0.05 degrees over a 2-hour period and over the same temperature range as in Tests 1, 2, and 3.

III. Conclusion

These synthesizer tests are the first of a series to determine the capability of the Block IV Receiver for VLBI measurements. The total effect of the synthesizer phase delay variations on the data accuracy must take into consideration the multipliers in the local oscillators. Table 1 lists the frequency multiplication factor for each receiver mode in the open-loop configuration and the effect the synthesizer phase delay variations would have on VLBI data due to the multiplication factor. As seen from Table 1, in the open-loop configuration, the Block IV Receiver has less phase delay variation due to synthesizer drift than the Block III by a factor of at least 23.

References

1. Donnelly, H., Shallbetter, A. C., and Weller, R. E., "Block IV Receiver-Exciter Development," in *The Deep Space Network*, Space Programs Summary 37-66, Vol. II, pp. 115–124, Jet Propulsion Laboratory, Pasadena, Calif., Nov. 30, 1970.

2. Wick, M. R., "DSN Programmed Oscillator Development," in *The Deep Space Network Progress Report*, Technical Report 32-1526, Vol. VIII, pp. 111–124, Jet Propulsion Laboratory, Pasadena, Calif., Apr. 15, 1972.

Table 1. Synthesizer phase delay variation contribution to data inaccuracy

Receiver (open-loop configuration)	Local oscillator frequency multiplier	Synthesizer phase delay variation/°C	Receiver phase delay variation/°C due to synthesizer
Block III			
S-band	48	3.0	144
X-band	176	3.0	528
Block IV			
S-band	40	0.13	5.2
X-band	170	0.13	22.1

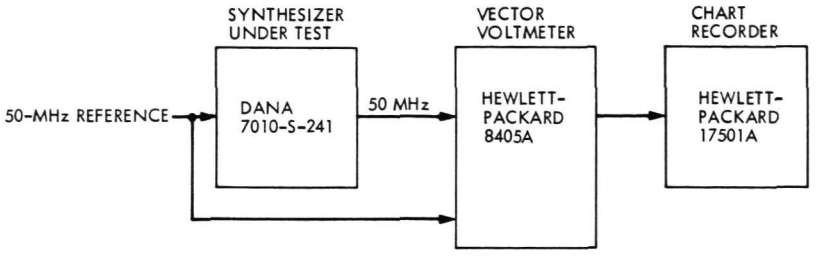

Fig. 1. Phase stability test: Dana Model 7010-S-241

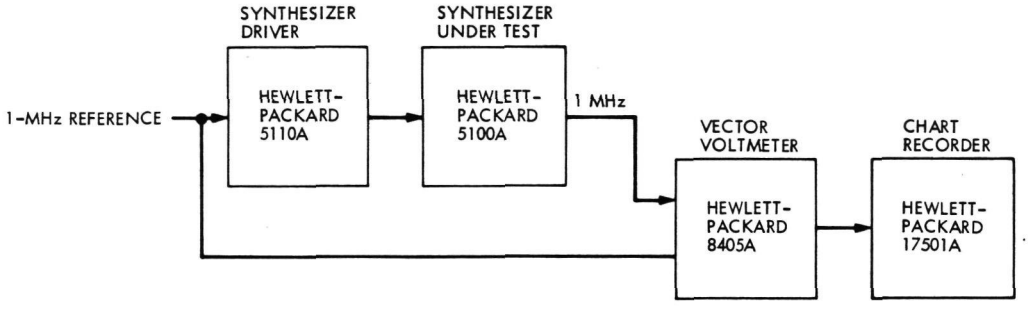

Fig. 2. Phase stability test: HP Model 5100A

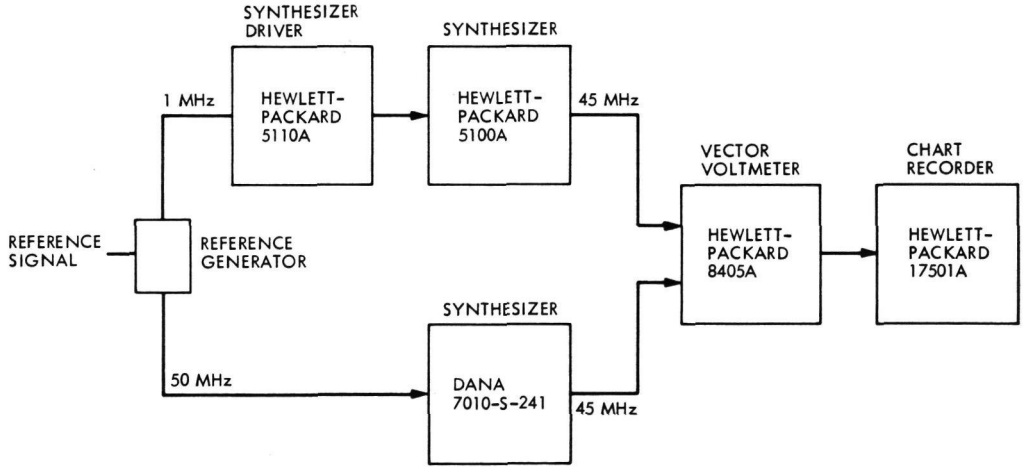

Fig. 3. Phase stability test: Dana vs HP

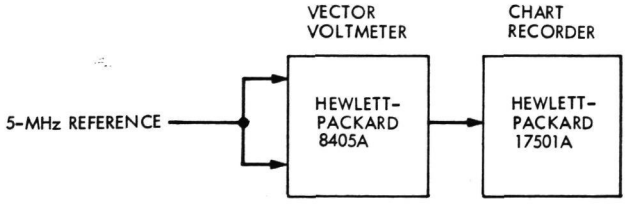

Fig. 4. Phase stability test: Instrumentation

Effect of Phase Distortion on Effective Signal Power—A Simple Mathematical Model

J. I. Molinder
DSN Systems Engineering Office/Harvey Mudd College

A simple mathematical model of the effect of phase distortion on effective signal power is developed. The model is used to determine the approximate degradation of a single-sideband downconverter used for recording the output of an open-loop receiver.

I. Introduction

Recording and playback of open- and closed-loop receiver data produces phase distortion due to additional signal processing both external and internal to the recorder itself. To record the output of an open-loop receiver, for example, a single-sideband (SSB) downconverter (or double-sideband downconverter and bandpass filter) is used to move the spectrum of the receiver output signal to a suitable offset frequency. The recording is then played back through an upconverter into a closed-loop receiver to recover the data. Closed-loop receiver baseband data, on the other hand, is recorded at the output of the video amplifier in the receiver telemetry string and then recovered by playing it back through the balanced modulator of the subcarrier demodulator assembly (SDA). In either case, phase nonlinearities of the signal processing system and recorder itself reduce the effective signal power. The purpose of this article is to develop a simple mathematical model of degradation due to phase distortion that will be useful in predicting system performance.

II. Analysis

The output signal of an open-loop or closed-loop receiver can be written as

$$v(t) = (2P_T)^{1/2} \cos\left[\omega_{os} t + \theta S(t)\, d(t)\right] \tag{1}$$

where

P_T = total power

$\omega_{os} = 2\pi f_{os}$ = offset frequency (f_{os} = 10 MHz for a closed-loop receiver)

θ = modulation index

$d(t) = \pm 1$ = data

$S(t) = \pm 1$ = square-wave subcarrier

Using phasors or trigonometric identities we may rewrite (1)

$$\underbrace{v(t) = (2P_T)^{1/2} \cos\theta \cos\omega_{os} t}_{\text{carrier}} - \underbrace{(2P_T)^{1/2} \sin\theta\, S(t)\, d(t) \sin\omega_{os} t}_{\text{sidebands}} \tag{2}$$

Since only the relative amplitudes of the sidebands will enter into the analysis, we need only consider the term (normalized to unity power)

$$f'(t) = \sqrt{2}\, S(t)\, d(t) \sin\omega_{os} t \tag{3}$$

Expanding the square-wave subcarrier $S(t)$ in a Fourier series and substituting into (3) yields

$$f'(t) = \sqrt{2}\, d(t) \left[\sum_{n=1}^{\infty} a_n \cos n\omega_{sc} t\right] \sin\omega_{os} t$$

where the reference is chosen so $S(t)$ is even,

$$a_n = \begin{cases} \dfrac{4}{\pi(2n-1)} & n \text{ odd} \\ 0 & n \text{ even} \end{cases} \tag{4}$$

and $\omega_{sc} = 2\pi f_{sc}$ = fundamental frequency of the square-wave subcarrier.

In any actual system, bandwidth limitations will limit the number of square-wave subcarrier harmonics. Thus the waveform of concern is

$$f(t) = \sqrt{2}\, d(t) \left[\sum_{n=1}^{N} a_n \cos n\omega_{sc} t\right] \sin\omega_{os} t \tag{5}$$

Expanding (5) yields

$$f(t) = \frac{d(t)}{\sqrt{2}} \sum_{n=1}^{N} \underbrace{[a_n \sin(\omega_{os} + n\omega_{sc})t}_{n\text{th upper sideband}} + \underbrace{a_n \sin(\omega_{os} - n\omega_{sc})t]}_{n\text{th lower sideband}} \tag{6}$$

Consider the nth upper sideband

$$nSB = \frac{d(t)\, a_n}{\sqrt{2}} \sin(\omega_{os} + n\omega_{sc})t$$

and suppose that it is shifted in phase by θ_n^U due to the signal processing system. If the data $d(t)$ is at a low frequency, the spectrum it produces about $\omega_{os} + n\omega_{sc}$ will be narrow band. This means that the spectral components of $d(t)$ are all shifted in phase by approximately θ_n^U. Thus, after the phase shift, the nth upper sideband may be expressed as

$$nSB' = \frac{d(t)\, a_n}{\sqrt{2}} \sin[(\omega_{os} + n\omega_{sc})t + \theta_n^U]$$

Following this procedure for each sideband of (6) yields

$$f''(t) = \frac{d(t)}{\sqrt{2}} \sum_{n=1}^{N} \{a_n \sin[(\omega_{os} + n\omega_{sc})t + \theta_n^U] + a_n \sin[(\omega_{os} - n\omega_{sc})t + \theta_n^L]\} \tag{7}$$

Now suppose a perfect carrier and subcarrier reference (with the exception of the θ_n^U and θ_n^L) is available. Multiplying (7) by a unity power carrier and passing the result through a low-pass filter yields

$$[f''(t)\sqrt{2}\sin\omega_{os} t]_{L.P.} = \frac{d(t)}{2} \sum_{n=1}^{N} [a_n \cos(n\omega_{sc} t + \theta_n^U) + a_n \cos(n\omega_{sc} t - \theta_n^L)] \tag{8}$$

Multiplying by a perfect square-wave subcarrier, then multiplying the result by $d(t)$ and averaging over a symbol time of $d(t)$ yields the effective power available (relative to unity)

$$S = \frac{1}{4} \sum_{n=1}^{N} \{a_n^2 \cos\theta_n^U + a_n^2 \cos\theta_n^L\} \tag{9}$$

Note that θ_n^U and θ_n^L are thus considered deviations of the phase of the nth upper and lower sidebands, respectively, from a linear relationship (discussed further in the example of the next section) centered at ω_{os}. Any linear phase shift would contribute only a time delay and would be taken care of by shifting the phase of the reference square-wave subcarrier. If $\theta_n^U = \theta_n^L = 0$ for $n = 1, \cdots, N$, (9) reduces to

$$S = \frac{1}{2} \sum_{n=1}^{N} a_n^2 \tag{10}$$

which is of course the relative power available if all subcarrier sidebands above the Nth are completely filtered out.

The degradation of signal power in dB is given by

$$\rho = 10 \log_{10} S \tag{11}$$

III. Example—Single-Sideband Downconverter Loss Due to Phase Shift

A plot of phase shift vs frequency for a single-sideband downconverter used for open-loop receiver recording is shown in Fig. 1. Suppose system filtering limits the subcarrier harmonics to 5 with a subcarrier fundamental $f_{sc} = 32.8$ kHz and a data rate of 64 symbols/sec. Consider an offset frequency $f_{os} = \omega_{os}/2\pi$ of 174 kHz. A straight line must be drawn intersecting the curve at this frequency to form the reference for measurement of θ_n^U and θ_n^L, $n = 1, \cdots, N$. The line should be drawn to correspond to the delay introduced by the subcarrier demodulator assembly subcarrier tracking loop. Since this delay will vary in a complicated way depending on the specific phase distortion, only an approximate lower bound to the degradation in signal power will be attempted. This can be done by adjusting the slope of the line intersecting the curve at f_{os} until the degradation appears to be minimized. The values of θ_n^U and θ_n^U for $n = 1, 3, 5$ (even harmonics are absent anyway) are given in Table 1, using straight line references A, B, and C.

Substituting the values of Table 1 into (9) yields

$$\begin{aligned} \rho_A &= -0.48 \text{ dB} \\ \rho_B &= -0.45 \text{ dB} \\ \rho_C &= -0.45 \text{ dB} \end{aligned} \tag{12}$$

where ρ_A is the degradation using reference line A, etc. Actual measurements at CTA 21 yielded a downconverter/upconverter degradation of 0.7 dB.

Acknowledgment

The author is indebted to S. Kent for the general approach used in this analysis as well as for numerous extremely helpful discussions.

Table 1. θ_n^L and θ_n^U for $n = 1, 3, 5$ for reference lines A, B, and C of Fig. 1

	A, deg	B, deg	C, deg
θ_5^L	138	124	97
θ_3^L	32	24	8
θ_1^L	6	3	−3
θ_1^U	0	44	8
θ_3^U	−2	8	24
θ_5^U	2	17	44

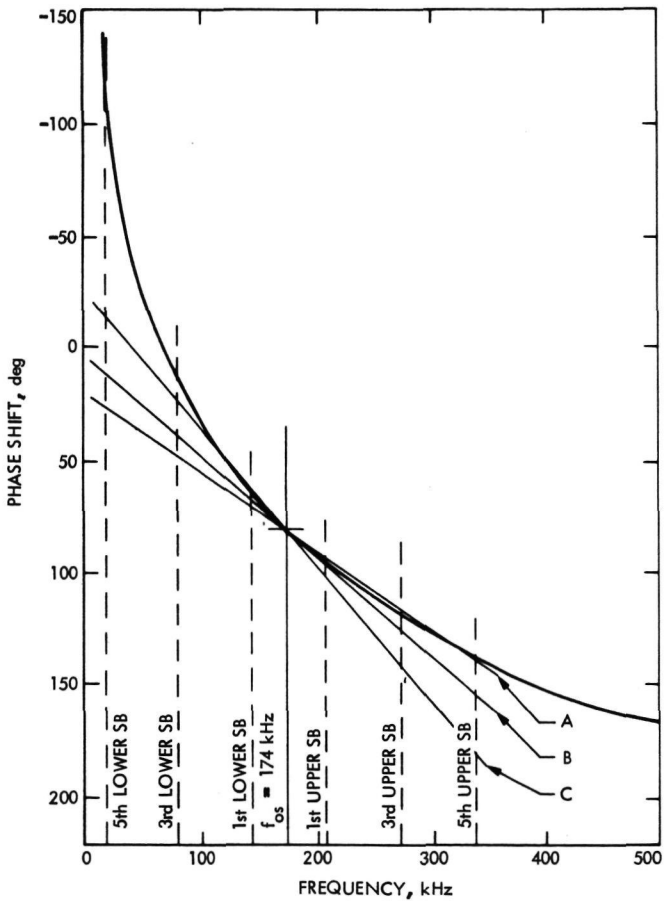

Fig. 1. Single-sideband downconverter phase response

Goldstone Wind Speeds for the SENSMOD Program

R. Levy
DSN Engineering Section

G. Lorden
California Institute of Technology

Sample months of hourly wind speeds, constructed from two years of observed data in combination with adjustments to reflect a longer data base, are generated for the Goldstone Mars antenna site. The adjustments are determined using a 14-year data base that is available for another site and determining the correlation at the two sites for contemporary periods of observation.

I. Introduction

This paper describes the data analysis and estimation procedures used to establish sample annual records of Goldstone hourly average wind speeds (24 × 365 records per year) from a data base assembled from Goldstone Deep Space Communications Complex and Edwards Air Force Base records. These wind speed records are established to provide input for the SENSMOD[1] energy analysis program (Ref. 1), which is being developed as part of the Goldstone Energy System Project.

The objective is to determine 12 probability distributions of wind speeds, one for each calendar month. The developed distribution for any particular month is to be a representation of the historical speed distribution for that month at the Goldstone site. Samples (including stratified random samples with reduced variance) can then be generated from these 12 distributions to yield independent measurements on an hourly basis and combined to yield "sample years" of wind speed data. No requirement was imposed to model the correlations of successive hourly measurements, which would have imposed a substantial additional program. Consequently, with the present simplification, the distributions of wind speeds are not representative of time intervals shorter than one-month duration.

The form of the distribution function of wind speeds for a given month was assumed to be

$$Prob(Speed \leq s) = F(s) = 1 - \exp\left[-(as + bs^2)\right] \quad \text{for } s \geq 0 \tag{1}$$

where a and b are positive parameters characteristic of the month. Thus, for the ith month ($i = 1, \cdots, 12$), two

parameters, a_i and b_i, are to be determined. This form of distribution has been found to provide good fits for the available data sets.

The data base consisted of the following three groups of wind speed records:

Set	Location	Anemometer height, ft	Period of record, yr/mo to yr/mo	No. of entries
A	Goldstone, Mars site	150	66/11–68/10	9100
B	Edwards AFB	13	66/11–68/10	17,500
C	Edwards AFB	13	57/1 –70/12	122,700

The Goldstone data consisted of average wind speeds for 5-min periods. The sampling rate was hourly except for December 1966 through August 1967, when the rate was 1 every 3 hours. Considering the number of observations that could have been made at these two sampling rates during the entire period, it has been found that about 25% of the data is missing. Sets B and C (Edwards data) were extracted from United States Weather Bureau archive tapes (by Meteorology Research Corporation at our request) and are complete sets of hourly records with no entries missing. Set B is actually a subset of C and was assembled for comparison with contemporary Goldstone data.

Since the actual data for Goldstone, set A, covers a period of less than two years, it is not necessarily a reliable basis for the desired probability models. As a means of assuring that the models represent long-term Goldstone phenomena, the following steps were taken, incorporating data sets B and C into the analysis:

(1) Using a chi-square criterion for goodness of fit, 12 sets (a_i, b_i) of monthly parameters were chosen based on the A data.

(2) Using data sets A and B, the degree of correlation between monthly wind power (= speed^3) at Goldstone and Edwards was estimated.

(3) Based on the results of step 2, the long-term data set C from Edwards was used together with A and B to obtain "corrections" of the parameter values found in step 1, the corrected values being designed to incorporate the long-term information provided by set C.

II. Computation Methods

A. Procedure 1 — Generation of Sample from the Distribution of Eq. (1)

A simulated monthly sample of wind speeds s, sample size N (1 per hour), can be constructed from a given distribution by drawing

$$u_i = \text{uniform } (0,1)$$

$$i = 1,2,\cdots,N \qquad (28 \times 24 \leq N \leq 31 \times 24)$$

and letting

$$s_i = F^{-1}(u_i)$$

where F^{-1} is the inverse distribution function. Using the inverse function of Eq. (1) will provide

$$s_i = \frac{(a^2 - 4bc)^{1/2} - a}{2b}$$

where

$$c = \ln(u_i)$$

If desired, variance of the samples so constructed can be reduced by dividing the range (0,1) into p strata and drawing N/p uniform numbers for each stratum, then finding the inverse functions of these numbers as before. The variance of the sample can be made to approach zero by letting p approach N. When p equals N, the sample is no longer a random simulation, but instead tends to replicate the generating distribution. Note that when stratified, the samples will occur as p ordered clusters of N/p numbers. This ordering can readily be removed later by random scrambling of the sample.

B. Procedure 2 — Long-Term Distribution Function Parameters (Steps 1–3, Section I)

1. Step 1. Prior to the present requirement, field data from Goldstone and other weather stations had been processed by a moderate-size computer program WINDMAPW. This consisted of about 1000 source card images plus references to several JPL 1108 FORTRAN V library and IMSL library subroutines for analysis and plotting. After reading the field data from tapes or files, one of the operations of the program was to fit Pearson and Weibull distributions to the data. For the current requirement, the Weibull fit was dropped and fitting methods for the function of Eq. (1), as will be described, were substituted. With these changes, this version of the

program was renamed WINDMAPW. The program currently resides in a catalogued file (52219RIL) on the 1108A computer.

Fitting parameters to empirical data was performed in two substeps. A preliminary regression analysis step was executed to provide class boundaries and starting points for a final chi-square calculation step.

a. Preliminary regression estimate for parameters a and b of a sample. By taking the logarithm of both sides of Eq. (1) and rearranging, we have

$$(a + bs) = -\frac{\ln[1 - F(s)]}{s}$$

Then let $Y_i = a + bs_i$ be the model equation for regression analysis of Y on s, and let

$$\frac{-\ln[1 - F(s_i)]}{s_i}$$

be the observed values of Y_i, where $F(s_i)$ is the empirical distribution function of S.

The regression is performed in a subroutine FITEXP. The input to this subroutine is

(1) Sample = $S(I), I = 1,NT$
where NT = total number of terms in sample and S has been sorted in ascending order.

(2) $XMIN$, $XMAX$, = lower and upper threshold speeds that bound the speed region of interest. The values used were 8 and 40 km/h (5 and 25 mi/h) based on typical low-speed threshold and high-speed generator capacity level, respectively.

This subroutine performs the following operations:

(1) Find $IBOT$, $ITOP$, indices of S such that

$$S(IBOT) \geq XMIN$$

$$S(ITOP) \leq XMAX$$

(2) Perform regression on $S(I)$ ($IBOT \leq I \leq ITOP$), using the following algorithm:

(a) $FX = I/(NT + 1)$ = empirical distribution

(b) $X = S(I)$

(c) $Y = -\ln(1 - FX)/X$

(d) $SY = \Sigma Y$

$$SX = \Sigma X$$

$$SXY = \Sigma XY$$

$$SXX = \Sigma X^2$$

Then:

$$NET = ITOP - IBOT + 1$$

$$\text{DET} = NET*SXX - SX*SX$$

The resulting initial estimates for a and b are:

$$a = (SXX*SY - SX*SXY)/DET$$

$$b = (NET*SXY - SX*SY)/DET$$

b. Final chi-square calculation estimate for parameters a, b *of a sample.* Divide the speed range between $XMIN$ and $XMAX$ into 8 interior classes and add one class at the low end to include all speeds below $XMIN$ and one class at the high end to include all speeds above $XMAX$.

Let 0_i = observed number of speeds in class "i" (from the empirical sample)

E_i = expected number in class "i"

Let B_i = lower speed class boundary for class "i"; then

$$E_i = NT * [F(B_i + 1) - F(B_i)]$$

where F(.) is found by evaluating Eq. (1) using the current estimates of a and b.

$$\text{Let } FUNCT(a,b) = \Sigma (0_i - E_i)^2/E_i$$

$$i = 1, 2, \cdots, 10 \qquad (2)$$

The estimate of a and b is made by choosing a, b to minimize the function in Eq. (2).

The operations are performed by subroutines FITEXP and CHIPAM.

FITEXP

(1) After regression has been performed to obtain the preliminary estimate of a, b, classes are set up for the calculation of $FUNCT$ (Eq. 2) as follows:
Let NCHI = number of interior classes between $XMAX$ and $XMIN$ (typically 8). Using Eq. (1) compute the difference in distribution function between $XMAX$ and $XMIN$. This difference is divided into $NCHI$ parts, each part representing an equal probability of occurrence. Beginning with

$F(XMIN)$ and adding these part differences successively is equivalent to evaluating the current distribution function at the interior class boundaries. Consequently, evaluation of the inverse distribution function (see Eq. 1) furnishes the class boundaries. At this point, these classes have been established so that $E_i = E_j$ for all the i, j interior classes. However, as the estimates of a and b change from minimization of Eq. (2), the equality is not maintained because class boundaries are not recomputed.

(2) The number of terms in each of these classes is computed (0_i)

(3) Calls subroutine CHIPAM.

CHIPAM

CHIPAM calls a JPL library subroutine to perform a conjugate direction search to find a and b that minimize Eq. (2). The search is performed by means of many (50 to 100) evaluations of the function in Eq. (2). At each evaluation, the E_i are computed using the current values of a and b. The search terminates based upon tolerance tests of 1×10^{-3} for a, 1×10^{-4} for b, and 1×10^{-3} on the function. This last tolerance is equivalent to a very small fraction of the actual function (one part in 10,000 to 70,000).

As a comment on the method of obtaining the final chi-square estimate of the parameters, we find no great changes from the preliminary parameters or function values obtained by regression.

2. Step 2. The correlation between data sets A and B was analyzed in terms of wind power P_f, defined as a summation of $\min[S,25]^3$ ($=\min[S^3,25^3]$), where S = wind speed in miles per hour. The computational equation is included in Table 1, and the computed values of P_f for each monthly record in sets A and B are given in columns 1 and 4 of Table 1 (Goldstone) and column 5 of Table 2 (Edwards). It is assumed that the true correlation ρ between total power at Goldstone and Edwards in contemporary months is chronologically invariant. It is also assumed that the pair (Goldstone monthly power, Edwards monthly power) has a specific distribution for each calendar month, so that for any specified month the result for any given year is an independent sample from this distribution. It follows from these assumptions that ρ is also the (true) correlation of the pairs of differences, which are defined as follows:

$$(G_{1i} - G_{2i}, E_{1i} - E_{2i}), i = 1, \cdots, 12$$

where G_{1i} and G_{2i} represent Goldstone power in the ith month of year 1 and year 2, respectively, and E_{1i} and E_{2i} are defined correspondingly for Edwards. Because of missing September and October data at Goldstone, Tables 1 and 2 provide only 10 values of i where data from two years are available. These were used to estimate ρ by computation of the sample correlation coefficient of these 10 pairs, yielding the estimate:

$$\hat{\rho} = 0.486$$

This correlation coefficient appears to be sufficiently large to confirm that the approach outlined is reasonable; e.g., there is a statistical connection between the random deviations from monthly norms at the two locations, Goldstone and Edwards.

For the analysis that will be described in step 3 below, it is necessary also to estimate the ratio of the standard deviations of G_i and E_i, which are the monthly powers for the ith month. This ratio is assumed to be independent of i and was estimated by the ratio of the two sample standard deviations that are determined for the 10 values of $G_{1i} - G_{2i}$ and for the 10 values of $E_{1i} - E_{2i}$. The result was the estimate

$$\hat{R} = \sigma_G/\sigma_E = 953/664 = 1.44$$

3. Step 3. To determine "corrected" (a_i, b_i) pairs, it is necessary first to utilize the correlation information in a rational way. The approach adopted was the following:

(1) Estimate the long-term average of the Goldstone total power for the ith month, for $i = 1, \cdots, 12$.

(2) Use the results of (1) to correct the values of a_i and b_i obtained by the chi-square fit in step 1.

To obtain the long-term Goldstone power for $i = 1, \cdots, 12$ let

g_i = true mean total power for the ith month (Goldstone)

A_i = average of G_{1i} and G_{2i} (data set A, Table 1, Col. 4)

B_i = average of E_{1i} and E_{2i} (data set B, Table 2, Col. 6)

C_i = average of $E_{1i}, \cdots, E_{14i}$ (data set C, 14 years, Table 2, Col. 7)

(For September and October, A_i and B_i were based on only one months' record, not two.)

The estimate used for g_i was

$$\hat{g}_i = A_i + \hat{\rho}\hat{R}(C_i - B_i) \quad (3)$$

The values of A_i, B_i, C_i and g_i are shown in columns 4, 2, 3, and 5, respectively, in Table 3. By the results of step 2,

$$\hat{\rho}\hat{R} = 0.486 \times 1.44 = 0.7$$

Equation (3) defines the appropriate "least weighted squares" estimator of g_i in terms of the available data, A_i, B_i, and C_i, as shown in the Appendix. This interpretation depends on the correlation ρ and the standard deviation ratio R being *known*. Using estimates instead, as we have done, is natural and reasonable. More exact analysis is not feasible without knowledge of the form of the joint density functions describing wind at Goldstone and Edwards.

Note that the effect of Eq. (3) is to correct the direct estimate A_i of Goldstone wind power by adjusting for the difference between Edwards short-term power in the contemporary period and long-term power. For example, January data at Edwards (Table 2) shows B_i slightly less than C_i (i.e., $1045 < 1101$), indicating that the short-term wind was slightly below the long-term average and suggesting a positive correction (increase) in the estimate of Goldstone wind power for January. Columns 4 and 5 of Table 3 show the estimated power before (2856) and after (2895) the correction was applied.

Having the estimates g_i of Goldstone wind power for the long term, it is necessary now to use these to correct the a_i and b_i previously obtained. To clarify the method, it is helpful to rewrite Eq. (1) in the form

$$F(s) = 1\text{-}exp\left\{-d\left[\frac{s}{c} + \left(\frac{s}{c}\right)^2\right]\right\}$$

where $c = a/b$ and $d = a^2/b$. Written this way, the family of distribution functions is seen to have a "scale factor" parameter c and a "shape" parameter d. For example, doubling all the wind speeds has the effect of doubling c, leaving d unchanged. On the other hand, if c is held fixed while d is changed, the "shape" changes. The shape effect is that, for very large d, the distribution is close to an exponential distribution, whereas for smaller d, it has thinner tails that are more like those of a normal distribution.

The choice of a distribution to represent the ith month at Goldstone was made as follows: Let $d_i = a_i^2/b_i$ (estimated in step 1) and determine c_i so that the average total power agrees with the value g_i estimated in (1). Thus, a model is chosen which predicts total power in accord with the estimate previously derived and, among all sets of parameters satisfying this restriction, the choice is made to yield the same "shape" as was estimated directly in step 1.

Letting a_i^* and b_i^* denote the parameters of the final distribution chosen for the ith month,

$$a_i^* = a_i/c_i$$

$$b_i^* = b_i/c_i^2,$$

which are shown in columns 7 and 8 of Table 3. The values of the c_i's are shown in column 6. Note that most of the c_i's are close to 1, indicating that the corrections made are small and that the short-term Goldstone data are, on the evidence of sets A, B, and C, likely to be representative of the long-term wind parameters at Goldstone.

Figure 1 shows a diagrammatic summary of the logic underlying the generation of the wind speed samples.

Table 1. Fitting parameters and power terms

Month	From observations on individual months				From data pools within corresponding months				Average
	Year	a	b	P_f	Year	a	b	P_f	P_f
Jan	67	0.019700	0.000268	3695	67, 68	0.08927	0.000765	2570	2856
	68	0.085847	0.001345	2017					
Feb	67	0.028782	0.002222	3028	67, 68	0.100611	0.002506	1476	2111
	68	0.109335	0.002781	1194					
Mar	67	0.013132	0.002406	5230	67, 68	0.048574	0.001700	3872	4258
	68	0.047229	0.00133	3285					
Apr	67	0.007951	0.003035	5347	67, 68	0.025546	0.002326	4530	4801
	68	0.030524	0.002258	4255					
May	67	0.021088	0.002853	3966	67, 68	0.034341	0.002600	3722	3782
	68	0.044651	0.003081	3598					
Jun	67	0.026241	0.003175	2986	67, 68	0.023422	0.003705	3248	3158
	68	0.022351	0.004697	3329					
Jul	67	0.000001	0.006994	2097	67, 68	0.003654	0.006917	1907	1928
	68	0.004859	0.006800	1758					
Aug	67	0.058394	0.005100	1475	67, 68	0.043111	0.004707	1981	1875
	68	0.030681	0.005051	2275					
Sep	68	0.070572	0.003518	1681					1681
Oct	68	0.144353	0.000544	1088					1088
Nov	66	0.076671	0.000677	2265	66, 67	0.102385	0.001346	1933	1803
	67	0.132794	0.000640	1341					
Dec	66	0.106911	0.000412	3090	66, 67	0.074673	0.000618	3489	3365
	67	0.068373	0.000811	3631					
				•		•	•		•
				(1)		(2)	(3)		(4)

•Indicates that data in the column above was used in either correlation coefficient computation or in long-term Goldstone projection.

$$P_f = \int min(S^3, 25^3) p(s) ds \simeq \sum min(C_i^3, 25^3)\ p(C_i)\ \Delta C$$

where

C_i = class mark

ΔC = class interval (1 mph)

Table 2. Edwards AFB data

Month	Year	P_f	Power terms			
			Year	Average P_f	Year	Pooled P_f
Jan	67	1021	67, 68	1045	57–70	1101
	68	1070				
Feb	67	728	67, 68	1018		1477
	68	1308				
Mar	67	2679	67, 68	2325		2453
	68	1971				
Apr	67	2831	67, 68	2792		2814
	68	2754				
May	67	2580	67, 68	3124		3377
	68	3665				
Jun	67	2660	67, 68	3064		3179
	68	3467				
Jul	67	1547	67, 68	2058		2061
	68	2568				
Aug	67	958	67, 68	1584		1724
	68	2211				
Sep	68	1532				1464
Oct	68	1225				1211
Nov	66	894	66, 67	750		1088
	67	605				
Dec	66	1624	66, 67	1428		960
	67	1232				
		•		•		•
		(5)		(6)		(7)

•See Table 1 note.

Table 3. Goldstone long-term projected parameters

	P_f = power term				Speed factor	Long-term parameters	
	Edwards		Goldstone				
①	② 66–68	③ 57–70	④ 66–68	⑤ Projected	⑥ c	⑦ a	⑧ b
Jan	1045	1101	2856	2895	1.0575	0.08442	0.00068
Feb	1018	1477	2111	2432	1.2581	0.07997	0.00158
Mar	2325	2453	4258	4348	1.0776	0.04506	0.00146
Apr	2792	2814	4801	4817	1.0220	0.02500	0.00223
May	3124	3377	3782	3959	1.0303	0.03333	0.00245
Jun	3064	3179	3158	3239	0.9911	0.02363	0.00377
Jul	2058	2061	1928	1930	0.9650	0.00379	0.00743
Aug	1584	1724	1875	1973	1.00045	0.04339	0.00470
Sep	1538*	1464	1681	1633	0.9711	0.01267	0.00373
Oct	1225*	1211	1088	1078	0.9448	0.15278	0.00061
Nov	750	1088	1803	2404	1.1364	0.09010	0.00104
Dec	1428	960	3365	3037	0.9251	0.08072	0.00072
	Reference						
	Table 2 (6)	Table 2 (7)	Table 1 (4)	④ + 0.7 [③ − ②]	From computer search	$1/c \times$ (2), Table 1	$(1/c)^2 \times$ (3), Table 1

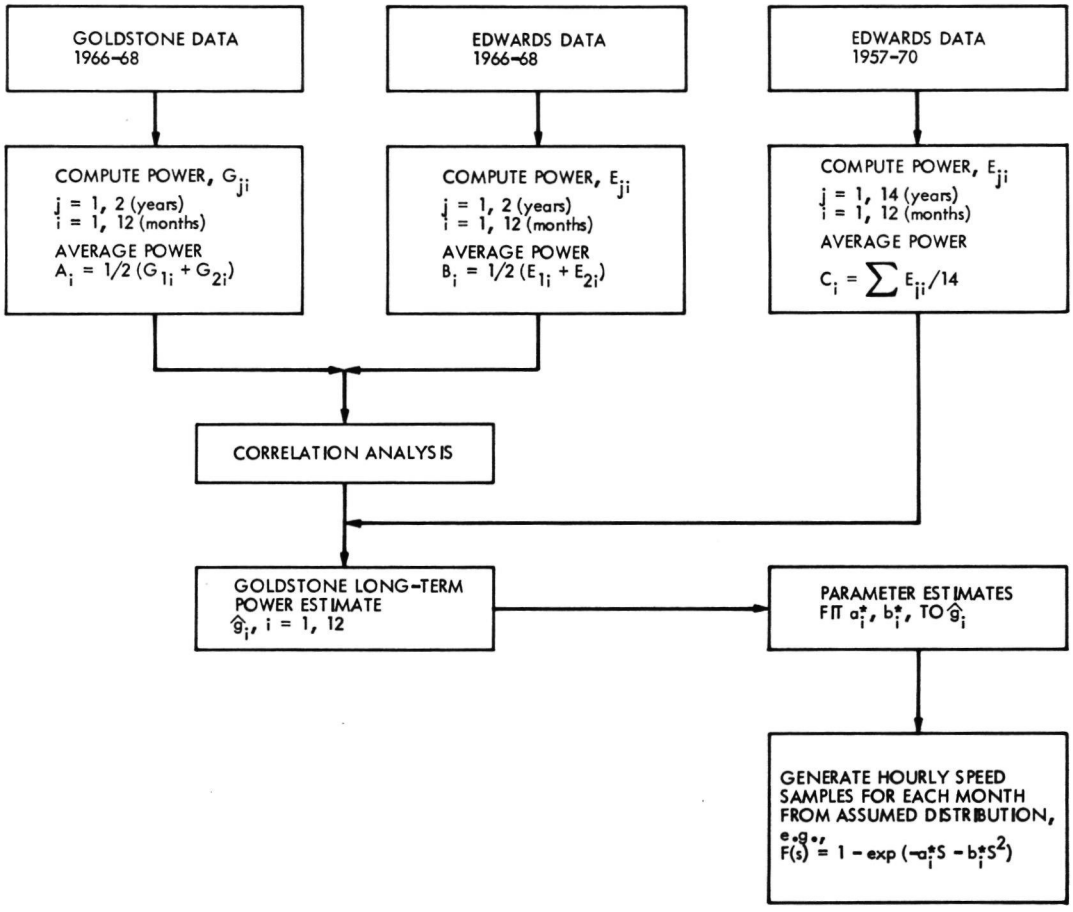

Fig. 1. Goldstone wind speed model for SENSMOD Program

Appendix

Estimation Method

Assume that X and Y are random variables with known correlation coefficient ρ ratio of standard deviations σ_x/σ_y, but with unknown means μ_x and μ_y. We wish to estimate μ_y from data available within two independent samples: the first sample consisting of n paired sets of (X,Y) data, denoted as (X_1,Y_1), $\cdots$, (X_n,Y_n); the second sample consisting of m observations of a set of X data only, denoted as X_{n+1}, $\cdots$, X_{n+m}. The following sample means can be computed for these data:

$$X_n = \frac{(X_1 + \cdots + X_n)}{n}$$

$$Y_n = \frac{(Y_1 + \cdots + Y_n)}{n}$$

$$X_m = \frac{(X_{n+1} + \cdots X_{n+m})}{m}$$

$$X_{n+m} = \frac{(X_1 + \cdots X_{n+m})}{n+m}$$

The approach here will be to select as the estimator of μ_y the estimate with smallest variance that can be determined from the set of unbiased estimators that can be constructed as linear combinations of the data. In the special case where (X,Y) are normally distributed, this is also the estimator that would be derived by the maximum likelihood method. An alternative derivation would be to use a least squares approach via a transformation to a problem of uncorrelated variables.

As a linear combination of the data, let

$$T = a_1X_1 + \cdots a_nX_n + b_1X_{n+1} + \cdots + b_mX_{n+m} + c_1Y_i + \cdots + c_nY_n$$

be the general form for the estimators to be considered. It will simplify matters to verify first that the variance-minimizing T has all a's equal, all b's equal, and all c's equal.

To see this, consider an unbiased estimator T, not satisfying this condition. By permuting the a's if they are unequal (or the b's or c's if the a's are equal), we can write another estimator $T_2(\neq T_1)$, which obviously has the same mean and variance as T_1. In particular, T_2 is also unbiased and thus $(T_1+T_2)/2$ is also unbiased.

Now,

$$\frac{Var(T_1+T_2)}{2} = \frac{1}{4}VarT_1 + \frac{1}{4}VarT_2 + \frac{1}{2}Cov(T_1,T_2)$$

$$= \frac{1}{2}VarT_1 + \frac{1}{2\rho}(T_1,T_2)\,(VarT_1)^{1/2}\,(VarT_2)^{1/2}$$

$$= \frac{1}{2}[1+\rho(T_1,T_2)]VarT_1$$

which is less than $VarT_1$, unless $\rho(T_1,T_2) = 1$. This last cannot be the case or else there would be a linear relationship between T_1 and T_2, and then by virtue of the equality of their means and variances, T_1 and T_2 would have to be equal. Thus, $(T_1+T_2)/2$ is better than T_1 so that T_1 cannot be the best linear unbiased estimator.

It suffices, therefore, to consider estimators which can be written in the form

$$T = a\overline{X}_n + b\overline{X}_m + c\overline{Y}_n$$

for which the expected value is

$$ET = (a+b)\mu_x + c\mu_y$$

The condition of unbiasedness requires that $a + b = 0$ and $c = 1$. Hence,

$$T = \overline{Y}_n + a(\overline{X}_n - \overline{X}_m)$$

and

$$VarT = Var(\overline{Y}_n + a\overline{X}_n) + Var(a\overline{X}_m)$$

$$= \frac{\sigma_y^2}{n} + \frac{a^2\sigma_x^2}{n} + 2\,Cov(\overline{Y}_n\,\overline{X}_n) + \frac{a^2\sigma_x^2}{m}$$

Since

$$Cov(Y_n,X_n) = \frac{Cov(\overline{Y}_1,\overline{X}_1)}{n} = \frac{\rho\sigma_x\sigma_y}{n}$$

$$VarT = \frac{\sigma_y^2}{n} + a^2\sigma_x^2\left(\frac{1}{n+1}\right) + \frac{2a\rho\sigma_x\sigma_y}{n}$$

The minimum is attained at $a = -\rho(\sigma_y/\sigma_x)m/(m+n)$ and equals $\sigma_y^2/n[1-\rho^2 m/(m+n)]$. Using the fact that $\overline{X}_{n+m} = (n\overline{X}_n+m\overline{X}_m)/(m+n)$, the estimator can be written in the form

$$T = \overline{Y}_n - \rho\left(\frac{\sigma_y}{\sigma_x}\right)(\overline{X}_n - \overline{X}_{n+m})$$

Comparing with the estimator $\overline{Y}_n$, which has variance σ_y^2/n, it is seen that the variance is reduced by a factor of $(1-\rho^2)$, when m is much larger than n.

In the application to estimation of monthly wind powers at Goldstone, since the correlation ρ and the standard deviation ratio σ_y/σ_x were unknown, it was necessary to use estimates of these quantities in the formula for T.

Reference

1. Hamilton, C. C., "A Dynamic Model for Analysis of Solar Energy Systems," in *The Deep Space Network Progress Report 42-27*, pp. 41-45, Jet Propulsion Laboratory, Pasadena, Calif., June 15, 1975.

Meteorological Monitoring Assembly

H. Burnell, H. Phillips, and R. Zanteson
DSN Engineering Section

The DSN 64-meter antenna stations are being equipped with automated meteorological monitoring assemblies as a part of the Deep Space Station (DSS) Technical Facilities Subsystem. These assemblies provide data on atmospheric conditions necessary for calibrating metric data in support of flight project navigational requirements. Ground level temperature, barometric pressure, humidity and precipitation rate are sensed. Insolation is measured in support of solar energy monitoring. A polarization tracking receiver will be added to determine the Faraday rotation angle of a linearly polarized signal from a synchronous satellite. The paper describes the system components, organization, and output data.

I. Introduction

The DSN 64-meter antenna stations are being equipped with automated meteorological monitoring assemblies as a part of the DSS Technical Facilities Subsystem. These assemblies provide data on atmospheric conditions necessary for calibrating metric data in support of flight project navigational requirements. Ground level temperature, barometric pressure, humidity and precipitation rate are sensed. These data, together with antenna pointing direction and radio frequency (RF) parameters are processed digitally as a function of time, are recorded within the assembly, and are transmitted on a non-real-time basis through the High-Speed Data Subsystem (HSS) to the Network Operations Control Center (NOCC) and to Mission Operations Centers (MOCs). Insolation is measured and recorded in support of solar energy monitoring. A polarization tracking receiver will be added to determine Faraday rotation angle of a linearly polarized signal from a synchronous satellite. In the future (1977 era) data transmission to the NOCC and MOCs will be on a real-time basis through the metric data assembly. Provision is made for the future incorporation of wind velocity and direction measurement. A block diagram of the assembly is shown in Fig. 1.

II. Description of the Meteorological Monitoring Assembly

A. General Description

The meteorological monitor assembly consists of temperature, dewpoint, and static pressure sensors mounted on a tower near the control room building; a rain gage, solar sensor and ionospheric receiver antenna mounted

conveniently at ground level; and a barometer, hygrometer, ionospheric receiver and data processing equipment mounted in a rack in the control room.

Data on antenna position, S-band polarization angle and mode status, and S- and X-band noise temperature are received from appropriate locations within the control room. Time signals are received from the Frequency and Timing Subsystem. There is a standard output interface to the High Speed Data Subsystem.

B. Tower-Mounted Sensors

Temperature is sensed by a thermistor mounted in a motor-aspirated temperature shield. The analog output is conditioned in the translator assembly in the control room rack. This unit has a resolution of 0.1°C and an rss error of 0.14°C, combining a 0.1°C sensor error and a 0.1°C solar effect.

Dewpoint is measured by an aluminum oxide capacitor transducer which is mounted in a sample cell for high humidity application. Solid-state analog circuitry in the control room rack drives a local panel meter display which requires a calibration chart for dewpoint interpretation. The dewpoint accuracy is ±2°C from +30 to +60°C, ±1°C from −20 to +30°C and ±3°C from −50 to −20°C, where the ranges are the actual dewpoints. The dewpoint data are processed by the calculator to put out both dewpoint in °C and water vapor partial pressure.

A static pressure head which provides a pressure input for the barometer is mounted adjacent to the dewpoint transducer on the tower.

C. Ground Level Sensors

Sensors are located at convenient points at ground level, in positions unaffected by adjacent structures:

Precipitation is measured by a tipping bucket rain gage, which tips to empty each time it is full. Measurement is by counting the number of times the bucket, which is heated to convert falling snow, is emptied. The count is kept in the translator assembly of the control room rack. This device has a resolution of 0.25 mm of water and accuracies of ±0.8 mm/hr at 75 mm/hr, ±13 mm/hr at 25 mm/hr and ±5% of total rainfall.

Incident solar radiation (insolation) is measured by an Eppley differential thermopile, with a total sun and sky response from 280 to 2800 nm. An analog data conditioning circuit card is installed in the translator assembly of the control room rack. Combining errors due to temperature effect (±2%), linearity (±1%), cosine response (±2% elevation 10 to 90 deg), the rss error of measurement is ±3%.

The polarization tracking receiver antenna will be mounted conveniently at ground level or on the control building roof. This antenna, compatible with the receiver installed in the control room, will be pointed permanently at a synchronous satellite, whose linearly polarized signal is used to measure the Faraday rotation angle.

D. Control Room Equipment

Control room equipment is mounted in a single rack (Fig. 2).

A transducer senses barometric pressure by measuring the frequency difference between two oscillators timed by the atmospheric pressure. The output is directly in binary-coded decimal (BCD) form. Combining system linearity, hysteresis, repeatability and temperature errors, the rss accuracy at 38°C is 0.41 millibars.

An analog-to-digital (A-D) converter and scanner converts the analog signals received from the various sensors to BCD format for input to the programmed calculator. The scanner has a capacity as installed of 20 analog channels, with an ultimate capability of 50 channels. Channel selection is automatic, under control of the calculator. Ranges and accuracies are as follows:

Range	Accuracy
100 mV	0.1% of reading +0.04 mV
1.0 V	0.01% of reading +0.1 mV
10.0 V	0.01% of reading +1 mV

The translator provides data conditioning for analog transducers and an interface for various sources of digital data. Digital data interfaces are provided for the Frequency and Timing Subsystem, antenna angles, metric data assembly, incremental recorder, and rain gage storage register. A system malfunction alarm is also incorporated.

A Hewlett-Packard programmable calculator, Model 9821A, serves as the automation control and data processing center for the meteorological monitoring assembly. The calculator has 679 internal program and data registers, together with an additional 8000-word capacity in an auxiliary tape cassette. When used with the I/0 expander, there are 13 input/output ports, 9 general purpose and

4 dedicated to peripherals. Each digital input interface has a capacity of 9 decades of parallel 8, 4, 2, 1 BCD data, while the TTL input/output interface has 7 lines serial with data in binary or ASCII format.

Input and processed data records are kept on a Kennedy Model 1600 incremental tape recorder. This recorder stores 200 bits per inch on ½-in. magnetic tape, using 6 tracks plus parity. Up to 10 days of data can be recorded on one 8.5-in. tape reel.

The ionospheric receiver measures Faraday rotation angle of the signal received from a synchronous satellite. Total diurnal rotation angle is measured to an accuracy of less than 5 deg, with a resolution of 1 deg.

E. Other Input Data

Other, nonmeteorological data are input into the computer for record purposes and for computational use as required. These data, received from other racks in the control room, are listed in Table 1.

F. Data Handling Capability

Data are sampled and stored on 20-s intervals. Data output is by selected data types on intervals of 1, 2, 3, 4, 5, 6, 10, 15, 20, 30 or 60 min. In addition, a special calculator program, requiring the operator to set in an alternate program, will provide a 1-s sample rate for 10 min at a time, limited to two data types. In normal usage there are 10 output data types available (Table 2).

These data are output in binary form for transmission by the High Speed Data Subsystem to the Network Operations Control Center or to Mission Operation Centers.

G. Local Data Readout

In addition to the basic output to remote locations, local readout is available in two forms. In the first, any parameter may be selected for local display when the operator inserts a binary number, selected from a register index, in binary switches on the translator control panel. The contents of that register are then displayed in decimal format on the calculator readout.

In the second form the tape printer output of the calculator is used to print out the day and time followed by the numerical content (in decimal format) of each data type in order listed in Table 2, followed by the internal power supply voltages. This printout occurs each 15 min under program control.

Table 1. Other input data

Data	Source	Form
Time	Frequency and Timing Subsystem	BCD
S-band ambient load temperature	Manual input	BCD
X-band ambient load temperature	Manual input	BCD
S-band system noise temperature	To be determined	Analog voltage
X-band system noise temperature	To be determined	Analog voltage
Polarization angle S-band polarization diversity (SPD) cone linear polarization angle, SPD polarization mode	Microwave Subsystem polarizer control	BCD
64-m antenna pointing Azimuth 0–359.9 deg Elevation 0–90 deg	Angle encoding system	BCD

Table 2. Output data types

Data type	Parameter	Bits/parameter	Least significant bit	Range	Comments
1	Data type	6	–	–	
	Time, seconds past 0^h GMT	24	$s \times 10^{-2}$	0 – 8,640,000	
	Dewpoint, °C	12	deg × 10^{-1}	0 – 1100	
	Temperature, °C	12	deg × 10^{-1}	0 – 1000	Offset + 500
	Barometric pressure, mbar	18	mbar × 10^{-1}	8900 – 10,600	
	Partial pressure, mbar	12	mbar × 10^{-1}	2 – 2000	
	Total bits for data type = 1	84 bits			
2	Data type	6	–	–	
	Time, seconds past 0^h GMT	24	$s \times 10^{-2}$	0 – 8,640,000	
	Precipitation rate, mm/hr	18	mm × 10^{-1}	0 – 3000	
	Total precipitation, mm	18	mm × 10^{-1}	0 – 9999	
	Total bits for data type = 2	66 bits			
3	Data type	6	–	–	High rate ionosphere data, 3 samples/min
3	Time, seconds past 0^h GMT	24	$s \times 10^{-2}$	0 – 8,640,000	
	Diurnal Faraday rotation angle, deg	18	deg × 10^{-1}	0 – 60,000	Offset 30,000
	Faraday rotation angle 0, deg	18	deg × 10^{-1}	0 – 1800	3 samples per DT
3	Faraday rotation angle 0 + 180, deg	18	deg × 10^{-1}	1800 – 3600	3 samples per DT
	Signal strength, V	12	V × 10^{-2}	0 – 500	
	Total bits for data type = 3	228 bits			
4	Data type	6	–	–	
	Time, seconds past 0^h GMT	24	$s \times 10^{-2}$	0 – 8,640,000	
	Diurnal Faraday rotation angle, deg	18	deg × 10^{-1}	0 – 60,000	Offset 30,000
	Faraday rotation angle 0, deg	18	deg × 10^{-1}	0 – 1800	
	Faraday rotation angle 0 + 180, deg	18	deg × 10^{-1}	1800 – 3600	
	Signal strength, V	12	V × 10^{-2}	0 – 500	
	Total bits for data type = 4	96 bits			
5	Data type	6	–	–	
	Time, seconds past 0^h GMT	24	$s \times 10^{-2}$	0 – 8,640,000	
	Satellite azimuth, deg	12	deg	0 – 360	
	Satellite elevation, deg	12	deg	0 – 90	
	Total bits for data type = 5	54 bits			
6	Data type	6	–	–	
	Time, seconds past 0^h GMT	24	$s \times 10^{-2}$	0 – 8,640,000	
	Undefined	18			
	Undefined	18			
	Undefined	18			
	Undefined	18			
	Total bits for data type = 6	102 bits			
7	Data type	6	–	–	
	Time, seconds past 0^h GMT	24	$s \times 10^{-2}$	0 – 8,640,000	
	Solar insolation, g-cal/min/cm²	12	gm-cal/min/cm² × 10^{-2}	0 – 200	
	Solar energy per 24 hours	12	W-hr/cm² × 10^{-2}	0 – 200	
	Total bits for data type = 7	54 bits			

Table 2 (contd)

Data type	Parameter	Bits/parameter	Least significant bit	Range	Comments
8	Data type	6	–	–	
	Time, seconds past 0^h GMT	24	s × 10^{-2}	0 – 8,640,000	
	System noise temperature, S-Band	12	K × 10^{-1}	100 – 3000	
	System noise temperature, X-Band	12	K × 10^{-1}	100 – 3000	
	Azimuth angle, deg	12	deg × 10^{-1}	0 – 3600	
	Elevation angle, deg	12	deg × 10^{-1}	0 – 900	
	Ambient load, S-band	12	°C × 10^{-1}	0 – 1000	
	Ambient load, X-band	12	°C × 10^{-1}	0 – 1000	
	Total bits for data type = 8	102 bits			
9	Data type	6	–	–	
	Time, seconds past 0^h GMT	24	s × 10^{-2}	0 – 8,640,000	
	Microwave polarization angle, deg	18	deg × 10^{-2}	0 – 36,000	
	Microwave mode	6	–	–	1 = linear auto 2 = linear manual 3 = RCP 4 = LCP
	Total bits for data type = 9	54 bits			
10	Data type	6	–	–	
	Time, seconds past 0^h GMT	24	s × 10^{-2}	0 – 8,640,000	
	Microwave polarization angle 1	18	deg × 10^{-2}	0 – 36,000	1 sample per 20 sec
	Microwave polarization angle 2	18	deg × 10^{-2}	0 – 36,000	
	Microwave polarization angle 3	18	deg × 10^{-2}	0 – 36,000	
	Microwave mode 1	6	–	–	1 = linear auto 2 = linear manual 3 = RCP 4 = LCP
	Microwave mode 2	6	–	–	
	Microwave mode 3	6	–	–	
	Total bits for data type = 10	102 bits			
11	Data type	6	–	–	Once per block
	Time, seconds past 0^h GMT	24	s × 10^{-2}	0 – 8,640,000	Once per block
	Microwave polarization angle,[a] deg	18	deg × 10^{-2}	0 – 36,000	
	Diurnal Faraday rotation angle,[a] deg	18	deg × 10^{-1}	0 – 60,000	Offset 30,000
	Faraday rotation angle 0, deg[a]	18	deg × 10^{-1}	0 – 1800	
	Faraday rotation angle +180,[a] deg	18	deg × 10^{-1}	1800 – 3600	
	Microwave mode[a]	6	–	–	1 = linear auto 2 = linear manual 3 = RCP 4 = LCP
	Signal strength (ionosphere receiver)	12	V × 10^{-2}	0 – 500	Once per block
	Total bits per block	978 bits			

[a]12 1-s samples per high-speed data block.

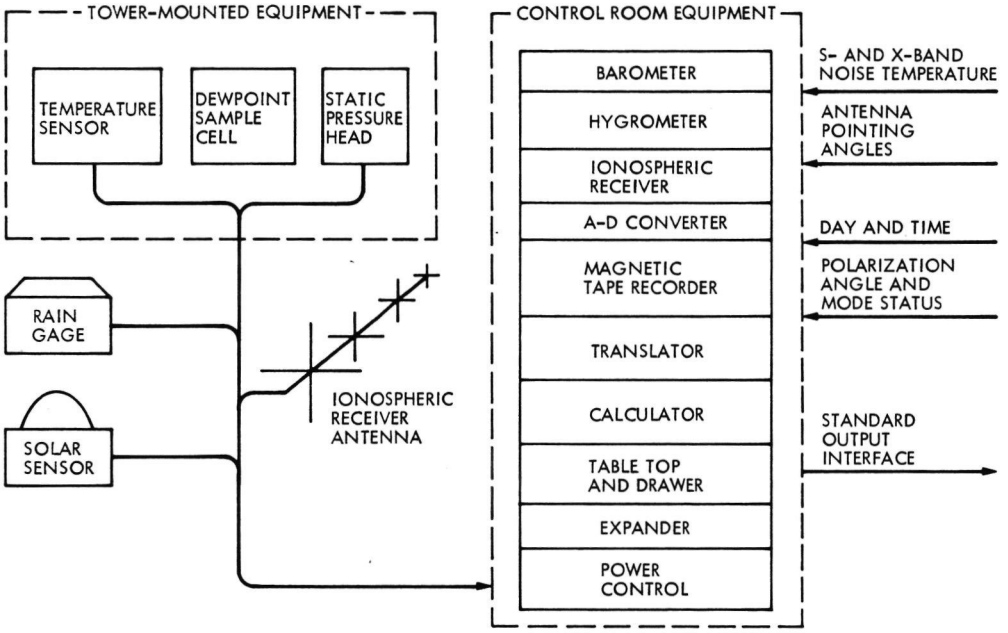

Fig. 1. Meteorological monitoring assembly block diagram

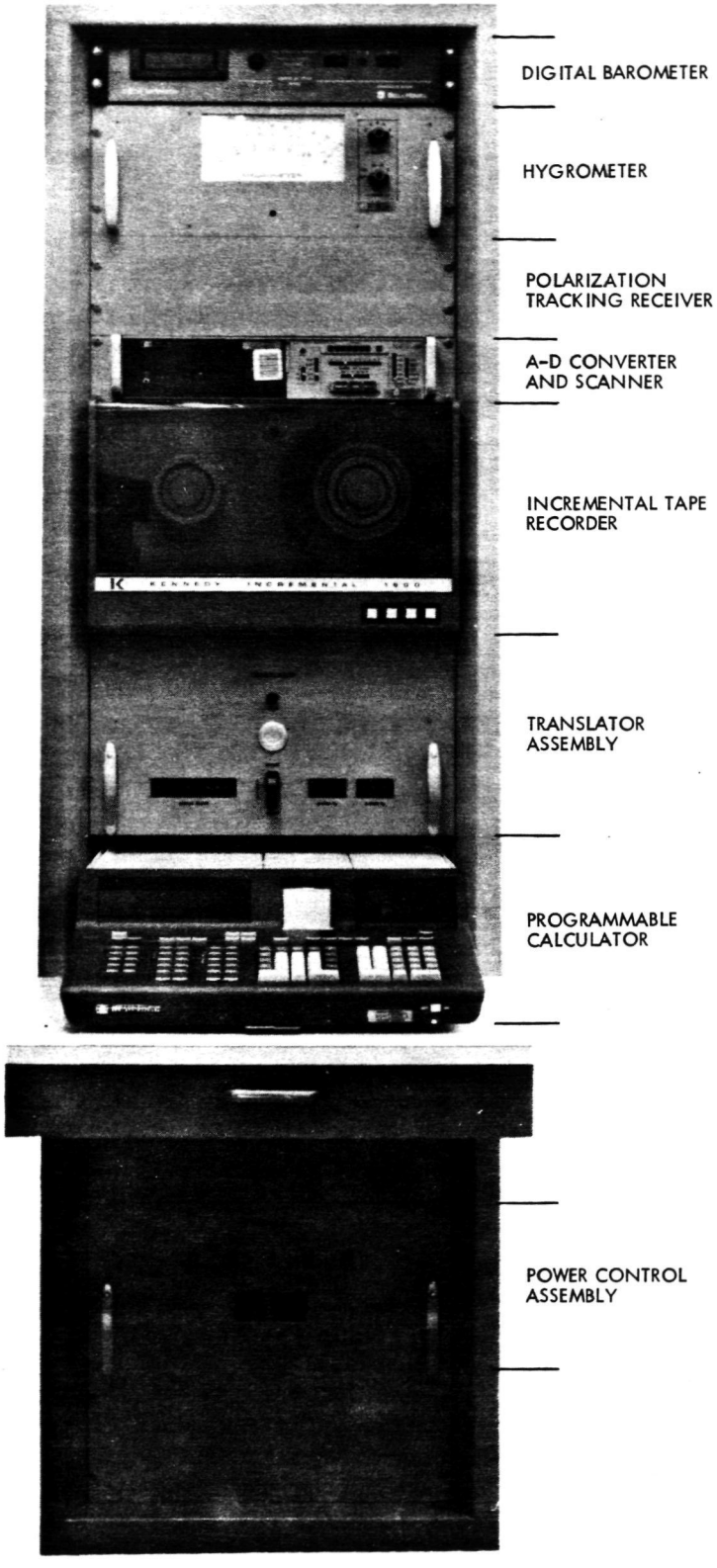

Fig. 2. Meteorological monitoring assembly control rack

The Minimanual: A New Concept in Operation and Maintenance Handbooks

J. Nathenson
DSN Engineering Section

Reduced fiscal budgets for DSN engineering documentation have necessitated a search for new and more cost-effective methods of producing the technical data required for equipment procurements and for operation and maintenance support of equipment already on-line at the Deep Space Stations. In the major documentation area of technical manuals, a new plan has been devised for achieving substantial monetary savings without sacrificing the integrity of the manuals or their utility as the central source of operation and maintenance information. Called "the minimanual," the new type of handbook has thus far shown an effective response to the exigencies of today's economics. This article describes the minimanual concept, its content and format characteristics, and the results of its first few months of implementation.

I. Introduction

Traditionally, full-scale operation and maintenance (O&M) manuals have been a compilation of the most pertinent existing technical data on the subject equipment. The categories of information generally included a physical description, a short functional description, installation instructions, pre-operational testing, a functional description of controls and indicators, standard and emergency operating procedures, a detailed theory of operation, a circuit analysis, preventive maintenance procedures, troubleshooting procedures, repair and replacement, qualification testing, a replaceable parts list, and a selection of the most important engineering drawings (i.e., electrical schematics, wiring diagrams, cable diagrams, signal flow diagrams, and logic diagrams).

Because they contained the aforementioned wealth of data, the standard O&M manuals were justifiably used as the prime authoritative source of information for operation and maintenance of the equipment. But they have become costly to produce in a time of diminishing funds and blistering deadlines. Clearly, a new concept of technical manual production was needed, one that would provide the same essential information with a lesser time and cost expenditure.

In examining the problem, it was seen that the three largest cost factors were the writing time, the illustrating time, and the typing time, both for number of hours and cost per hour. Other accrued costs, such as editing time, materials, and printing and binding, were all on the lower end of the scale in dollar value. It appeared that an attack had to be made on the three largest cost factors if the overall price of manuals was to be brought down to a realistic level for the times.

By far, the largest expense in manual production was the writing time. It is the responsibility of the writer to gather the existing data from a multitude of sources and to rewrite, reprocess, and properly organize the material into a cohesive whole that conforms to the pre-established outline for the manual. He must also generate new data which may be required for use in the manual alone; such data are obtained from interviews with the cognizant engineers and technicians and from laboring over a great number of schematic and wiring diagrams. This is the time-consuming, hard-core technical writing that has always presented a challenge to cost-conscious management.

In examining the problem further, a few enlightening questions arose. Was it absolutely necessary to have the redundancy of information that the standard manual created? If a large portion of the manual is extracted from existing data in the documentation system, was it practical from an economic standpoint to reprocess the data just for the sake of having a single, all-encompassing manual? Under the current financial pinch, was it still worthwhile to continue the compilation process that gave us large, bulky manuals that were highly authoritative and definitive in coverage but were a drain on precious funds that could be used for many other practical purposes? The answers had to be in the negative. Yet, effective O&M manuals were needed. It became a certainty, however, that they would have to be restructured to meet the needs, or limitations, of current conditions.

II. Birth of the Minimanual

The major element in the solution reached was the reversal of the compilation process. Instead of bringing the operator or maintenance technician to the one, all-encompassing manual for the data he is seeking, we send him back to the original source of the information. This is done by providing the proper source reference in the Table of Maintenance Support Documentation in the manual, unless, of course, the data have been newly generated for the manual itself and are contained within the covers. Thus, the new type of manual becomes a central document, the hub point of a wheel of information whose spokes lead to existing test procedures, engineering drawings, data lists, design specifications, parts lists, commercial handbooks, and other documentation. It becomes, in many instances, the guiding light to essential data rather than the home for it.

Christened the "minimanual" for its abbreviated size and coverage, the newly implemented handbook has taken its place alongside the minicomputer and other "minis" as a compact, highly functional element operating in the DSN. It is not, however, solely an index document. The minimanual maintains its integrity as a bona fide O&M handbook by providing all the essential data that are required for a basic understanding of how the equipment works and what it takes to maintain it.

The high cost of writer time is cut to a minimum. No longer does the technical writer have to spend countless hours assembling diverse categories of information and rewriting the data into technical manual format. He is required only to identify the data by their existing document numbers and titles and to furnish the references in the Table of Maintenance Support Documentation. His creative efforts are thus confined to the basic task of writing original operation and maintenance procedures and a lucid theory of operation at the technician level. In instances where the engineer himself furnishes adequately written inputs, the writer's task is even further reduced to an editorial function, bringing the cost of the manual down to a very low figure.

Permissible shortcuts in writing style and format have also helped to reduce the overall costs. Boilerplate terms and paragraphs, once thought essential for reader comprehension, are not considered valid for minimanual text; the language is required only to be clear and concise, unburdened by stock phrasings and embellishments. Format shortcuts take the form of non-rigid page make-up, the elimination of typeset section headings, the freedom to reproduce existing artwork in its original form, and the use of illustrations sparingly.

III. A Harvest of Advantages

The question of whether the maintenance technician would be getting short shrift by having to use a minimanual was considered from the beginning. The surprising answer was that not only was he not getting short shrift but he was being aided in his tasks by being forced to go to other sources for much of the peripheral data he needed. Contradictory as this may seem, it must be remembered that the manual is usually the last

document to be updated for technical accuracy. Indeed, as funds dwindle and sometimes vanish, the manual is not updated at all. It is far, far better for the maintenance technician needing an accurate schematic to go to his blueprint or microfiche file where he is more likely to find the latest revision of the drawing. The same philosophy would apply to parts lists, test procedures, wire lists, cabling diagrams, and the like. The minimanual provides the accurate reference to these documents by number and title; the technician must provide the legwork to obtain the actual data. But it is all worthwhile. No longer will the technician have doubts about the latest effectivity of the schematic in his hand. He will have the most recent revision obtainable, for the drawing system is usually the very first to be kept up-to-date.

In producing minimanuals, drastic reductions can be effected both in costs and time schedules. Late beginnings can be offset by fewer pages to be generated. The writer, knowing exactly what information is to be included in the manual and what information is to be supplied by reference only, will have a smoother, more straightforward path to follow and will have a better chance of completing his assignment on schedule. Successful completion on schedule, or ahead of schedule, will mean the availability of documentation where and when it is needed. The reduced costs may possibly create additional funds for other critical documentation or for resolution of equipment problems that were unforeseen.

The publications production work on minimanuals calls for no specialized equipment or for any personnel other than the normal repro typist and production editor. As a non-computerized effort, the production work can be quickly and efficiently done in the universally employed methods and procedures for creating camera-ready reproducibles. This is particularly advantageous, since many DSN manuals are prepared by outside vendors, small and large, who do not have computerized equipment for publications graphics. The minimanuals produced in-house by the DSN would likewise require no expensively leased or purchased data processing devices, cathode-ray tubes, magnetic tapes, and the like. A by-product of this standard, long-established production method would be sets of reproducibles for O&M manuals which are all uniform in regard to type face, cameo size, and camera reduction ratio. The manual revision process is thereby simplified, since no matching of diverse type faces and sizes would be necessary. Also, fewer revisions would have to be initiated for the minimanual; most likely, it would be the reference document that would require changing, and not the minimanual itself. Instead of revising two documents, we revise only one—with accompanying cost savings.

The minimanual is published in standard 8-1/2 × 11-inch (22 × 28-cm) size and is bound either in thin, flexible cardboard covers or in hard, three-ring binders, depending on engineering preference for the individual manual. In use, it is highly portable and may be taken to any location where it is needed. When it is not being used, it takes up only a minimal amount of desk or bookshelf space.

IV. Minimanual Content

The restructuring of O&M handbooks into the minimanual concept has eliminated four of the standard sections that were previously used: General Description, Installation, Parts List, and Drawings. The three remaining sections, however, do contain the most essential information for effective operation and maintenance of the equipment. Together with fairly standard front matter and any required appendices, the three sections suffice to provide the on-line technician with the basic facts he needs to do his job.

A. Front Matter

A combined Title Page and List of Effective Pages is the initial page in the manual. This is followed on the reverse side by a Foreword page that gives a brief description of the equipment's purpose, its physical make-up, and its location in the hierarchy of assemblies, units, groups, and subsystems. The third page contains the beginning of the Table of Contents, List of Illustrations, and List of Tables, which are run in consecutively until completion. A Safety Summary page follows, if one is required.

B. Section I—Operation

Section I contains a functional description of all controls and indicators on the equipment, which is accompanied by at least one illustration that visually displays the items discussed. This is followed by the usual equipment turn-on procedures and any pre-operational procedures that may be required. The operating procedures themselves give full sequential instructions on how the equipment is operated under normal circumstances. Emergency operating procedures, if any, and equipment turn-off procedures conclude the section.

C. Section II—Theory of Operation

Section II contains both a general and detailed theory of operation of the overall equipment and its subassemblies. Depending on the electronic, hydraulic, or mechanical

complexity of the equipment, a circuit analysis is provided to explain or clarify the internal operation of unusual circuits or component parts.

D. Section III—Maintenance

Section III contains both preventive and corrective maintenance. The preventive maintenance paragraphs provide instructions for inspection, cleaning, and lubricating, as necessary. Corrective maintenance contains a listing of test equipment and special tools, and instructions for calibrating, testing, troubleshooting, and repairing and replacing malfunctioning components. Included in the section is a Table of Maintenance Support Documentation which contains a listing, by name and number, of the most pertinent drawings, specifications, procedures, commercial manuals, and other documents that may be needed for equipment maintenance purposes.

E. Appendices

Appendices are an optional item in the minimanual concept. Data not properly falling into the three existing sections of Operation, Theory of Operation, and Maintenance, but which are considered necessary for inclusion in the handbook, may be placed at the rear of the manual as an appendix. Such items as computer printouts, a glossary of special terms, complicated installation instructions, or special equipment modifications are proper subjects for minimanual appendices.

V. Implementation

Of the five minimanuals completed to date, the smallest has 16 pages and the largest 130 pages. Writing, typing, and printing costs have been about 40% below the cost of standard manuals. No complications were experienced in the writing and production. The manuals have been released to operations personnel and are being used at the Deep Space Stations. Their utility and effectiveness is under study.

Automatic Control Techniques Used on 64-Meter-Diameter Antenna Power Systems

J. Dorman
DSN Engineering Section

New power plant equipment installed at DSS 61/63 (Robledo, Spain) and at DSS 42/43 (Tidbinbilla, Australia) was designed to supplement the existing equipment for the additional electrical load of 64-m-diameter antennas recently constructed at these sites. The existing power plant equipment (Section A) at each site consisted of manually controlled generators operating at 480 volts. The new equipment (Section B) uses completely automatic generator control operating at 2400 volts. This report describes the automatic controls and also the techniques used for independent or combined operation of both sections. Features provided for possible future operation with commercially produced power, and future automation of Section A equipment are described.

I. Introduction

The installation of 64-m-diameter antennas at DSS 61/63 (Robledo, Spain) and at DSS 42/43 (Tidbinbilla, Australia) demanded increased power-generating facilities. The existing power plant (Section A) operating at 480 volts at each station was supplemented by new generating equipment (Section B) operating at 2400 volts.

This progress report describes automatic control features of the Section B equipment, which allow combined or separate operation of the two sections. Controls for future parallel operation of the generators with commercially produced power and future automation of Section A during integration of the two power-generating sections are also described.

A brief description of the manual controls performed by an operator in a non-automatic power plant indicates the functions requiring automation and prefaces the description of the automatic control.

II. Manually Controlled Power Plant Operation

At a typical power plant the operator is responsible for the following control operations:

(1) Establishes the power load requirements of the system and determines the required number of engine-generators to provide sufficient generating capacity.

(2) Starts and adjusts the speed of each engine prior to connecting the driven generator to the electrical power system.

(3) Sets the engine-generator speed so that a small difference in frequency exists between the incoming generator and that of the power bus before paralleling. This difference in frequency is indicated on a synchroscope by the speed of its pointer rotation.

(4) Adjusts the incoming generator voltage to coincide with the power bus voltage before paralleling.

(5) Closes the incoming generator circuit breaker to connect the incoming generator to the power system at the precise moment that the generator and power bus are in phase. This is indicated by the synchroscope pointer at the 12:00 o'clock position. This requirement for correct phase relationship is mechanically analogous to meshing two rotating spur gears at the moment when the teeth are in the correct position. To achieve this condition it is necessary to have a slight frequency (i.e., speed) difference between the power bus and the incoming generator voltage so that the phase angle will cycle and pass the "in phase" condition. If an attempt is made to connect the incoming generator out of phase with the power bus, severe overcurrents and voltage dips will occur and the equipment could sustain heavy damage. In the mechanical analogy, the spur gear teeth would be stripped or damaged.

To back up the operator in this operation a permissive synchronization check relay monitors the phase angle of the running and incoming voltages and prevents circuit breaker closing despite control switch operation unless the phase angle difference is close to zero.

(6) Having synchronized and then paralleled the new generator to the power system, adjusts the diesel engine fuel manually by a governor control switch. The increase in fuel would tend to increase the diesel-generator speed but this is constrained to correspond with the power bus frequency and, instead, the generator increases its share of the kilowatts (real power load) demanded by the power system.

(7) Adjusts the reactive load on the generator by a voltage adjusting rheostat. This rheostat controls the generator field excitation. When the excitation is increased, the voltage of the generator tends to increase but is constrained to correspond with the power bus voltage and instead the generator reactive load (kilovars) increases.

NOTE: The constraints on generator frequency and voltage depend on the capacity of the power system. The greater the power load, and number of generators running in parallel, the greater the constraints.

(8) Monitors the power generation equipment, making necessary adjustments of governors and excitation as required to share the load kilowatts and kilovars between the connected generators in proportion to their individual power ratings.

(9) Unloads generators and disconnects them as load demand decreases; then stops the diesel engine of the disconnected generator.

III. Automatically Controlled Devices

The automatic control devices used to perform the above operations in Section B of the power plant are discussed below.

A. Power System Sequencer

The power system sequencer (Fig. 1) is built almost completely of solid-state components. It is designed to start and stop the engine-generators as power load increases or decreases. The sequence of starting and stopping of individual machines is manually set by control knobs at the front which allow any machine out of the four installed to be first, second, third or fourth to start. Once preset for starting sequence, the machines stop in the reverse sequence. Following a period of operation of two or three months, the running time of the first engine-generator in the sequence will be greater than the other machines and the sequence will then be manually changed to balance running times. The sequencer is also equipped with control knobs which allow presetting of load kilowatts at which generators will automatically start. Load kilowatt sensing is an integral function of the sequencer.

With one machine generating, the first control knob setting determines the percentage of that machine's power capacity at which a second machine should be started and connected to the power bus to share the load demand. The second control knob setting is set at a percentage of the combined power capacity of the running engine-generators which will start a third machine. The third control knob similarly sets the percentage of the combined power capacity of three

engine–generators which will start and connect the fourth machine.

The sequencer presently installed is equipped to handle the four generators presently existing in Section B but can be retrofitted to accommodate the four additional machines in Section A.

B. Automatic Synchronizer

The automatic synchronizer (Fig. 2) is predominantly of solid-state construction. It differs from the synchronizer check relays previously described by incorporating active controls for regulating the incoming diesel-engine speed. When a machine is started by the power system sequencer, the synchronizer automatically assumes control of the machine, brings it into synchronism, and then automatically closes the circuit breaker to connect the generator to the power bus. Following this operation the synchronizer disconnects itself and engine–generator control is passed to its electronic governor and voltage regulator as described later.

Two independent monitors are used in the synchronizer to establish correct synchronizing conditions prior to circuit breaker closing. Both monitors must be satisfied before the generator connects to the power bus. Each monitor checks voltage differential and phase angle difference between the incoming and running generators, and control knobs mounted on the front of the synchronizer permit presetting of acceptable voltage and phase angle tolerances which are suitable for synchronizing. If only one monitor signals that synchronizing conditions are met, the circuit breaker will not close, and an indicator light on the synchronizer will signal a malfunction.

Other lights on the synchronizer allow visual monitoring of the incoming machine status to indicate overspeed, underspeed, overvoltage, and undervoltage.

A feature of the synchronizer is the ability to set the control for circuit breaker closing time, i.e., the short time required for the closing mechanism to respond to its closing signal and physically close its contacts. The synchronizer anticipates the moment of precise synchronism and signals the circuit breaker slightly early so that contact closure is at synchronism.

C. Electronic Power Sharing Governor

Each engine–generator is equipped with an electronic governor control. The fuel setting of the engine is determined by the position of its actuator shaft which is directly proportional to a dc signal from an electronic control assembly. Figure 3 is a block diagram of the fundamental components. This shows that the fuel delivered to the engine, and therefore the electrical power derived from the associated generator, depends on speed and load sensor signals transmitted to the actuator through an integrating and power amplifier. The function of the ramp generator is to control the acceleration of the machine when starting and bringing it up to rated no-load speed prior to synchronizing the generator. Control of the acceleration precludes the possibility of overspeeding the machine on starting.

The normal operation of the power plant, unless interconnected with other power sources, will be isochronous mode (i.e., constant frequency) with load sharing between parallel connected generators. The connection shown in Fig. 3 going to paralleling lines on other machines provides the load sharing function. Mode switching is provided automatically within the control circuits developed for the system.

A short review of fundamentals of stable parallel operation of generators may be of value.

D. Review of Diesel Generators Operating in Parallel

A diesel generator operating singly and supplying electric power independent of any other generator would normally operate in an isochronous (constant speed frequency) mode. The governor would automatically adjust the fuel setting as the power load varies to keep the speed constant (Fig. 4a).

Unless electronic governors are used with forced load sharing provisions, two or more generators cannot be operated in parallel with all generators in isochronous mode. Each machine would attempt to compensate individually for any speed variation and the machines would "fight" each other. The loads on the individual generators would be indeterminate and would swing from no-load up to the maximum load connected to the power bus. This would cause protective gear to operate and disconnect the generators due to overload.

One way of overcoming this instability is to speed droop each of the machines in proportion to the power it is delivering. Any machine tending to take a higher proportion of the load will tend to slow down below the speed of the other generators, but as it is forced to stay in synchronism with the others it will shirk the additional load. On the other hand, any machine tending to deliver less than its proportionate share of the total load will naturally tend to increase its speed. As the speed is contrained to correspond with the power system fre-

quency, this will result in additional load being delivered by the generator (Fig. 4b).

The resulting stability of operation is achieved at the cost of overall power system frequency droop with load. Compensation is usually manually performed by governor control switch.

A second mode of operation that gives stability is to operate all machines in droop except one which operates isochronously. The isochronous machine functions to maintain power system frequency constant (Fig. 4c).

Considering operation under varying power system loads, all machines in the droop mode tend to increase speed as load decreases. The isochronously operating machine shirks its proportion of the load when this occurs, and its share is imposed on the drooped machines to hold them down to system frequency. Conversely, load increase tends to slow down the machines in droop, while the isochronous machine regulates its fuel for the desired speed. The isochronous machine delivers increased load, while the drooped machines shirk any additional load.

The price paid for this solution is that the isochronously operating machine can not be run normally at the same load as the drooped machines. It must have reserve power capacity to supply increased load beyond the preset loads of the machines in droop. Another problem can occur if the total load of the system drops below that normally carried by the drooped machines. This causes the isochronous machine to motor on the drooped machines at a speed above that required for 60-hertz operation.

The most satisfactory solution of the problem can be achieved only by electrically operated governors which are employed in the power systems. Each governor can be set for isochronous operation with its load sensor control interconnected by bus wires to the load sensor circuits of the other machine governors. Any unbalance in generator kilowatt loading causes an error signal on the bus wires which automatically force-shares all generator kilowatts.

E. Voltage Regulation With Cross-Current Reactive Load Control

The voltage regulators installed are of the solid-state type. Their function is to maintain a preset generator and power system voltage value when generators are operating singly or in parallel with others.

With one generator connected to the power system, the voltage regulator action is to control the excitation of the generator and maintain the preset generator voltage under varying load conditions. The function of the voltage regulator is to compensate for inherent generator voltage droop as load increases, by increasing field excitation. This compensation is achieved by comparing the generator output voltage with a reference voltage, and the error difference is amplified and fed to the exciter.

With machines operating in parallel, if the individual voltage regulators attempted to maintain precisely constant individual generator voltage, this would produce unstable reactive load sharing. The problem is very similar in nature to that already described for real power (kilowatt) sharing of isochronous engine-generators. If reactive power is considered instead of real power and the voltage regulator action substituted for the governor action, the similarities in the problem can be noted (Fig. 5).

To prevent "fighting" of the voltage regulators and the resulting reactive power load swings between generators, it is common practice to introduce voltage droop into each generator voltage regulator action. This drooping action is required to give stable reactive load sharing and is therefore introduced into the voltage regulator action as a direct function of the reactive component of the generator total load current.

Figure 6 shows paralleled generators operating with simple voltage regulator droop compensation. The minimum droop to achieve stable reactive power loading is set by the adjusting rheostats to minimize the power system voltage degradation. Manual voltage adjusting control is used to compensate for the droop and bring the power system voltage within acceptable limits.

A better method of maintaining stable reactive load sharing between machines is shown in Fig. 7 and has been used in these power systems. This is achieved by interconnecting the current transformers and voltage regulators of the paralleled generators. The popular term given to this interconnection is "cross-current compensation," and the current transformers are said to be "polygon-connected."

The method of connection forces reactive power load sharing between generators without accompanying voltage droop.

Referring to Fig. 7 it will be noted that current transformers are connected to their associated voltage regulators in a manner similar to that used for droop control but interconnections (a), (b), and (c) cause a completely different reaction. The individual current transformers generate current i_b. When each current value

is the same, this current passes through interconnections (a), (b), and (c), and the current transformers behave as though their secondary windings are short-circuited. The voltage regulator elements E1, E2, and E3 carry virtually zero current, provided the interconnections (a), (b), and (c) have low impedance.

For the case indicated, however, generator 1 is delivering more than its share of reactive power, leading to a difference current (Δi) which is superimposed on the balanced value i_b. Element E1 receives most of Δi and the reactive component of this current is active in causing the voltage regulator to reduce generation excitation.

The remainder of Δi passes through the interconnection (a) to the second voltage regulator, through element E2 in the direction causing increased excitation of generator 2. This current then passes through interconnection (b) and through the voltage regulator element E3, which increases excitation of generator 3 and then completes its circuit through interconnection (c) back to the current transformer. In this case with three machines in parallel, 2/3 of Δi will act through element E1 to reduce generator 1 excitation, and 1/3 of Δi will act through elements E2 and E3 to increase the excitation of generators 2 and 3.

Although it may appear that some of Δi passing through elements E2 and E3 would be shunted by CT2 and CT3, these current transformers represent such high impedances to Δi that their shunting effect is negligible.

The foregoing techniques provide all the normal control functions associated with an automatically operated plant. Further consideration had to be given to the controls to allow parallel operation of the automatic plant with an independent commercial power source if this is considered economically feasible in the future. Also, the design allows parallel operation with the manually operated Section A of the power plant.

F. Parallel Operation of Power Plant With Commercial Power Source

If commercial power is connected to the system, the commercial source will be isochronous. The automated power plant controls will automatically revert to speed droop operation and will carry a preset power load. As described in Subsection D, this provides good, stable operation. The commercial source will provide all variations in power required in excess of that generated by the plant.

To allow manual synchronizing of the two power systems and also to preset the kilowatts provided by the generators, the power plant is equipped with a power transfer control device (Fig. 8). This device is actually a simple dc power supply with manually variable output voltages compatible with the paralleling bus wire voltage levels of the electric governors. The output voltage of the power transfer control is manually set to correspond with the value across the governor bus wires by use of a built-in balancing indicator and then manually switched to the bus wires. Following this, movement of a control knob on the device varies the signal voltage on the bus wires which control all governor fuel settings on the connected engine-generator sets. By this control the power plant-generated frequency can be varied to allow manual synchronization and interconnection with the commercial power source. After interconnection, adjustment of the power transfer control knob allows presetting the kilowatts to be contributed by the power plant.

Reactive power division between the power plant and the commercial power source is treated differently from the kilowatt power division. It is desirable to keep reactive power load from the commercial system to a low value and use the power plant to supply all reactive power. The generators are fully rated to supply all the reactive load at no fuel cost, while commercial power companies charge for reactive power. The power plant equipment is therefore equipped to monitor the reactive power loading of the commercial power source (Figs. 9 and 10).

The monitoring meter is equipped with manually settable contacts which close whenever reactive power flows in the commercial power source interconnection. The contacts drive a motor-operated variable transformer which injects a voltage into the cross-current compensation circuit of the generator voltage regulators as shown in Fig. 9.

When the variable transformer is in the null position, corresponding with its center point, the voltage induced in the cross-current circuit is in phase with phase 2 voltage, and this has no effect on the voltage regulators. When the variable transformer is in other positions, the vector phase angle of the induced voltage changes, and the quadrature component of this voltage acts on the voltage regulators to raise or lower the generator excitations. The resulting effect is to maintain commercial power source reactive

power loading within the manual settings of the monitoring meter.

G. Parallel Operation of Power Plant Sections A and B

The present configuration demands that the manually operated Section A be considered as an isochronous power source. This means that the automatic Section B must be operated in the droop mode (governors and voltage regulators). The automatic Section B will deliver a preset portion of the load kilowatts and kilovars while the manually operated section will supply a variable portion of the load as power demand varies.

Complete integration of Sections A and B of the power plant is underway. This will provide a totally automated system, incorporating all the automatic features to both sections of the generator plant. The operation of the integrated system will be isochronous with zero frequency or voltage droop, load sharing of kilowatt and reactive load between generators in proportion to their ratings, and automatic starting and stopping control of all generators.

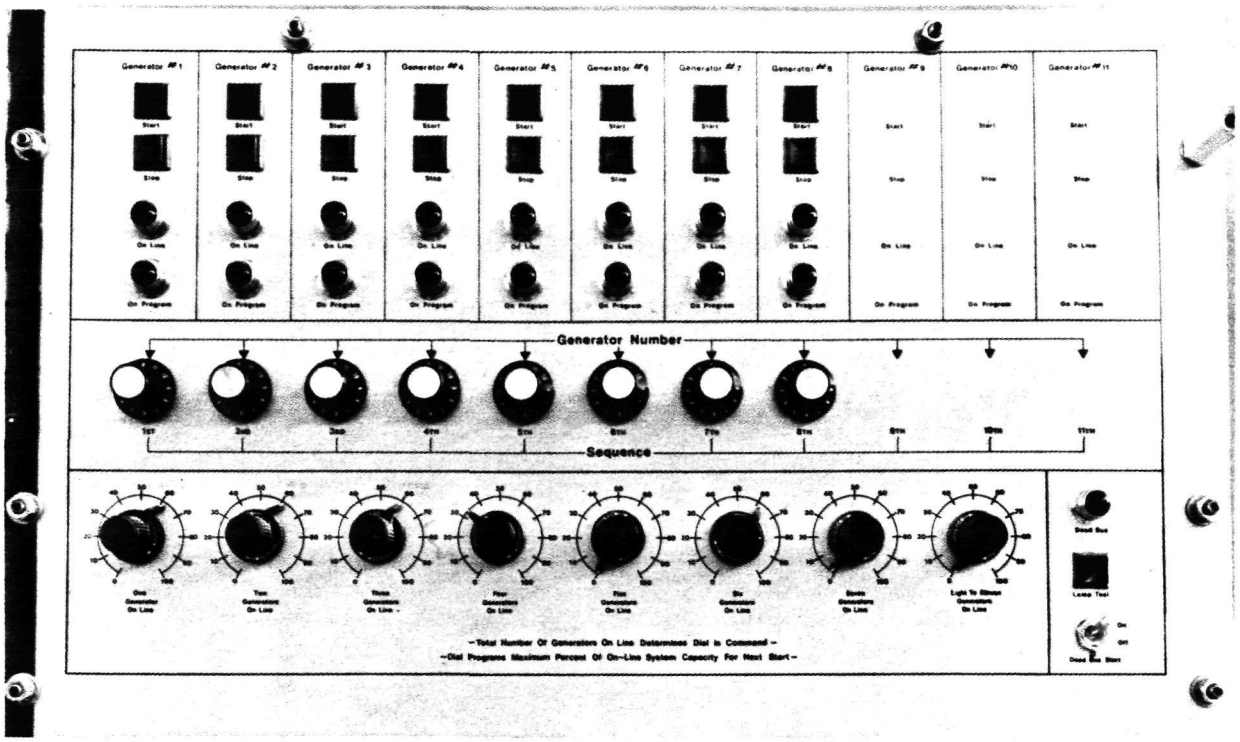

Fig. 1. Power system sequencer

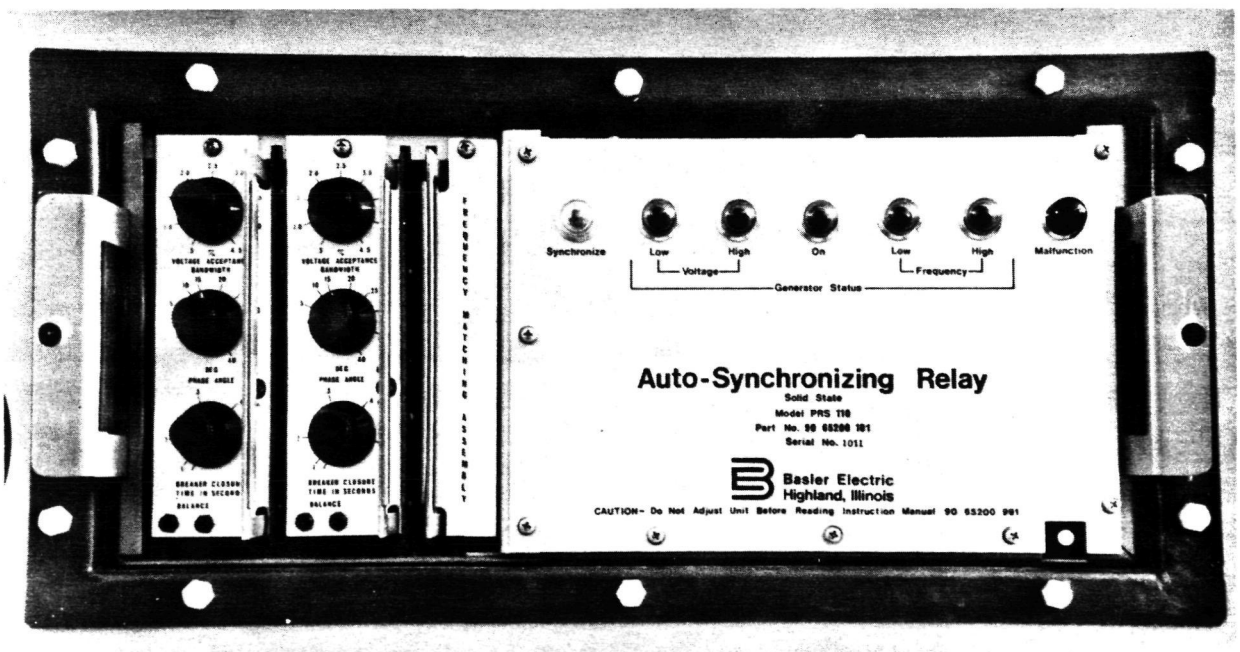

Fig. 2. Automatic synchronizer

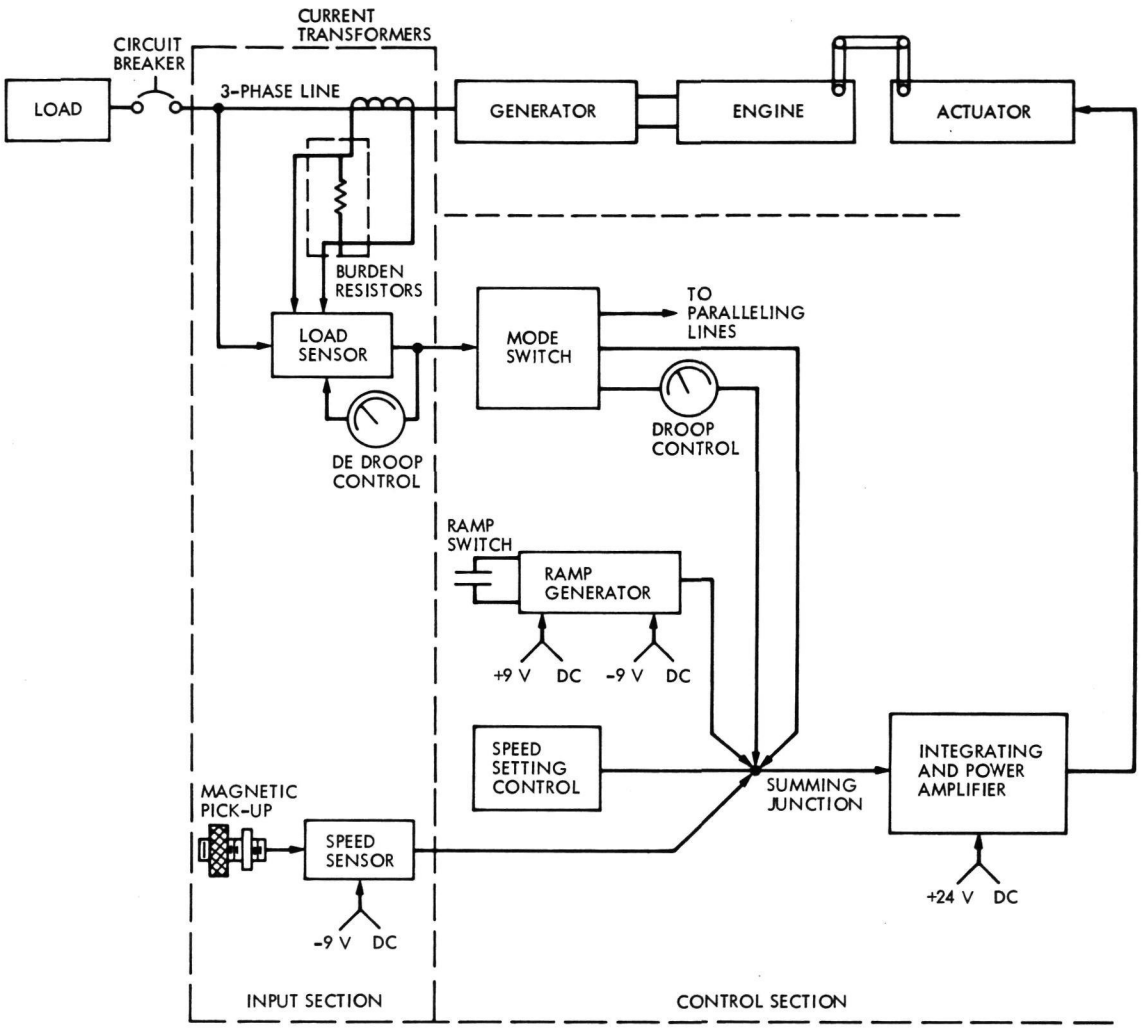

Fig. 3. Block diagram of electronic governor system

(a) SINGLE GENERATOR OPERATION - ISOCHRONOUS MODE

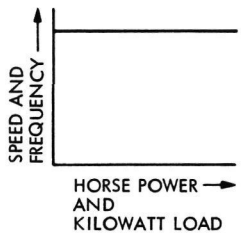

(b) MULTIPLE GENERATOR OPERATION - DROOP MODE

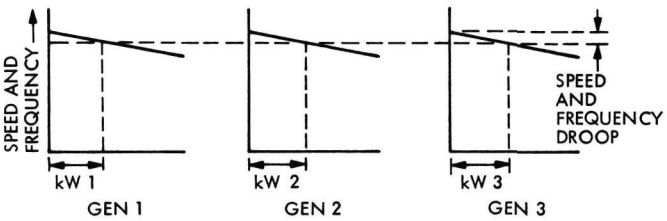

TOTAL kW LOAD = kW 1 + kW 2 + kW 3
kW 1 = kW 2 = kW 3

(c) MULTIPLE GENERATOR OPERATION - ONE GENERATOR ISOCHRONOUS

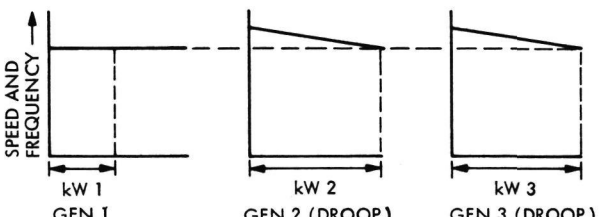

TOTAL kW LOAD = kW 1 + kW 2 + kW 3
kW 2 = kW 3 = CONSTANT: kW 1 VARIABLE

Fig. 4. Diesel-generator operating modes

(a) SINGLE GENERATOR OPERATION - CONSTANT VOLTAGE MODE

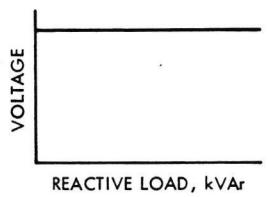

(b) MULTIPLE GENERATOR OPERATION - VOLTAGE DROOP MODE

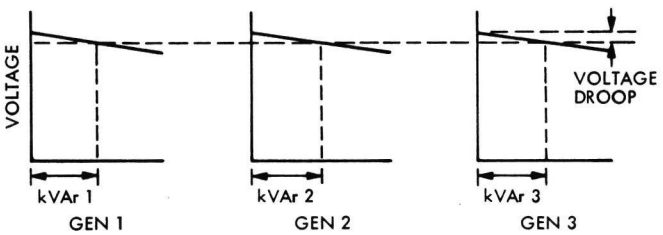

TOTAL kVAr LOAD = kVAr 1 + kVAr 2 + kVAr 3
kVAr 1 = kVAr 2 = kVAr 3

Fig. 5. Kilovar loading of generators

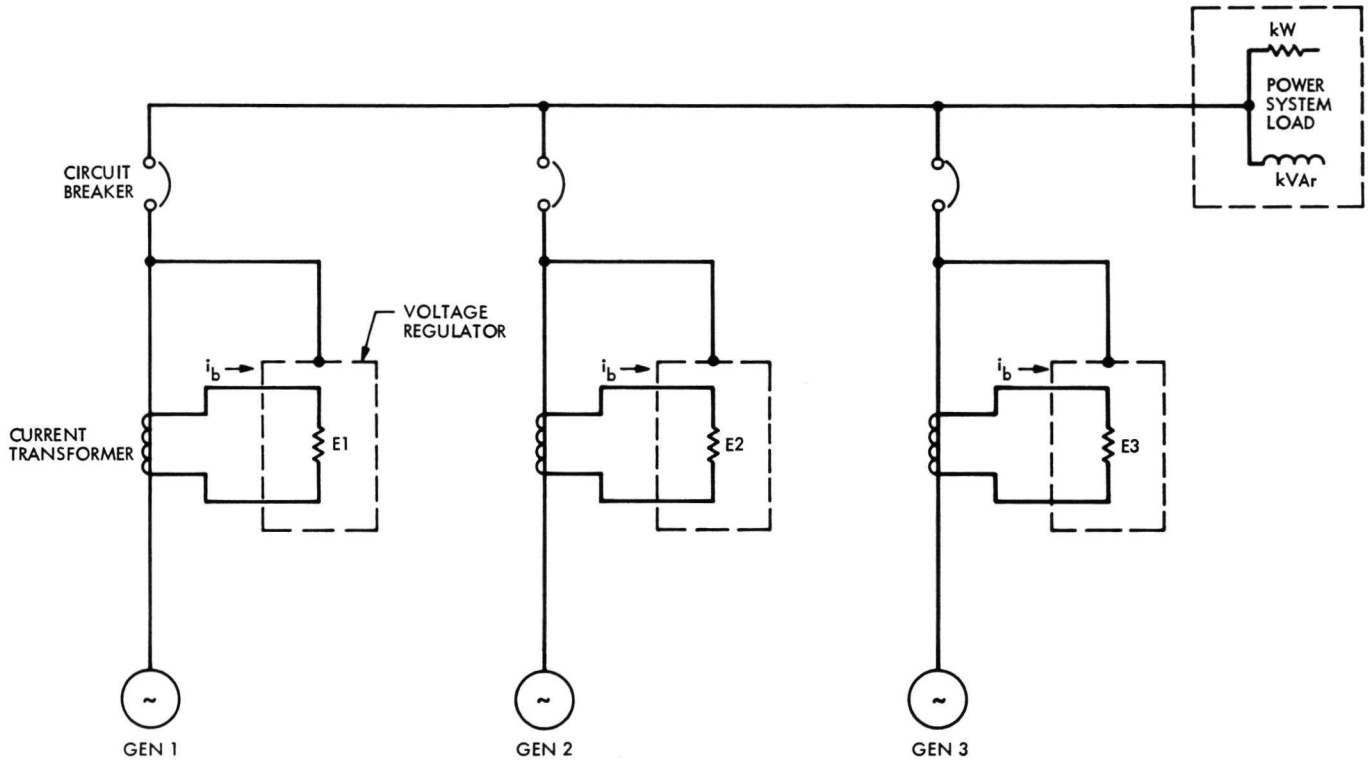

NOTE: REACTIVE COMPONENT OF i_b IN DIRECTION SHOWN REDUCES GENERATOR EXCITATION THROUGH VOLTAGE REGULATOR ELEMENTS E1, E2, AND E3

Fig. 6. Generator voltage regulators in droop mode

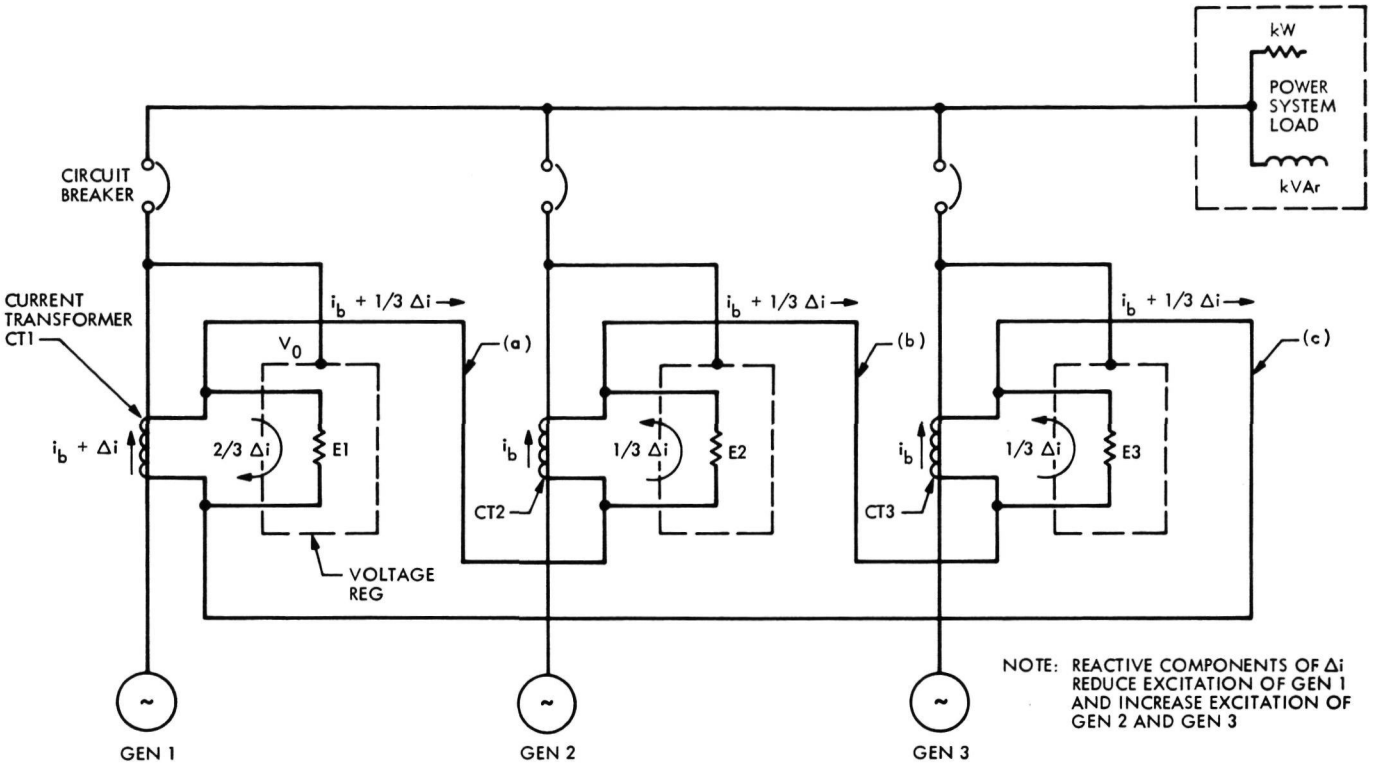

Fig. 7. Generator voltage regulators with cross-current compensation

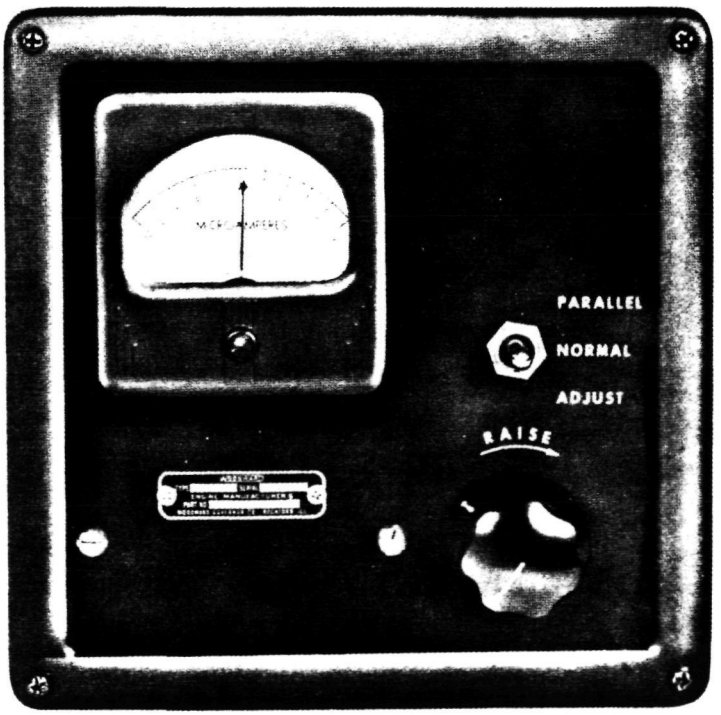

Fig. 8. Power transfer control

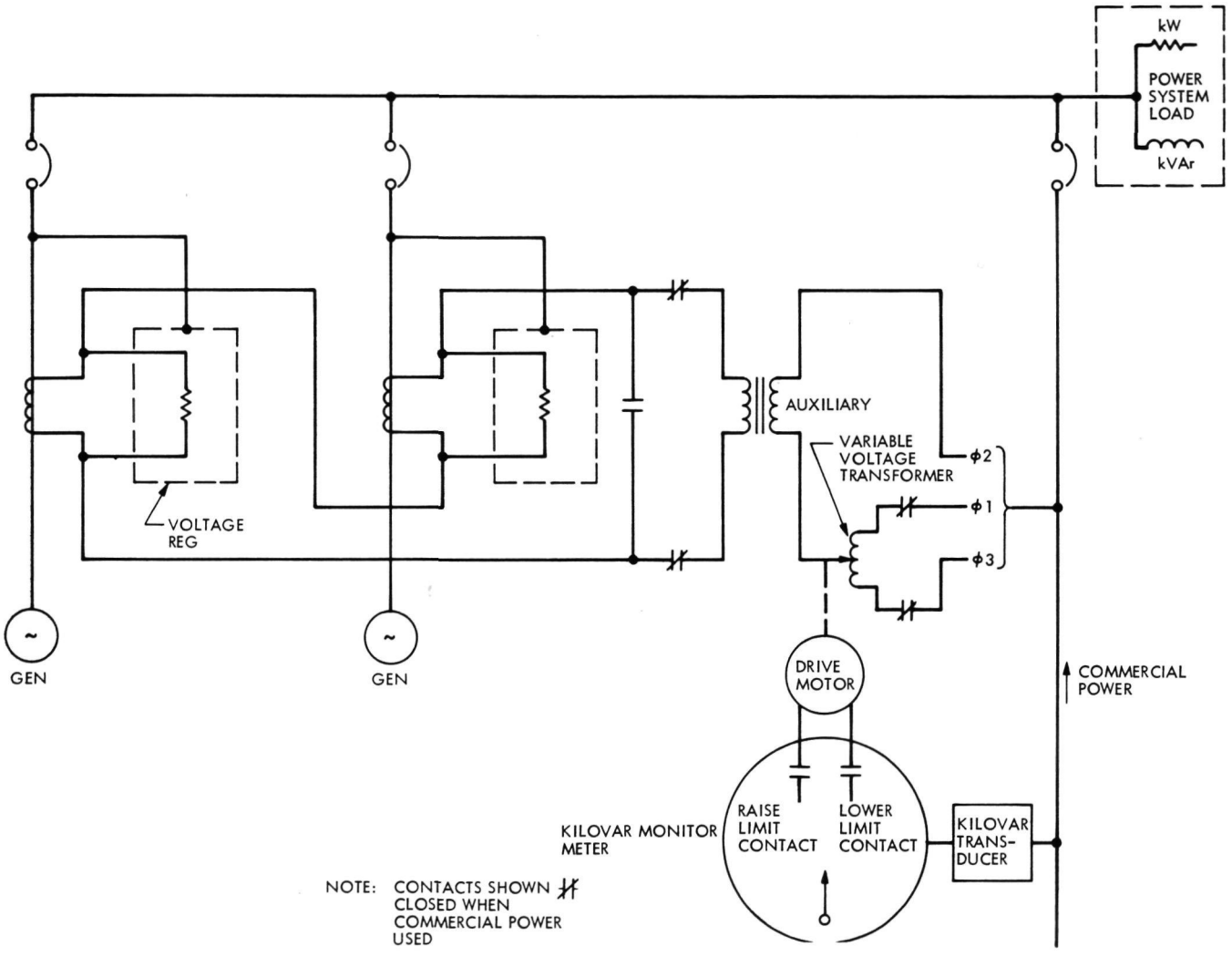

Fig. 9. Simplified circuit of modified cross-current compensation of generator voltage regulators when commercial power connected

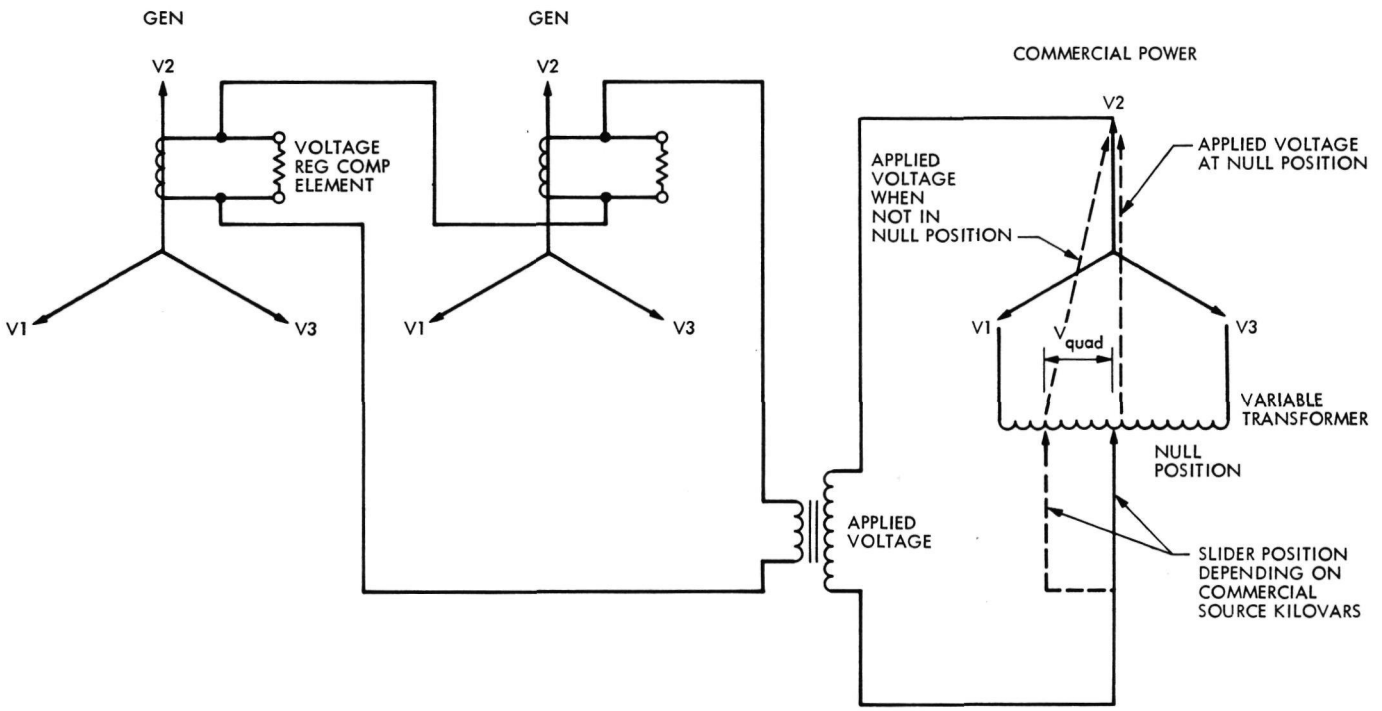

Fig. 10. Voltage vectors applied to voltage regulator cross-current compensation circuits

Upgrade of Heating System for Energy Conservation at DSS 62, Cebreros, Spain

J. M. Urech
Station Director, Cebreros, Spain

This report presents a description of the modification performed as part of the energy conservation program at the Cebreros, Spain, Deep Space Station (DSS 62) and the results obtained. The article was excerpted from the final engineering report on this project by E. H. Thom.

I. Summary

This report presents a description of the modification performed as part of the energy conservation program at the Cebreros, Spain, Deep Space Station (DSS 62) and the results obtained. The modification is based on the elimination of the air-conditioning boiler and the heating of the operations building by the waste heat from the power generator engines. Consequently, by transporting dissipated heat from the powerplant to the operations building, this modification will represent an energy savings of 70,000 liters per year in boiler fuel and a cost savings (at current prices) of $12,000 per year.

II. System Comparison

The following is a comparison of the major heat producing components comprising the former and the new heating systems.

A. Boiler (Former System)

The boiler is located in the operations building and was previously used to provide hot water for heating and ordinary purposes. It is an automatic unit capable of maintaining a constant temperature of 65–85°C and a flow of 220 liters per minute up to a maximum 140,000 kcal/hour. The annual fuel consumption of this unit is 70,000 liters under normal weather conditions.

B. Generators (New System)

The station powerplant contains four diesel generators capable of producing a total of 1,850 kW, divided as follows:

Three 500-kW units

One 350-kW unit

Normal station operations require about 400 kW with a normal generator configuration of two generators on the

C 3

line. Generator engine cooling is accomplished by radiators with electric fans. In this arrangement, the cooling water reaches a temperature of 85°C — heat which is wasted into the atmosphere.

The heat dissipated in the radiator is proportional to the load. Figure 1 shows the upper and lower load limits over a 24-hour period, as well as the heat dissipated at each limit. As indicated, the heat wasted at the lower limit (190,000 kcal/hour) is higher than the maximum output of the referenced boiler, thus providing a clear advantage over the former system.

III. Implementation

A. Technical Background

The possibility of bringing the water from the engines directly to the operations building was rejected primarily for the following reasons:

(1) Danger of failures which would affect the engines.

(2) Incompatibility between circuit flows.

(3) Pressure drops or increases which would jeopardize engine operation.

(4) Static pressure increases, caused by variations in building heights, which would affect the engine circuit.

These and other reasons recommended the use of a heat exchanger in order to maintain the independence of both circuits while transferring heat from one to the other. Heat exchanger capacity permits a maximum heat transfer of 225,000 kcal/hour from the primary to the secondary circuit when the temperatures of both circuits are:

Primary	inlet	85°C
	outlet	65°C
Secondary	inlet	60°C
	outlet	75°C

B. Configuration and Materials

Since the amount of heat to be dissipated in the primary circuit is always greater than the requirements of the second circuit, some of this heat must continue to be dissipated in the radiator. To facilitate this function, a three-way motorized valve has been added. This valve divides the water flow to permit direct flow to the engine and indirect flow via the radiator. In this way, the water entering the engine can be maintained at 60°C.

The temperature of the return water is kept at 60°C to ensure that the thermostatic bypass of the engine permits sufficient flow in the outside circuit and thereby maintains adequate heat exchanger performance. Each engine has been provided with a proportional thermostat connected via a selector switch to the heating engine. This controls the motorized valve which maintains the inlet temperature at the pre-established 60°C.

The valve drive motor contains a spring that returns the valve to the radiator position. This setting allows the entire flow to circulate through the radiator. The purpose of the device is to eliminate the possibility of an engine shutdown due to overheating indirectly caused by an electrical failure in the valve control.

C. Costs

It should be noted that the implementation has been performed employing on-hand or surplus materials whenever possible. Furthermore, no additional costs for project preparation or implementation are applicable since these tasks were undertaken entirely by station personnel. In summation, this item includes only the costs of purchased materials as follows:

Heat exchanger	$ 4,330
Pumps	1,025
Three-way valve	687
Insulation	2,760
Piping, manual valves, supports, screws, etc.	5,629
Total	$14,431

IV. Conclusions

System operation has been completely satisfactory with an available water flow of 250 liters/minute and a temperature on arrival at the operations building of 71°C. Moreover, a potential increase of 60,000 kcal/hour has been obtained over the previous system.

Despite the fact that no extremely cold days have been experienced since its implementation (minimum temperature 10°C), the new system promises to yield excellent performance due to its large heat reserve.

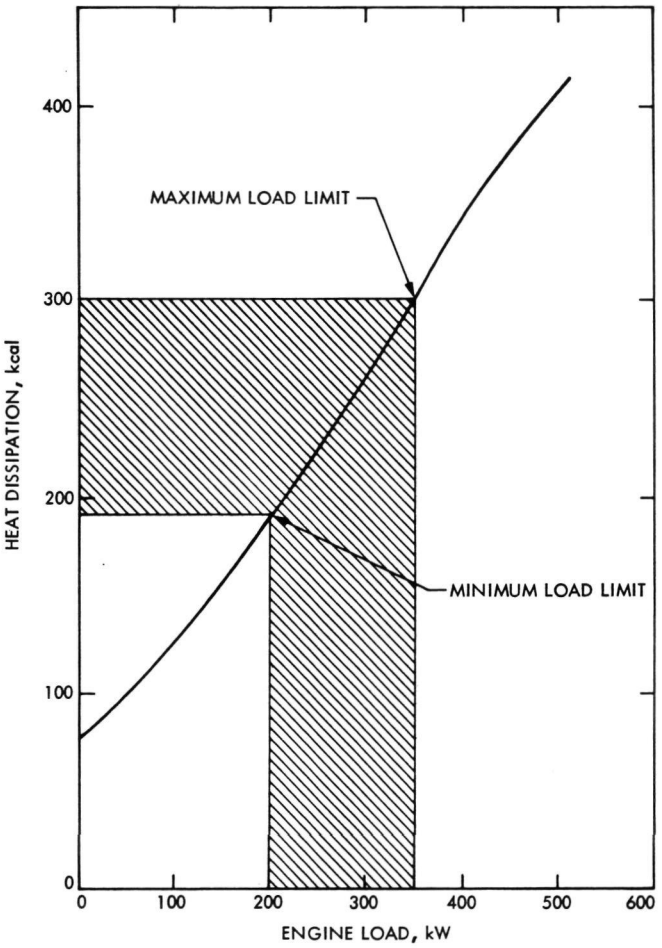

Fig. 1. Engine heat dissipation vs generator load

Pseudo-DRVID: A New Technique for Near-Real-Time Validation of Ranging System Data

A. L. Berman
Network Operations Office

Near-real-time validation of doppler and angular radio metric data has been quite successful and an established fact for the last decade. Near-real-time validation of ranging system data, however, has for the most part been ineffective. Reasons are here presented as to why the doppler and angle validation techniques cannot successfully be applied to ranging system data. A new technique is described which can validate sequential range acquisitions in near-real-time to the 10-meter level.

I. Introduction

Near-real-time validation of doppler frequency data (the primary orbit determination data type) has been generally performed since 1965 and has proved to be enormously successful in identifying problem areas within the Deep Space Network (DSN) tracking system in a convenient and timely fashion. On the other hand, near-real-time validation of ranging system data (the secondary, but very important, orbit determination data type), although an oft-iterated and earnestly sought after goal, has in general proved both elusive and unsatisfactory. In particular, near-real-time validation of ranging system data from the current prime ranging system, the Planetary Ranging Assembly (PRA), has (until recently) been superficial and unevenly performed. The reasons why the current near-real-time radio metric data validation techniques, which have proved so successful with doppler data, fail when applied to ranging system data become apparent when the differences in the nature of doppler data acquisition vs ranging system data acquisition are considered. The crux of these differences is that the doppler system makes frequent measurements which are independent in and of themselves, while the PRA makes infrequent measurements of a quantity (not identically range!) which will, when combined with very precise orbital foreknowledge, produce a range measurement. In the following sections, the difficulties with and the inappropriateness of applying the current near-real-time radio metric data validation techniques to ranging system data will be explored. Finally, a new and far more satisfactory technique, referred to as "Pseudo-

DRVID"[1] will be presented, in combination with some preliminary, but illustrative results of the new technique.

II. Description of Current Near-Real-Time Radio Metric Data Validation Techniques

The current near-real-time radio metric data validation techniques, which have so successfully validated acquired radio metric data for navigation purposes and have additionally served to rapidly pinpoint malfunctions in the tracking system, begin with the simple expedient of comparing each time-dependent radio metric data sample with a corresponding "predicted" value. To facilitate a discussion of the technique, the following notation is defined:

If

$X(t)$ = radio metric data type

then

$$\Delta_X(t_i) \equiv X_A(t_i) - X_P(t_i)$$

where

$\Delta_X(t_i)$ = the "residual" of data type X at time t_i

$X_A(t_i)$ = acquired ("actual") data type X at time t_i

$X_P(t_i)$ = expected ("predicted") data type X at time t_i

If one has only a single or perhaps a few residuals during any particular time interval of interest, the amount of information that is yielded by this process is perforce severely limited. Basically, about the most that one can conclude with reasonable assurance is that:

Occurrence	Conclusion
Large residual	Invalid data
Small residual	Valid data, with the residual indicative of the magnitude of the prediction error

One of course strives to use accurate predictions in the process as it is the level of confidence in the predictions which determines what is "large" and what is "small" for the above. On the other hand, if one has a large population of residuals to work with, as is the usual case with the acquisition of both doppler and angular data, one can infer a great deal in addition to the above. These inferences can be broadly categorized as follows:

(1) *Signature.* By examining a large population of residuals, one can detect patterns ("signatures") of various types of systematic tracking system malfunctions. A prime example of this effect would be an error in the station time standard.

(2) *Noise.* By examining the standard deviation ("noise") of a large population of residuals (after a least squares curve fit), one can detect tracking system malfunctions which result in random errors. A prime example of this effect would be a failure of the doppler resolver counter.

As has already been stated, the above procedures have worked very well indeed for validating doppler data for navigation purposes as well as monitoring the health of the tracking system. It is now necessary to examine the applicability of the above techniques to Ranging System data (specifically the PRA).

III. Applicability of Current Near-Real-Time Radio Metric Data Validation Techniques to PRA Data

The PRA has been designed for use in cases where a very accurate estimate of the range at any given time already exists. The relationship between range and the output of the PRA is as follows:

$$R(t) = K[M(t)] + RPRA(t)$$
$$0 \leq RPRA(t) < K$$

where

$R(t)$ = range at time t

K = ambiguity resolution factor (a quantized input, in units of $R(t)$)

$M(t)$ = integer, determined from independent orbital knowledge

$RPRA(t)$ = "scaled" output of the PRA (i.e., in the same units as $R(t)$)

The ambiguity resolution factor K is extremely small when compared to the absolute range R, and in practice is selected (from 20 possible values) to be somewhat

[1]Differenced range vs integrated doppler. The name was chosen because one can discern a faint similarity between the relationship of "Pseudo-DRVID" to actual (PRA-produced) DRVID and of "Pseudo-Residuals" to actual (orbit-determination-produced) angle and doppler residuals.

larger than the current navigation estimate of the range uncertainty. It is not chosen indiscriminately larger than the range uncertainty as there is a penalty associated with increasingly large Ks (lengthened acquisition time).

In the past, it has always been somewhat blithely assumed that a "range" residual could be obtained from the PRA output and range predictions, and most probably it has been this assumption which has confused the issue of ranging system data validation and stymied efforts to approach the problem with differing viewpoints. The pith of the matter is:

> One cannot obtain a "range" residual from PRA output as one directly obtains doppler residuals from doppler data; one can only obtain, at best, a "PRA output" residual!

It is then necessary to inquire as to the composition and usefulness of a "PRA" residual; more specifically, one would like to determine what relationship the PRA residual bears to a range residual. The determination of this relationship is as follows:

Let the actual range at a time t_i be

$$R_A(t_i) \equiv K[M(t_i)] + RPRA_A(t_i)$$

so that a valid PRA acquisition would yield

$$RPRA(t_i) \cong RPRA_A(t_i)$$

(The above assumes that $RPRA_A$ is not within a few meters of 0 or K—this event having a very low probability of occurrence for typical acquisitions.)

Now assume that the predictions to be used have an error $Z(t_i)$ so that

$$R_P(t_i) \equiv K[M(t_i)] + RPRA_A(t_i) + Z(t_i)$$

One can now calculate a "predicted" PRA output

$$\begin{aligned} RPRA_P(t_i) &\equiv R_P(t_i) \text{ modulo } K \\ &= \{K[M(t_i)] + RPRA_A(t_i) + Z(t_i)\} \text{ modulo } K \end{aligned}$$

Having now obtained R_A, R_P, $RPRA_A$, and $RPRA_P$, one can construct a range residual and a corresponding PRA residual as follows:

$$\begin{aligned} \Delta_R(t_i) &\equiv R_A(t_i) - R_P(t_i) \\ &= \{K[M(t_i)] + RPRA_A(t_i)\} \\ &\quad - \{K[M(t_i)] + RPRA_A(t_i) + Z(t_i)\} \\ &= -Z(t_i) \end{aligned}$$

and

$$\begin{aligned} \Delta_{PRA}(t_i) &\equiv RPRA_A(t_i) - RPRA_P(t_i) \\ &= RPRA_A(t_i) \\ &\quad - \{K[M(t_i)] + RPRA_A(t_i) + Z(t_i)\} \text{ modulo } K \end{aligned}$$

$$= \begin{cases} -Z(t_i) \\ \quad \text{if } 0 \leq RPRA(t_i) + Z(t_i) < K \\ -Z(t_i) - JK \qquad J = \text{integer} \\ \quad \text{if } RPRA(t_i) + Z(t_i) < 0 \\ -Z(t_i) + JK \qquad J = \text{integer} \\ \quad \text{if } RPRA(t_i) + Z(t_i) \geq K \end{cases}$$

The final result is that:

$$\Delta_R(t_i) = \Delta_{PRA}(t_i) \text{ if } 0 \leq RPRA(t_i) + Z(t_i) < K$$

$$\Delta_R(t_i) \neq \Delta_{PRA}(t_i) \text{ if } RPRA(t_i) + Z(t_i) \begin{cases} < 0 \\ \geq K \end{cases}$$

Since K is selected on the basis of being only somewhat larger than the estimated uncertainty ($\approx Z(t_i)$), the inequality (above) will occur quite frequently, and hence there is no way that a PRA residual can be confidently equated to a range residual in near-real-time. Rendering the PRA residual even more useless in an absolute sense is the modulo character of the PRA data, which means that no matter how the PRA might malfunction, an "invalid" PRA residual statistically has an (averaged) 50% chance of being a smaller (magnitude) number than the corresponding "valid" PRA residual (assuming prediction accuracies are never significantly below the smallest possible K, or about 300 meters)—this property being in sharp contrast to the doppler and angle situation.

To illustrate with a very possible case, consider the following:

Let

$$K \equiv 18.2 \text{ km}$$

and

$$Z(t_i) \equiv 9.1 \text{ km}$$

Then

$$\Delta_R(t_i) = -9.1 \text{ km}$$

and

$$\Delta_{PRA}(t_i) = \begin{cases} -9.1 \text{ km if } RPRA(t_i) < 9.1 \text{ km} \\ +9.1 \text{ km if } RPRA(t_i) \geq 9.1 \text{ km} \end{cases}$$

The above results in the following:

(1) 50% chance of $\Delta_{PRA} \neq \Delta_R$.

(2) 50% chance of any random PRA output yielding a smaller absolute PRA residual than the correct PRA residual.

Finally, even if one could somehow obtain range residuals in near-real-time from PRA residuals, the powerful tool of examining a population of residuals for signature and noise, as is done with angle and doppler validation, would not be available because only a few PRA range acquisitions are normally made during a typical pass.

To recapitulate: past efforts to validate PRA data with the same techniques used so successfully to validate doppler and angle data were foreordained to failure because:

(1) It was falsely assumed that one could obtain range residuals, when in fact one can only obtain "PRA" residuals.

(2) Because of the very small (relative to absolute range) span of PRA output ($0 \leq$ PRA data $< K$), invalid (or random for that matter) PRA residuals are (on average) the same size as valid PRA residuals, thus to a considerable extent destroying the usefulness of a PRA residual—in marked contrast to the situation with doppler and angle residuals.

(3) Since few PRA measurements are usually made in any given pass, little "signature" or "noise" information would be available, even if range residuals could be reconstructed from PRA residuals in near-real-time.

IV. The Pseudo-DRVID Technique

It was shown in Section III that the technique of directly forming "actual" minus "predicted" residuals cannot be effectively applied to PRA data; the Pseudo-DRVID technique can be viewed as a slightly rearranged variation of the basic residual scheme, viz:

> Consider that two or more PRA ranging acquisitions are performed within a single pass. Allow the earliest PRA acquisition to be the "predict," which is updated to the time of a latter PRA ranging acquisition (the "actual") with ease and extreme accuracy by means of integrated doppler between the two PRA acquisitions. Using this process a "range" residual between the two PRA measurements can be formed which will include only the actual PRA data errors plus DRVID. Normally, the DRVID effect is on the order of meters[2], so that one might expect validation between the two acquisitions down to the several-meter level. The pivotal feature of this scheme is that it obviates the necessity for any orbital predictions, which is the very requirement that hamstrings the current techniques when applied to PRA data.

The derivation of the Pseudo-DRVID equations begins with the two way doppler equation

$$D2 = 96\frac{240}{221}TSF_R - 96\frac{240}{221}TSF_T\left\{1 - \frac{1}{c}\left[\left(\frac{dr}{dt}\right)_{up} + \left(\frac{dr}{dt}\right)_{dn}\right]\right\} + \text{bias}$$

where

TSF_R = track synthesizer frequency (cps) at received time

TSF_T = track synthesizer frequency (cps) at transmitted time

$\left(\frac{dr}{dt}\right)_{up}$ = 2-way uplink range rate, m/s

$\left(\frac{dr}{dt}\right)_{dn}$ = 2-way downlink range rate, m/s

c = speed of light, m/s

bias = doppler bias frequency (cps), normally:
Block III receiver, 10^6 cps
Block IV receiver, 5×10^6 cps

[2]Except near solar conjunctions, when DRVID becomes 10s or 100s of meters.

However, during a ranging pass the TSF is not (usually) changed, so that

$$TSF_R = TSF_T$$

and

$$D2 = 96\frac{240}{221}\,TSF - 96\frac{240}{221}TSF\left\{1 - \frac{1}{c}\left[\left(\frac{dr}{dt}\right)_{up} + \left(\frac{dr}{dt}\right)_{dn}\right]\right\} + \text{bias}$$

$$= 96\frac{240}{221}\left(\frac{TSF}{c}\right)\left[\left(\frac{dr}{dt}\right)_{up} + \left(\frac{dr}{dt}\right)_{dn}\right] + \text{bias}$$

or

$$D2 - \text{bias} = 96\frac{240}{221}\left(\frac{TSF}{c}\right)\left[\left(\frac{dr}{dt}\right)_{up} + \left(\frac{dr}{dt}\right)_{dn}\right]$$

Assuming that the difference in round trip range (RTR) is desired between the times t_a and t_b (and ignoring DRVID), one merely integrates the above equation as follows:

$$\int_{t_a}^{t_b}[D2 - \text{bias}]\,dt = \int_{t_a}^{t_b} 96\frac{240}{221}\left(\frac{TSF}{c}\right)\left[\left(\frac{dr}{dt}\right)_{up} + \left(\frac{dr}{dt}\right)_{dn}\right]dt$$

defining

$CNTS(t)$ = doppler counter reading at time t, cycles

with

RTR = round trip range, m

$= r_{up} + r_{dn}$

r_{up} = uplink range, m

r_{dn} = downlink range, m

$$\left(\frac{dr}{dt}\right)_{up} = \frac{d}{dt}(r_{up})$$

$$\left(\frac{dr}{dt}\right)_{dn} = \frac{d}{dt}(r_{dn})$$

so that one has

$$\int_{t_a}^{t_b}(D2 - \text{bias})\,dt = \int_{t_a}^{t_b}[D2]\,dt - \int_{t_a}^{t_b}(\text{bias})\,dt$$

$$\int_{t_a}^{t_b}(D2)\,dt = CNTS(t_b) - CNTS(t_a)$$

$$\int_{t_a}^{t_b}(\text{bias})\,dt = (t_b - t_a)(\text{bias})$$

and

$$\int_{t_a}^{t_b} 96\frac{240}{221}\left(\frac{TSF}{c}\right)\left[\left(\frac{dr}{dt}\right)_{up} + \left(\frac{dr}{dt}\right)_{dn}\right]dt$$

$$= 96\frac{240}{221}\left(\frac{TSF}{c}\right)\int_{t_a}^{t_b}\left[\left(\frac{dr}{dt}\right)_{up} + \left(\frac{dr}{dt}\right)_{dn}\right]dt$$

$$\int_{t_a}^{t_b}\left[\left(\frac{dr}{dt}\right)_{up} + \left(\frac{dr}{dt}\right)_{dn}\right]dt$$

$$= \int_{t_a}^{t_b}\left[\frac{d}{dt}(r_{up}) + \frac{d}{dt}(r_{dn})\right]dt$$

$$= \int_{t_a}^{t_b}\frac{d}{dt}(r_{up} + r_{dn})\,dt$$

$$= \int_{t_a}^{t_b} d(r_{up} + r_{dn}) = \int_{t_a}^{t_b} d(RTR)$$

$$= RTR(t_b) - RTR(t_a)$$

finally yielding

$$RTR(t_b) - RTR(t_a) = \frac{CNTS(t_b) - CNTS(t_a) - \text{bias}\,(t_b - t_a)}{96\frac{240}{221}\left(\frac{TSF}{c}\right)}$$

Thus, simply by using the TSF, the doppler bias, and the doppler (cumulative) counter readings, one can rather easily and extremely accurately translate one range to a subsequent range, and hence be in a position to validate sequential PRA ranging acquisitions.

The complete algorithm is detailed below. It is essentially the equation above; however, it is presented in the form

$$\text{Pseudo-DRVID} = \Delta PRA(t_b, t_a) - \Delta DOP(t_b, t_a)$$

where

$$\Delta PRA(t_b, t_a) = \begin{cases} RPRA(t_b) - RPRA(t_a) \\ \text{if } RPRA(t_b) - RPRA(t_a) \geqq 0 \\ RPRA(t_b) - RPRA(t_a) + K \\ \text{if } RPRA(t_b) - RPRA(t_a) < 0 \end{cases}$$

and

$$\Delta DOP(t_b, t_a) = \begin{cases} [RTR(t_b) - RTR(t_a)] \text{ modulo } K \\ \quad \text{if } RTR(t_b) - RTR(t_a) \geqq 0 \\ [RTR(t_b) - RTR(t_a)] \text{ modulo } K + K \\ \quad \text{if } RTR(t_b) - RTR(t_a) < 0 \end{cases}$$

Additionally, doppler counter rollovers are accounted for, the explicit functional dependence of K upon the number of ranging components is displayed, and the quantities are scaled to be in meters.

Assume two PRA acquisitions at acquisition times of t_a and t_b and define

$PRTR(t)$ = PRA data in RU, for acquisition time $(T0) = t$

N = number of components

$RLOVRS$ = number of doppler counter "rollovers" between t_a and t_b

$$K = K(N) = \frac{c}{48(TSF)}(2^{N+10})$$

so that

$$\Delta PRA(t_b, t_a) = \frac{c}{48(TSF)}[PRTR(t_b) - PRTR(t_a) + Y]$$

where

$$Y = \begin{cases} 0 & \text{if } PRTR(t_b) - PRTR(t_a) \geq 0 \\ 2^{N+10} & \text{if } PRTR(t_b) - PRTR(t_a) < 0 \end{cases}$$

and

$$\Delta DOP(t_b, t_a) = \left\{\frac{221}{96(240)}\left(\frac{c}{TSF}\right)[CNTS(t_b) - CNTS(t_a) + RLOVRS(10^{10}) - \text{bias}(t_b - t_a)]\right\} \text{ modulo}\left[\left(\frac{c}{TSF}\right)\frac{2^{N+6}}{3}\right] + W$$

where

$$W = \begin{cases} 0 & \text{if } RTR(t_b) - RTR(t_a) \geqq 0 \\ \left(\frac{c}{TSF}\right)\frac{2^{N+6}}{3} & \text{if } RTR(t_b) - RTR(t_a) < 0 \end{cases}$$

with the final result of

$$\text{Pseudo-DRVID} = \Delta PRA(t_b, t_a) - \Delta DOP(t_b, t_a)$$

V. Pseudo-DRVID Results

Tables 1 through 4 present results of applying the Pseudo-DRVID algorithm to selected Mariner 10 ranging passes. The tables are arranged to span the type of results possible (i.e., in terms of percent of valid acquisitions and degree of correspondence for the valid acquisitions) as follows:

Table	DSS	Date, 1975	Characterization of results
1	43	March 15	Excellent
2	63	March 15	Excellent
3	63	February 12	Fair
4	43	February 27	Poor

Table 5 presents some miscellaneous statistics for the data presented in the first four tables (it should be noted that all the Pseudo-DRVID results in Table 1 through 5 have been presented as absolute differences). The net result of the data presented in the tables is to show that the Pseudo-DRVID algorithm can validate good (sequential) PRA acquisitions by showing correspondence between acquisitions down to the 10-meter level.

VI. Conclusions

Past attempts at ranging system near-real-time data validation have generally been ineffective, primarily because the vast differences in the nature of ranging system data and, in particular, PRA ranging data, as compared to doppler and angular radio metric data, were not completely considered—thus leading to attempts to use techniques for ranging system data validation which are not really applicable. The "Pseudo-DRVID" technique presented here can validate sequential PRA acquisitions down to the 10-meter level and is now operational for near-real-time validation of PRA data.

Acknowledgment

The author wishes to acknowledge the contribution of Larry E. Bright, who coded the pseudo-DRVID algorithm for operational use and processed the Mariner 10 data presented herein.

Bibliography

Berman, A. L., "Validation of Sequential Range Measurements—Or, Do-It-Yourself DRVID," IOM 421G-75-048, Jet Propulsion Laboratory, Pasadena, Calif., March 18, 1975 (an internal document).

Martin, W. L., "Information Systems: A Binary-Coded Sequential Acquisition Ranging System," Space Programs Summary 37-57, Volume II, Jet Propulsion Laboratory, Pasadena, California, May 31, 1969.

Spradlin, G., and Schlaifer, R., "The Planetary Operational Ranging Subsystem (PRA)," IOM 421G-75-019, Jet Propulsion Laboratory, Pasadena, Calif., Jan. 30, 1975 (an internal document).

Table 1. Pseudo-DRVID PRA data validation, DSS 43, March 15, 1975

$(T0)_b^a$	$(T0)_a^a$	Pseudo-DRVID	
		Meters	RU
Valid acquisitions			
21:15:00	20:30:00	5	17
23:25:00	22:00:00	7	23
00:55:00	00:10:00	2	8
02:50:00	01:40:00	9	32
06:00:00	03:45:00	5	19
Invalid acquisitions			
20:30:00[b]	19:45:00	272	953
04:30:00	03:45:00[b]	33,957	118,851
05:15:00	03:45:00[b]	287	1,004

[a]Times in GMT.
[b]The "good" acquisition of the pair.

Table 2. Pseudo-DRVID PRA data validation, DSS 63, March 15, 1975

$(T0)_b^a$	$(T0)_a^a$	Pseudo-DRVID	
		Meters	RU
Valid acquisitions			
09:45:00	09:15:00	16	57
10:45:00	10:15:00	14	51
11:45:00	11:15:00	8	27
13:15:00	12:45:00	6	22
14:15:00	13:15:00	13	46
Invalid acquisitions			
12:15:00	11:45:00[b]	2,349	8,222
13:45:00	13:15:00[b]	40,406	141,421

[a]Times in GMT.
[b]The "good" acquisition of the pair.

Table 3. Pseudo-DRVID PRA data evaluation, DSS 63, February 12, 1975

$(T0)_b^a$	$(T0)_a^a$	Pseudo-DRVID	
		Meters	RU
Valid acquisitions			
06:55:00	06:20:00	5	19
07:40:00	06:55:00	5	19
10:30:00	09:05:00	26	93
11:15:00	10:30:00	9	33
Invalid acquisitions			
08:30:00	07:40:00[b]	4,686	16,401
09:05:00[b]	08:30:00	8,765	30,676
09:45:00	09:05:00[b]	74,871	262,050
12:45:00	11:15:00[b]	23,408	81,929

[a]Times in GMT.
[b]The "good" acquisition of the pair.

Table 4. Pseudo-DRVID PRA data evaluation, DSS 43, February 27, 1975

$(T0)_b^a$	$(T0)_a^a$	Pseudo-DRVID	
		Meters	RU
Valid acquisitions			
02:55:00	00:35:00	62	219
Invalid acquisitions			
00:35:00[b]	18:50:00	24,216	84,756
00:35:00[b]	20:30:00	23,336	81,676
00:35:00[b]	22:20:00	2,475	8,662
00:35:00[b]	23:30:00	60,738	212,584
01:45:00	00:35:00**	18,731	65,560
05:00:00	02:55:00**	10,347	36,214

[a]Times in GMT.
[b]The "good" acquisition of the pair.

Table 5. Pseudo-DRVID PRA evaluation statistics

Station	Date, 1975	Valid acquisitions	
		Mean, m	Standard deviation, m
43	March 15	5.6	2.6
63	February 15	11.4	4.2
63	February 12	11.3	10.0
Combined above		9.3	6.2

Automatic Total Recall System Test Program

G. L. Mock
Network Operations Office

The Automatic Total Recall System (ATRS) Operational Program provides a very important data retrieval function from the Deep Space Stations to the Mission Control Center. The operational integrity of this program must be verified after any software changes have been made to it or after any hardware modifications have been made at the Deep Space Stations. The ATRS Test Program provides this capability by simulating the ATRS function of the Mission Control Center.

I. Introduction

The Deep Space Station (DSS) Telemetry and Command Subsystem (TCD), along with the Ground Communications Facility (GCF), provides a communications link between the spacecraft and the Mission Control Center. The TCD is responsible for transmitting commands to the spacecraft and recovering incoming telemetry data from the spacecraft. The TCD generates a real-time Digital Original Data Record (DODR) of all telemetry and command data transmitted over the communications link between the DSS and the Mission Control Center. If, for any reason, an incomplete data record is received at the Mission Control Center, the DSS can replay the data from the DODR by using the Automatic Total Recall System (ATRS) Operational Program (Ref. 1).

II. Purpose

The purpose of the ATRS Test Program is to provide an independent on-station means of testing and verifying the ATRS function at the DSS. This task is accomplished by simulating the Mission Control Center ATRS function and performing tests on the response made by the ATRS Operational Program. This effectively eliminates the need for scheduling the Mission Control Center for the development, implementation, and testing of the ATRS function until it is considered operational.

III. Program Structure

The ATRS Test Program was designed and implemented for use on either the Digital Instrumentation

Subsystem (DIS) or Telemetry and Command Processor (TCP) computers located at the DSSs. The program was designed to be mission-independent and implemented in modularly structured assembly language to facilitate future expansions and modifications. The program resides on magnetic tape and is loaded by means of a paper tape bootstrap loader.

IV. Functional Description

Under operator control, the ATRS Test Program formats and displays ATRS initialization and recall request blocks and transmits them to the ATRS Operational Program over the high-speed data (HSD) or wide-band data (WBD) communications lines. These blocks contain descriptions of, and requests for, blocks of data from the DODR. Additionally, the ATRS Test Program retains the information from these blocks as a means of testing the ATRS Operational Program's responses.

When the ATRS Operational Program receives both the initialization and recall request blocks, it searches the DODR and plays back the data over the HSD/WBD communications line to the ATRS Test Program. The ATRS Test Program receives these blocks and compares the data block type, the data block time, and the sequencing of the blocks against the reference information. Any discrepancies are noted by the outputting of error messages on the operator-selected input/output device. The ATRS Test Program also has the capabilities of selectively displaying any data block received and writing its own ODR of all data blocks received.

V. Conclusions

The ATRS Test Program is a very useful tool in that it has helped to automate the implementation and testing of the ATRS function at the DSSs. It also has proved to be very useful in the development of the ATRS operational software due to its ability to simulate the ATRS function of the Mission Control Center.

Figure 1 shows the configuration and interface of the ATRS Operational Program and the ATRS Test Program at the Deep Space Stations.

Reference

1. Hlavaty, F. M., "Automatic Total Recall Program for Replay of DSN 7-Track DODRs," in *The Deep Space Network Progress Report 42-25*, pp. 137–141, Jet Propulsion Laboratory, Pasadena, Calif., Feb. 15, 1975.

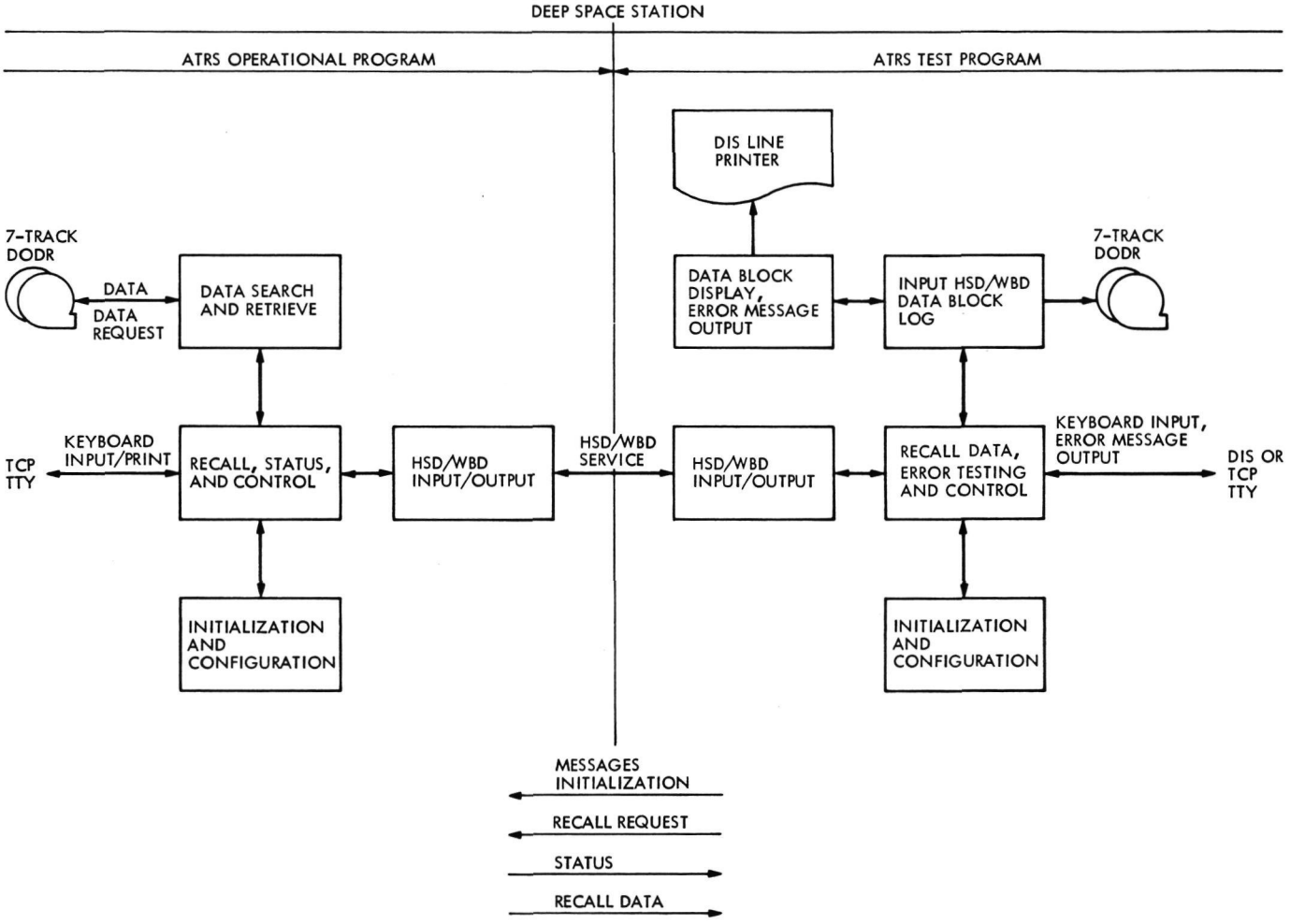

Fig. 1. Automatic Total Recall System test configuration

Operations Analysis of Intermediate Data Record Production in the Viking Era

D. C. Card
Network Operations Office

As a final step in the operations analysis of Intermediate Data Record (IDR) production capability, dynamic system simulation models have been constructed and executed within the context of the General Purpose Simulation System (GPSS) applications program on the Univac 1108 system. The dynamic models simulate all activity in the DSN ground systems which contributes to data flow characteristics and ultimate throughput times for the IDRs.

Two basic model versions have been constructed, representing alternative configurations at the merge processor: Model A simulates 4 tape-drive units at the merge processor; Model B simulates 8 tape-drive units. It has been confirmed subsequently that the 8 tape-drive configuration will be implemented. Both basic models were "driven," in dynamic simulation runs, by the same "worst case" mission support profile, representing the heaviest possible support requirement during the Viking encounter and planetary experiment period.

Quantitative specification for system parameters, flow logic, and support profiles has been derived from internal JPL documents. Much of the essential specification for dynamic models was immediately at hand as a consequence of earlier "static" analysis studies.

A 4 tape-drive configuration was found to meet a 24-hour throughput time requirement for IDRs. However, the simulated facilities are heavily loaded by the "worst case" profile; therefore, significant deviations from assumed facility availability or operational capabilities may have a critical effect upon performance to the requirement.

With an 8 tape-drive configuration, the Merge Processor easily meets the throughput time requirement. The simulated facilities show no severe utilization

stress, and the configuration provides sufficient input/output capability that recall operations are not delayed on-queue waiting for Merge Processor facility availability (not the case for the 4 tape-drive configuration).

I. Introduction

This article reports the principal results of an operations analysis task which has culminated in the development and application of computer-based dynamic simulation models of data flow in the DSN systems essential to the production of Intermediate Data Records (IDRs). The immediate motivation has been to determine whether specific systems configurations possess sufficient capability to produce IDRs within 24 hours of end-of-pass during heavy demand periods on the network, such as that anticipated during Viking encounter and planetary experiment.

The effort is the logical extension of a series of operational capabilities studies; it has been carried out in the period from March 1 to June 30, 1975, resulting in the completion of working, programmed simulation models of mission data flow from deep space station (DSS) site to IDR production.

The impetus for analyzing the operational capabilities to produce IDRs was provided by a network commitment to provide engineering and science IDRs within 24 hours from the end of the associated station tracking and data acquisition pass. This performance requirement originally arose as a defined requirement of the Viking project. It was subsequently reflected as a general DSN performance requirement in the DSN Operations Control Center Requirements.

Because of anticipated heavy support demands upon the Network during the Viking era, there was concern in the Network Operations organization that such a performance requirement might not be met uniformly using the planned facility configurations. In response to these concerns, several "static" time-line studies were performed. These studies showed that, under ideal conditions and in a "worst case" network loading period, the planned configuration with 4 tape-drive units at the Merge Processor appeared to be adequate to meet the requirement. However, the time-line approach was essentially deterministic in structure and could not admit random events, such as equipment failure or operations variability, just from a practical standpoint. As a result, the bounds on feasible system and operations characteristics which would permit the requirement to be met remained uncertain. The logical continuation of the operational performance analysis was to construct relatively detailed dynamic models to simulate operations, using a digital computer. This approach makes accessible results that reflect a broader, more complete representation of the system characteristics which will affect performance, including the pertinent random events.

The extended dynamic simulation analysis has been performed using the General Purpose Simulation System (GPSS) program on the 1108 system. This choice was made on the basis of accessibility of the 1108 systems programs and availability of GPSS modeling expertise in the Network Operations organization.

The results of this approach to operations analysis for a complex system operation have the further distinction of demonstrating both the effectiveness and utility of this technique as applied to network operations analysis.

II. Objective

The principal objective of this operations analysis effort has been to develop an effective tool capable of providing the information necessary to determine whether or not designed network control configurations, along with their specified functional design, will meet established requirements. The general criteria for effectiveness which have been followed in this effort are:

(1) The models and analytic methods used should be valid representations of the operating systems and their functional design; further, the representations should be visible such that validity may be assessed.

(2) The analytic models should permit the incorporation of realistic system specification and assumptions, insofar as these are known or can be estimated at any time.

(3) Analysis should be able to respond to engineering and management needs for quantitative evaluation of system design.

(4) Access to results from fully developed analysis models should be timely (a few days) and economical.

(5) The output results of analytic models must be readily interpreted into usual system engineering

descriptive parameters, such as throughput times, element availability, and facility utilization.

III. Operations Analysis Approach

In order to meet the objective, it was decided to use the General Purpose Simulation System (GPSS) application program as the central tool in the operations analysis. The reasons for this choice include:

(1) GPSS is a developed, available user applications program.

(2) Extensive past experience with GPSS is available in the system support group.

(3) GPSS, in its organization and design, is directly suited to the detailed analysis of traffic-flow systems having discrete traffic units.

(4) Use of a powerful and versatile montecarlo system allows effective automation of operations analysis, minimizing the amount of analytic modeling requiring other methods.

Because the Network systems, the data records production, and the systems functional design and specification were at a fairly advanced state, it was anticipated that the requisite specification for quantitative modeling, at a useful level of detail, would be available, thereby shortening that part of the simulation model task which is generally the most consuming of resources; this hope was happily confirmed.

GPSS, in its structure, permits modular development of the elements which will ultimately comprise a model. This feature was used to advantage to develop the various elements which constitute a final model of the overall data records production processes. Furthermore, care has been taken to preserve modularity in the end-product simulation models, thereby increasing model structure generality such that variations in specification or modification of configuration or functional design can be incorporated into production analysis models relatively quickly.

The remaining sections of this report describe the configurations and functional design of the system, the details of model assumptions and specification, and the quantitative results yielded by these simulation models.

IV. Requirements of the Analysis Approach

Because development of the system models themselves "simulates" the design and implementation of a functioning system, the requirements which the analyst must meet are the following:

(1) System block diagram. This provides a general "map" of traffic flow from initiation to destination, as well as a general indication of the boundaries of functional independence within the overall system (the "blocks").

(2) Description and diagrams of the functional logic of each element of the system. This must be provided to the level of detail which is comparable with system status and interactions which have a significant effect upon the observable measures of traffic flow.

(3) System and functional element specification. This includes primarily the quantitative specification of processes and events which affect traffic flow, such as traffic density, element capacities, reliability statistics, process times, and priorities.

(4) Description of the system dynamic "drivers." A profile of the input dynamic flow, including description of all associated parameters which distinguish traffic types in significant ways in the functional operation.

These requirements have been met sufficiently to produce the operating models described here. The sources for these requirements are the documents mentioned at the beginning of the memorandum.

Because of these relatively demanding requirements, the initiation of system simulation efforts early in the functional design process often is useful in identifying areas where design details are poorly understood, require more specific attention, or where conflicts and ambiguities exist.

V. Brief Description of the System

Figure 1 depicts graphically the data record flow system, from input to output, which is the subject of the analysis models. The modules of the computer simulation models correspond with the major elements of the system, shown as blocks in the diagram. The basic unit of traffic considered is the data block, so that the dynamic units "flowing" in the simulation models provide for events and model bookkeeping at the data block level (although each dynamic entity during simulation generally represents a collection of data blocks, the objective being economy of required computing without sacrifice of mode validity or flexibility). The first level of distinction among data flow types, introduced at the input, is the triple specification:

mission, deep space station source, and high-speed or wideband type.

VI. Brief Description of the Models

There is currently available for analysis purposes one basic model of the data flow and data records production in the Network for the Viking era. Two versions of this model exist and have been used to generate numerical results: one version provides for 4 tape-drive units at the Merge Processor (Model A); the other provides for 8 tape-drive units (Model B), a network configuration design which arose while Model A was being developed.

The simulation models are modular in structure, with logic modules and their associated assumptions and attributes as, follows:

(1) *DSS Module.* Routes real-time data pass representatives to the Comm Log Processor module, and creates a digital original data record representative for records bookkeeping and later coordination with recall activity. Assumes existence of a single-thread, serial facility which is not interrupted by ancillary activity (such as recall) during real-time pass activity. Any particular complement of DSSs, providing mission support during a time-span of interest, may be represented in the models.

(2) *Comm Log Processor Module.* Provides two basic model functions: network data log (NDL) coordination and bookkeeping, and generation of gap statistics to be associated with each data stream representative. This module is subdivided into three submodules which provide the necessary logical structure:

(a) High-Speed (HS) Data NDL Module. Generates NDL representatives and performs the bookkeeping which assigns to each representative a unique identifier and the number of passes associated with it. The current models assume NDLs are recorded according to a fixed schedule which is coordinated with pass support.

(b) High-Speed Data Module. Associates with each high-speed data stream representative the identifiers of the NDLs which are active during the pass period, and the gap statistics generated for each particular pass.

(c) Wideband Data Module. Associates with each wideband (WB) data stream representative the number of NDL tapes generated during the pass, and gap statistics for the data stream.

(3) *Network Data Log Transfer Logic.* Provides for direct transfer of NDLs to the Merge Processor, except in the case of Real-Time Monitor outage during production, in which case NDLs are first captured to fill-in the RTM outage, and then transferred to the Merge Processor. Allowance for RTM needs so far affects only the HS data streams in the models, since the precise effect on WB streams was unknown to the author. Wideband logs are therefore transferred directly to the Merge Processor at the end-of-pass.

(4) *Gap Edit and Recall Request Module.* Receives the data stream representatives after the pass, for both wideband and high-speed data. Simulates any additional time required for Gap Lists to be turned over from the monitor (there is currently no active module for monitor subsystems, since it is assumed that monitor does not impinge directly on the data records throughput except in the two ways mentioned). Simulates the process time required to generate edited gap lists and data recall requests. Priority is then assigned the data stream representatives to give data recall activity priority over intermediate data record (IDR) merge processing in competition for facilities at the Merge Processor. The data stream representatives become "recall request" representatives as they pass into the Merge Processor job sequencing chain at this point. A Gap Editor Availability module is associated with the Gap Edit module to represent intervals during each simulated day when the edit operator is not available, and edit jobs which become active or are waiting at these times are further delayed until the edit operator resumes activity.

(5) *Merge Processor Module.* Provides for the logical control and simulation of recall data tape production and data merge for IDR production. In order to accomplish these functions, the module is partitioned into several logical units:

(a) Recall Chain. Receives any entering recall task which must wait for available facilities. Strict control of task sequencing is maintained by use of a "chain" entity. Recall tasks have priority over merge tasks. Within the recall class, the order is first-in first-out.

(b) IDR Chain. Receives merge tasks which must wait for facilities. Ordering within the merge class is first-in first-out.

(c) Three additional chain entities, NDL, Merge, and Temp, provide ordering and flow control for

HS NDL representative transactions at the Merge Processor.

(d) Tape-drive unit facilities represent "single-thread" operation of the tape drives in both models. Jobs awaiting facility availability on the Recall or IDR chains will wait until sufficient tape-drive facilities are available before proceeding to execute task simulation at the Merge Processor.

(6) *Reliability/Availability Modules.* In addition to the Gap Editor availability module, there are also present in the current models reliability simulation modules for Real-Time Monitor (insofar as the flow of NDLs is affected), Merge Processor, and Merge Processor Tape-Drive Units.

VII. Description of the Dynamic Drivers

The discrete dynamic entities in GPSS models are referred to as "transactions." Transactions, which simulate the traffic units in a dynamic traffic-flow simulation, may be assigned and carry with them various parametric values of significance to the particular model. In this model, three classes of transactions are generated as the dynamic system drivers:

(1) Data pass representative transactions.

(2) HS data NDL transactions.

(3) Drivers for the various unreliability/availability modules.

VIII. Data Pass Representatives

The models are designed to allow for an arbitrary number of DSS-mission-data type generators. The current models incorporate 14 distinct "data pass" representatives of this type. The module which generates these dynamic entities associates with them:

(1) Pass start time.

(2) Pass duration.

(3) DSS identifier.

(4) Project identifier.

(5) Data type identifier (high speed or wideband).

(6) Data rate for telemetry stream represented.

Each pass generator may initiate passes according to a predetermined and specified view period profile. In the current versions, a simple, fixed view period profile is assumed wherein each pass for a particular stream has a fixed duration and successive passes begin 24 hours after the beginning of the next preceding pass, for the whole interval simulated. All these simplifying assumptions may be relaxed in order to incorporate more realistic view period profiles, if there are cases in which these parameters have a significant effect upon the outcome. Table 1 summarizes the complement of telemetry data streams represented in the current models. The simulator clock unit is *minute.*

The profile models are designed to represent a "worst case" support load during Viking encounter. Time can be simulated continuously in any model run up to 90 days. Driver profiles may be constructed to simulate support schedules and data profiles which change over time.

IX. High-Speed Data Network Data Log Representatives

The production of wideband data network data logs (NDLs) at the Comm Log Processor appears to be heavily dependent upon each WB data pass, since, otherwise, none are produced. Therefore, it is not necessary to simulate a separate NDL entity flow; all necessary information can be carried along by each WB data pass transaction. High-speed data NDLs, on the other hand, may be produced successively according to a schedule which is not dominated by any single data pass consideration; because of this essential "pass-independence," the HS NDLs must be represented as separate model entities. The NDL module generates a sequence of contiguous NDLs according to a specified schedule. The NDLs and the HS data passes which should be associated with them (i.e., passes which are actively yielding HS data during the recording time of the NDL) are mutually coordinated in the model by cross-indexing the NDL identifiers to associated data pass transactions.

Beginning at model "epoch," the HS NDLs have record times of 7, 9, and 8 hours, in succession, a sequence which is periodic throughout model runs. Since data passes and HS NDL cycles are periodic with periods of 24 hours, the NDL cycle has been chosen to yield a convenient recording schedule. Figure 2 shows graphically the association between HS NDLs and telemetry stream data passes recorded on them.

The HS NDLs pass from active "recording" status to:

(1) Merge Processor to await IDR production for each of the data streams associated, or

(2) The "Real-Time Monitor (RTM)–System Performance Record (SPR) fill-in" model if an RTM outage

has occurred during the active time of the NDL, then to (1).

X. Drivers for Unavailability Modules

Each reliability or availability module in the models generates its own independent dynamic event driver. The event driver controls failure event initiation (or other facility unavailability) for its particular associated system element. It also controls the associated down-time for each of these events. Both the intervals between outage and outage duration are sampled according to analyst-specified distributions. Table 2 summarizes the various down-time and unavailability events associated with the current models.

XI. General Model Assumptions and Model Specification

A. General Assumptions and Model Features

(1) Telemetry data streams, including post-pass recall, are simulated according to the system-driver time table and rates given in Table 1. These streams and their interactions with the functional systems are the most directly related to the throughput times for IDR production. Monitor, command, and metric data streams are not specifically simulated as distinct dynamic entities, but are maintained as a cumulative traffic composite in order to be accounted for in the production of HS data IDRs.

(2) Recall play-back begins after the real-time pass (reference documents indicate that this is a valid assumption).

(3) Recall tape production has priority over IDR merge processing.

(4) For each data pass, the merge process may begin only when all associated NDLs and the Recall Data tape are available at the Merge Processor job sequence chains.

(5) Each of the distinct data passes represented is associated one-to-one with production of a separate IDR.

B. Model Specification

(1) Input data specification for the data passes has been described above.

(2) Gap simulation for wideband data streams (all).

(a) Time between gaps: Poisson distributed with mean 1 gap/414 seconds.

(b) Gap length: Poisson distributed with mean 10 wideband data blocks (WBDB)/gap.

Result will be: expected number of gaps in 12 hours = 104; expected number of blocks lost = 1040, each 12-hour pass.

(3) Gap simulation for high-speed data streams (all).

(a) Time between gaps: Poisson, with mean 1 gap/800 seconds.

(b) Gap length (in high-speed data blocks HSDB): Poisson, with mean 2 HSDB/gap, Result: expected number of gaps in 12 hours = 54; expected number of blocks lost = 108, each 12-hour pass. These statistical parameters for HS data are hypothetical. For the 11 data streams included, these statistics yield a weighted average 0.75% recoverable data loss over all streams (99.25% of HSDB received at Comm Log Processor in real-time, ignoring nonrecoverable losses). The data quality statistics for the simulation are summarized in Table 3.

(4) Numbers of data blocks recorded per Digital Original Data Record (DODR):

(a) High-speed DODR: 85140 HSDB

(b) Wideband DODR: 54750 WBDB

(5) SPR "outages" (Model is not based on quantitative data, since none are available; the only statement in the reference documents claims that outage is a "fairly infrequent event"):

(a) Time to failure: Poisson, with mean 360 hours (15 days).

(b) Times to recover: Uniform on [13, 17] minutes (average: 15 minutes).

(6) Gap list edit time. Computed as the sum of:

(a) 0.2 minutes per gap.

(b) "Variability" factor, uniformly distributed on [0, 0.05 × (number of gaps)]; with mean 0.025 × (number of gaps) minutes.

(c) Typical values for edit times: for 50 gaps, 11.25 minutes; for 100 gaps, 22.5 minutes.

(7) Time to recall data from DSS (assuming facilities at both ends are acquired and ready):

(a) 15 ± 5 minutes "set-up" time (uniform on [10, 20]).

(b) 8 minutes read time per DODR.

(c) 2.4 minutes rewind time per DODR.

(d) 2 ± 1 minute "tape handling" time per DODR (uniform on [1, 3]).

Table 4 contains average recall times for all characteristic data streams.

(8) Wideband data pass merge process time:

(a) Number NDLs per pass: (number WBDB)/79660.

(b) Read time per NDL: 7.27 min.

(c) Rewind time per NDL: 2.4 min.

(d) Tape handling time: 2. min.

(e) Write time. Assumes 11616 Logical Data Records (LDRs) per IDR tape (11616 × 5 WBDB/LDR = 58080 WBDB/IDR tape). Write rate: 0.0356 sec/LDR, 6.9 min/IDR.

Typical merge process times which result:

DSS 14: 334 minutes (5 hours 34 minutes).

DSS 43 and 63: 225 minutes (3 hours 45 minutes).

(9) High-speed data pass merge process time:

(a) Read time per NDL: 7.27 min.

(b) Rewind time per NDL: 2.4 min.

(c) Tape handling time: 2 min.

These factors are applied to the number of NDLs on which the HS data for the particular pass are written; (a) and (b) should apply to the actual (fractional) number, and (c) applies to the integral number of tapes represented. In the case of HS NDLs, HS data pass terminations generally do not coincide with the end of the last NDL written upon. For the model, it was found that an average (over all data passes) fraction of NDL not read (after pass termination) is about 0.125 of the total NDL time. Therefore, a compensating factor has been incorporated into the general formula used to compute HS merge times, so that (a) and (b) become 0.94 × 7.27 min and 0.94 × 2.4 min, respectively.

(d) Write time: 0.02315 sec × number (LDRs).

(e) Rewind: 2.4 min × number (IDRs).

(f) Tape handling: 3 min × number (LDRs) where:

Number (LDRs) = (total HSDBs)/5

Number (IDRs) = (total HSDBs)/93430.

Some typical HSD merge process times which result are:

DSS 11: 32 min.

DSS 12: 28.4 min.

DSS 14(A): 33 min.

In case Network Operations Control Center (NOCC) were required to verify the computer compatibility of written IDR tapes, it is assumed that verification would be performed at the Merge Processor as a sequential part of the IDR production operation. The verification process model assumed by the analyst is: read IDR tapes, rewind IDR tapes. A separate simulation model version was created which includes the verification process, the additional process times having been specified as follows:

(10) Wideband IDR verification:

(a) Read-to-verify: 0.03565 sec per LDR.

(b) Rewind: 2.4 min per IDR tape.

(c) Tape handling: 3 min per IDR tape.

Verify times computed by these formulas are:

DSS 14: 140 min.

DSS 43 and 63: 94 min.

(11) High-speed IDR verification:

(a) Read-to-verify: 0.02315 sec per LDR.

(b) Rewind: 2.4 min per IDR (or fraction).

(c) Tape handling: 2 min per IDR tape.

(12) Job sequence policy at Merge Processor:

(a) Recall tape processing has priority over merge processing; i.e., if there are any recall jobs waiting on the job chain, they will always take precedence over merge processing.

(b) Within the two priority classes, jobs are sequenced according to oldest waiting job first.

The performance at the Merge Processor, compared with facility utilization and requirement to produce IDRs within 24 hours from end-of-pass, is essentially dependent upon the job sequencing policy. Nearly any quantifiable policy could be implemented as a policy model.

As of this writing, no attempt has been made to incorporate modified sequencing policies into the model runs.

XII. Simulation Results

Simulation runs have been made with both basic versions of the Automatic Total Recall System/IDR models, i.e., Model A having 4 tape-drive units, and Model

B, having 8 tape-drive units. These simulation runs have simulated 3 and 10 days support to IDR production, using the mission profile defined in a previous section. These results are tabulated in Tables 5 and 6. Other cases have been simulated, especially cases which include variable mission data profiles. These data are not included here, however, since they would not add anything significant to this summary.

Model output data in Table 5 show that the Merge Processor with 4 tape-drive units available for input/output (I/O) operations can perform within the network requirement for finished IDRs within 24 hours of end-of-pass. Obviously these results are qualified by the validity of the assumptions used (and described in a previous section). Model output statistics show the tape-drive utilization factors to be relatively high, the implication being that, in order to perform to requirement, it is necessary that a very tight control be maintained on the job sequencing schedule for 24 hours each day that such a support level is required. Furthermore, the reader is reminded that, although the model support profile may be a realistic "worst case," other model features to which throughput time is quite sensitive may be lenient; e.g., no consideration for possible wait on communications link outages, etc. These features are easily modified in the models, should there be data available to indicate that further analysis would be of some value. Therefore, it is hoped that the reader may give serious consideration to the validity of the model parametric specification.

Table 6 shows that a Merge Processor facility with 8 tape-drive units handles the load of the support profile rather easily (although model output "bookkeeping" statistics indicate that all eight units would be in use on occasion, if the job-sequencing policy were to process jobs as soon as they enter the facility, and I/O units are available).

A significant feature of the 8 tape-drive version is that it permits two simultaneous, independent merge process jobs to be done, with margin to handle one or two recall jobs. The 4 tape-drive version is strictly limited to "single-thread" merge processing.

A further analytic result which may be of some operational significance is that, on the 8 tape-drive version, no recall job waits on queue for I/O facilities, whereas, on the 4 tape-drive version, as many as three recall jobs may wait on queue at some time before I/O facilities are available for acquiring recalled data.

With the further requirement for IDR compatibility verification imposed upon the Merge Processor, under the quantitative assumptions made for verification processing times, the 4 tape-drive unit Merge Processor is no longer able to perform adequately to the 24-hour throughput requirement. The results are summarized in Table 7. Furthermore, additional model statistical output shows that I/O facilities used for merge processing (as well as recall) have a joint utilization factor over 0.92, a situation which indicates that the process is unstable and that, therefore, throughput becomes worse with increasing time.

The 8 tape-drive Merge Processor, with the additional burden of verification of IDR tapes, still meets the 24-hour requirement without difficulty; furthermore, the process remains quite stable. The throughput time statistics for 10 days simulated passes are displayed in Table 8.

Within the limitations of the initial model assumptions which have been adopted for this study and demonstration, it may be concluded that:

(1) Without the burden of IDR verification, the 4 tape-drive configuration Merge Processor would likely perform within the 24-hour throughput bound.

(2) With verification as an additional requirement, the 4 tape-drive-equipped processor is not capable of meeting requirements adequately.

(3) The 8 tape-drive configuration will meet the throughput requirement under all conditions considered thus far.

Table 1. Specification of model DSS data streams

DSS[a]	Data stream supported	Telemetry data rate, blocks/min	Data type (HS or WB)	Additional data rate (MON, TRK, CMD), (blocks/min)	Initial pass epoch[b]	Pass duration, min	Time between passes, min
DSS 11	Viking Orbiter (VO) Engr	12	HS	59	0	720	1440
DSS 12	Pioneer (PIO)	20	HS	17	1110	660	1440
DSS 14(W)	VO Sci	900	WB	0	0	720	1440
DSS 14(A)	VO Engr	24	HS	59	0	720	1440
DSS 14(B)	Viking Lander (VL) Sci + Engr	67	HS	14	30	180	1440
DSS 42	VO Engr	12	HS	59	450	720	1440
DSS 43(W)	VO Sci	600	WB	0	450	720	1440
DSS 43(H)	VO Engr	12	HS	59	450	720	1440
DSS 44	PIO	20	HS	17	270	360	1440
DSS 61	VO Engr	12	HS	59	990	690	1440
DSS 62	PIO	20	HS	17	540	660	1440
DSS 63(W)	VO Sci	600	WB	0	990	690	1440
DSS 63(A)	VO Engr	24	HS	59	990	690	1440
DSS 63(B)	VL Sci & Engr	67	HS	14	30	180	1440

[a](W) is designator for wideband data channel; (A), (B), and (H) are designators for high-speed data channels.

[b]Relative to simulated clock time, in minutes.

Table 2. Time table of events which compete for facility availability

Model facility	Event	Mean time to event	Mean duration, min	Model facility availability
Real-Time Monitor	Monitor outage	15 days		
	Downtime (at outage)		15	0.9993
Gap Edit Operator	Edit Operator "out"	4 hours	20	0.923
Merge Processor	Processor failure	10 days	20	0.9986
Tape-drive units (for 4 units)	Drive unit failure (each unit)	40 days	15	0.999 (facility)
(for 8 units)		80 days (each unit)	15	0.999 (facility)

Table 3. High-speed data loss during real-time operations (recoverable science and engineering telemetry)[a]

DSS[b]	Pass duration, min	Telemetry data rate, blocks/min	Total telemetry data blocks per pass	Blocks lost (avg) (recoverable)	Comm quality ratio
DSS 11	720	12	8640	108	0.9875
DSS 12	660	20	13200	99	0.9925
DSS 14(A)	720	24	17280	108	0.9938
DSS 14(B)	180	67	12060	27	0.9978
DSS 42	720	12	8640	108	0.9875
DSS 43(H)	720	12	8640	108	0.9875
DSS 44	360	20	7200	54	0.9925
DSS 61	690	12	8280	104	0.9875
DSS 62	660	20	13200	99	0.9925
DSS 63(A)	690	24	16560	104	0.9938
DSS 63(B)	180	67	12060	27	0.9978

[a]Weighted average data quality over all HS streams: 0.9925.

[b](A), (B), and (H) are designators for high-speed data channels.

Table 4. Expected recall times for high-speed and wideband data streams

DSS[a]	Number DODRs	Data type	Expected recall time, min
11, 12, 14 (A), 14 (B), 42, 43 (H), 61, 62, 63 (A), 63 (B)	1 (for all HS passes)	HS	25.9
14 (W)	12	WB	167.8
43 (W)	8	WB	116.2
63 (W)			

[a](A), (B), and (H) are designators for high-speed channels; (W) is designator for wideband data channel.

Table 5. Throughput time statistics to completed IDR: Model "A" (4 tape-drive units at Merge Processor) 3- and 10-day pass support simulated

DSS[a]	Number of passes[b]		Mean throughput time, hours		Standard deviation, hours	
	3 days	10 days	3 days	10 days	3 days	10 days
DSS 11	3	10	11.00	10.3	0	1.73
DSS 12	3	10	5.00	6.4	1.41	1.63
DSS 14 (W)	3	10	9.67	10.0	0.47	0.77
DSS 14 (A)	3	10	12.67	10.9	1.70	2.47
DSS 14 (B)	3	10	5.00	6.6	0	1.56
DSS 42	3	10	8.67	9.0	0.47	0.45
DSS 43 (W)	3	10	7.67	7.9	0.47	0.30
DSS 43 (H)	3	10	9.00	9.0	0	0.45
DSS 44	3	10	12.00	11.0	0	2.00
DSS 61	3	10	6.00	7.3	1.41	1.62
DSS 62	3	10	8.67	9.0	0.47	0.63
DSS 63 (W)	3	10	8.67	7.7	1.25	1.35
DSS 63 (A)	3	10	5.67	7.1	0.94	1.37
DSS 63 (B)	3	10	4.33	6.5	0.47	1.69

[a](A), (B), and (H) are designators for high-speed data channels; (W) is designator for wideband data channel.

[b]Profile generator starts, at time 0, on a "blank" system; at the end of three and ten days, respectively, the pass profile generator is "turned off" and the simulated systems complete tasks remaining without additional loading.

Table 6. Throughput time statistics to completed IDR: Model "B" (8 tape-drive units at Merge Processor) 3- and 10-day pass support simulated

DSS[a]	Number of passes[b]		Mean throughput time, hours		Standard deviation, hours	
	3 days	10 days	3 days	10 days	3 days	10 days
DSS 11	3	10	6.00	5.7	0	0.90
DSS 12	3	10	4.00	4.0	0	0
DSS 14 (W)	3	10	9.67	9.8	0.47	0.40
DSS 14 (A)	3	10	6.00	5.6	0	1.20
DSS 14 (B)	3	10	4.67	4.6	0.47	0.49
DSS 42	3	10	6.33	6.2	0.47	0.40
DSS 43 (W)	3	10	7.00	7.0	0	0
DSS 43 (H)	3	10	6.00	6.0	0	0
DSS 44	3	10	7.00	6.5	0	1.50
DSS 61	3	10	5.00	4.9	0	0.30
DSS 62	3	10	6.00	6.0	0	0
DSS 63 (W)	3	10	7.00	6.9	0	0.30
DSS 63 (A)	3	10	4.67	5.0	0.47	0
DSS 63 (B)	3	10	4.33	4.6	0.47	0.49

[a]See footnote a, Table 5.

[b]See footnote b, Table 5.

Table 7. Throughput time statistics for IDR: Model "A" with verification processing 10-day support simulated

DSS[a]	Number of IDRs[b] completed	Mean throughput time, hours	Standard deviation, hours	Range of throughput times, hours
DSS 11	10	12.20	3.89	6–18
DSS 12	9	15.44	4.19	10–21
DSS 14 (W)	10	19.20	3.99	12–25
DSS 14 (A)	10	12.40	3.53	7–17
DSS 14 (B)	10	11.10	3.48	5–16
DSS 42	10	14.60	4.80	7–23
DSS 43 (W)	10	18.50	3.75	12–23
DSS 43 (H)	10	15.10	5.01	8–24
DSS 44	10	12.50	3.59	7–17
DSS 61	10	14.70	4.67	8–22
DSS 62	10	18.20	3.92	13–24
DSS 63 (W)	9	16.78	3.85	9–21
DSS 63 (A)	9	14.44	4.79	8–22
DSS 63 (B)	10	11.10	3.70	4–16

[a]See footnote a, Table 5.

[b]See footnote b, Table 5.

Table 8. Throughput time statistics for IDR: Model "B" with verification 10-day pass support simulated

DSS[a]	Number of IDRs[b] completed	Mean throughput time, hours	Standard deviation, hours	Range of throughput times, hours
DSS 11	10	5.9	1.04	3–7
DSS 12	10	4.9	0.30	4–5
DSS 14 (W)	10	12.1	0.30	12–13
DSS 14 (A)	10	6.3	1.49	2–7
DSS 14 (B)	10	4.8	0.40	4–5
DSS 42	10	6.5	0.50	6–7
DSS 43 (W)	10	8.7	0.46	8–9
DSS 43 (H)	10	6.5	0.50	6–7
DSS 44	10	6.6	1.20	3–7
DSS 61	10	5.3	0.64	4–6
DSS 62	10	6.8	0.40	6–7
DSS 63 (W)	10	8.5	0.50	8–9
DSS 63 (A)	10	5.5	0.50	5–6
DSS 63 (B)	10	4.7	0.46	4–5

[a]See footnote a, Table 5.

[b]See footnote b, Table 5.

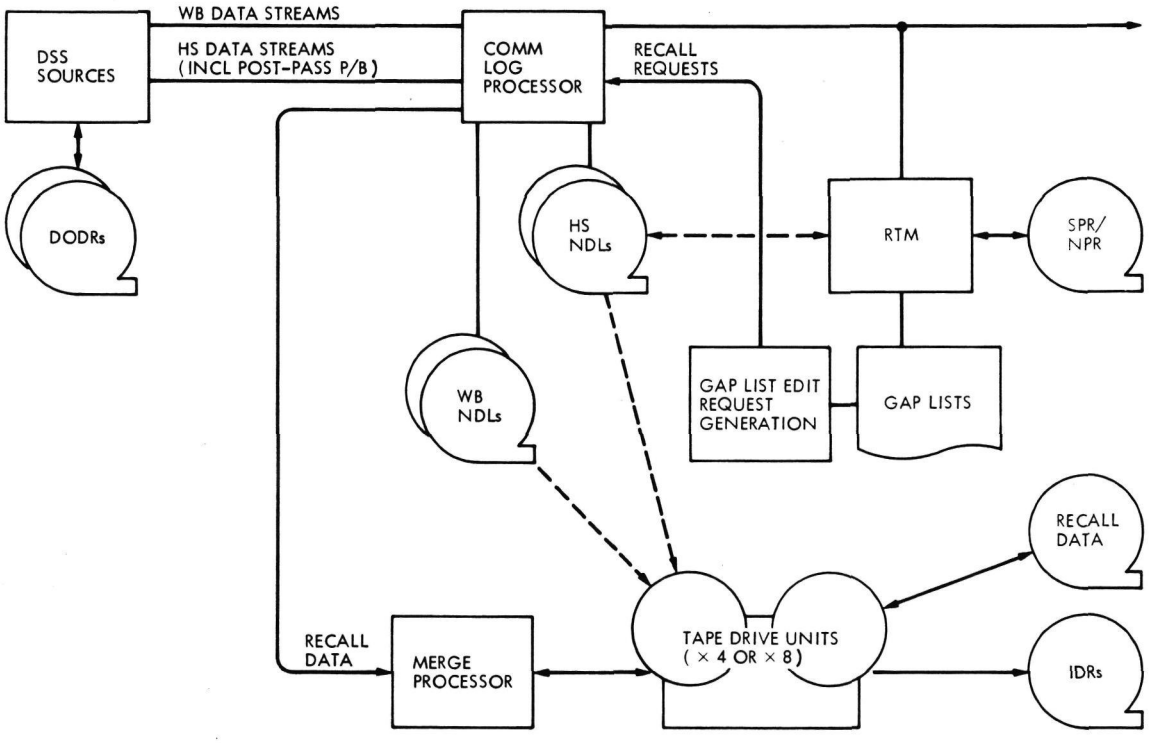

Fig. 1. Network data records block diagram

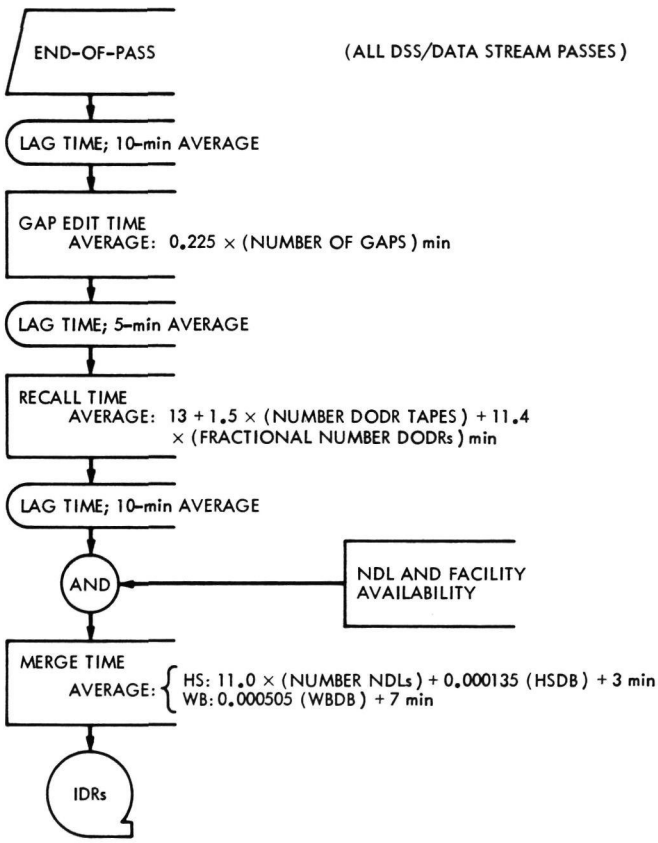

Fig. 2. Flow sequence to IDR production

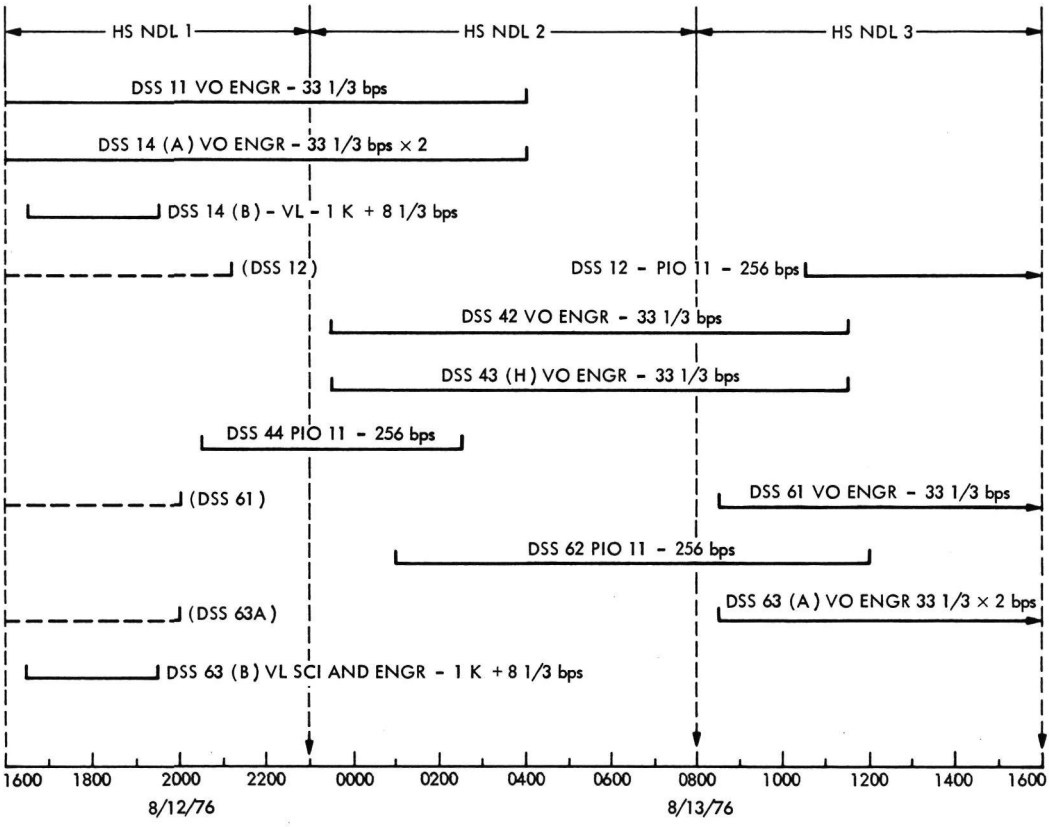

Fig. 3. High-speed data passes and high-speed data NDL (telemetry data)

Coordinate Measuring Machine and Programmable Calculator

H. A. Greth and J. Kundrat
Quality Assurance DSN and Mechanical Hardware Section

Quality Assurance Mechanical Inspection, anticipating the need for improved measuring techniques for the various Laboratory programs, has purchased a Coordinate Measuring Machine which has the capability of significantly reducing inspection time while increasing reliability.

I. Introduction

It was necessary for JPL Quality Assurance to find improved methods of performing inspections with speed and reliability. Commercially available equipment would have to meet the following criteria:

(1) Expand measurement capabilities.

(2) Reduce set-up time (man-hours).

(3) Increase speed and accuracy.

(4) Have English (inch)/metric display and printout capabilities.

The Coordinate Measuring Machine, equipped with a programmable calculator, expands measuring capabilities and, in place of time-consuming manual recording and calculations, instantly computes and prints out measurements.

II. Description of Equipment

The Coordinate Measuring Machine (Fig. 1) is a three-axis X,Y,Z measuring device. Each axis is provided with bronze air bearings which allow all measuring axes a frictionless noncontact movement, assuring a deflection-free measurement.

The measuring system employs a principle of reading fluctuations of light intensities through photocells. These photocells pick up the changes in intensities which are 90 deg out of phase. Then, through electronic circuitry, these measurements are digitally displayed in either English or metric.

A feature of the machine is the touch trigger probe. This probe is an omnidirectional electronic null-sensing device with a repeatability of 1.0 μm (0.00005 in.) and feather-touch sensitivity of 0.04 N (4 g). The touch trigger probe, for example, with a contact point having a right angle bend, could be used to check in any direction the

depth and height of internal grooves or bores having stepped diameters.

The programmable calculator (Fig. 2) is the heart of the Coordinate Measuring Machine and uses a pre-programmed cartridge tape to perform operations previously requiring the use of a computer. It has a 12-digit readout display and a hard copy printer which permanently records all measurements.

A choice of measuring systems (Cartesian or Polar) is provided, and single-point or multipoint measuring methods (Fig. 3) may be programmed. The Cartesian System is for determining the location of a point in relation to two straight lines. This is frequently used in box-type rectangular dimensioning. The Polar Coordinate System determines the location of a point in relation to its radius vector from a fixed origin. Polar coordinates are frequently used for measuring bolt holes and circles.

The single-point method is for measuring the center distance between patterns with a tapered probe or a ball probe, or for measuring along the edge of a part. Multipoint methods are used for measuring hole diameters and determining the center by measuring points on the wall of the hole with a ball probe. All desired information is provided by the calculator.

An important feature is automatic alignment, which compensates for misalignment between the workpiece on the measuring table and the measurement axes by calculating a correction factor and applying that factor to the measurements taken.

Specifications

Resolution: 0.002 mm or 0.0001 in.

Measurement accuracy: ±0.012 mm or ±0.0005 in.

Repeatability: ±0.005 mm or ±0.0002 in.

Work table: Solid black granite with stainless steel thread inserts

Bearings: Frictionless air bearings (open adjustable type)

Measuring range: X 685 mm or 27 in.; Y 508 mm or 20 in.; Z 457 mm or 18 in.

III. Previous Test Methods Versus Coordinate Measuring Machine

Previously used methods of inspecting hardware were generally confined to the use of height gages, dial indicators, and depth gages. These instruments were used to measure such parameters as roundness, flatness, true position, etc. The hand method of measurements is slow and subject to human error.

The Coordinate Measuring Machine can be programmed to handle parameters of true position, roundness, and flatness. The following are examples of calculator measurement programs:

Example 1 (Fig. 4) illustrates a program which measures the center in polar coordinates and the diameter of holes and bosses using the multipoint method with ball probe which permits use of automatic alignment. Measurements are taken in any of three planes, with a printout of radius angle, diameter of holes, and X, Y dimensions.

Example 2 (Fig. 5) illustrates a program which measures the concentricity of two features, with the second feature taken at maximum material condition (MMC). The multipoint method using a ball probe for measurements and deviations is expressed as a diameter or total indicator reading (TIR). The printout shows concentricity limit as a tolerance, with deviations of out-of-tolerance conditions.

Example 3 (Fig. 6) illustrates a program which measures the roundness of a feature, holes or bosses, and inside or outside radii, using the multipoint method.

Example 4 (Fig. 7) illustrates a program which measures true position regardless of feature size, using the Cartesian Coordinate System. If the diameter being measured does not lie within the prescribed diameter tolerance, the closer deviation limit is used in the true position calculation.

Example 5 (Fig. 8) illustrates a program which measures a pattern generation. This program, having axis starting point and axis spacing with the offset angle along each axis, is all that is required to generate a rectangular or circular pattern.

IV. Summary

When dealing with a number of parts having many critical tolerances, the hand method is very time-consuming, and very often costly attachments are needed to perform the inspection required. By using the Coordinate Measuring Machine with calculator and touch trigger probe, hardware is inspected quickly and accurately, with all measurements automatically printed out for a complete record of dimensions.

This machine is definitely cost-effective and reduces Quality Assurance costs in the following ways:

(1) It increases inspection productivity by a factor of three to one (as compared to the conventional surface plate, height gage, and indicator method).

(2) Its use requires no special tooling (eliminates the cost of jigs and fixtures).

(3) It eliminates human error. Problems that are inherent in transcribing data manually are nonexistent and thus inspection down time is reduced.

Bibliography

Validator 50 Manual, Brown & Sharpe Manufacturing Co., North Kingstown, R. I., June 15, 1974.

"Computer Capabilities," Fact Sheet Val-CC, Brown & Sharpe, North Kingstown, R. I.

"Val-Calculator," by Textronix, Fact Sheet Val-Cal, Brown & Sharpe, North Kingstown, R. I.

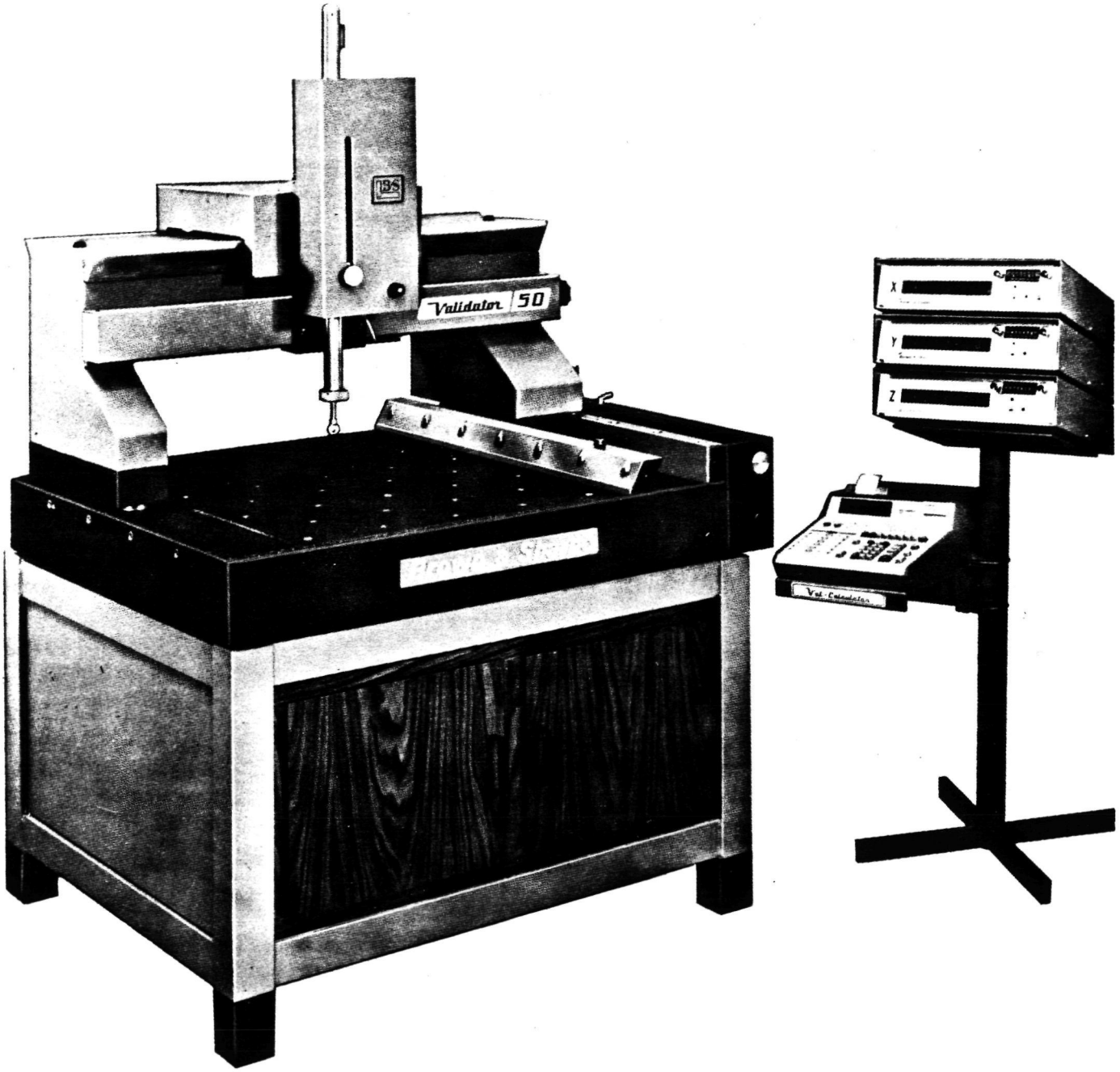

Fig. 1. Coordinate measuring system

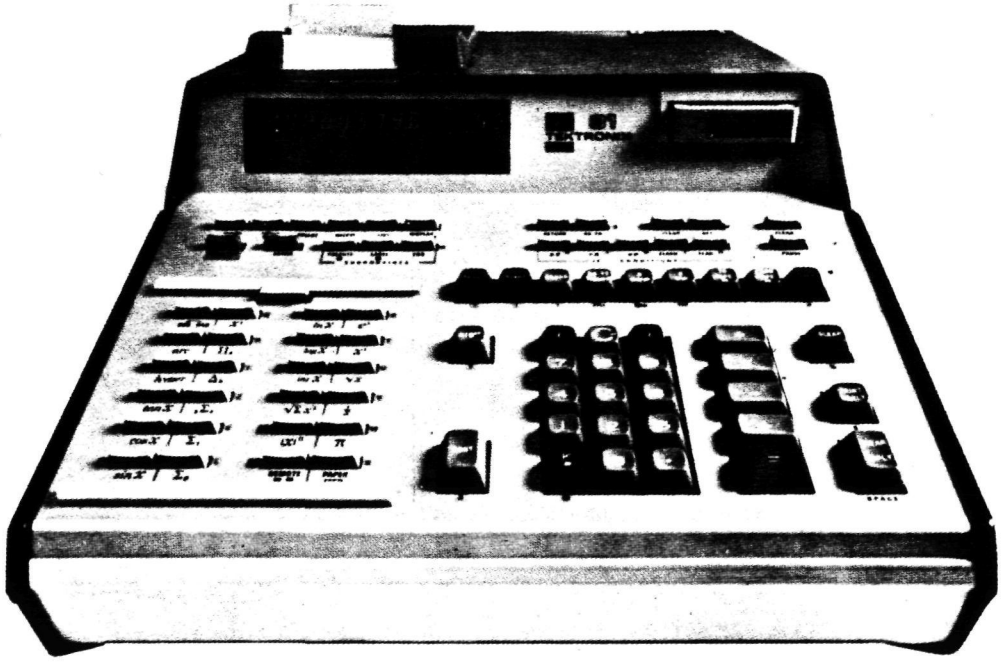

Fig. 2. Programmable Val-Calculator

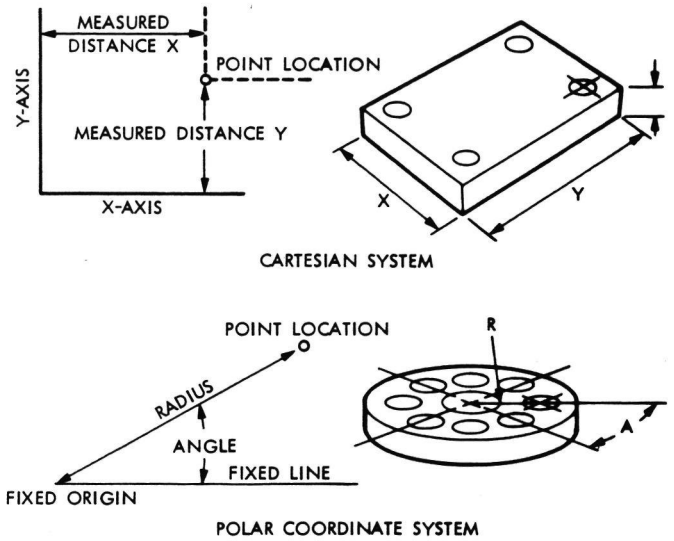

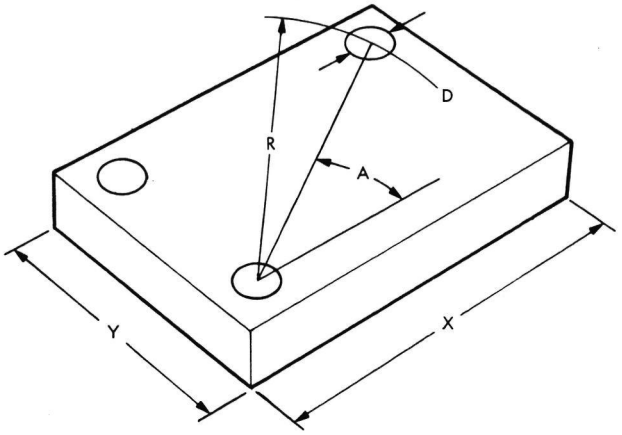

Fig. 4. Three-plane measurement

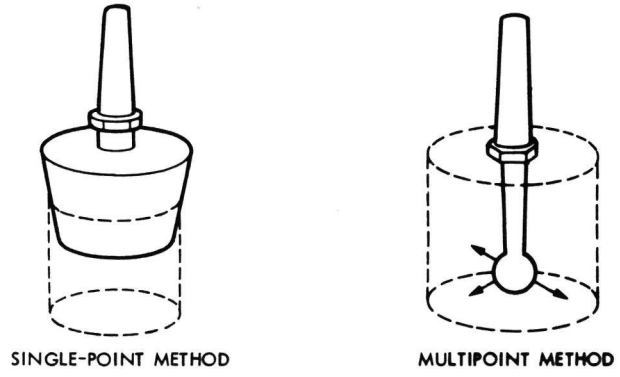

Fig. 3. Single-point and multipoint measuring methods

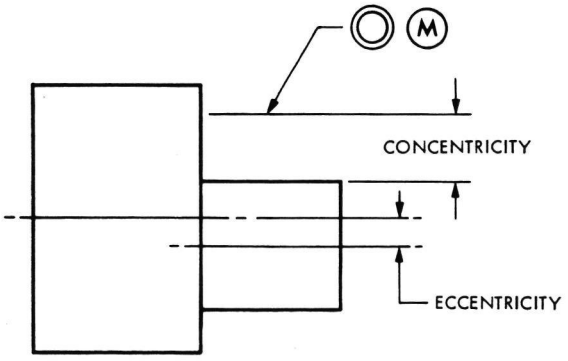

Fig. 5. Concentricity measurement

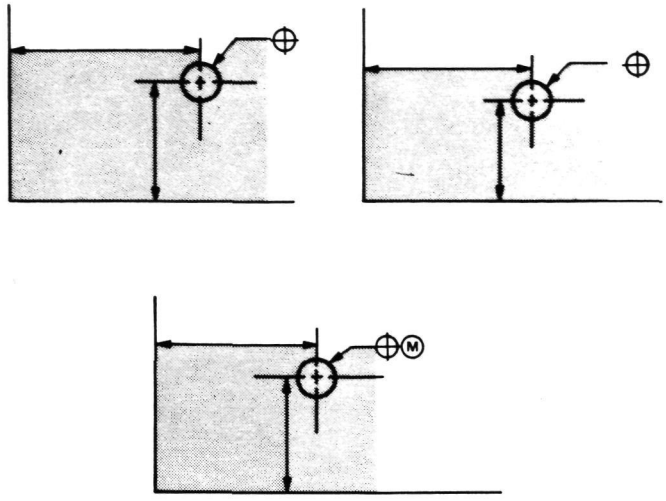

Fig. 7. True position measurement

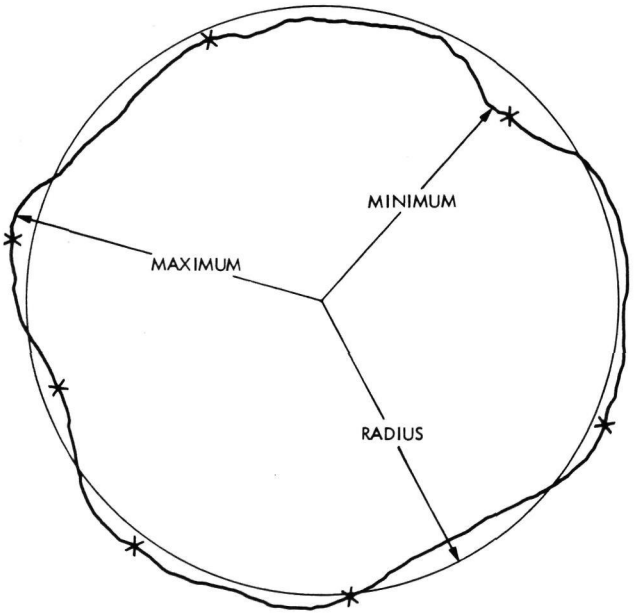

Fig. 6. Roundness measurement

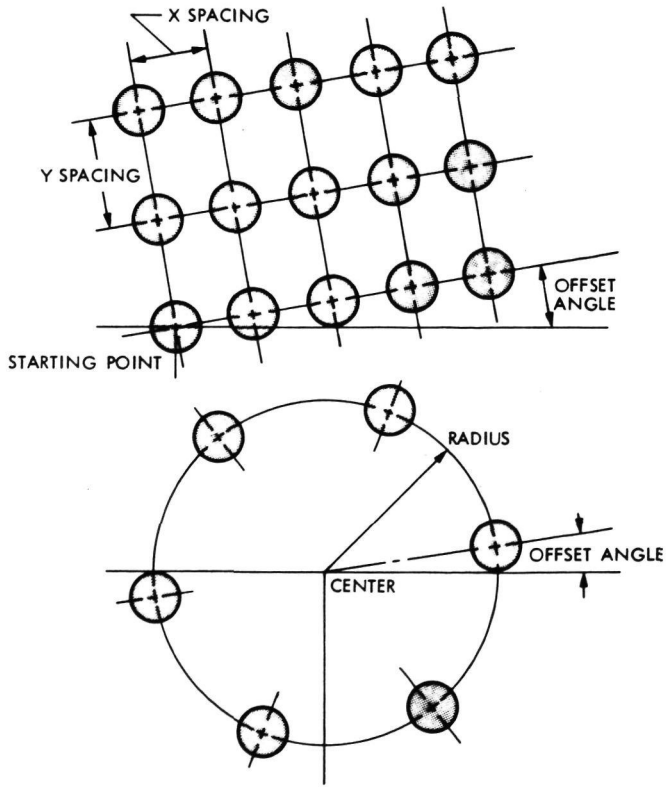

Fig. 8. Pattern generation measurement

NASA — JPL — Coml., L.A., Calif.